

INTEGRATED STRATIGRAPHIC, STRUCTURAL,  
TECTONIC, AND PETROLEUM SYSTEMS ANALYSIS  
OF THE MISSISSIPPIAN CANEY SHALE, ARDMORE  
BASIN, SOUTHERN OKLAHOMA

By

IAN ANTHONY ALLAN COX

Bachelor of Science in Geology

Western Colorado University

Gunnison, Colorado

2019

Submitted to the Faculty of the  
Graduate College of the  
Oklahoma State University  
in partial fulfillment of  
the requirements for  
the Degree of  
MASTER OF SCIENCE  
December, 2021

INTEGRATED STRATIGRAPHIC, STRUCTURAL,  
TECTONIC, AND PETROLEUM SYSTEMS ANALYSIS  
OF THE MISSISSIPPIAN CANEY SHALE, ARDMORE  
BASIN, SOUTHERN OKLAHOMA

Thesis Approved:

Dr. Jack C. Pashin

---

Thesis Adviser

Dr. Mohamed G. Abdelsalam

---

Dr. James O. Puckette

---

## ACKNOWLEDGEMENTS

This research was funded primarily by the National Energy Technology Laboratory of the U.S. Department of Energy under Grant DE-FE0031776. Cost share was provided by Continental Resources, the principal industry partner in the study, and by the other participants in the grant.

I thank Dr. Jack Pashin for advising my studies and suggesting the Caney Shale as an area of research. His ability to offer guidance, inquisitive commentary, and support while enabling me to formulate my own project ideas and progress in my research has been the basis of a great partnership. Thanks are also extended to my committee members, Drs. Mohamed Abdelsalam and James Puckette, for their insightful advice, critiques, and administrative support during mostly unplanned meetings and Tectonics Group presentations.

Thanks to Brian Cardott of the Oklahoma Geological Survey for providing maturity data and for enlightening emails and phone calls. Generous software grants from Schlumberger, Esri, and Wolfram have facilitated computational work for this project. Well and production data were kindly provided by Enverus.

I would also like to thank my geology professors at Western Colorado University, especially Drs. Bradford Burton, Elizabeth Petrie, and Mr. Gary Steffens, for preparing me for a career in geology and for their continued advice and support.

Finally, much gratitude is owed to my family, especially my mother, father, and sister, for the many ways they have supported and encouraged me throughout all of my schooling. Thank you.

Ian A. Cox

Name: IAN ANTHONY ALLAN COX

Date of Degree: DECEMBER, 2021

Title of Study: INTEGRATED STRATIGRAPHIC, STRUCTURAL, TECTONIC, AND  
PETROLEUM SYSTEMS ANALYSIS OF THE MISSISSIPPIAN  
CANEY SHALE, ARDMORE BASIN, SOUTHERN OKLAHOMA

Major Field: GEOLOGY

Abstract: Burial and thermal history modeling were used to assess the thermal maturity of the Mississippian (Chesterian) Caney Shale in the Ardmore Basin, southern Oklahoma, to determine the formation's viability as an unconventional oil and gas play. All models display a similar tectonic evolution with subsidence during and following Cambrian Iapetan rifting, tectonic stability during a passive margin phase from the Silurian–Late Mississippian, synorogenic subsidence during the Pennsylvanian, post-orogenic subsidence during the Permian, regional uplift and unroofing from the Late Permian to Early Cretaceous and Gulf of Mexico Coastal Plain subsidence during the Early Cretaceous to Paleogene. Rapid, episodic Pennsylvanian subsidence appears to have been synchronous with sequential uplift of the Wichita Mountains and then the Arbuckle Mountains in response to major left-lateral transpression. The rapidity of subsidence suggests that the Ardmore Basin functioned episodically as an elevator basin, which is typical of sedimentary basins in oblique-slip mobile zones.

Calculated vitrinite reflectance and geothermal gradients were calibrated to measured vitrinite reflectance and temperature data (corrected bottom-hole temperatures) respectively, to ensure model validity. A source of uncertainty is modeling Permian–Cretaceous erosion. Calibration of these models requires erosion of approximately 5,000 ft of strata. The eroded overburden section was not uniformly distributed, as areas of high structural relief, such as the Arbuckle Uplift, appear to have had significantly less sediment cover than the basin proper. Regional variation in the thickness of eroded Permian sediment, which apparently formed a wedge that thickened toward the Anadarko Basin, and the Cretaceous–Paleogene Gulf of Mexico sedimentary wedge, which apparently thickened southeastward, affected the burial and maturation history of the Ardmore Basin. Regional thermal maturation was apparently arrested during Mesozoic–Cenozoic unroofing of the basin.

The Devonian–Mississippian shale section has a broad range of thermal maturity ranging from immature ( $R_o < 0.6\%$ ) to the dry gas window ( $R_o > 2.0\%$ ). Thermal maturity is strongly dependent on structural position, with immature strata preserved in the flanks of the uplifts and highly mature strata preserved in the synclines. Variations in heat flow related to thermal conductivity, structural history, and general variability of organic composition, particularly at low maturity levels, have resulted in a modest degree of scatter in the reflectance-depth data.

## TABLE OF CONTENTS

Chapter	Page
I. INTRODUCTION.....	1
Background.....	2
Study Area .....	2
Present-Day Physiography and Climate .....	4
II. LITERATURE REVIEW.....	6
Structural Styles, Geometry, and History .....	6
Tectonic Evolution.....	9
Basin Stratigraphy and Depositional Environments.....	14
Previous Study .....	19
III. METHODS .....	22
Geologic Mapping .....	22
Well Log Correlation and Analysis .....	23
Geophysical Mapping and Thermal Gradient Analysis.....	25
Vitrinite Reflectance Analysis .....	26
Burial and Thermal History Modeling.....	29
IV. RESULTS.....	36
Geologic Mapping .....	36
Well Log Correlation and Analysis .....	39
Geophysical Mapping and Thermal Gradient Analysis.....	54
Vitrinite Reflectance Analysis .....	61
Basin Tectonism and Sediment Deposition .....	76
Erosion .....	91
Boundary Conditions .....	93
Thermal Maturation .....	93
Hydrocarbon Generation.....	96

Chapter	Page
V. DISCUSSION .....	110
Basin Tectonism.....	110
Sedimentation .....	112
Erosion .....	114
Heat Flow.....	115
Thermal Maturation .....	115
Hydrocarbon Generation.....	117
VI. CONCLUSION.....	118
Future Work.....	120
REFERENCES .....	122
APPENDICES .....	128

## LIST OF TABLES

Table	Page
1. Wells used in burial and thermal history modeling of the Ardmore Basin. ....	29
2. Modeled depositional events for the Ardmore Basin. ....	33
3. Approximate present-day depth for thermal maturity windows in the Ardmore Basin. ....	72
4. Boundary conditions and modeled erosional thickness used to make burial history models of wells in the Ardmore Basin. ....	92
5. Modeled thermal maturities of the Woodford and Caney Shales in selected wells in the Ardmore Basin. ....	95
6. Modeled formation temperatures of the Woodford and Caney Shales in selected wells in the Ardmore Basin. ....	95
7. Modeled time vs. transformation ratio (type II kerogen) results for the Woodford and Caney Shales in the Ardmore Basin. ....	106
8. Modeled depth vs. transformation ratio (type II kerogen) results for the Woodford and Caney Shales. ....	107
9. Modeled temperature vs. transformation ratio (type II kerogen) results for the Woodford and Caney Shales. ....	107
10. Locations and depths of corrected bottom-hole temperatures used in geothermal calculations. ....	129
11. Thermal maturity data from the Woodford Shale in the Ardmore Basin. ....	132



## LIST OF FIGURES

Figure	Page
1. Map displaying present-day location of the Ardmore Basin and associated structures in southern Oklahoma. ....	4
2. Reflection seismic profile displaying a positive flower structure and convergent (or transpressional) wrench faults in the in the northwest part of the basin Ardmore Basin. ....	7
3. Balanced structural cross section of the Criner Hills uplift showing basement-cored fault propagation fold interpretation. ....	8
4. Cross section of the Arbuckle Anticline. ....	8
5. Schematic block diagram illustrating the Iapetan rifted margin of southern Laurentia (Ouachita Embayment) from the Argentine Precordillera. ....	10
6. Generalized surface and subsurface stratigraphic column for the present-day Ardmore Basin. ....	18
7. Map showing locations of 52 Woodford Shale vitrinite reflectance measurements in the Ardmore Basin. ....	27
8. Map showing locations of wells used for burial and thermal history models of the Ardmore Basin. ....	30
9. Surface geologic map displaying spatial localities of rock units in the Ardmore Basin. ....	38
10. Stratigraphic cross-section A–A’ in the Ardmore Basin displaying well log signatures and formation tops. ....	41
11. Cross section B–B’ in the Ardmore Basin displaying well log signatures and formation tops. ....	42
12. Cross section C–C’ in the Ardmore Basin displaying well log signatures and formation tops. No horizontal scale. ....	43
13. Topographic map of the Ardmore Basin. ....	44
14. Structural contour map of the top of the Caney Shale. ....	44
15. Structural contour map of the top of the Sycamore Formation. ....	45
16. Structural contour map of the Woodford Shale. ....	45
17. Structural contour map of the Hunton Group. ....	46
18. Structural contour map of the top of the Sylvan Shale. ....	46
19. 3D structural contour map of the top of the Caney Shale. ....	47
20. 3D structural contour map of the top of the Sycamore Formation. ....	47
21. 3D structural contour map of the top of the Woodford Shale. ....	48
22. 3D structural contour map of the top of the Hunton Group. ....	48
23. 3D structural contour map of the top of the Sylvan Shale. ....	49

Figure	Page
24. Contour map of measured depth to the top of the Caney Shale in the Ardmore Basin. ....	49
25. Contour map of measured depth to the top of the Sycamore Formation. ....	50
26. Contour map of measured depth to the top of the Woodford Shale. ....	51
27. Contour map of measured depth to the top of the Hunton Group. ....	51
28. Contour map of measured depth to the top of the Sylvan Shale. ....	52
29. Isochore map of the Caney Shale in the Ardmore Basin. ....	52
30. Isochore map of the Sycamore Formation in the Ardmore Basin. ....	53
31. Isochore map of the Woodford Shale in the Ardmore Basin. ....	53
32. Isochore map of the Hunton Group in the Ardmore Basin. ....	54
33. Aeromagnetic anomaly map of the Ardmore Basin and surrounding region. ....	55
34. Gravity anomaly map of the Ardmore Basin and surrounding region. ....	56
35. Graph of corrected bottom-hole temperatures vs. true vertical depth from wells in the Ardmore Basin. ....	57
36. Contour map of geothermal gradient in the Ardmore Basin. ....	58
37. Contour map of <i>in situ</i> temperature at the top of the Caney Shale in the Ardmore Basin. ....	59
38. Contour map of <i>in situ</i> temperature at the top of the Sycamore Formation in the Ardmore Basin. ....	59
39. Contour map of <i>in situ</i> temperature at the top of the Woodford Shale in the Ardmore Basin. ....	60
40. Contour map <i>in situ</i> temperature at the top of the Hunton Group in the Ardmore Basin. ....	60
41. Contour map <i>in situ</i> temperature at the top of the Sylvan Shale in the Ardmore Basin. ....	61
42. Vitrinite reflectance-elevation plot for the Woodford Shale showing thermal maturity trends in the Ardmore Basin. ....	62
43. Vitrinite reflectance-depth plot for the Woodford Shale showing thermal maturity trends in the Ardmore Basin. ....	63
44. Vitrinite reflectance vs. <i>in situ</i> temperature of the Woodford Shale showing thermal maturity trends and temperature trends in the Ardmore Basin. ....	64
45. Calculated vitrinite reflectance contour map of the Caney Shale. ....	65
46. Calculated vitrinite reflectance contour map of the Sycamore Formation. ....	66
47. Calculated vitrinite reflectance contour map of the Woodford Shale. ....	67
48. Calculated vitrinite reflectance contour map of the Hunton Group. ....	68
49. Calculated vitrinite reflectance contour map of the Sylvan Shale. ....	69
50. Calculated 3D vitrinite reflectance map of the Caney Shale draped over Caney Shale structure. ....	69
51. Calculated 3D vitrinite reflectance map of the Sycamore Formation draped over Sycamore Formation structure. ....	70
52. Calculated 3D vitrinite reflectance map of the Woodford Shale draped over Woodford Shale structure. ....	70
53. Calculated 3D vitrinite reflectance map of the Hunton Group draped over Hunton Group Structure. ....	71

Figure	Page
54. Calculated 3D vitrinite reflectance map of the Sylvan Shale draped over Sylvan Shale structure.....	71
55. Calculated vitrinite reflectance contour map for the Woodford Shale superimposed by 499 GOR data points measured after six months of production from the Woodford Shale.....	73
56. Vitrinite reflectance vs. oil API gravity plot for the Woodford Shale showing how maturity affects petroleum gravity in the Ardmore Basin. ....	74
57. API gravity vs. depth plot for the Woodford Shale showing how petroleum weight changes with depth in the Ardmore Basin. ....	75
58. API gravity vs. <i>in situ</i> temperature plot for the Woodford Shale showing how petroleum weight changes with temperature in the Ardmore Basin.....	76
59. Burial and thermal history models of the B&W Tyson 1-8 well in the Ardmore Basin. ....	78
60. Burial and thermal history models of the Badger 2-23 well in the Ardmore Basin. ...	79
61. Burial and thermal history models of the Brock 9-1H well in the Ardmore Basin ....	80
62. Burial and thermal history models of the Dansby 1-3H well in the Ardmore Basin...81	81
63. Burial and thermal history models of the Hays 1-1H well in the Ardmore Basin.....82	82
64. Burial and thermal history models of the J Little A-1-6 well in the Ardmore Basin. .83	83
65. Burial and thermal history models of the J Paul 1-7 well in the Ardmore Basin. ....84	84
66. Burial and thermal history models of the Martin 8-2 RD well in the Ardmore Basin. ....	85
67. Burial and thermal history models of the Martin 1-14 well in the Ardmore Basin. A) Burial history model showing evolution of thermal maturity windows. ....	86
68. Burial and thermal history models of the Starr 1-25 well in the Ardmore Basin. ....87	87
69. Burial and thermal history models of the Stephen 1-6H well in the Ardmore Basin. .88	88
70. Burial and thermal history models of the Tomaney 1-35-34-27XHW well in the Ardmore Basin. ....	89
71. Kerogen quality diagram displaying the presence of various kerogen types within the Caney Shale in the core recovered from the Tomaney 1-35-34-27XHW well.....97	97
72. Burial history model of the B&W Tyson 1-8 well showing how transformation ratio (TR) for Type II kerogen evolved through geologic time and burial. ....	98
73. Burial history model of the Badger 2-23 well showing how transformation ratio (TR) for Type II kerogen evolved through geologic time and burial. ....	98
74. Burial history model of the Brock 9-1H well showing how transformation ratio (TR) for Type II kerogen evolved through geologic time and burial. ....	99
75. Burial history model of the Dansby 1-3H well showing how transformation ratio (TR) for Type II kerogen evolved through geologic time and burial. ....	99
76. Burial history model of the Hays 1-1H well showing how transformation ratio (TR) for Type II kerogen evolved through geologic time and burial. ....	100
77. Burial history model of the J Little A-1-6 well showing how transformation ratio (TR) for Type II kerogen evolved through geologic time and burial. ....	100
78. Burial history model of the J Paul 1-7 well showing how transformation ratio (TR) for Type II kerogen evolved through geologic time and burial.....	101

Figure	Page
79. Burial history model of the Martin 8-2 RD well showing how transformation ratio (TR) for Type II kerogen evolved through geologic time and burial. ....	101
80. Burial history model of the Martin 1-14 well showing how transformation ratio (TR) for Type II kerogen evolved through geologic time and burial. ....	102
81. Burial history model of the Starr 1-25 well showing how transformation ratio (TR) for Type II kerogen evolved through geologic time and burial. ....	102
82. Burial history model of the Stephen 1-6H well showing how transformation ratio (TR) for Type II kerogen evolved through geologic time and burial. ....	103
83. Burial history model of the Tomaney 1-35-34-27XHW well showing how transformation ratio (TR) for Type II kerogen evolved through geologic time and burial. ....	103
84. Time vs. transformation ratio plot showing how oil was generated from the Caney Shale through geologic time in seven wells.....	104
85. Time vs. transformation ratio plot showing how oil was generated from the Woodford Shale through geologic time for seven wells. ....	105
86. Structural contour map of the top of the Woodford Shale and locations of wells used in burial and thermal history modeling. ....	128
87. Geophysical well log of the B&W Tyson 1-8 well.....	134
88. Geophysical well log of the Badger 2-23 well.....	135
89. Geophysical well log of the Brock 9-1H well. ....	136
90. Geophysical well log of the Dansby 1-3H well. ....	137
91. Geophysical well log of the Hays 1-1H well. ....	138
92. Geophysical well log of the J Little A-1-6 well.....	139
93. Geophysical well log of the J Paul 1-7 well. ....	140
94. Geophysical well log of the Martin 8-2 RD.....	141
95. Geophysical well log of the Martin 1-14 well. ....	142
96. Geophysical well log of the Starr 1-25 well. ....	143
97. Geophysical well log of the Stephen 1-6H well. ....	144
98. Geophysical well log of the Tomaney 1-35-34-27XHW well.....	145

## CHAPTER I

### INTRODUCTION

The Mississippian (Chesterian) Caney Shale is an emerging Midcontinental unconventional oil and gas resource play in the Anadarko, Ardmore, Marietta, and Arkoma Basins (Andrews, 2007). The formation is composed of fossiliferous, dark-grey to black, carbonaceous shale. Hydrocarbon production from the Caney Shale has been sparse and unpredictable, especially when compared to the success achieved with the time-equivalent Fayetteville Shale in the eastern Arkoma Basin and Barnett Shale in the Ft. Worth Basin (Cardott, 2017a). This limited success can be attributed in part to deficiencies in knowledge of tectonic influences on structure and thermal maturity.

Using modern basin analysis techniques to understand the burial and thermal history of a sedimentary basin are essential steps in reducing exploration risk. This study uses one-dimensional (1D) burial and thermal history modeling of the Ardmore Basin to constrain timing of tectonic events, rates and magnitudes of basin subsidence, as well as thermal maturity of the Caney Shale. Additionally, transformation of kerogen within the Caney Shale is modeled to determine rates of oil and gas generation. Published maturity data are relatively scarce for the Ardmore Basin and even more lacking for the Caney Shale. Accordingly, basin modeling is a valuable approach for evaluating source rock maturity. Basin modeling helps define the

depositional, tectonic, and geothermal controls on reservoir quality in the Caney Shale, which in turn helps guide exploration and development.

## **Background**

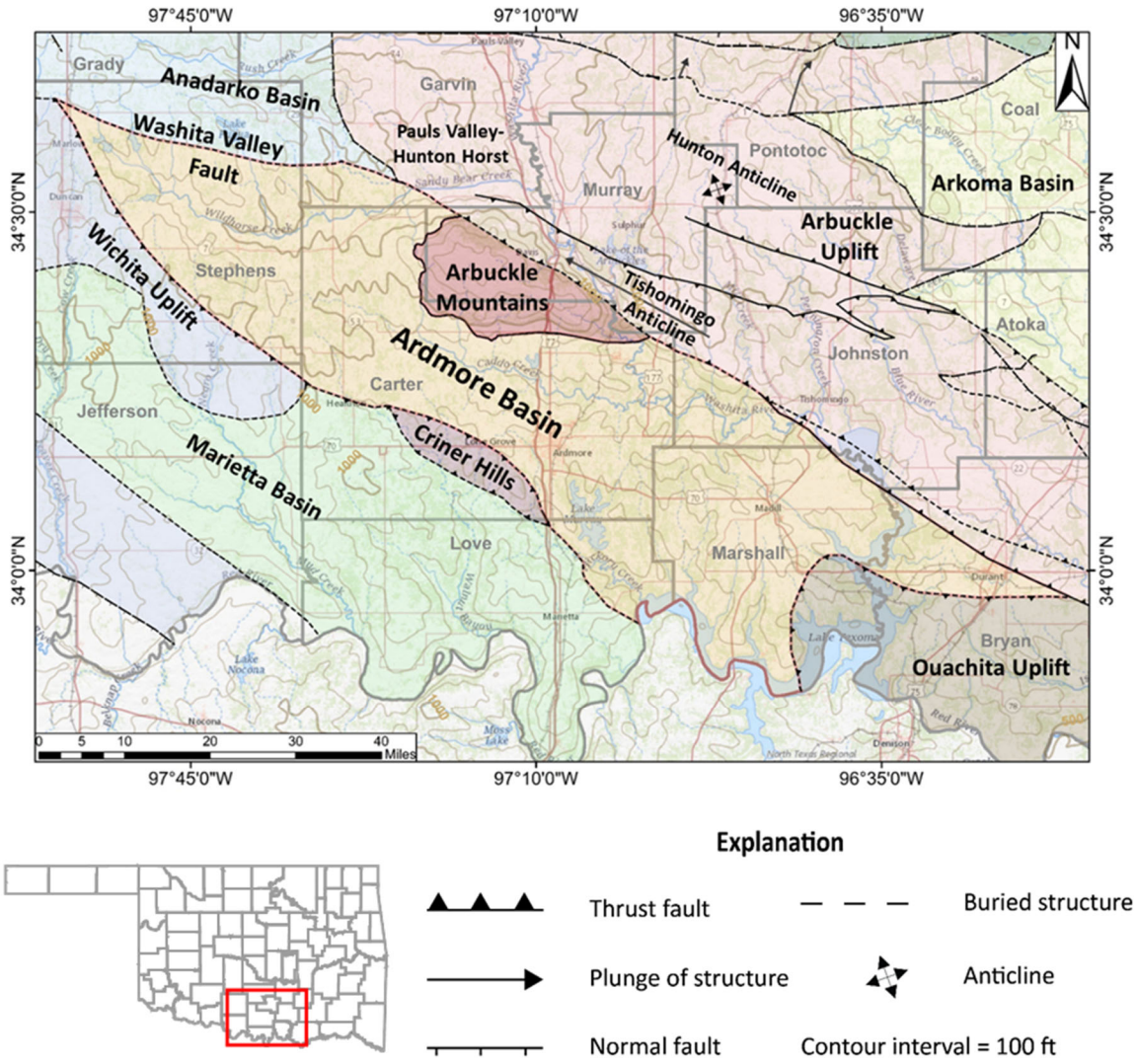
This project will contribute to a best-practices manual that will facilitate accelerated development of the Caney Shale and offer suggested characterization and completion techniques. In February 2020, Continental Resources drilled the Tomaney 1-35-34-27XHW well within the Ardmore Basin in Stephens County, Oklahoma. A core through a complete section of the Caney Shale that includes adjacent strata in the underlying Sycamore Limestone and the overlying Goddard Shale was recovered from the Tomaney 1-35-34-27XHW well. A full suite of well logs was run in the Caney stratigraphic interval. A full tight-rock analysis suite, including Rock-Eval pyrolysis, was run on the Caney Shale core at Chesapeake Energy's Reservoir Technology Center in Oklahoma City.

## **Study Area**

The Ardmore Basin is a narrow, northwest-trending, Late Paleozoic sedimentary basin in south-central Oklahoma (Figure 1). The basin is southeast of the adjacent Anadarko Basin. These basins have similar depositional histories, and the Ardmore Basin is commonly considered a southeast extension of the Anadarko Basin (Ham, 1969). Large-scale, Pennsylvanian reverse faults bound the Ardmore Basin and form the Arbuckle, Tishomingo, Paul's Valley, and Hunton

anticlines to the north and east as well as the Criner Hills Uplift and Ouachita Orogen to the southeast (Northcutt and Campbell, 1995; Granath, 1998). These bounding highlands clearly establish the Ardmore Basin as an intermontane sedimentary basin. The Ardmore basin has a surface area of  $\sim 2,200$  mi<sup>2</sup> and exhibits an elongate-asymmetric geometry in which folds verge toward the northeast (Northcutt and Campbell, 1995). The basin includes parts of Stephens, Jefferson, Carter, Garvin, Murray, Love, Johnston, Marshall, and Bryan Counties in Oklahoma as well as northern Cook and Grayson Counties in Texas (Northcutt and Campbell, 1995). Basin fill comprises folded and faulted Paleozoic strata overlain by younger strata that are less intensely deformed (Stanley and Chang, 2012). These younger units conceal the products of a complicated geologic history and mask giant folds with structural relief greater than 30,000 ft.

Exploration for petroleum has contributed greatly to knowledge of subsurface features in the Ardmore Basin; however, the mostly proprietary nature of geologic data presents considerable challenges for research. Oil and gas was first produced from the basin during the early 1900s with discoveries of the Healdton and Hewitt oil fields northwest of the Criner Hills in 1913 and 1919, respectively (Pritchett, 2015; Suneson, 2020). Discovery of these fields was followed by the discovery of seventy-four additional oil and gas fields with the largest being the Sho-Vel-Tum field ( $\sim 330$  mi<sup>2</sup> surface area) in the northwest part of the basin (Pritchett, 2015). Estimated cumulative production from the Ardmore Basin since 1965 totals almost one billion barrels of oil and 2.74 trillion cubic feet of gas (production data from Enverus, 2021).



**Figure 1.** Map displaying present-day location of the Ardmore Basin and associated structures in southern Oklahoma (after Northcutt and Campbell, 1995; elevation data from USGS National Map Database (Gesch et al., 2009)).

### Present-Day Physiography and Climate

In sharp contrast to high-relief subsurface structures, the present-day surface expression of the Ardmore Basin is characterized chiefly by rolling hills and ridges with total topographic relief of about 700 ft. Surface elevation gradually decreases from approximately 1,300 ft in the



northwestern part of the basin in Stephens County to 600 ft in the southeastern part in Bryan County (Gesch et al., 2009).

The Arbuckle Mountains are north of the Ardmore Basin in Carter, Johnston, Murray, and Pontotoc Counties (Northcutt and Campbell, 1995). Topographically, the Arbuckle Mountains are characterized as undulating hills, ridges, and valleys with moderate reliefs of 100–600 ft (Johnson, 2008). These hills have a maximum elevation of approximately 1,400 ft and consist of northwest-striking panels of folded and faulted Paleozoic strata (Huffman et al., 1978). Associated surface and subsurface structures include folds such as the Arbuckle Uplift, Tishomingo Anticline, Mill Creek Syncline, Belton Anticline, and Hunton Anticline (Ham, 1969). These structures are separated by northwest-trending reverse and oblique-slip faults (Huffman et al., 1978).

The Wichita Mountains rise from surrounding redbed plains to the southwest of the Ardmore Basin (Suneson, 2020). These highlands form isolated peaks and rounded hills with relief ranging from 400–1,100 ft (Suneson, 2020). The Wichita Mountains consist mostly of granite with some Early Paleozoic (Arbuckle Group)–Permian sedimentary cover (Heran et al., 2003).

The Ouachita Mountains are southeast of the Ardmore Basin and extend through Bryan and Marshall Counties as well as western Arkansas (Northcutt and Campbell, 1995). These mountains comprise a complex system of thin-skinned folds and faults that topographically resemble curved valleys and subparallel ridges with relief ranging from approximately 500–1,500 ft (Huffman et al., 1978; Johnson, 2008).

The present-day climate of southern Oklahoma is characterized as humid subtropical with an annual mean surface temperature of 62°F and precipitation averaging 56 in/yr (Oklahoma Climatological Survey, 2021).

## CHAPTER II

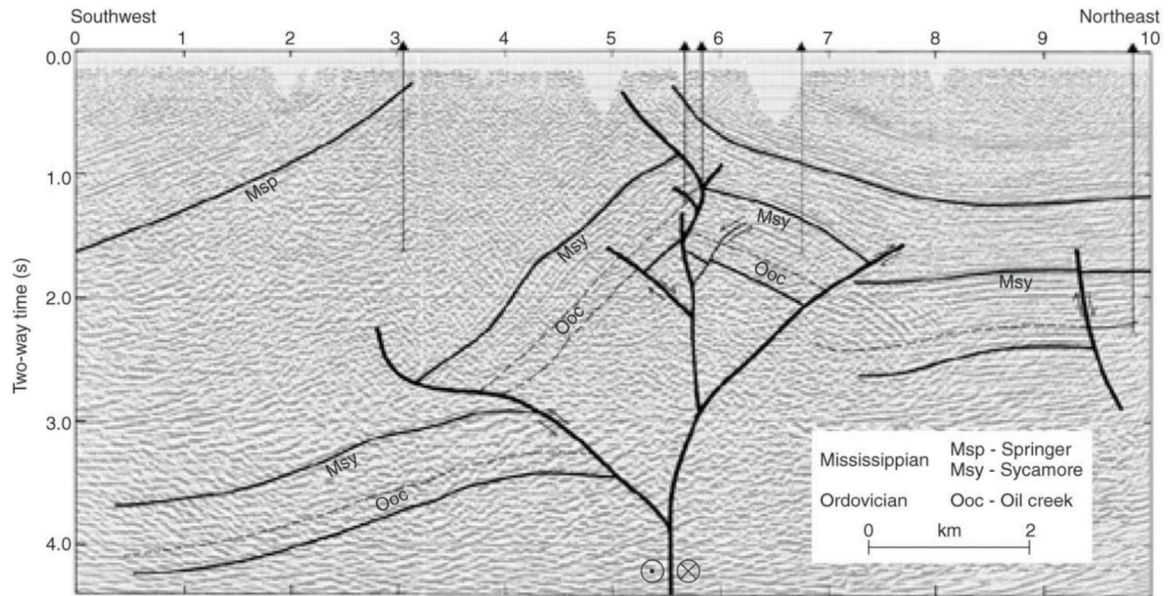
### LITERATURE REVIEW

#### **Structural Styles, Geometry, and History**

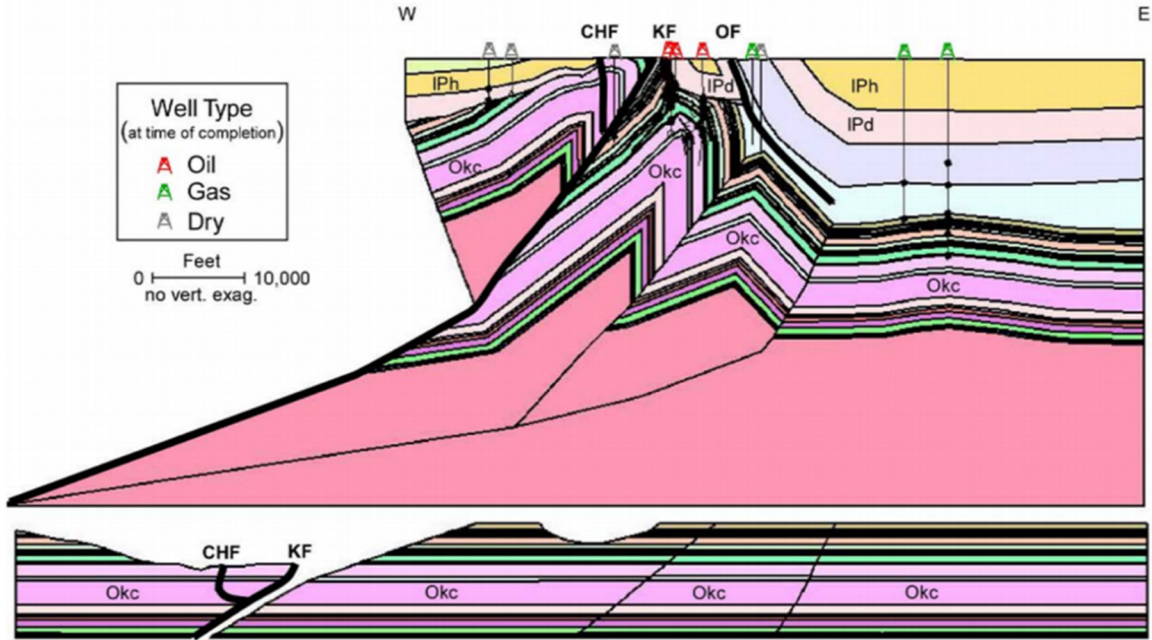
Structures in the Ardmore Basin and the surrounding region are complex. Kinematic analysis of Morrowan–Atokan deformation indicates that multiple left-lateral shear zones served as mechanisms for uplift as well as development of convergent wrench faults and positive flower structures (Harding et al., 1983) (Figure 2). Offset of Ordovician strata and sub-horizontal slickensides along the main Washita Valley Fault indicate up to 40 mi of Early Pennsylvanian left-lateral slip (Harding et al., 1983). Granath (1998) suggested the Washita Valley and Criner Hills fault systems are connected through a system of *en echelon*, northwest-trending folds, as well as transpressional synthetic and antithetic faults.

Analysis of the Criner Hills and Arbuckle uplifts indicates an origin by oblique-slip fault propagation folding during the Carboniferous. Balanced cross sections from Walker (2006) suggest the Criner Hills are basement cored fault propagation folds (Figure 3), and the Arbuckle Uplift is interpreted as a breakthrough fault propagation fold containing Upper Carboniferous growth strata (Figure 4). The Criner Hills Fault transects the southwest flank of the Criner Hills, juxtaposing Ordovician strata against Pennsylvanian strata (Suneson, 2020).

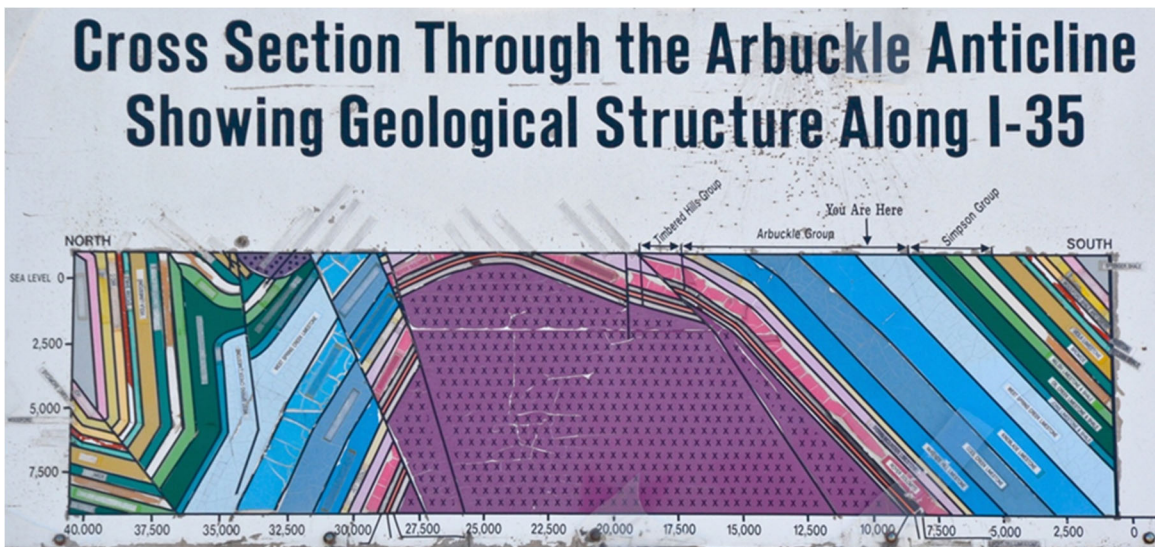
At their inception, elevations of these bounding highlands were much greater than they are now, however, deformation was coincident with major subsidence, and so topographic relief was a fraction of structural relief. Surrounding boulder and conglomerate aprons record uplift and erosion of the late Paleozoic mountains (Granath, 1989; Suneson, 2020).



**Figure 2.** Reflection seismic profile displaying a positive flower structure and convergent (or transpressional) wrench faults in the in the northwest part of the basin Ardmore Basin (from Harding et al., 1983). Newer literature (e.g., Turko, (2019)), suggest this line could be interpreted differently with Morrowan Springer Group growth on a listric transtensional basement fault.



**Figure 3.** Balanced structural cross section of the Criner Hills uplift showing basement-cored fault propagation fold interpretation. Notice how faults are interpreted in the footwall of synclines (from Walker, 2006).



**Figure 4.** Cross section of the Arbuckle Anticline. This was a sign the Ardmore Geological Society placed at a pullover by the northbound lane of I-35, near the Arbuckle Mountains (the sign is no longer present). The captured forelimb faulting supports the interpretation that the Arbuckle Anticline constitutes a breakthrough fault propagation fold.

## Tectonic Evolution

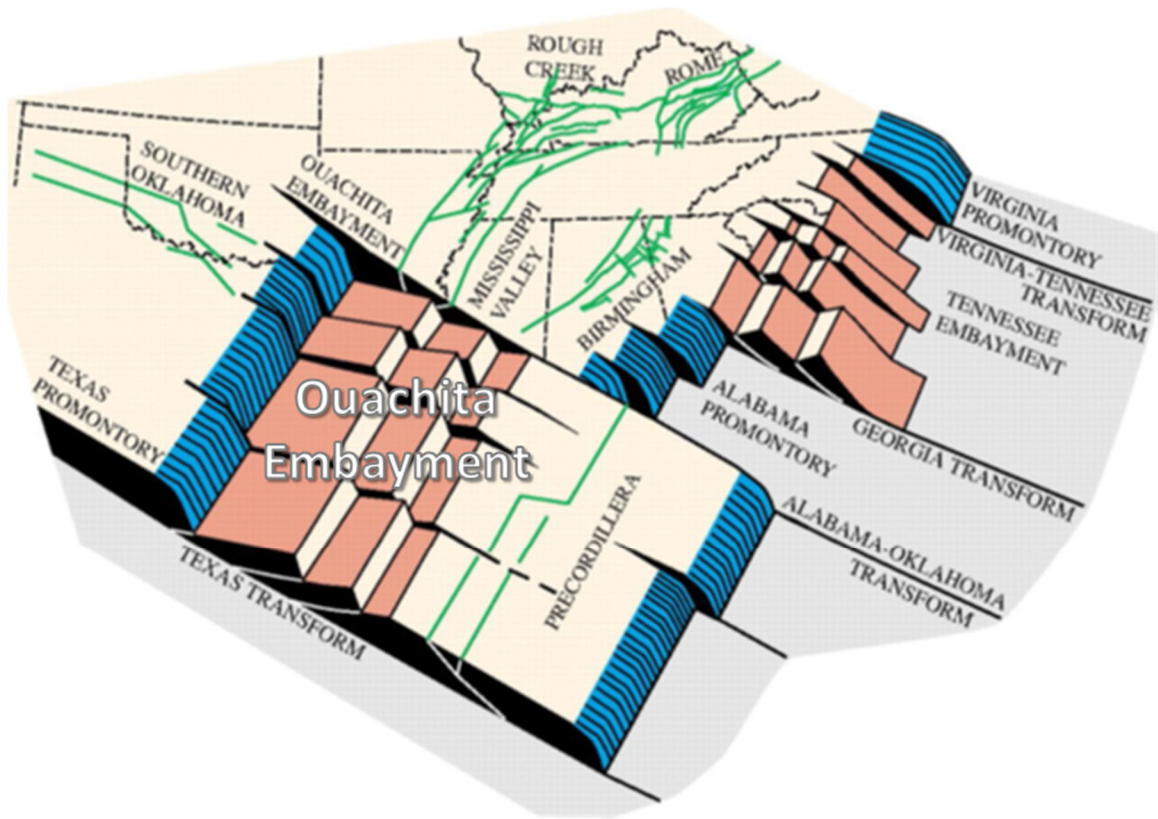
The tectonic history of southern Oklahoma in the vicinity of the Ardmore Basin is characterized by five tectonic events: (1) Iapetan oblique-slip rifting and associated plutonism and volcanism during the Late Precambrian–Early Cambrian; (2) thermal subsidence and passive margin development during the Early Paleozoic; (3) Pennsylvanian orogeny and associated deformation, (4) structural and depositional quiescence from the Triassic–Early Cretaceous, and (5) subsidence of the Gulf of Mexico coastal plain in the eastern part of the basin during the Cretaceous and possibly into Paleogene time. These tectonic events profoundly influenced structure, deformation, timing of sediment deposition and associated rates, as well as burial depth and thermal maturation of organic carbon.

During the Neoproterozoic–Early Cambrian, the ancient craton encompassing what is now southern Oklahoma was assembled in the supercontinent Rodinia (Scotese, 2002; Brueseke et al., 2016), which began to rift apart during the Early Cambrian (Brewer et al., 1983). Continental breakup is thought to have resulted in emplacement of one of the largest bimodal volcanic and intrusive provinces in North America with a volume of more than 60,000 mi<sup>3</sup> (Hoffman et al., 1974; Hanson et al., 2013).

Events during dismantling of the Precambrian supercontinent are enigmatic, and multiple hypotheses have been proposed to explain the continental partitioning and associated igneous complex formation. Some authors have interpreted that a transtensional, left-lateral shear zone developed into a large pull-apart basin (McBee, 1995), while others proposed integrated rift and transform components that are responsible for the igneous activity and subsequent continental breakup (Thomas, 2014) (Figure 5). The most common explanation calls upon rifting and development of the Southern Oklahoma Aulacogen (Shatski, 1946; Burke and Dewey, 1973; Hoffman et al., 1974), although the Iapetan sedimentary fill in the area of the Ardmore Basin is

very thin compared to that of the other Iapetan rifts, which include the Mississippi Valley Graben, Rough Creek Graben, Rome Trough, and Birmingham Graben (Figure 4). This proto basin is also commonly referred to as the Southern Oklahoma Trough (Perry, 1989).

The commonly cited connection of Ardmore structure to an aulacogen is weakly supported as there are few rift-related faults (Harding et al., 1983) or rift-fill deposits apparent. Although southern Oklahoma did subside during the Cambrian–Ordovician in response to the Iapetan thermal regime, which affected the entire Laurentian continental platform, the thick syn-rift Cambrian shale and extensional faults characteristic of other Iapetan rifts are absent.



**Figure 5.** Schematic block diagram illustrating the Iapetan rifted margin of southern Laurentia (Ouachita Embayment) from the Argentine Precordillera. Rifting comprised a combination of extensional and transform faults (after Thomas, 2011).

From the Late Cambrian–Late Ordovician, the rift system continued to open to form the Iapetus Ocean in concert with southward migration of the paleo mid-oceanic ridge (Johnson, 1989; Thomas, 1991). During the Late Cambrian, southern Oklahoma was a locus for sedimentation and resided on the passive continental margin of southern Laurentia and near the Ouachita Embayment and Southern Oklahoma Aulacogen (Scotese, 2002). The Oklahoma Shelf was flooded by an epicontinental sea that resulted from eustatic sea-level rise during late-stage thermal subsidence (Johnson, 1989). Thick, expansive successions of Cambrian–Devonian carbonate were deposited, emplacing a crustal load that was isostatically and thermally compensated (Feinstein, 1981). The structure that became the Ardmore basin had low topographic relief during this time, allowing for interregional deposition of Cambrian–Devonian sediment. Decelerating thermal subsidence culminated in relative cratonic stability during the Silurian–Early Mississippian, with only minor subsidence accommodating continued sedimentation (Feinstein, 1981). Crustal cooling and decreasing thermal subsidence during the Late Devonian–Mississippian were related to diminishing rates of sediment accumulation in the Ardmore Basin (Brown, 2002; Johnson, 2008).

The Late Mississippian–Pennsylvanian was a time of widespread tectonic activity associated with assembly of Pangea. Subduction of the Laurussian Plate under the northward-advancing Gondwana Plate in the Ouachita Embayment of the Rheic Ocean led to closure of the Iapetus Ocean and gave rise to the Ouachita-Marathon orogenic belt during the Mississippian–Pennsylvanian (Granath, 1989; Perry, 1989). This thin-skinned, foreland fold and thrust belt extended sinuously through present-day south Texas, east Texas, Oklahoma, and Arkansas, connecting with the Appalachian Mountains in Mississippi (Granath, 1989; Thomas, 1977).

Locally, the late Paleozoic Wichita and Arbuckle Orogenies are responsible for uplift of the northwest-trending Wichita and Arbuckle mountain ranges as well as renewed pulses of subsidence driven by intracratonic flexural loading (Ham, 1969; Perry, 1989; Ye et al., 1996). This mountain building event has been subdivided into three separate orogenies: the first

Wichitan Orogeny (323 Ma; Bashkirian; Morrowan), second Wichitan Orogeny (312 Ma; Moscovian; Late Atokan), and Arbuckle Orogeny (310-305 Ma; Moscovian–Kasimovian; Late Desmoinesian–Early Virgilian) (Granath, 1989).

Each major orogenic pulse is evidenced by a unique unconformity and associated conglomeratic unit in the Ardmore Basin (Huffman et al., 1978; Granath, 1989). The Joliff (Morrowan) and Bostwick (Atokan) Conglomerates in the Criner Hills are linked to the first and second Wichitan Orogenies, respectively (Huffman et al., 1978). Conglomerates within the Ardmore Basin, including the Collings Ranch Conglomerate (Early Virgilian) and Vanoss Conglomerate (Late Virgilian Pontotoc Group) reflect uplift and penecontemporaneous erosion of the Arbuckle Mountains (Huffman et al., 1978).

Deformation during the first Wichitan Orogeny was principally south of the Ardmore Basin with uplift of the Criner Hills (Granath, 1989; Walker, 2006). Deformation during the second Wichitan Orogeny was also mainly in the south; however, modest uplift to the north produced the Tishomingo, Hunton Arch, and Paul's Valley Anticlines (Granath, 1989; Brown, 2002). Combined, the first and second Wichitan Orogenies resulted in uplift of the Wichita Mountains (Huffman et al., 1978). The associated lithospheric load was isostatically compensated via subsidence of the Anadarko Basin (Walker, 2006). The Arbuckle Orogeny elevated the Arbuckle and Caddo Anticlines and spurred renewed uplift in existing structures (Granath, 1989; Walker, 2006). Perhaps as early as the Late Mississippian and certainly by Desmoinesian time, the Ardmore Basin was established as an independent area of subsidence between large-scale reverse faults (Granath, 1989). Major tectonic activity ceased by the end of the Pennsylvanian, and the Ardmore Basin continued to subside through the Early Permian (Thomas, 2014).

It is traditionally thought that simple compression from the Ouachita-Marathon collisional event was the principal driving force for Pennsylvanian orogenesis, however, connecting the two events is problematic as the geometric relationship between northwest-directed Ouachita compression and northeast-directed compression in the Arbuckle and Wichita



Mountains is conflicting. Furthermore, mountain building is normally limited to the region adjacent to the margin of collision, whereas the Arbuckle and Wichita mountains formed in response to intraplate motion.

Stress vectors as well as orientation and location of mountain belts can be resolved by examining pre-existing Iapetan rift-related faults and their orientation relative to Pennsylvanian stresses driven by orogenesis in the Ouachita orogen, particularly in the Ouachita salient, the Texas recess, and the Marathon salient, as well as intraplate stresses that may have existed along the zones of weakness established during Iapetan rifting. Proponents of this hypothesis (Granath, 1989; Ye et al., 1996; Turko, 2019) suggested northwest-trending zones of weakness, such as the Washita Valley fault, underwent reverse dip-slip and left-lateral strike-slip during the Pennsylvanian as compressional stress was transmitted through the region. A possible explanation for the transcurrent structures calls upon progressive clockwise rotation of the maximum horizontal stress direction during the Ouachita-Marathon Orogeny (Turko, 2019).

Conclusion of the Permian was marked by reduced rates and magnitudes of subsidence (Huffman et al., 1978). Southern Oklahoma has essentially been tectonically dormant since the Permian with exception of some far-field effects of the Late Cretaceous–Early Paleogene Sevier and Laramide Orogenies (Suneson, 2020). The Laramide Orogeny in the southern Rocky Mountains (~66–48 Ma) (Tweto, 1975) slightly elevated southern Oklahoma and possibly reactivated older basement faults (Johnson, 1989). Deposition of a Cretaceous sedimentary wedge recording encroachment and subsidence of the Gulf of Mexico Basin was pronounced in the eastern Ardmore Basin, and emplaced a crustal load that caused low-angle, regional south-southeastward tilting (Johnson, 2008).

## Basin Stratigraphy and Depositional Environments

Sedimentary rock in the Ardmore Basin nonconformably overlies Precambrian–Cambrian igneous basement that consists of plutonic and volcanic rocks (Hanson et al., 2013). The overlying sedimentary section primarily ranges in age from Cambrian–Cretaceous (Figure 6) and locally reaches thickness greater than 30,000 ft (Huffman et al., 1978; Suneson, 2020).

The Tishomingo and Troy Granites (~1.4 Ga) form the basement of the Ardmore Basin and comprise the erosional substrate upon which all volcanic and sedimentary units were deposited (Bickford and Lewis, 1979). After a long hiatus, emplacement of one of the largest bimodal volcanic provinces in North America initiated with intrusion and extrusion of tholeiitic gabbro and basaltic magma ( $552 \pm 7$  Ma) (Bowring and Hoppe, 1982). Following early mafic volcanism, continued lithospheric thinning and adiabatic melting led to extrusion of the Carlton Rhyolite Group around the Neoproterozoic–Cambrian boundary ( $539 \pm 5$  Ma; Ediacaran–Fortunian) and the time-equivalent Colbert Porphyry from fissure-type vents (Hanson et al., 2013). Effusive rhyolite flows cooled quickly to form a substrate upon which subsequent sedimentary units were deposited in the Ardmore Basin (Hanson et al., 2013).

Following Early Cambrian plutonism and volcanism, flooding associated with the Sauk transgression traversed southern Oklahoma from southeast to northwest, depositing sandstone, conglomerate, limestone, and dolomite of the Late Cambrian Timbered Hills Group (Ham, 1969; Johnson, 1989).

Flooding persisted through the Ordovician, which was a time of major cratonic carbonate deposition (Johnson, 1989). Limestone and dolomite of the Cambrian–Ordovician Arbuckle Group were deposited on a broad, nearly flat-lying ramp, which has been referred to as the “Great American Carbonate Bank” (Fritz et al., 2012). The Arbuckle Group conformably overlies the Timbered Hills Group and consists of grey to brown limestone and dolomite (Fritz et al., 2012)

Carbonate deposition was episodically interrupted by siliciclastic influx during deposition of the Middle Ordovician Simpson Group. The Simpson Group comprises alternating layers of quartzarenite, shale, and limestone (Ham, 1969) that were deposited in tropical eolian and shallow-marine environments (Johnson, 1989).

Carbonate deposition continued during the Tippecanoe transgression and deposition of Middle–Upper Ordovician Viola Group (Johnson, 1989). The group is composed of limestone that was deposited on a shallow-water platform in a widespread epeiric sea (Amati and Westrop, 2006). Southern Oklahoma remained inundated with seawater through the Middle Devonian, however, deposition of the Late Ordovician Sylvan Shale and Ordovician–Devonian Hunton Group brought an end to Early Paleozoic carbonate dominance. Multiple unconformities punctuate Middle Ordovician–Middle Devonian sedimentation in southern Oklahoma.

Following a ~15–20 m.y. period of erosion was advance of Late Devonian–Mississippian seas from the southeast and subsequent deposition of Devonian–Early Pennsylvanian carbonaceous and calcareous shale (Fritz et al., 2012). These units are the Woodford Shale, Sycamore Limestone, Caney Shale, Goddard Shale, and the Springer Group. The Devonian–Mississippian Woodford Shale is the main petroleum source and reservoir rock deposited during this time (Wavrek, 1992; Brown, 2002) and contains sapropelic Type II kerogen with about 1–14% total organic carbon (TOC) content with some intervals having TOC content of about 25% (Johnson and Cardott, 1992). Dark Devonian–Mississippian shale was deposited during the Kaskaskia transgression in an epicontinental sea that was largely oxygen-deficient (Johnson, 1989).

Pennsylvanian units consist of interbedded sandstone, carbonate, and shale (Suneson, 2020). Units comprise the Dornick Hills, Deese, Hoxbar, and Pontotoc Groups (Ham, 1969). During the Pennsylvanian, broad areas were uplifted and eroded, thus creating multiple unconformities (Ham, 1969). Sediment was mostly deposited in a broad, shallow sea that covered

south-central Oklahoma during the Pennsylvanian, but were also deposited in marginal marine and terrestrial settings (Johnson, 1989).

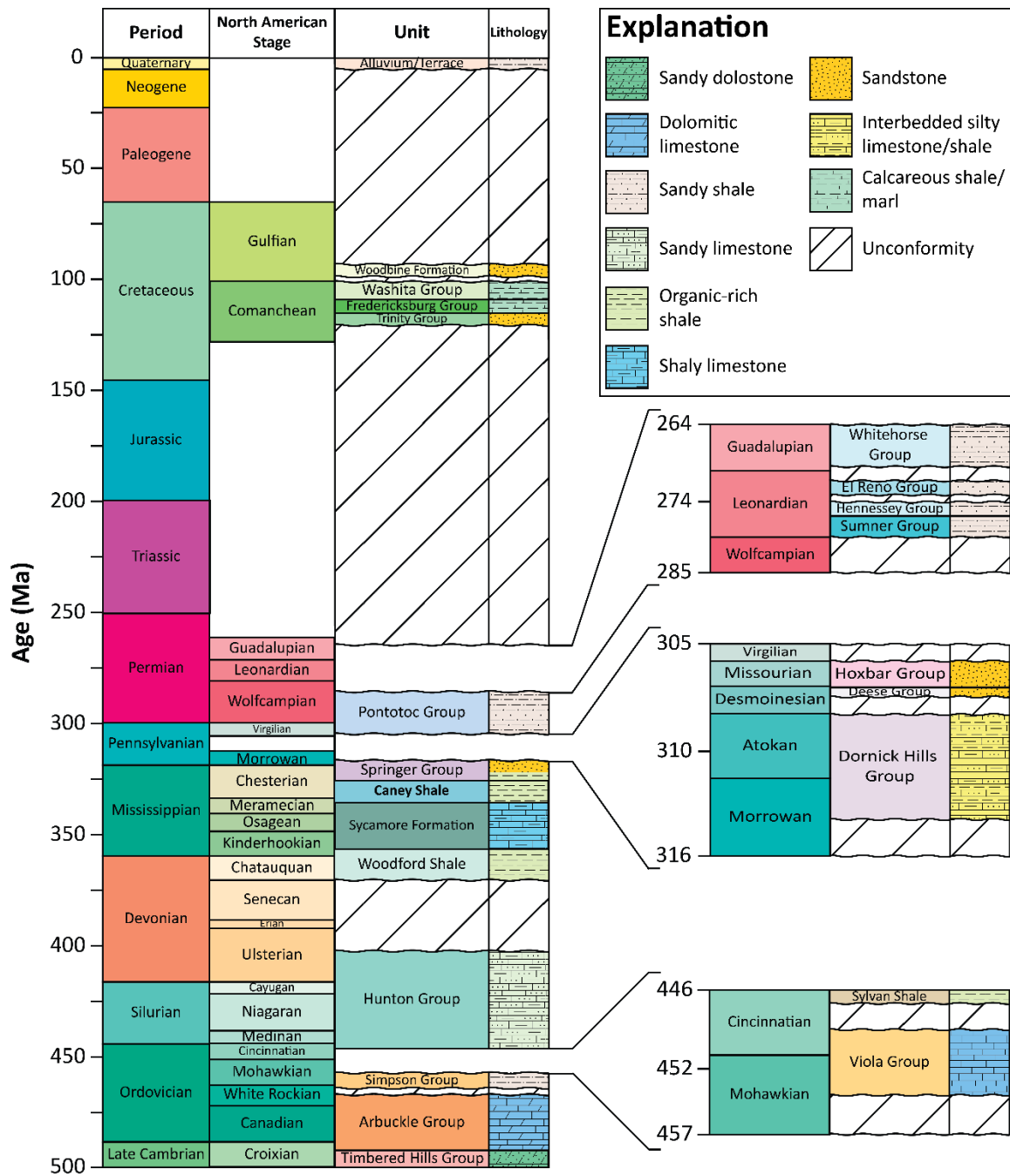
In the geology and mineral resource reports covering Marshall and Bryan Counties (Huffman et al., 1978, 1987), it has been reported that most Cretaceous strata disconformably overlie Mississippian units in the southeastern part of the Ardmore Basin. In these counties, the Pennsylvanian stratigraphic section is incomplete and Permian units are absent. No Permian units have been observed at the surface in the eastern Ardmore Basin (Heran et al., 2003).

The northwest Ardmore Basin is blanketed by a veneer of Permian strata, mainly red sandstone, shale, and evaporites (Northcutt and Campbell, 1995; Heran et al., 2003). Permian sediment was eroded off low-lying mountains and deposited in alluvial and deltaic environments proximal to a shallow sea that rose and fell cyclically (Johnson, 2008).

Triassic and Jurassic units are absent in the Ardmore Basin (Stanley and Chang, 2012). There is no evidence for Triassic, Jurassic, or pre-Albian Cretaceous deposition in southern Oklahoma (Johnson, 2008). This time is characterized by structural and depositional quiescence with minor erosion (Suneson, 2020).

A major unconformity separates Late Permian strata from Lower Cretaceous strata (Heran et al., 2003). After a period of nondeposition and erosion, a shallow sea advanced into southern Oklahoma from the south during the Early Cretaceous (Huffman et al., 1978). Sandstone, shale, and limestone were deposited in shallow marine and marginal marine environments as well as in meandering rivers and lakes in coastal plain environments (Huffman et al., 1978; Johnson, 1989). Sediment was sourced from distal highlands such as the Appalachian and Ancestral Rocky Mountains as well as locally sourced from surrounding highlands including the Arbuckle and Ouachita uplifts (Huffman et al., 1978). Load-induced subsidence from accumulation of Cretaceous sediment was likely expressed as a regional south-southeastward tilt (Johnson, 2008).

Uplift of the Rocky Mountains during the Late Cretaceous–Early Paleogene Sevier and Laramide Orogenies and progradation of Cretaceous sediment into the Gulf of Mexico Basin prompted withdrawal of the Cretaceous sea (Johnson, 2008).



**Figure 6.** Generalized surface and subsurface stratigraphic column for the present-day Ardmore Basin. Solid horizontal lines represent conformable contacts. Wavy horizontal lines indicate an unconformity and bracket time periods of nondeposition and/or erosion (unit ages from USGS National Map Database; Ham (1969); Huffman et al. (1978); Johnson (1989)).

## Previous Study

Few attempts have been made to model Ardmore Basin burial and thermal history. Brown (2002) modeled temperature, vitrinite reflectance (%R<sub>o</sub>), and transformation ratio for the Woodford Shale in the Ardmore Basin, Mill Creek Syncline, and Anadarko Basin to determine the origins of hydrocarbons in the Mill Creek Syncline, north of the Arbuckle Mountains. Methods included creating multiple graphs for each locality such as vitrinite reflectance vs. depth plots, vitrinite reflectance vs. temperature plots, and transformation ratio vs. age plots. Although these graphs are indicative of burial and thermal history, no actual burial history models were published. Conclusions of this study were that the Mill Creek syncline was charged by petroleum that likely originated from the Woodford Shale in the Ardmore Basin during rapid Desmoinesian–Missourian subsidence. Charge ceased when the Mill Creek syncline became isolated from the Ardmore basin by Virgilian uplift of the Arbuckle Mountains and Tishomingo Anticline. These conclusions are contingent upon the Woodford Shale attaining sufficient levels of maturity to produce petroleum before migration pathways were obstructed by Virgilian uplifts. Notably, Brown (2002) recognized the importance of subsidence and burial during the Demonian–Missourian as they relate to thermal maturation of Paleozoic source rocks.

A few attempts have been made to reconstruct Anadarko Basin burial and thermal history. Carter et al. (1998) showed the Woodford and Caney Shales passing through oil generation maturity windows by end of the Permian in two 1D burial history models.

A USGS Petroleum Systems Assessment (Higley et al., 2014) and other works (Higley 2011, 2013) used multi-dimensional basin modeling to evaluate thermal maturity and recoverable resource potential of various stratigraphic intervals within the Anadarko Basin. Higley et al. (2014) published two 1D burial history models based on a pair of wells within the Anadarko Basin: the Petree Ranch 1 and Bertha Rogers 1. These two models display similar subsidence

patterns with Cambrian–Ordovician Iapetan subsidence, two pronounced subsidence events at the end of the Pennsylvanian and Permian, respectively, minor erosion during the Triassic and Jurassic, deposition of a Cretaceous section (~3,000 ft), and Tertiary erosion. Maturation of the Devonian–Mississippian section is strongly influenced by Carboniferous–Permian burial.

Brian Cardott of the Oklahoma Geological Survey has compiled bibliographies for various geologic structures and stratigraphic units in Oklahoma. A bibliography for the Caney Shale (Cardott, 2018) contains only 46 citations. Most of this legacy literature focuses on surface geology. A bibliography covering the Woodford Shale in southern Oklahoma (Cardott, 2014) consists of 286 references. Another bibliography (Cardott, 2017b), contains 141 references to the Ardmore Basin. None of these references on the Ardmore Basin address basin-scale tectonism and its relationship to thermal and burial history.

Thermal maturity of the Woodford Shale in southern Oklahoma has been evaluated via vitrinite reflectance (%R<sub>o</sub>) by Cardott (1989, 2007, 2009, 2012, 2013); Cardott et al. (1990); and Cardott and Chaplin (1993). A database of 51 vitrinite reflectance measurements near the top of the Woodford Shale in the Ardmore Basin was provided in February 2020 by Brian Cardott in a written communication supporting this project.

The Caney Shale was originally named by Taff (1901) for two outcrops consisting of Carboniferous black shale overlying the Woodford Shale in the Coalgate quadrangle of what was then Indian Territory, Oklahoma. Since this original definition, the nomenclature, age, and type locality for the Caney Shale have gone through a long and complex evolution consisting of ten major amendments. This has exacerbated study of the Caney Shale as the formation varies in time and space throughout literature.

Wavrek (1992) chemically traced the origin of petroleum in the Ardmore Basin to six source rocks: Simpson shale, carbonaceous limestone in the Viola Group, the Woodford Shale, shale in the Sycamore limestone, the Caney Shale, and the Goddard Shale. The majority of



hydrocarbons in the Ardmore Basin are thought to have been sourced from the Woodford Shale (Wavrek, 1992).

Until 2020, only five cores covering short, partial sections of the Caney Shale had been available: three at the Oklahoma Petroleum Information Center (OPIC) and two that are stored at Oklahoma State University. Facies characterization has been completed on one core at Oklahoma State University (Radonjic et al., 2020). Further hampering subsurface study is the Caney Shale's high clay content and erosion of the flank of the Arbuckle Uplift, which has resulted in discontinuities in outcrop. Accordingly, outcrops are few and of variable quality.

## CHAPTER III

### METHODS

The following sections outline data and methods used in this study. A combination of geologic mapping, borehole data, and maturation data were used to create 1D burial and thermal history models of the Ardmore Basin.

#### **Geologic Mapping**

Burial and thermal history modeling requires quantitative estimation of the depth of basement without sediment and water loading. This geophysical analysis technique is called backstripping and is used to estimate the tectonic component of subsidence (Watts and Ryan, 1976). The net result of tectonic subsidence plus the additional effects of sediment accumulation and compaction are called total effective subsidence, which is what most burial history models display. Identifying the precise timing of all depositional and erosional events, as well as their respective thicknesses, is essential for creating a basin model that accurately illustrates tectonic history and predicts hydrocarbon maturity windows. Accordingly, a surface geologic map

provided important control for establishing basin stratigraphy, structure, present-day unit thickness, and thickness of eroded strata.

Consistent stratigraphic nomenclature for the Ardmore Basin is elusive because units vary both spatially and temporally in literature. Multiple published geologic maps display the locations of rock units in Oklahoma. Three of these maps (Miser, 1954; Heran et al., 2003; Stanley and Chang, 2012) were compiled to construct a surface geologic map of the Ardmore Basin. Each of these maps are slightly different, mostly because of variations in nomenclature as well as stratigraphic relationships, and so some interpretation was required to rectify differences among sources. The constructed geologic map was assembled in ArcGIS and was coupled with digital elevation data from the USGS National Map Database (Gesch et al., 2009), which controls surface elevation.

### **Well Log Correlation and Analysis**

To develop an understanding of the Ardmore Basin's stratigraphic and structural framework, approximately 24,000 stratigraphic tops were correlated in more than 1,600 wells using Petrel software. Stratigraphic tops range from Precambrian basement (locally) to the Pennsylvanian–Permian Pontotoc Group (common). This well density captures all major trends and folds (i.e., synclines and anticlines) in the basin as well as regional variation of stratigraphic thickness.

Wells in the dataset for this project are distributed throughout the Ardmore Basin. The most commonly logged interval is the Woodford Shale. Permian and Cretaceous units are typically not logged. It is clear that deep Caney and Woodford Shale-penetrating wells are mostly limited to localities that have source rock maturity and reservoir properties conducive to commercial petroleum development. Older wells are typically vertical and do not penetrate the

base of the Pennsylvanian System. Wells drilled recently (2000 and later) are typically deeper and often target Devonian and Mississippian shale reservoirs.

All mapping was performed using Petrel. A topographic map was generated for the surface of the Ardmore Basin using digital elevation data acquired from the USGS National Map database (Gesch et al., 2009). Structural contour maps were generated for the Sylvan Shale, Hunton Group, Woodford Shale, Sycamore Formation, and Caney Shale, which provide the densest and most consistent well control. Three-dimensional structure maps were constructed using Petrel software to visualize structure. Modern-day formation depth was approximated by subtracting a stratigraphic unit's elevation map from the surface topographic map. Isochore maps were also generated.

The Woodford Shale is consistently logged and thus provides greater well control than other formations in the dataset, and so the conformal gridding algorithm in Petrel was used to ensure that other stratigraphic surfaces are subparallel to the top of the Woodford Shale, which avoided intersecting surfaces in areas of sparse well control. Early Paleozoic units generally exhibit consistent structure and so the conformal gridding algorithm worked well for mapping these units. Pennsylvanian and younger units have variable structure related to syntectonic growth, and so the convergent interpolation gridding algorithm was used instead of the conformal gridding algorithm to map these units. Unlogged intervals of wells were interpolated using tops in surrounding wells and unit thickness reported in published literature (e.g., Ham, 1969; Huffman et al., 1978; Johnson, 1989). Structure and isochore maps were not smoothed so that they represent actual basin structure. Faults were not mapped, and so this can be a source of inaccuracy in the isochore maps.

## Geophysical Mapping and Thermal Gradient Analysis

Aeromagnetic and gravity anomaly maps of southern Oklahoma (Sweeney and Hill, 2005) were compiled using ArcGIS and are useful for visualizing basement structure and sediment thickness. These maps were superimposed by basin structures from Dionisio (1975) and Northcutt and Campbell (1995) to reveal anomaly signatures of macro-scale structures.

Geothermal gradients were calculated to constrain thermal dynamics. Bottom-hole temperatures (BHTs) from 98 well log headers were tabulated and corrected using ZetaWare's Time Since Circulation Calculator software. BHTs were acquired from wells at multiple structural locations and at various depths to capture variations in thermal conductivity and heat flow in the Ardmore Basin. Corrected BHTs were plotted against true vertical depth (TVD) to show the relationship between depth and temperature in the Ardmore Basin. A geothermal gradient was calculated for each BHT using Equation 1.

$$geothermal\ gradient = \frac{(BHT - MAST)}{Depth} \quad (1)$$

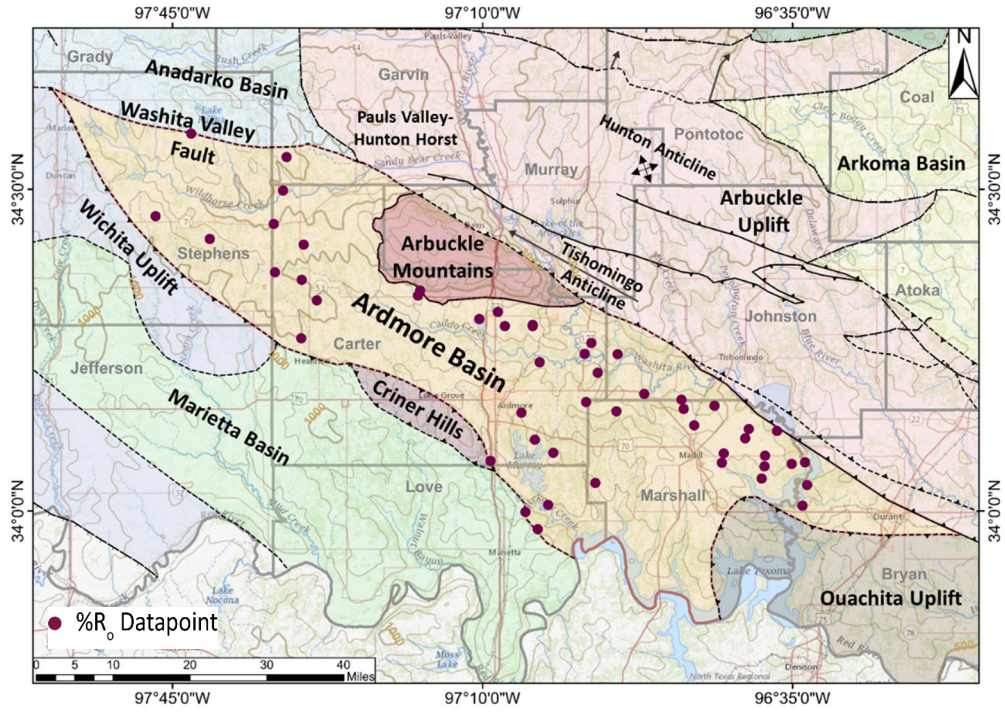
where BHT = corrected bottom-hole temperature (°F), MAST = mean air surface temperature in southern Oklahoma (68°F) (Wygrala, 1989), Depth = TVD of BHT measurement (ft)

Geothermal gradients were mapped using the convergent interpolation gridding algorithm in Petrel to display how temperature increases with depth throughout the Ardmore Basin. The geothermal gradient map was used to calculate *in situ* formation temperatures for tops of the Sylvan Shale, Hunton Group, Woodford Shale, Sycamore Formation, and Caney Shale in the Ardmore Basin. This was completed by multiplying the geothermal gradient by formation depth and then adding the present-day mean surface temperature (68°F) in Petrel.

## Vitrinite Reflectance Analysis

Thermal maturity data from the Caney Shale are few when compared to those from the Woodford Shale in southern Oklahoma. As such, this study used the vitrinite reflectance of the Woodford Shale as a proxy for estimating maturity of the Caney Shale in the Ardmore Basin. Woodford Shale vitrinite reflectance data are available in numerous publications (e.g., Cardott, 1989, 2007, 2009, 2012, 2013; Cardott et al., 1990; Cardott and Chaplin, 1993). A database of 52 vitrinite reflectance measurements from the Woodford Shale in the Ardmore Basin, was provided in February 2020 by Brian Cardott (written communication) (Figure 7). This database consists of mean-random vitrinite reflectance measurements averaged over an interval within the Woodford Shale at various locations throughout the Ardmore Basin. Additionally, Rock-Eval pyrolysis data, including  $T_{max}$ , were measured in the Caney Shale core from the Tomaney 1-35-34-27XHW well.

Vitrinite reflectance-depth plots were used to analyze relationships between thermal maturity and depth, and to estimate the amount of strata that has been eroded from above the Paleozoic section in the Ardmore Basin. A vitrinite reflectance-formation temperature plot was also made. Each plot was fitted with a logarithmic least squares regression line and 90% confidence interval for the slope of the regression line which helps constrain uncertainty when making projections of eroded overburden thickness.



**Explanation**

- ▲▲▲ Thrust fault
- Plunge of structure
- — — Buried structure
- ▲▲▲ Anticline
- — — Normal fault
- Contour interval = 100 ft

**Figure 7.** Map showing locations of 52 Woodford Shale vitrinite reflectance measurements in the Ardmore Basin (after Cardott, 2020, written communication; Northcutt and Campbell, 1995).

Vitrinite reflectance maps were calculated for the Sylvan Shale, Hunton Group, Woodford Shale, Sycamore Formation, and Caney Shale using the equation derived from the least squares regression of the Woodford Shale vitrinite reflectance-elevation plot. The least squares regression equation was rearranged to solve for vitrinite reflectance in the Ardmore Basin. This method allows for projection of vitrinite reflectance where measured vitrinite reflectance data are absent, such as in deep synclines where no wells have penetrated the Woodford or Caney Shales. The calculated vitrinite reflectance maps can serve as a metric for

calibrating burial and thermal history models where measured vitrinite reflectance data are absent. Furthermore, this method ensures that all basin structure is reflected in the vitrinite reflectance maps. 3D maturity maps were also constructed to facilitate comparison between basin structure and thermal maturity.

Although vitrinite reflectance maps were calculated for other formations, the Woodford Shale vitrinite reflectance map is the most accurate because it is based on measured values. Accordingly, the Woodford Shale vitrinite reflectance data and projections were used as the primary control for calibration of 1D burial history models.

The calculated Woodford Shale vitrinite reflectance map was compared to Woodford GOR data to help validate the maturity map as well as test the extent and impact of lateral hydrocarbon migration within the Woodford Shale. The locations of 499 gas-oil ratio (GOR) measurements, recorded after the first six months of production from wells that exclusively produced from the Woodford Shale in the Ardmore Basin, were plotted on the calculated Woodford Shale vitrinite reflectance map. GOR data points were color-coded according to GOR ranges.

API gravity data from oil produced from the Woodford Shale in the Ardmore Basin were plotted against vitrinite reflectance, Woodford Shale depth, and *in situ* Woodford Shale formation temperature (production data was acquired from Enverus, 2021). Each graph was fitted with a least squares regression line. Woodford Shale vitrinite reflectance and temperature were acquired from the calculated Woodford Shale vitrinite reflectance map and the Woodford Shale temperature map, respectively. In addition to the Woodford Shale GOR data, these graphs serve as a metric for validating accuracy of calculated maturity and for examining the extent and impact of lateral hydrocarbon migration within the Woodford Shale.

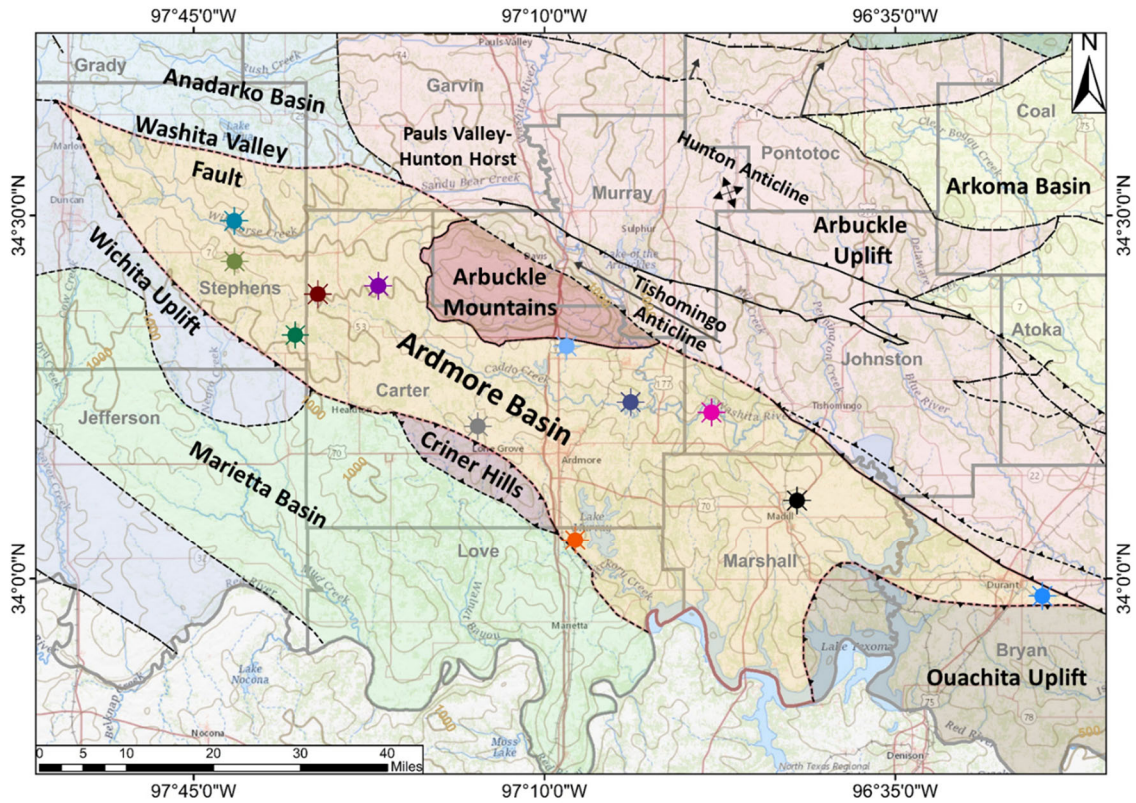


## Burial and Thermal History Modeling

Twelve one-dimensional burial and thermal history models were constructed using wells strategically chosen throughout the Ardmore Basin (Table 1; Figure 8). Modeling wells were chosen to ensure sufficient distribution and that all major structures (i.e., synclines and anticlines) were captured in the modeling effort. Additionally, wells that penetrate a significant thickness of strata, including Devonian–Mississippian source rocks, and have bottom-hole temperature data for calibrating maturation models were selected. Modeling was completed using Schlumberger PetroMod (2018) software. PetroMod is petroleum systems and basin modeling software that combines well and geological data to model the evolution of a sedimentary basin.

**Table 1.** Wells used in burial and thermal history modeling of the Ardmore Basin.


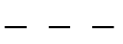
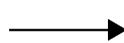

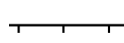
Well Name	UWI	Latitude	Longitude
B&W TYSON 1-8	35019255860000	34.392424	-97.543470
TOMANEY 1-35-34-27XHW	35137274810000	34.336325	-97.580984
J LITTLE A-1-6	35019218140000	34.320861	-97.129717
BADGER 2-23	35095204700000	34.108847	-96.746587
BROCK 9-1H	35069200940000	34.230071	-96.888920
DANSBY 1-3H	35013201500000	33.976198	-96.338768
J PAUL 1-7	35019252740000	34.403720	-97.442898
MARTIN 8-2 RD	35085210660000	34.053835	-97.115449
STARR 1-25	35137270400000	34.437225	-97.681972
MARTIN 1-14	35019221600000	34.211023	-97.277364
STEPHEN 1-6H	35019255370000	34.242216	-97.036950
HAYS 1-1H	35137271670000	34.492816	-97.682368



**Wells Used for Modeling**

- |  |   |  |   |
|--|---|--|---|
|  Starr 1-25   |  Martin 1-14   |  Dansby 1-3H    |  B&W Tyson 1-8         |
|  Hays 1-1H    |  Martin 8-2 RD |  Brock 9-1H     |  Badger 2-23           |
|  Stephen 1-6H |  J. Paul 1-7   |  J Little A 1-6 |  Tomaney 1-35-34-27XHW |

**Explanation**

- |   |  |
|---|--|
|  Thrust fault        |  Buried structure |
|  Plunge of structure |  Anticline        |
|  Normal fault        | Contour interval = 100 ft  |

**Figure 8.** Map showing locations of wells used for burial and thermal history models of the Ardmore Basin.

Modeling software inputs include stratigraphy, rock types, thermal conductivity, surface temperature through geologic time, and basement heat flow through geologic time. Stratigraphic inputs include estimated absolute ages of major depositional and erosional events as well as depositional and erosional thickness throughout a basin's history. All parameters are integrated to quantitatively model a basin's burial history and associated subsidence as well as durations and temperatures source rocks are subjected to as they are buried through geologic time. PetroMod uses the EASY %R<sub>o</sub> kinetic model (Sweeney and Burnham, 1990), to calculate thermal maturity, in the form of vitrinite composition, as a function of geologic time and temperature. This model is widely used and can be used to predict vitrinite reflectance and temperature at any depth or point in geologic time. Boundary conditions in this calculation typically include paleobathymetry, paleomean surface temperature, and basement heat flow. Bathymetric corrections were not performed in modeling efforts. The Ardmore Basin was at or near sea level during much of the Phanerozoic. Although the region was below storm wave base for much of the Late Devonian–early Chesterian, water depth apparently was not great enough to have a significant effect on the burial history models.

Depths of formation tops, lithologies, and estimated absolute ages of depositional and erosional events were acquired from numerous sources. Depths of formation tops were mostly interpreted from well logs of the Paleozoic section. If a formation top was not present in a well log, its depth was estimated using data from surrounding wells and unit thickness reported in the literature (e.g., Ham, 1969; Huffman et al., 1978; Johnson, 1989). Rock types within formations and groups are similar, and so most stratigraphic depositional events were characterized at formation or group level for modeling purposes. Estimated absolute ages of depositional and erosional events as well as generalized rock types were retrieved from multiple sources including the USGS National Geologic Map Database; Ham (1969); Huffman et al. (1978); and Johnson (1989). Eroded thicknesses of rock units were estimated using cross sections, structure and isochore/isopach maps, as well as reported stratigraphic thicknesses proximal to the Ardmore

Basin (e.g., Ham, 1969; Huffman et al., 1978). Calibration of burial and thermal history models helped in determining eroded thicknesses.

PetroMod has a large database of rock types with corresponding properties. When a rock type is selected for a specific depositional unit, its properties and compaction behavior (i.e., porosity, mineralogy, density, permeability, and compaction constant) are automatically assigned. Thermal lithologic properties such as heat capacity, specific heat, and thermal conductivity also are incorporated in the rock types.

Source rock properties such as TOC and hydrogen index (HI) are essential for modeling degradation of organic matter during hydrocarbon generation. TOC and HI properties for the Caney Shale were included in Rock-Eval pyrolysis data measured from the Caney Shale core at Chesapeake Energy's Reservoir Technology Center in Oklahoma City.

Ardmore Basin burial history models contain 24 depositional events (tabulated in Table 2) and 14 erosional events. If a unit was interpreted to have never been deposited at a model location, its ancient and present-day thickness were set to zero. Names of depositional events correspond to either a formation or group name. The youngest modeled unit was the Cretaceous Eagle Ford Group, which is no longer present in the Ardmore Basin but is present just west in Bryan County (Heran et al., 2003) and south in Grayson County, Texas (McGowen et al., 1991). There is no evidence to support significant deposition of Tertiary sediment in southern Oklahoma (Suneson, 2020).

**Table 2.** Modeled depositional events for the Ardmore Basin.

1. Eagle Ford Group	13. Dornick Hills Group
2. Woodbine Formation	14. Springer Group
3. Washita Group	15. Caney Shale
4. Fredericksburg Group	16. Sycamore Formation
5. Trinity Group	17. Woodford Shale
6. Whitehorse Group	18. Hunton Group
7. El Reno Group	19. Sylvan Shale
8. Hennessey Group	20. Viola Group
9. Sumner Group	21. Simpson Group
10. Pontotoc Group	22. Arbuckle Group
11. Hoxbar Group	23. Timbered Hills Group
12. Deese Group	24. Basement

PetroMod offers built-in modules to assist in calculating boundary conditions. Paleo mean surface temperatures were estimated using an approach developed by Wygrala (1989), which calculates a temperature at sea level over geologic time based on geographic location and latitude. Paleo mean surface temperatures for the southern part of the Laurussian craton were calculated and are reasonable for the paleolatitudes typically shown in the major paleogeographic reconstructions (i.e., Scotese, 2002). Another important parameter in thermal history modeling is sediment-water-interface temperature, which is the upper thermal boundary condition of a model and constrains thermal relationships between sediment and water during sediment deposition. Paleo sediment-water-interface temperatures were estimated using methods devised by Wygrala (1989). Basement heat flow through geologic time was specific to each model but was generally approximated using a method developed by McKenzie (1978), which semi-quantitatively estimates thermal histories of rift-related basins based on thermal decay associated with crustal stretching.

Heat flow is an influential parameter for modeling the thermal history of a basin. Heat flow emanating from the basement includes conduction and convection sourced from radioactive decay in the mantle and depends on thickness of the crust and the thermal conductivity of the

sedimentary column (Al-Hajeri et al., 2009). A generalized heat flow map of the United States (Blackwell et al., 2011) displays heat flow in southern Oklahoma ranging from ~30–40 mW/m<sup>2</sup>; however, sparsity of data limits the ability to precisely estimate heat flow values at specific locations directly from the map. Present-day heat flow was ultimately estimated for each model via a trial-and-error process by adjusting heat flow parameters so that simulated thermal and vitrinite reflectance gradients corresponded with direct measurements from the subsurface.

Simulated vitrinite reflectance and geothermal gradients (Sweeney and Burnham, 1990) were calibrated to measured vitrinite reflectance and temperature data (corrected bottom-hole temperatures) respectively, to ensure model validity. Vitrinite reflectance data for calibration originated from the Woodford Shale vitrinite reflectance map, which was constrained by direct measurements. Calibration entails adjusting a model so that calculated vitrinite reflectance and thermal gradients match measured data at varying depths in a well. Calibration was often performed by modifying basement heat flow through geologic time and/or the erosional and depositional thicknesses of the post-Pennsylvanian section, which are variable throughout the Ardmore Basin.

A kerogen quality plot (TOC vs. S<sub>2</sub>) was created using Rock-Eval pyrolysis data measured from the Caney Shale core recovered from the Tomaney 1-35-34-27XHW well to assess the type of kerogen present in the Caney Shale. Results from this plot were used to assign kinetic parameters to model timing and duration of petroleum generation in the Caney and Woodford Shales. Kinetic parameters relate burial depth, temperature, and duration of geologic time required for thermal maturation to occur within source rocks (Higley et al., 2014). PetroMod software offers a database of hydrous pyrolysis reaction kinetics to predict hydrocarbon properties and phases for various source rocks.

Transformation ratio is defined as the ratio of petroleum or natural gas formed by a specific type of kerogen to the total amount of oil or gas that the kerogen is capable of generating

and is often expressed as a percentage (Tissot and Welte, 1984). Transformation for the onset of oil and gas generation and expulsion is 0.1%, peak generation is 50%, and completion of generation is 100%. If a transformation percentage is less than 100%, all kerogen capable of generating oil or gas has not been transformed. Immature source rocks will have a transformation percentage less than 10%. If a transformation percentage is 100%, then all kerogen capable of generating oil or gas has exhausted its generative capacity. A transformation percentage of 100% may also indicate a source rock is overmature for oil and/or gas generation.

Transformation ratio windows were superimposed on each burial history plot to display the evolution of petroleum generation through time and burial. Transformation ratio plots were created to display how petroleum was generated from kerogen in the Woodford and Caney Shales through geologic time for applicable models. Models that project the Woodford and Caney Shales as submature were not included in transformation ratio plots as there has been minimal or no cracking of kerogen.

## CHAPTER IV

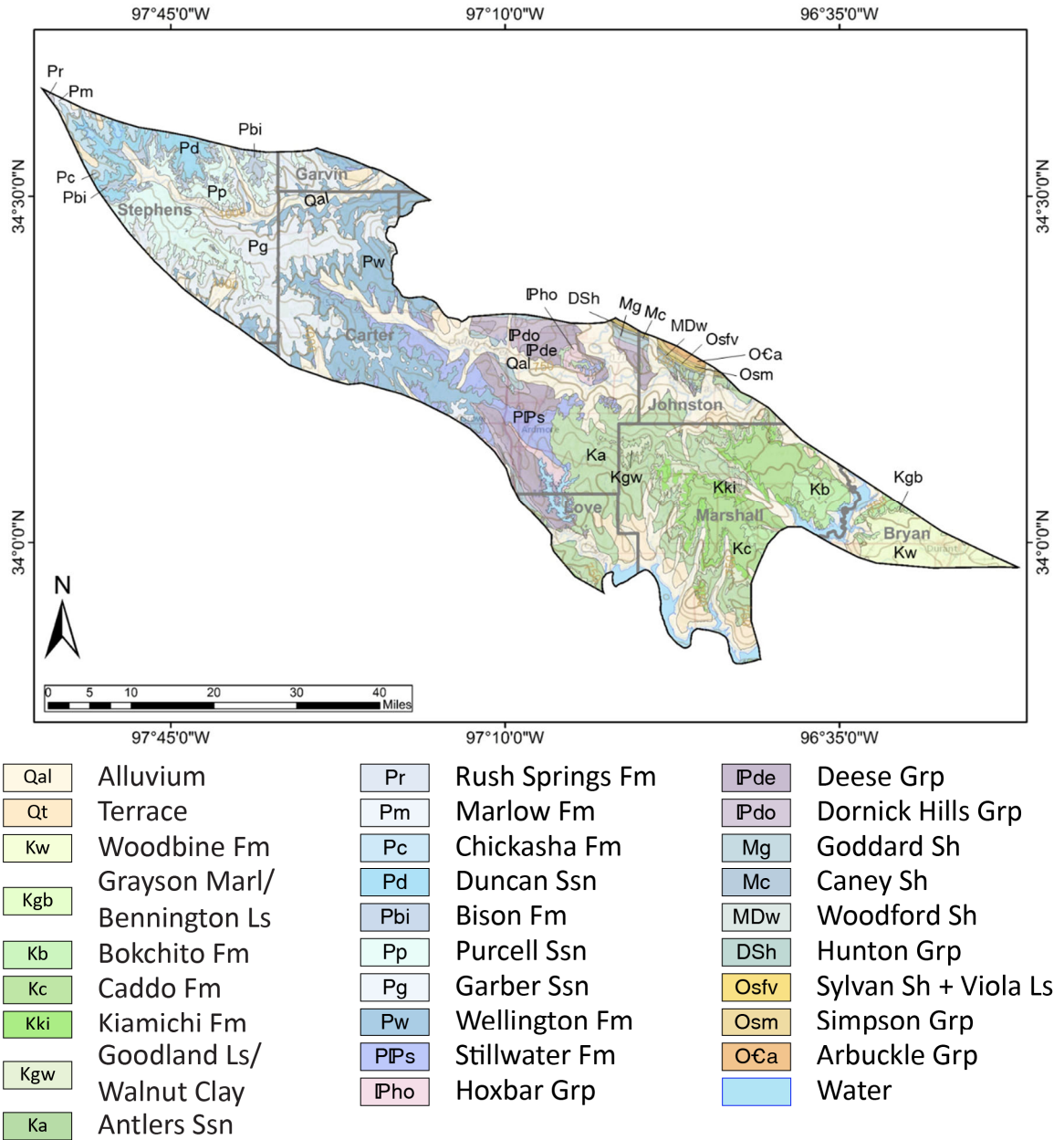
### RESULTS

#### **Geologic Mapping**

A surface geologic map (Miser, 1954; Heran et al., 2003; Stanley and Chang, 2012) (Figure 9) was an important control for establishing basin stratigraphy, structure, and spatial relations of rock units in the Ardmore Basin. Precambrian mafic and felsic volcanic rocks crop out in the Arbuckle Mountains and the Arbuckle Uplift (Heran et al., 2003). Paleozoic units, notably the Arbuckle Group, also are exposed in and around the Arbuckle Mountains and the Arbuckle Uplift. The Criner Hills are overlain by Pennsylvanian and Permian strata (Miser, 1954; Heran et al., 2003; Stanley and Chang, 2012). Pennsylvanian units including the Dornick Hills, Deese, and Hoxbar Groups are present at the surface near the center of the basin in Carter and Love Counties (Miser, 1954; Heran et al., 2003; Stanley and Chang, 2012). A major unconformity separates late Paleozoic and Permian strata from Cretaceous strata. A veneer of Permian strata blankets approximately 35% of the Ardmore Basin (Miser, 1954; Heran et al., 2003; Stanley and Chang, 2012). Permian strata thicken northwest towards the Anadarko Basin (Brown, 2002). Permian units are not preserved in the Arbuckle Mountains or the Arbuckle Uplift; however, Wolfcampian and Leonardian rocks surround the western Arbuckle Mountains (Miser, 1954; Heran et al., 2003; Stanley and Chang, 2012).



Cretaceous strata of the Gulf of Mexico Basin onlap deformed Paleozoic units in the southeastern Ardmore Basin and are not preserved in the northwestern part of the basin or in the Arbuckle Mountains. Cretaceous units overlying the Ardmore Basin represent approximately 20 m.y. of deposition (Huffman et al., 1978). Unlike the deformed Paleozoic strata, Cretaceous units are flat-lying and exhibit only minor deformation (Suneson, 2020). Quaternary alluvium and terrace deposits are present along modern fluvial drainages (Stanley and Chang, 2012).



Contour interval = 100 ft

**Figure 9.** Surface geologic map displaying spatial localities of rock units in the Ardmore Basin. Permian strata dominate the northwest. Pennsylvanian units outcrop in the center of the basin. A Cretaceous sedimentary wedge associated with the Gulf of Mexico Coastal Plain province is located in the southeast (after Miser, 1954; Heran et al., 2003; Stanley and Chang, 2012).

## Well Log Correlation and Analysis

The majority of Paleozoic stratigraphic units were readily correlated on the basis of consistently recognizable well log signatures (Figures 10–12). Correlation of Pennsylvanian and younger units was challenging due to inconsistent well log signatures related to variations in thickness, spatial distribution, and lithology.

In Garvin County, adjacent to the Washita Valley Fault, and in Bryan County, repeated Paleozoic sections are recorded in well logs due to overturned bedding in fold limbs and perhaps reverse faults. Permian strata thicken towards the Anadarko Basin to the northwest. Wolfcampian and Leonardian strata, where present, can be correlated throughout much of the western basin and thicken within synclines. Cretaceous strata thicken towards the Ouachita Uplift in the southeast. Guadalupian and younger strata have been subjected to erosion and are variable in distribution and thickness.

Elevation maps (Figures 14–23) and depth maps (Figures 24–28) demonstrate that two steeply-dipping ( $\sim 20\text{--}40^\circ$ ), doubly plunging synclines are present in the Ardmore Basin: (1) in the southeast corner of Stephens County in a structure known as the Harrisburg Trough (Harlton, 1956), and (2) the Berwyn Syncline (Dionisio, 1975), which is in Carter, Johnston, Love, and Marshall Counties. The Tomaney 1-35-34-27XHW well is located within the Harrisburg Trough. Total stratigraphic thickness in these synclines is greater than 30,000 ft. The Ardmore Basin also deepens to approximately 30,000 ft in the northwest, adjacent to the Anadarko Basin. Structural highs are proximal to the Wichita Mountains, Arbuckle Mountains, Criner Hills, and Arbuckle Uplift. Paleozoic strata clearly outcrop on and around the Arbuckle Mountains and Arbuckle Uplift.

Elevation of the top of the Woodford Shale ranges from about -21,100 ft in the Berwyn Syncline to about 900 ft adjacent to the Arbuckle Uplift (Figures 16 and 21). Elevation of the top

of the Caney Shale is similar, ranging from about -20,000 ft in the Berwyn Syncline to about 950 ft adjacent to the Arbuckle Uplift (Figures 14 and 19).

Isochore maps (Figures 29–32) show that some stratigraphic units thin significantly and are laterally discontinuous in the Ardmore Basin. The Hunton Group pinches out at various locations, notably in the southeastern part of the basin in Carter and Marshall Counties (Figures 11 and 32). Thinning and truncation of the Hunton Group are interpreted to be a result of disconformity development during the Devonian, prior to Woodford Shale deposition (Fritz et al., 2012). All other mapped stratigraphic units thin to 5 ft or less as well; typically on and proximal to structural highs such as the Wichita Uplift and Arbuckle Mountains. Despite thinning and lateral discontinuities, each stratigraphic unit was artificially assigned a minimum thickness of at least 5 ft for simplicity of surface gridding in Petrel. Areas of isolated thickening in the isochore maps could be due to compression-related structures.

Thickness of the Woodford and Caney formations vary greatly throughout the Ardmore Basin. The isochore map for the Woodford Shale displays a minimum thickness of 5 ft and maximum thickness of 1,402 ft (Figure 31). Average thickness of the Woodford Shale is 375 ft. The isochore map of the Caney Shale displays a minimum thickness of 5 ft and a maximum thickness of 872 ft (Figure 29). Average thickness of the Caney Shale is 307 ft.

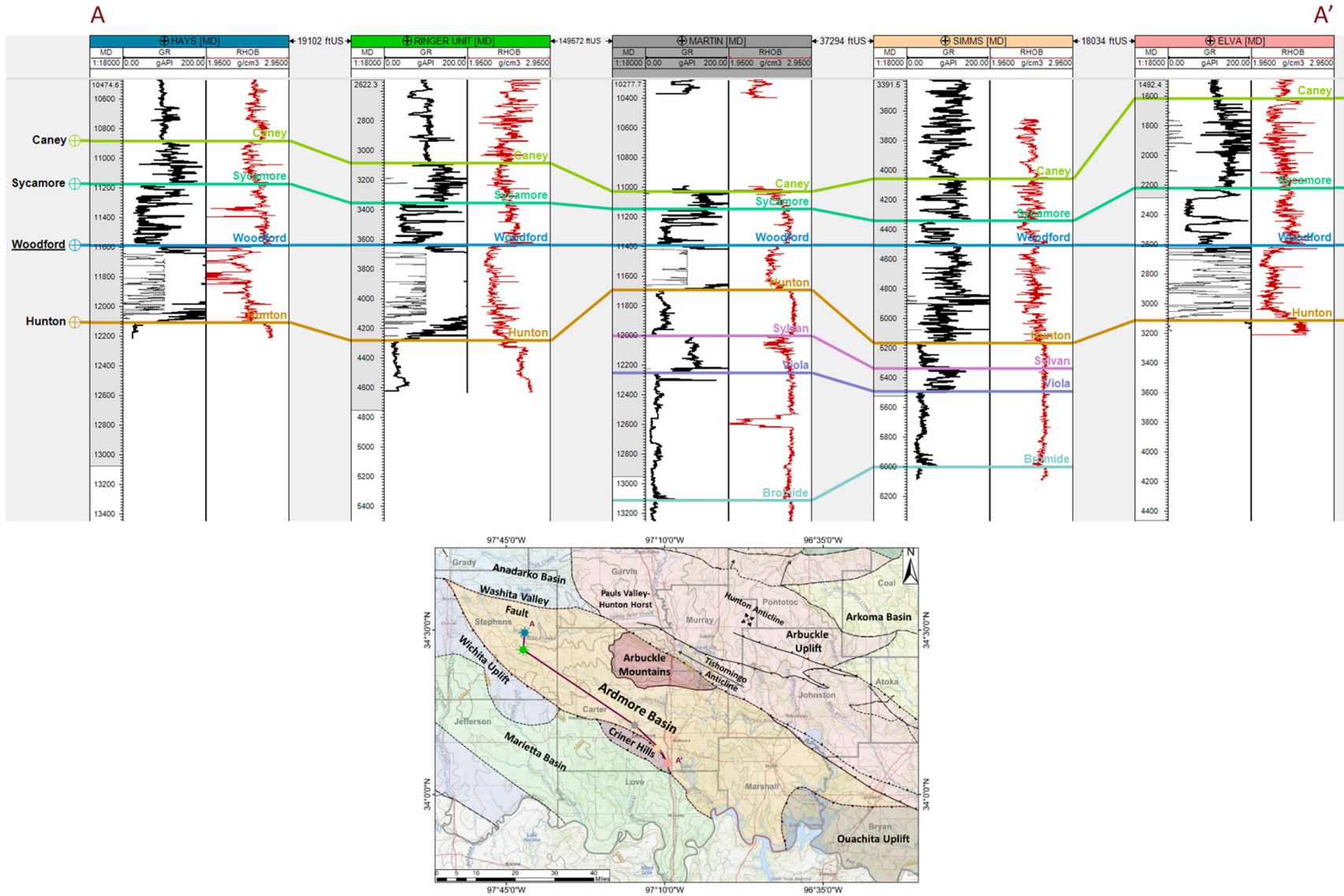
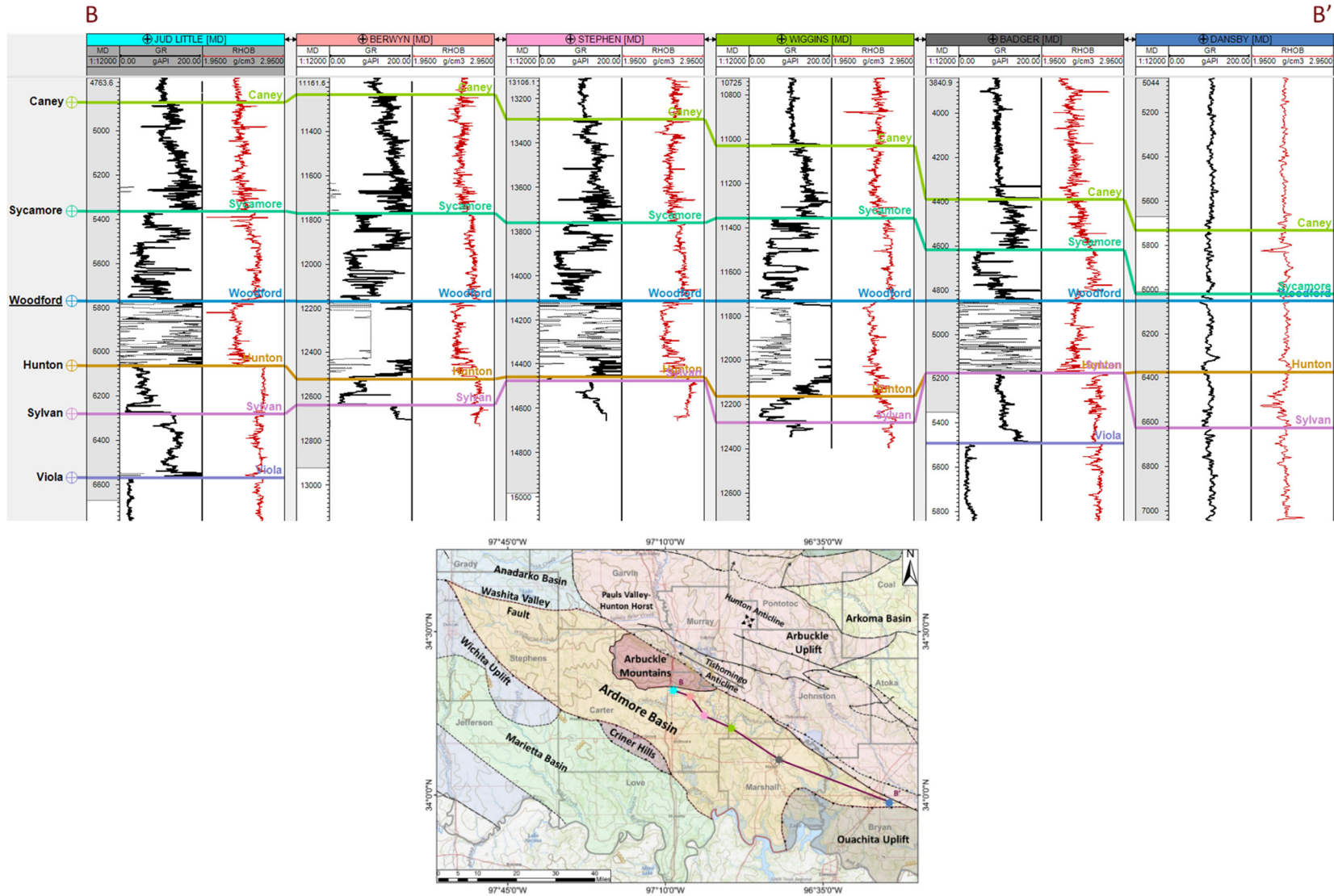


Figure 10. Stratigraphic cross-section A–A’ in the Ardmore Basin displaying well log signatures and formation tops. No horizontal scale.



**Figure 11.** Cross section B–B’ in the Ardmore Basin displaying well log signatures and formation tops. Notice complete truncation of the Hunton Group in the Badger well. No horizontal scale.

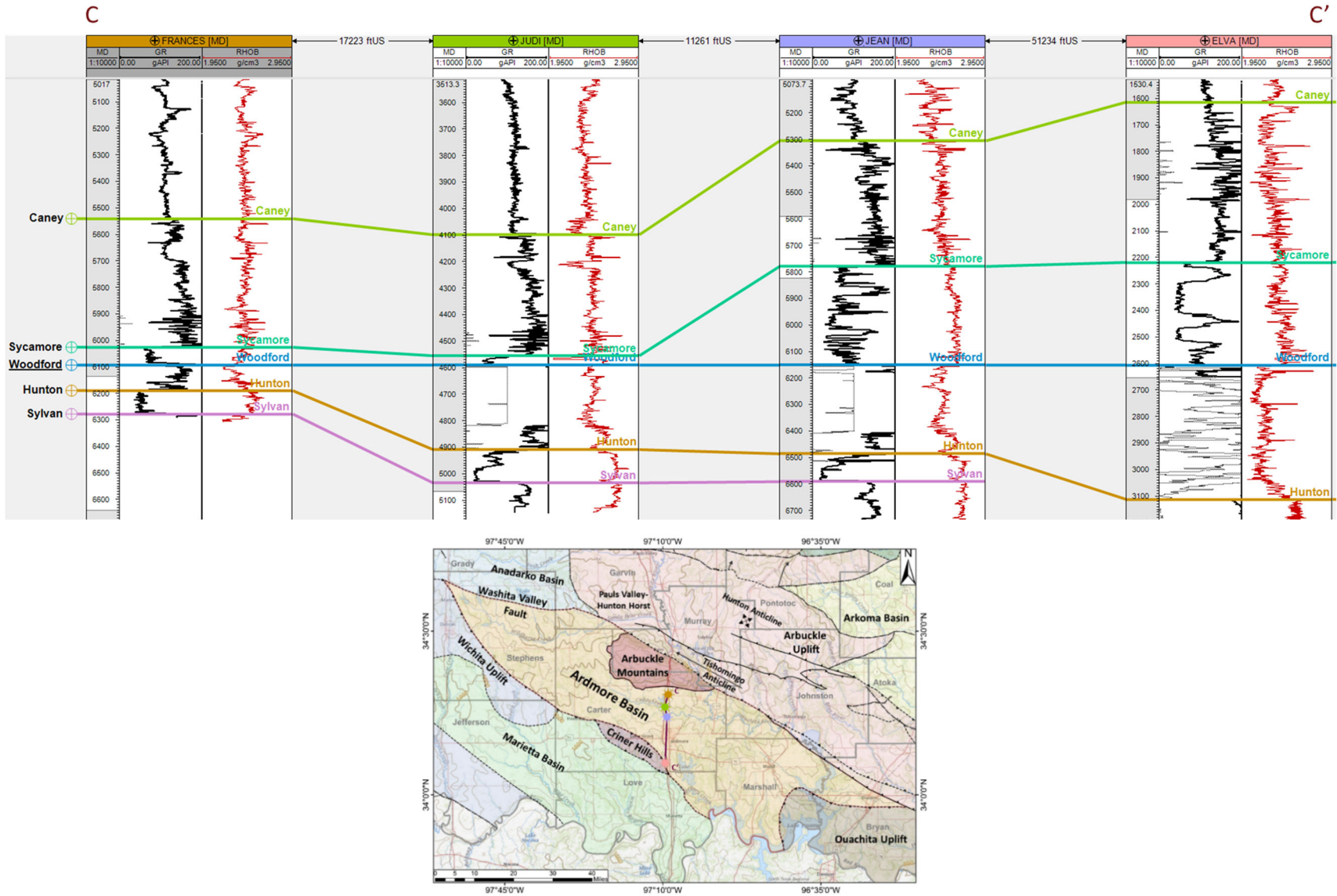
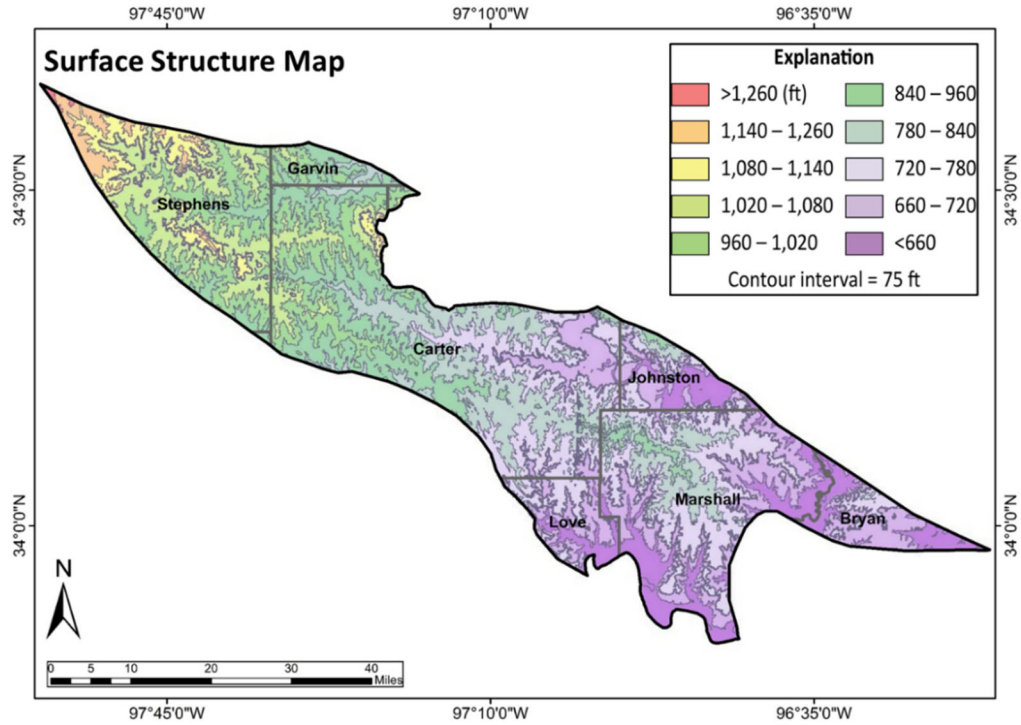
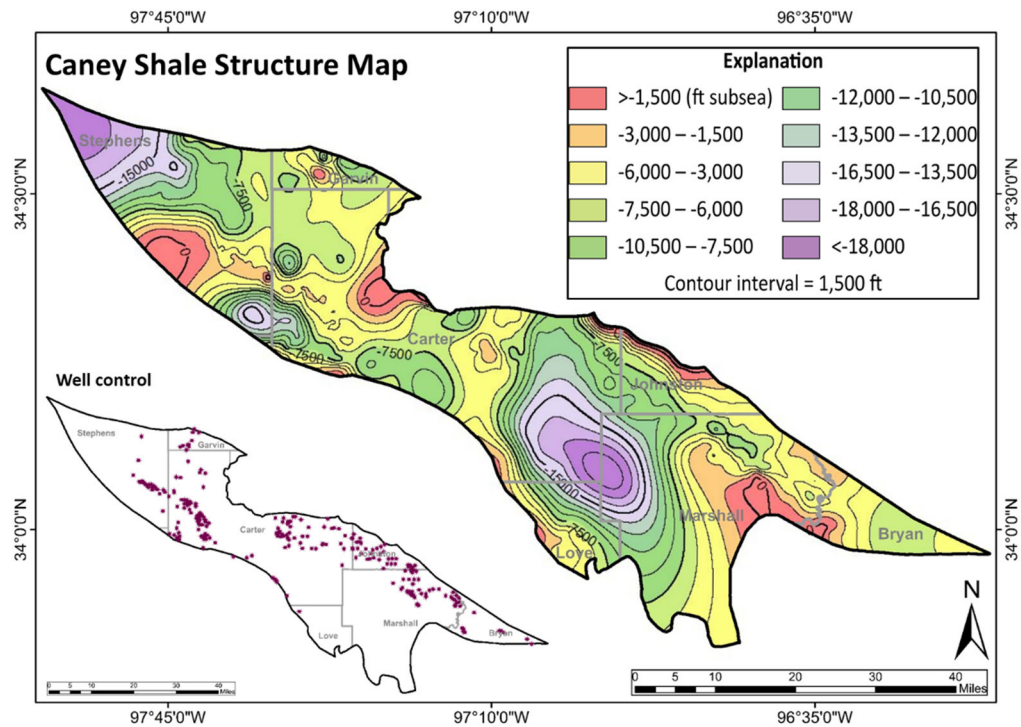


Figure 12. Cross section C–C' in the Ardmore Basin displaying well log signatures and formation tops. No horizontal scale.

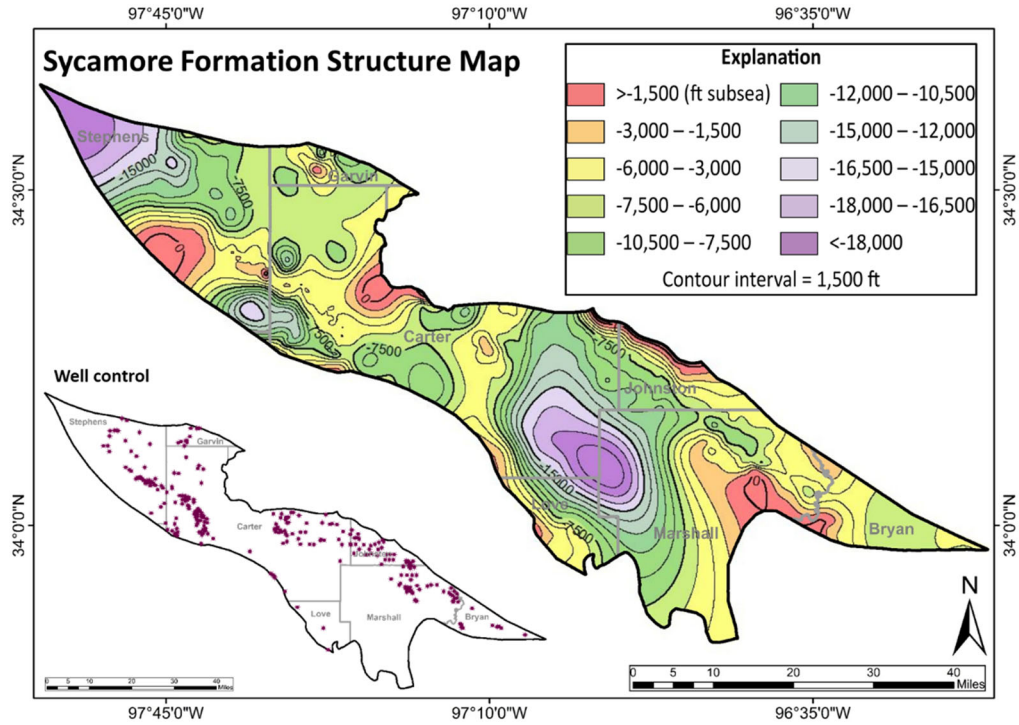


**Figure 13.** Topographic map of the Ardmore Basin (elevation data from Gesch et al., 2009). Maximum elevation is 1,313 ft in northwest. Minimum elevation is 570 ft in southeast.

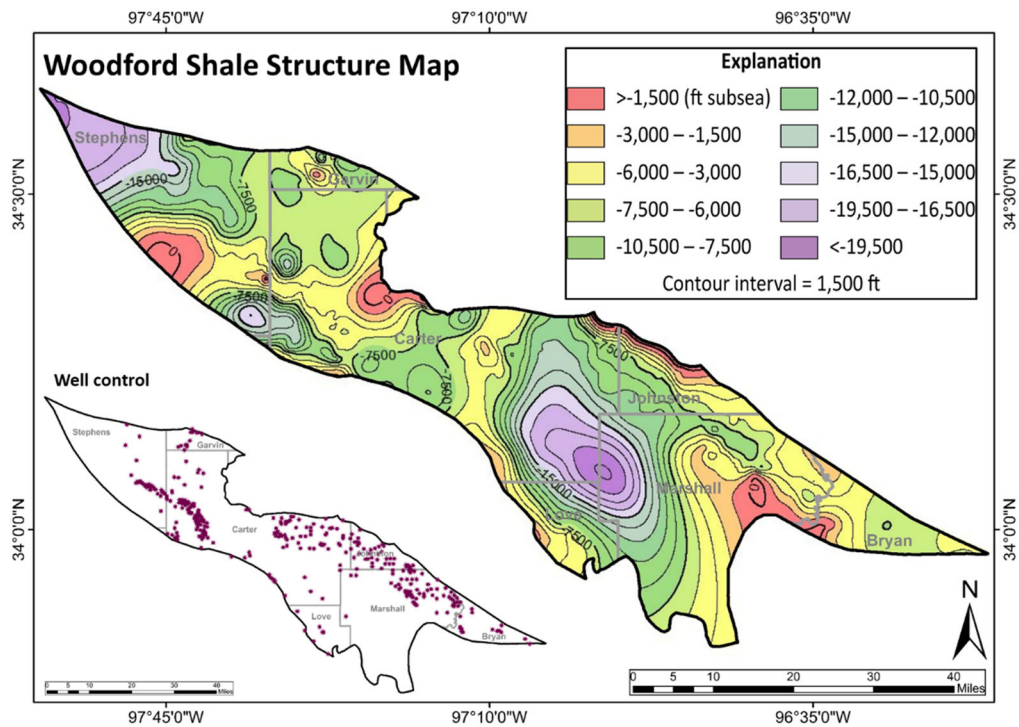


**Figure 14.** Structural contour map of the top of the Caney Shale. The well control map displays wells in which the Caney Shale is logged.

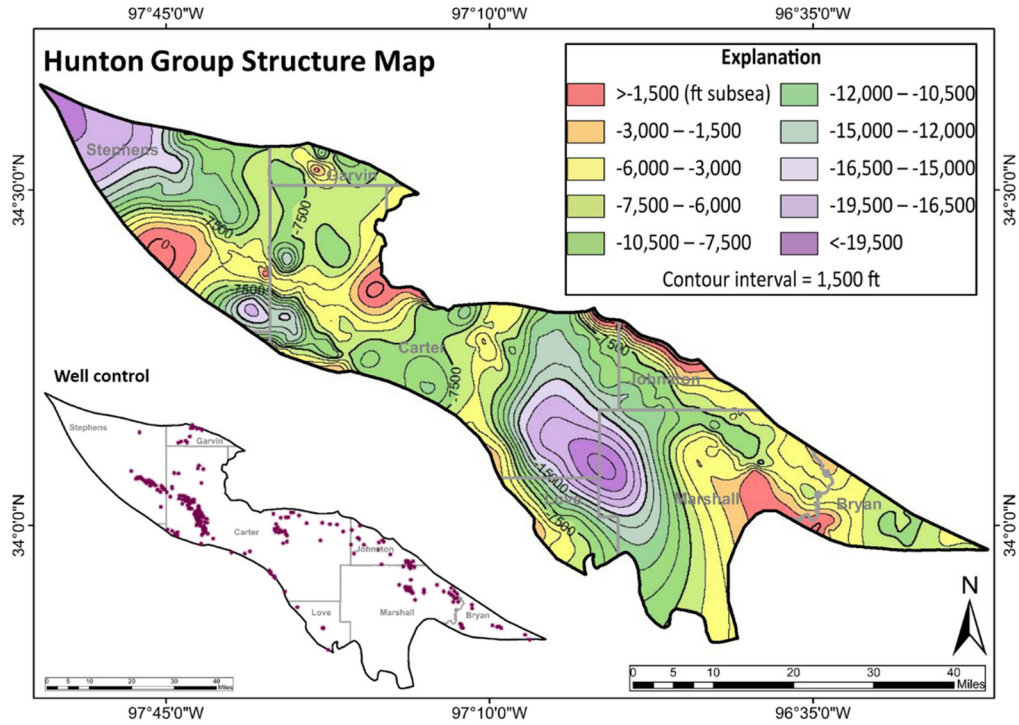




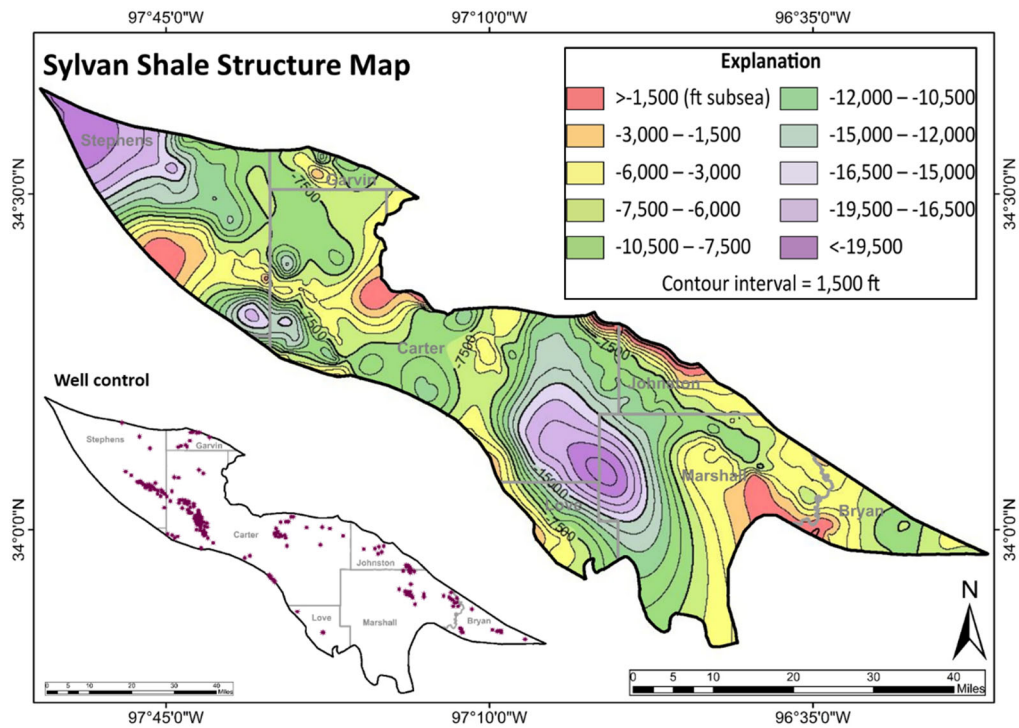
**Figure 15.** Structural contour map of the top of the Sycamore Formation. The well control map displays wells in which the Sycamore Formation is logged.



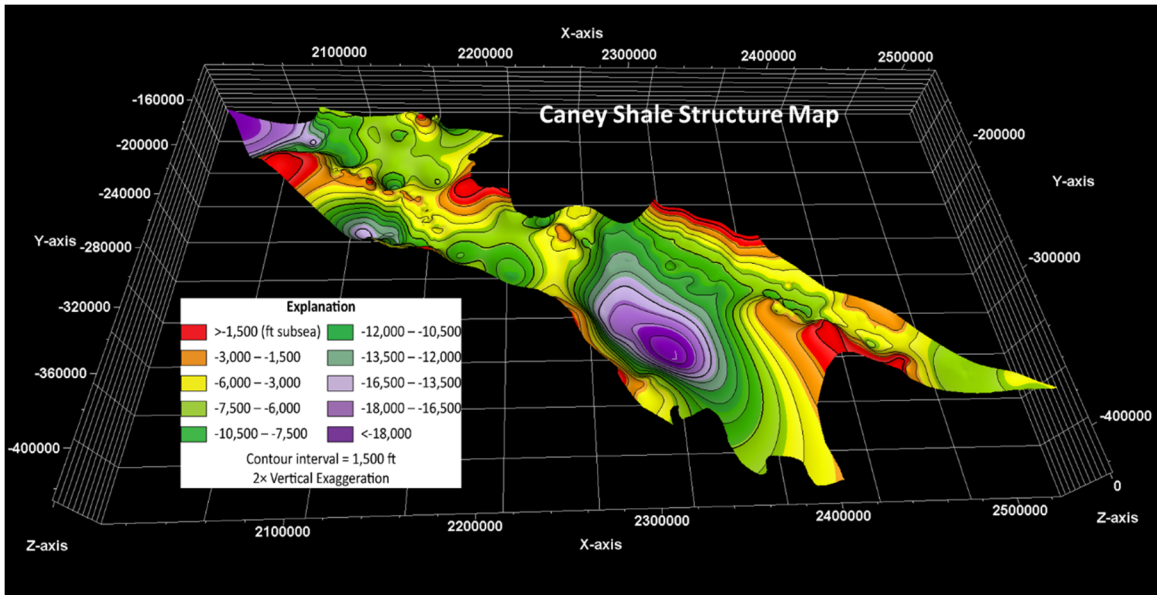
**Figure 16.** Structural contour map of the Woodford Shale. The well control map displays wells in which the Woodford Shale is logged.



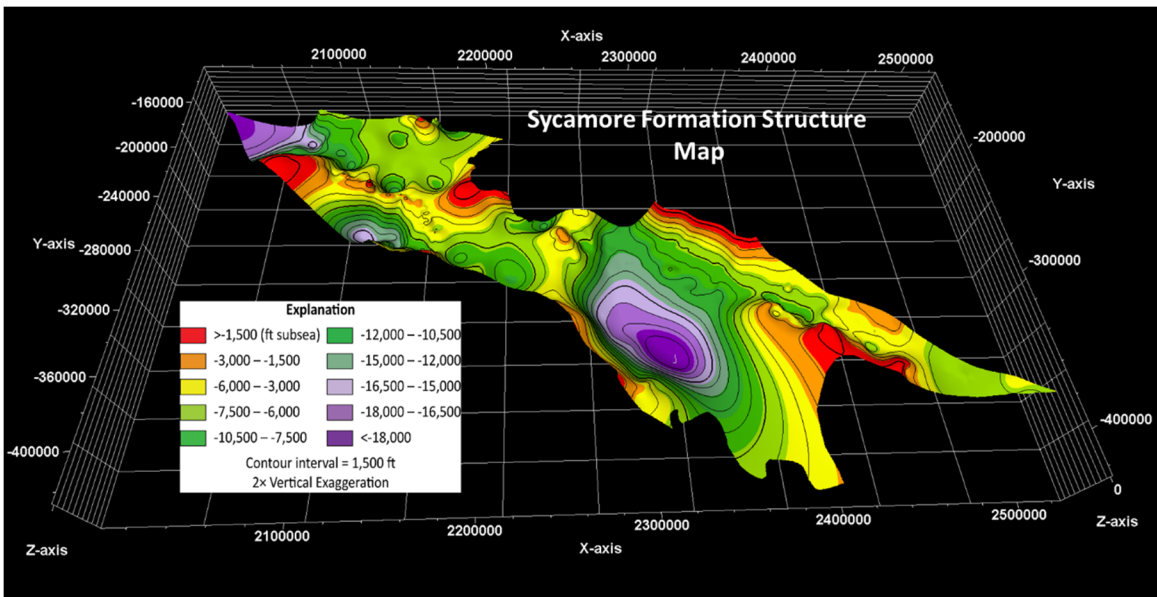
**Figure 17.** Structural contour map of the Hunton Group. The well control map displays wells in which the Hunton Group is logged.



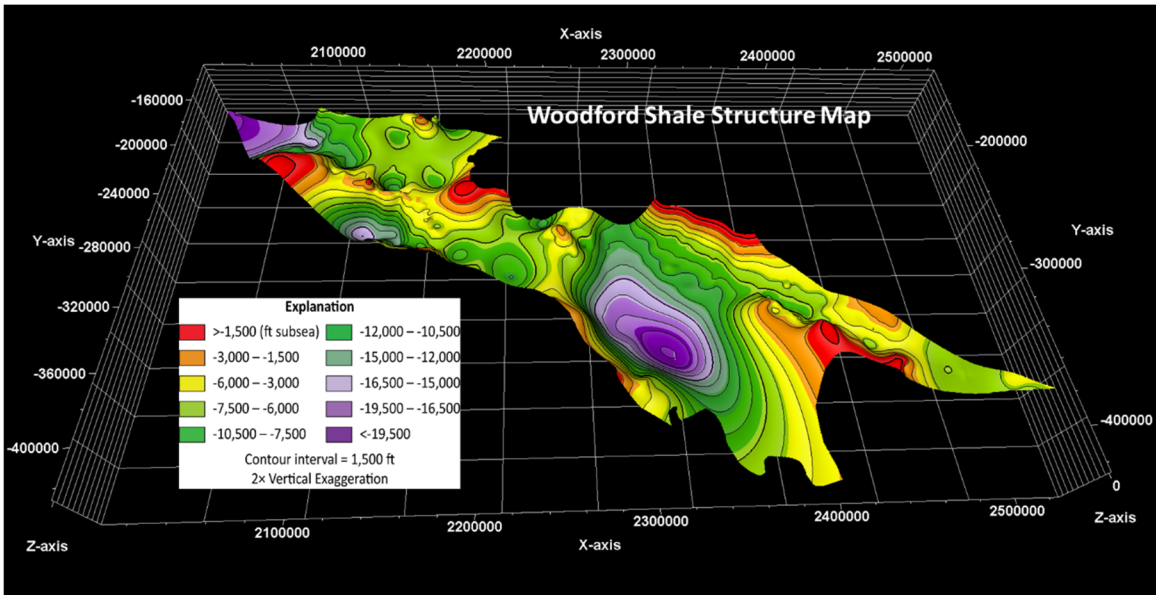
**Figure 18.** Structural contour map of the top of the Sylvan Shale. The well control map displays wells in which the Sylvan Shale is logged.



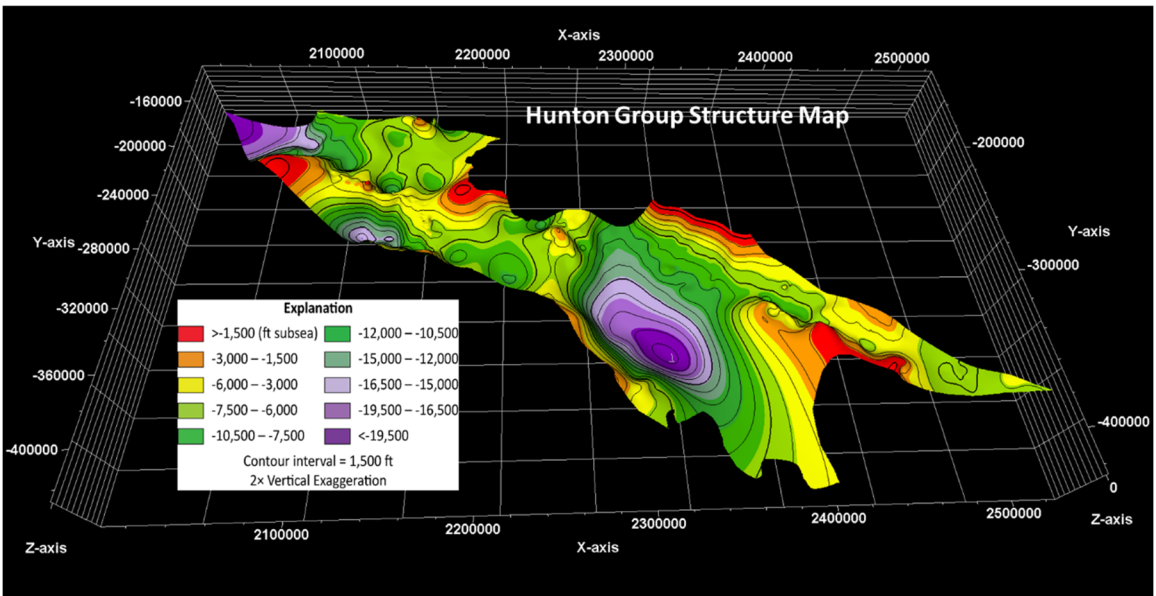
**Figure 19.** 3D structural contour map of the top of the Caney Shale. Units for axes are feet.



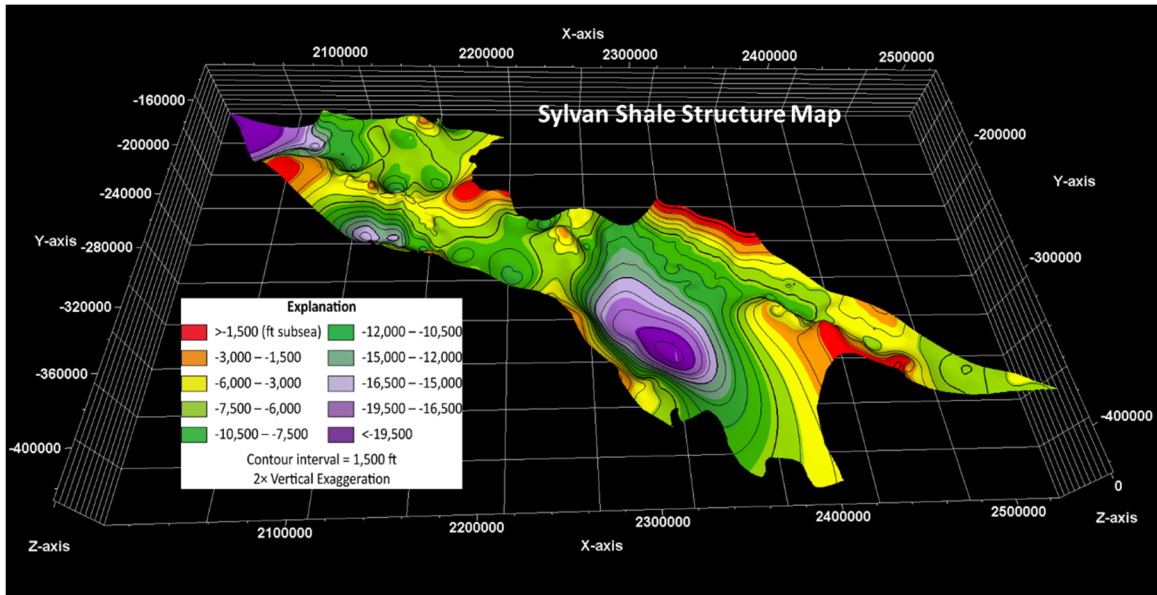
**Figure 20.** 3D structural contour map of the top of the Sycamore Formation. Units for axes are feet.



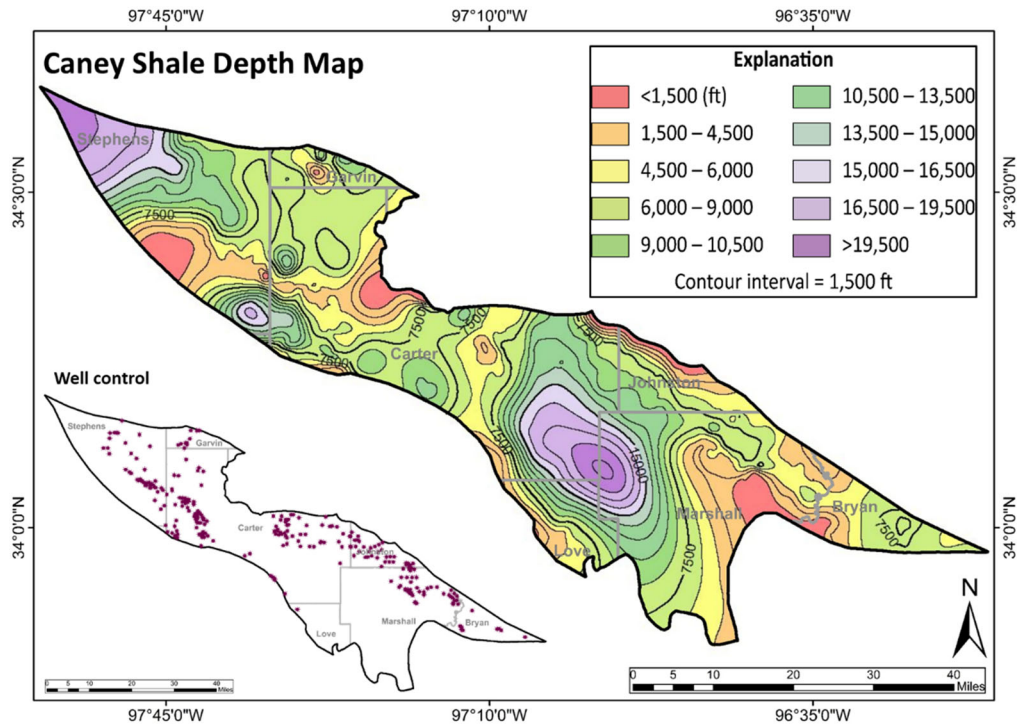
**Figure 21.** 3D structural contour map of the top of the Woodford Shale. Units for axes are feet.



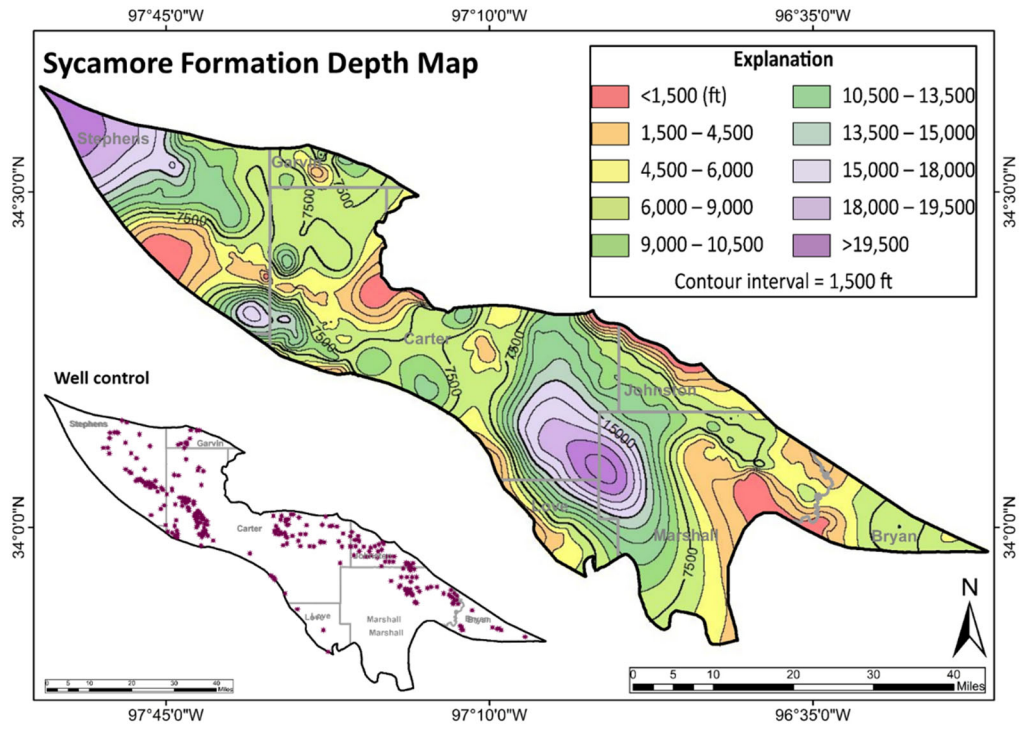
**Figure 22.** 3D structural contour map of the top of the Hunton Group. Units for axes are feet.



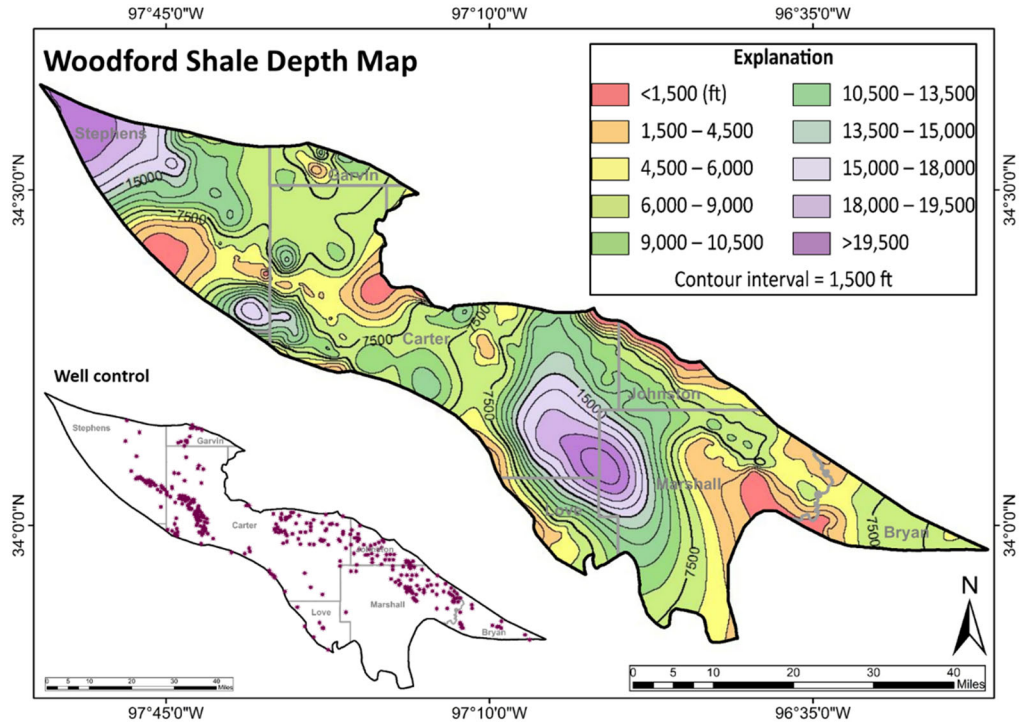
**Figure 23.** 3D structural contour map of the top of the Sylvan Shale. Units for axes are feet.



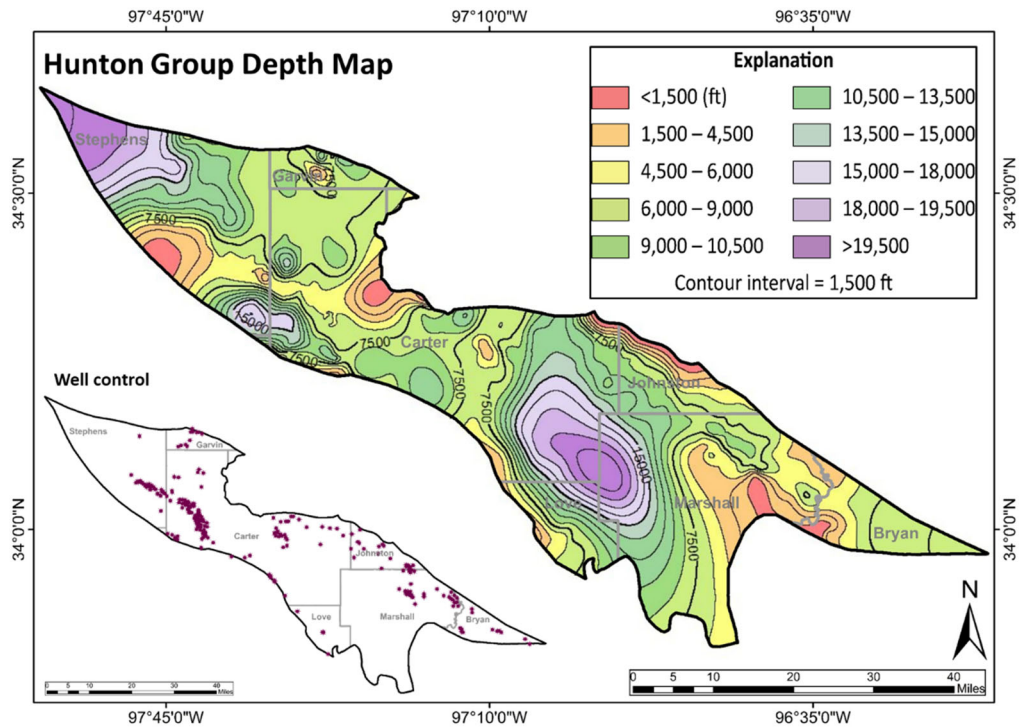
**Figure 24.** Contour map of measured depth to the top of the Caney Shale in the Ardmore Basin. The well control map displays wells in which the Caney Shale is logged.



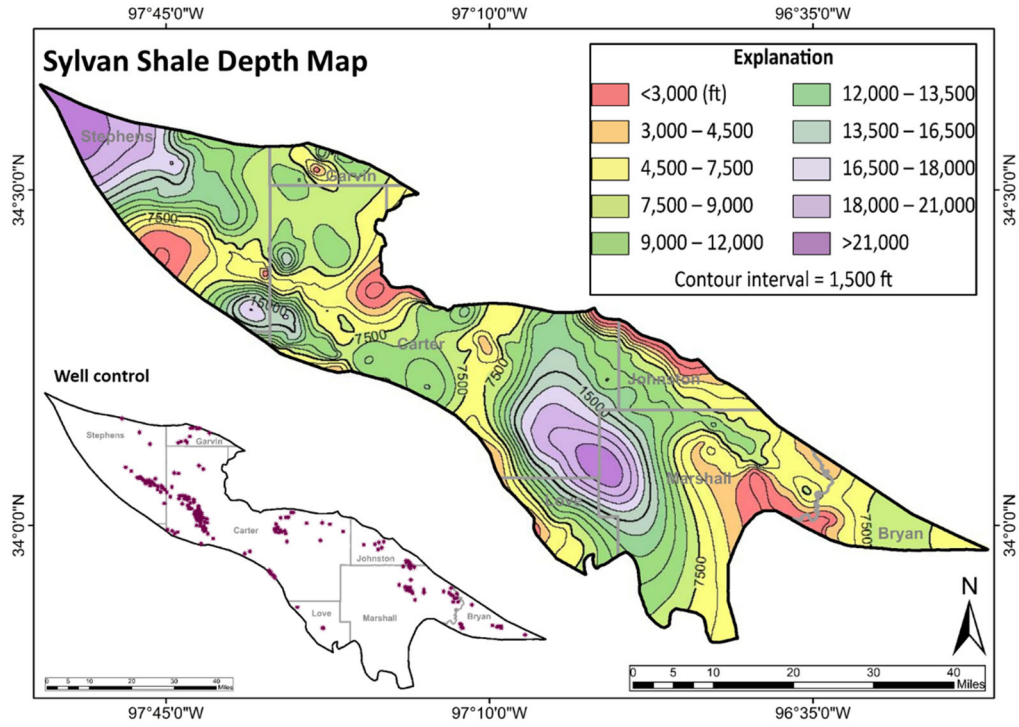
**Figure 25.** Contour map of measured depth to the top of the Sycamore Formation. The well control map displays wells in which the Sycamore Formation is logged.



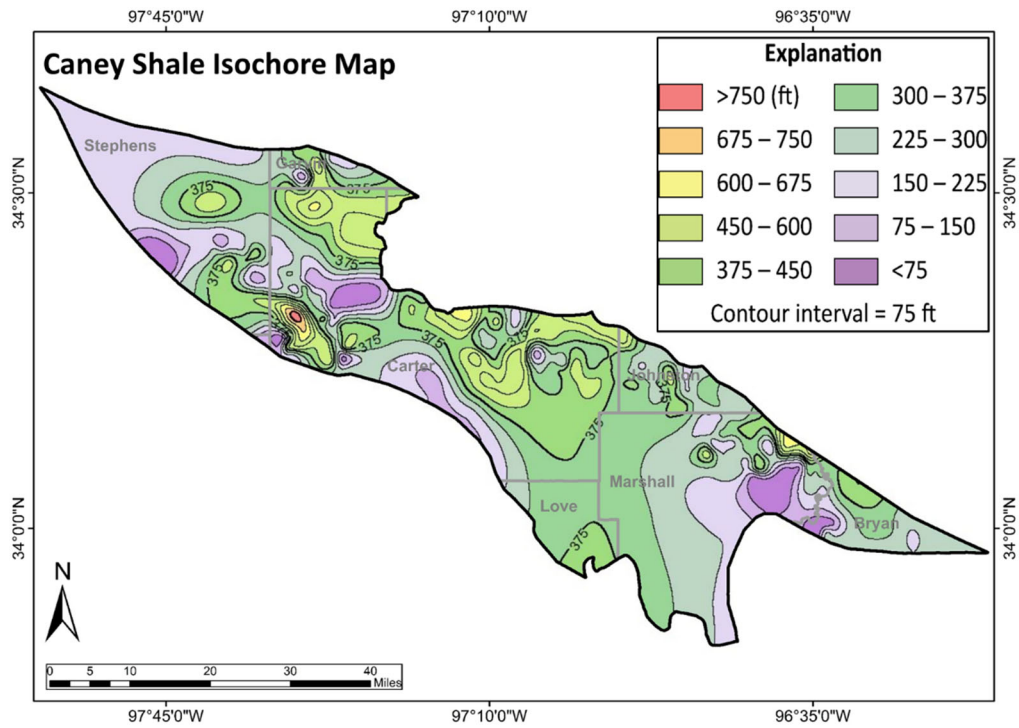
**Figure 26.** Contour map of measured depth to the top of the Woodford Shale. The well control map displays wells in which the Woodford Shale is logged.



**Figure 27.** Contour map of measured depth to the top of the Hunton Group. The well control map displays wells in which the Hunton Group is logged.

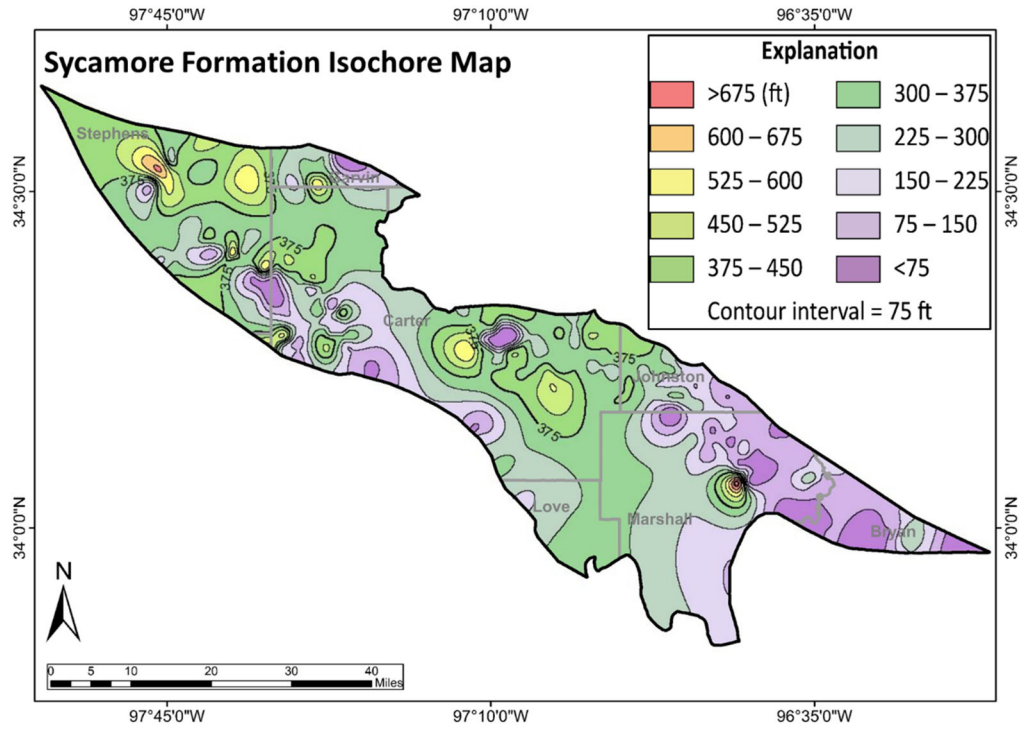


**Figure 28.** Contour map of measured depth to the top of the Sylvan Shale. The well control map displays wells in which the Sylvan Shale is logged.

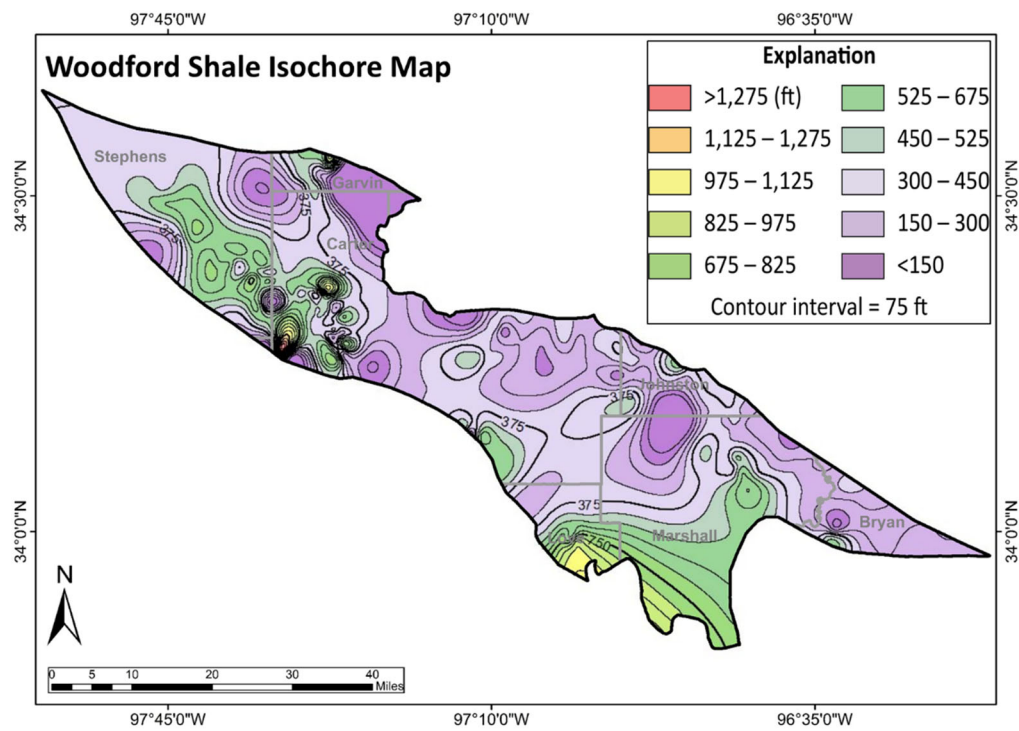


**Figure 29.** Isochore map of the Caney Shale in the Ardmore Basin.

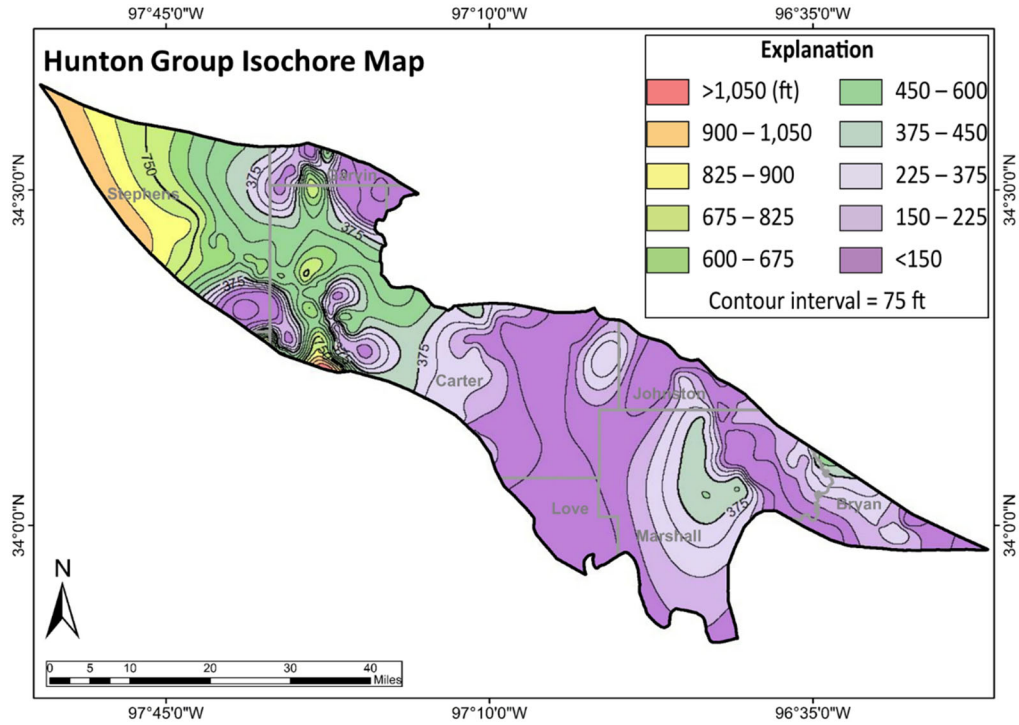




**Figure 30.** Isochore map of the Sycamore Formation in the Ardmore Basin.



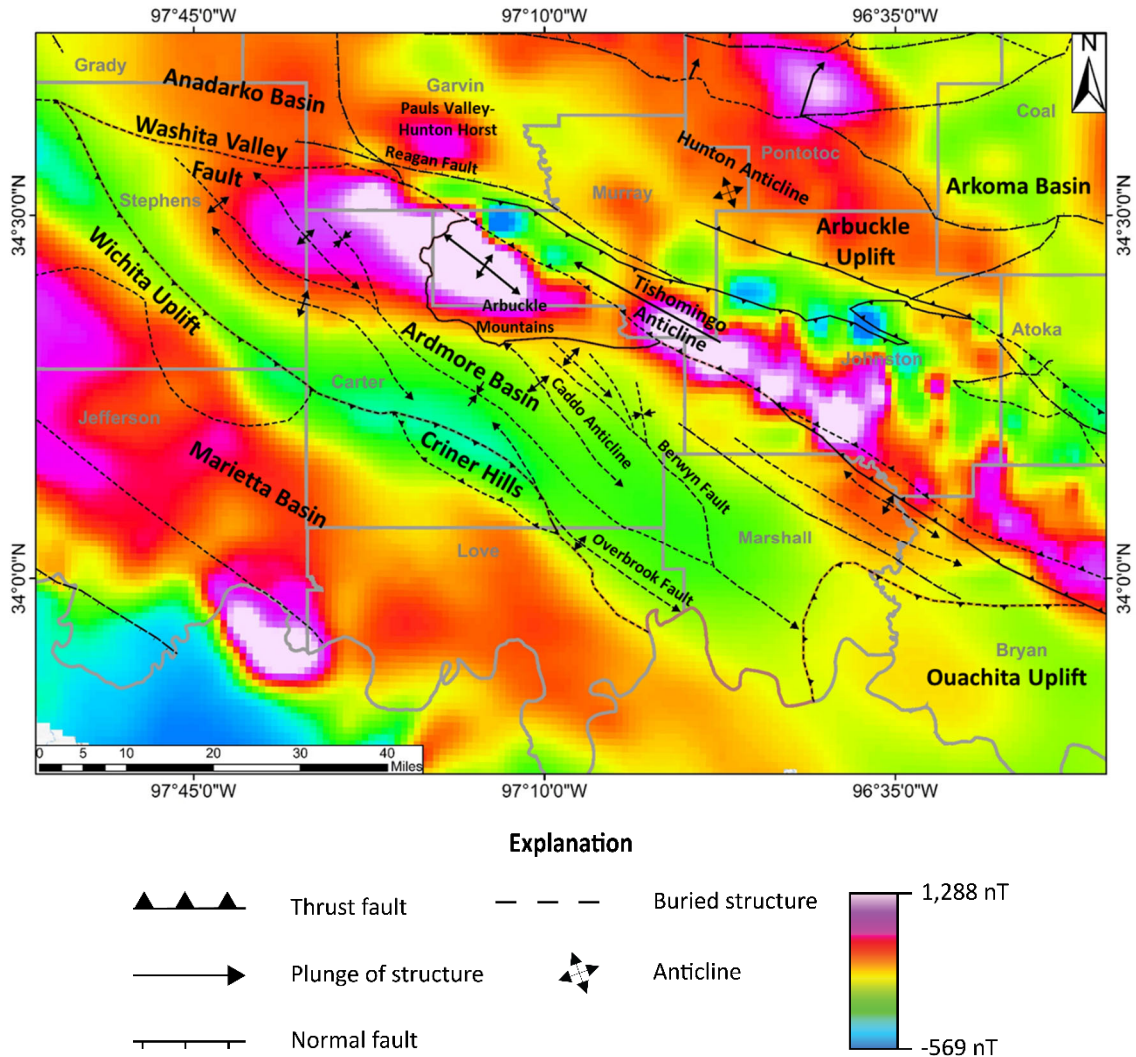
**Figure 31.** Isochore map of the Woodford Shale in the Ardmore Basin.



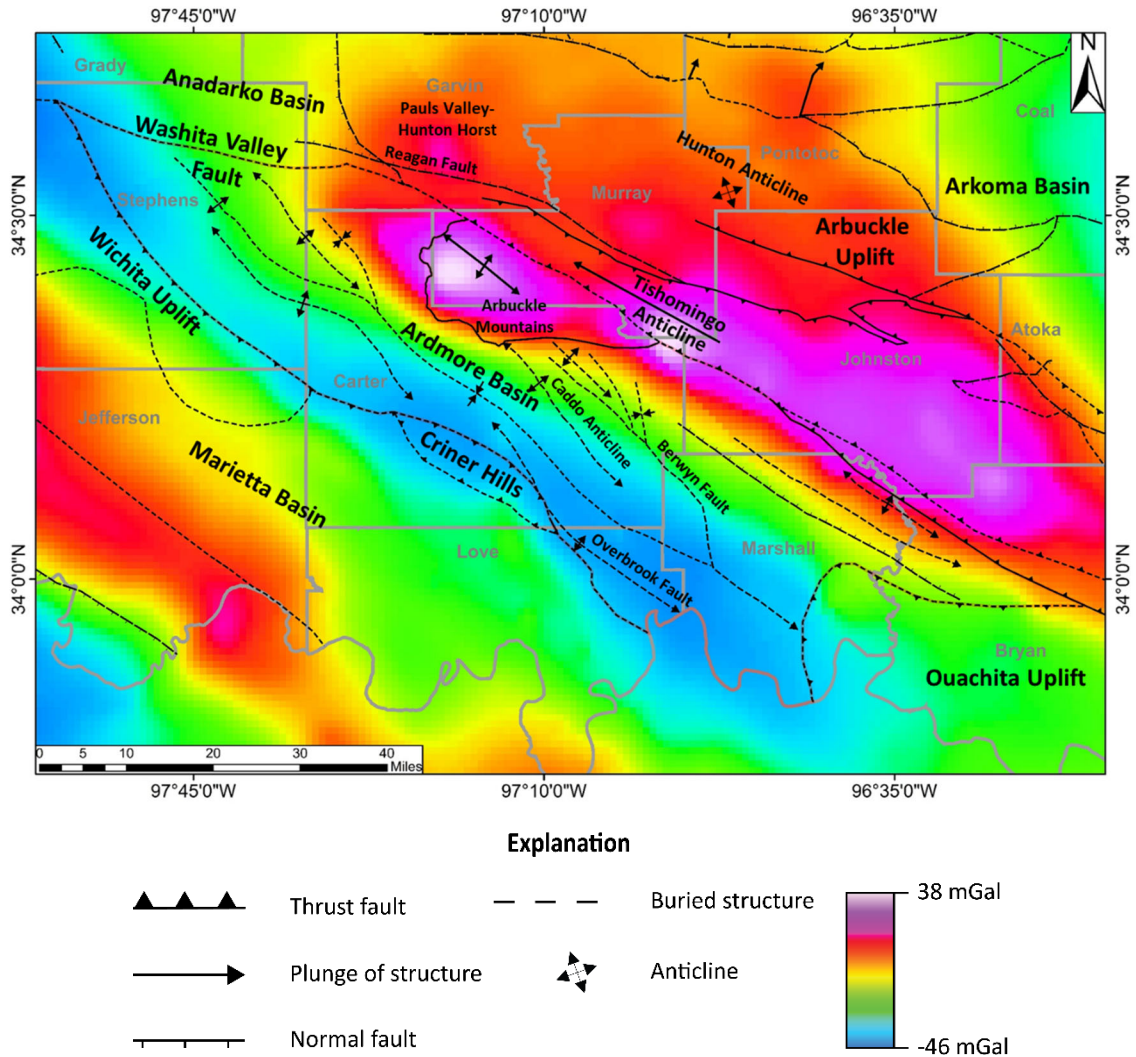
**Figure 32.** Isochore map of the Hunton Group in the Ardmore Basin.

### Geophysical Mapping and Thermal Gradient Analysis

Aeromagnetic anomaly (Figure 33) and gravity anomaly (Figure 34) maps display signatures of basement structures in the Ardmore Basin. Strong positive anomalies correspond with the Wichita Mountains, Arbuckle Mountains, and Arbuckle Uplift, which all contain dense granite and mafic or felsic volcanic rocks. Low anomaly values correspond with deep basement above which a thick Paleozoic sedimentary section is preserved. The aeromagnetic anomaly and gravity anomaly maps show similar structure to what is displayed on the structure maps generated from well log correlation (Figures 14–28).

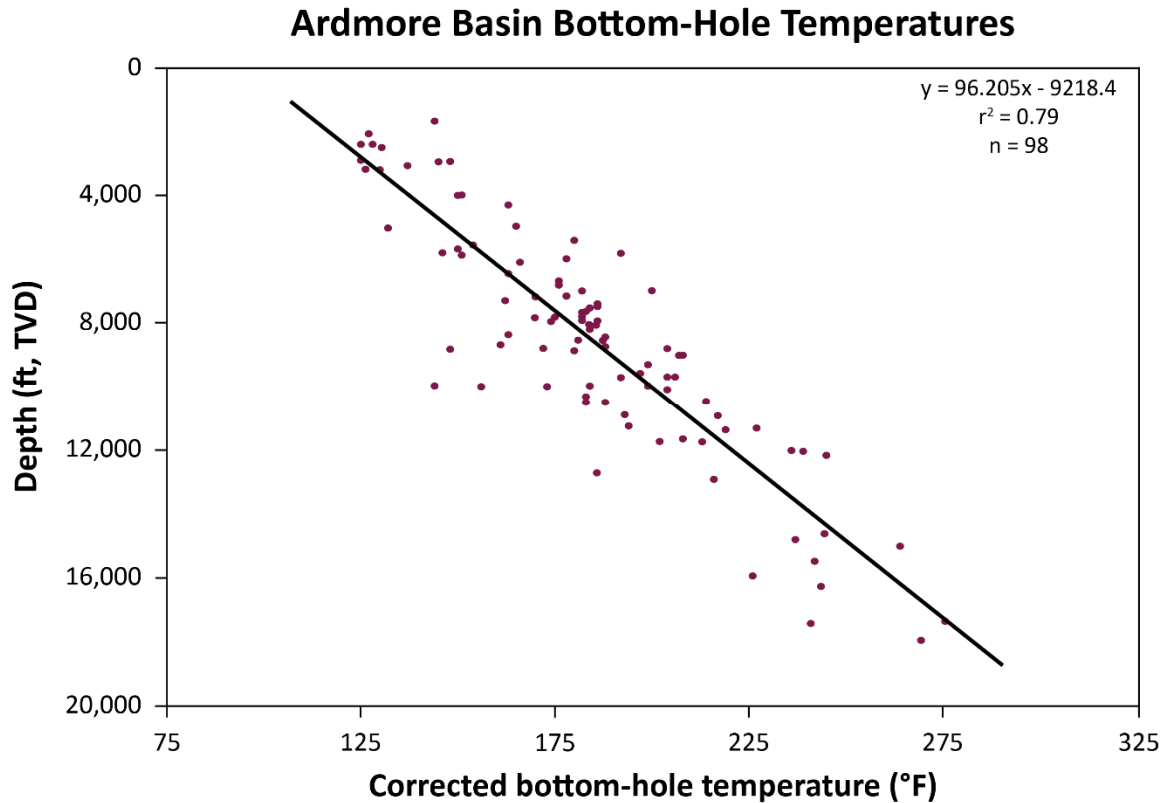


**Figure 33.** Aeromagnetic anomaly map of the Ardmore Basin and surrounding region (after Sweeney and Hill, 2005). High anomalies correspond with shallow basement rocks, and low anomalies correspond with thick sediment cover. Superimposed structures are from Dionisio (1976) and Northcutt and Campbell (1995).



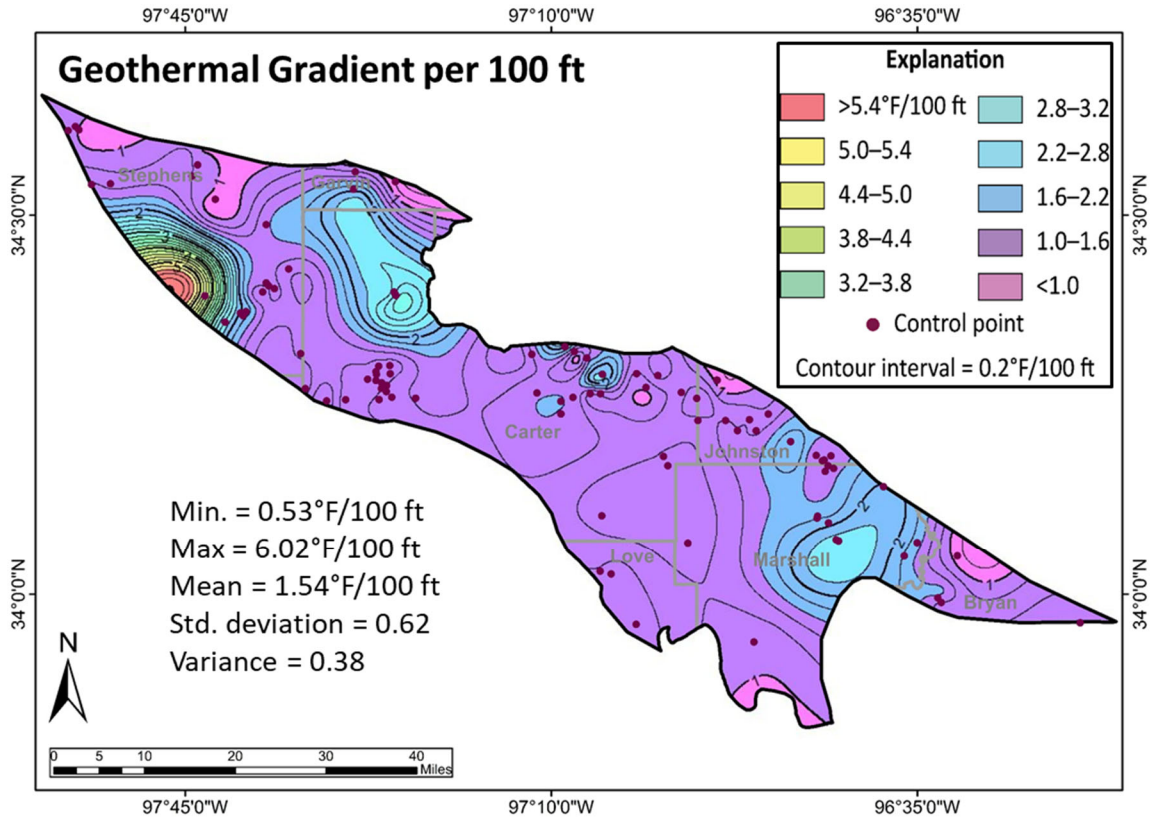
**Figure 34.** Gravity anomaly map of the Ardmore Basin and surrounding region (after Sweeney and Hill, 2005). High anomalies correspond with shallow basement, and low anomalies correspond with thick sediment cover. Superimposed structures are from Dionisio (1976) and Northcutt and Campbell (1995).

Tabulated BHT data were graphed and fitted with a linear least squares regression line that yielded a coefficient of determination ( $r^2$ ) of 0.79, indicating BHT increases relatively uniformly with depth in the Ardmore Basin (Figure 35).



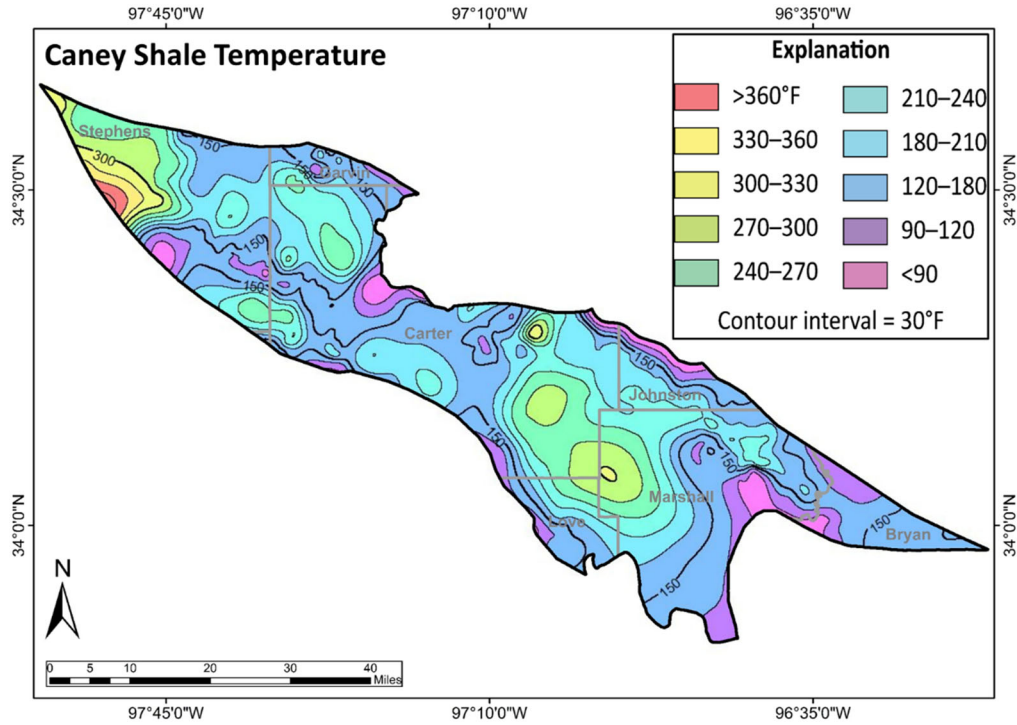
**Figure 35.** Graph of corrected bottom-hole temperatures vs. true vertical depth from wells in the Ardmore Basin. The data have been fitted with a least squares regression line (black line) that shows temperature increasing with depth.

A geothermal gradient was calculated for each BHT using Equation 1 and all geothermal gradients were compiled to construct a geothermal gradient map (Figure 36). The geothermal gradient map correlates with the aeromagnetic and gravity anomaly maps (Figures 33–34), because geothermal gradients are greater than 2.2°F/100 ft above shallow basement structures and less than 1.0°F/100 ft in areas with thick sediment cover. Geothermal gradient is highest in the southwest near the Wichita Uplift (>6.0°F/100 ft). The BHT graph and thermal gradient map indicate that the Ardmore Basin has a stable thermal regime which is consistent for a cool, tectonically-inactive basin.

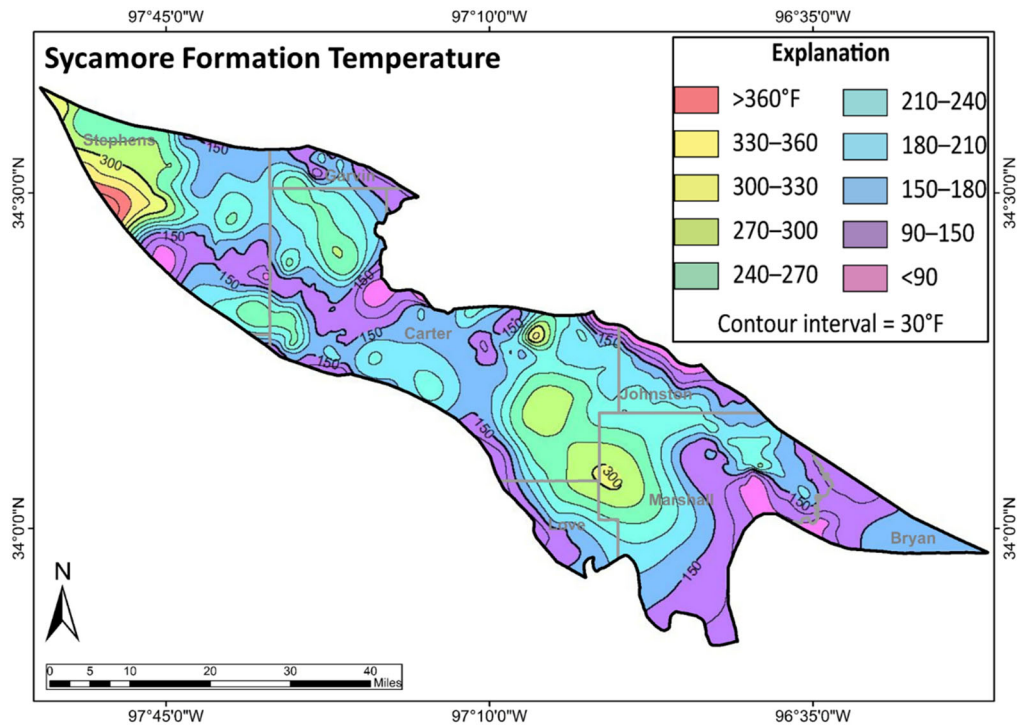


**Figure 36.** Contour map of geothermal gradient in the Ardmore Basin. Control points are the locations of BHT measurements.

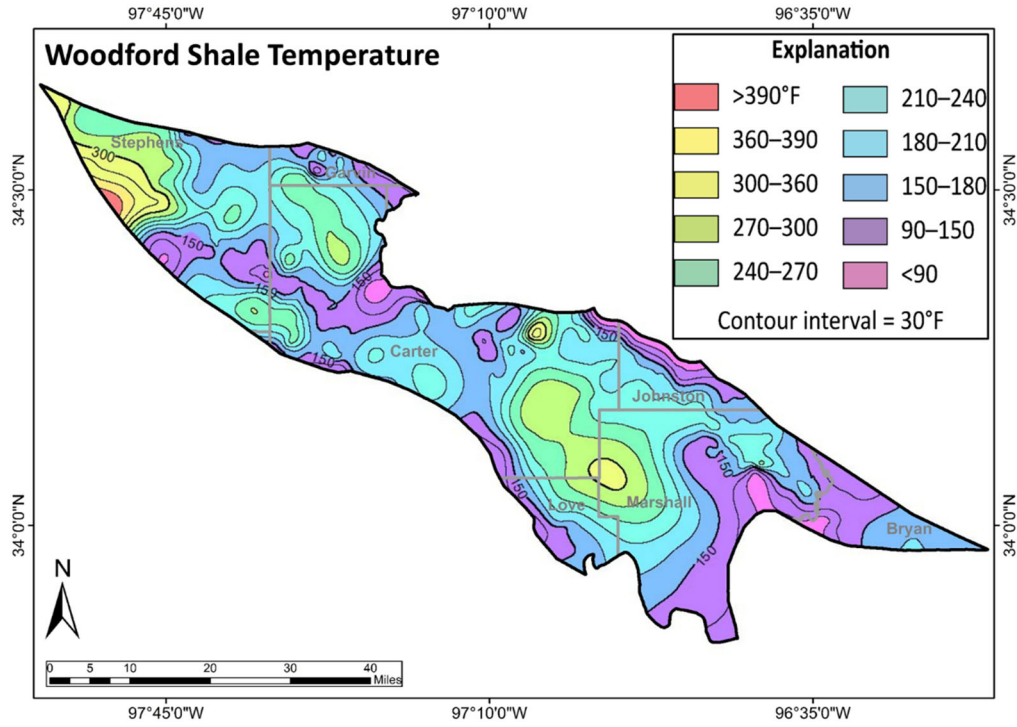
*In situ* formation temperature maps (Figures 37–41) show that temperatures of deep units are typically greater than those of shallow units. Temperature also increases at and near localities of high thermal conductivity such as the Wichita and Arbuckle Mountains which consist of thermally-conductive carbonate and mafic volcanic rocks. Calculated *in situ* temperature at the top of the Woodford Shale ranges from 68.0°F (near surface) to 417.1°F (Figure 39). Calculated *in situ* temperature at the top of the Caney Shale ranges from 68.0°F (near surface) to 402.4°F (Figure 37).



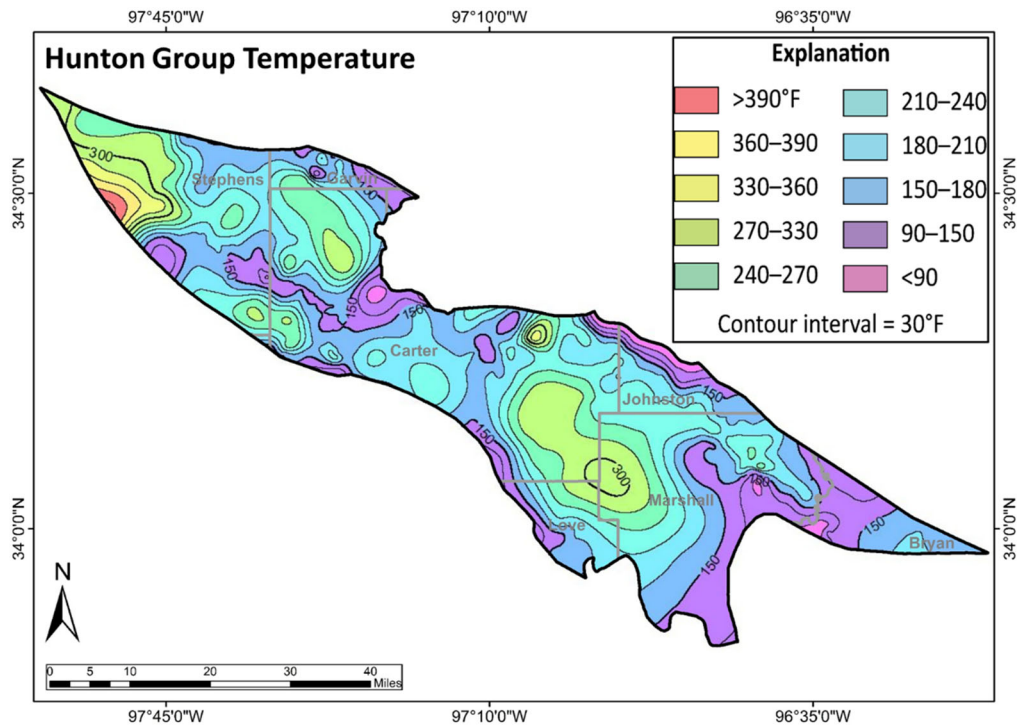
**Figure 37.** Contour map of *in situ* temperature at the top of the Caney Shale in the Ardmore Basin.



**Figure 38.** Contour map of *in situ* temperature at the top of the Sycamore Formation in the Ardmore Basin.

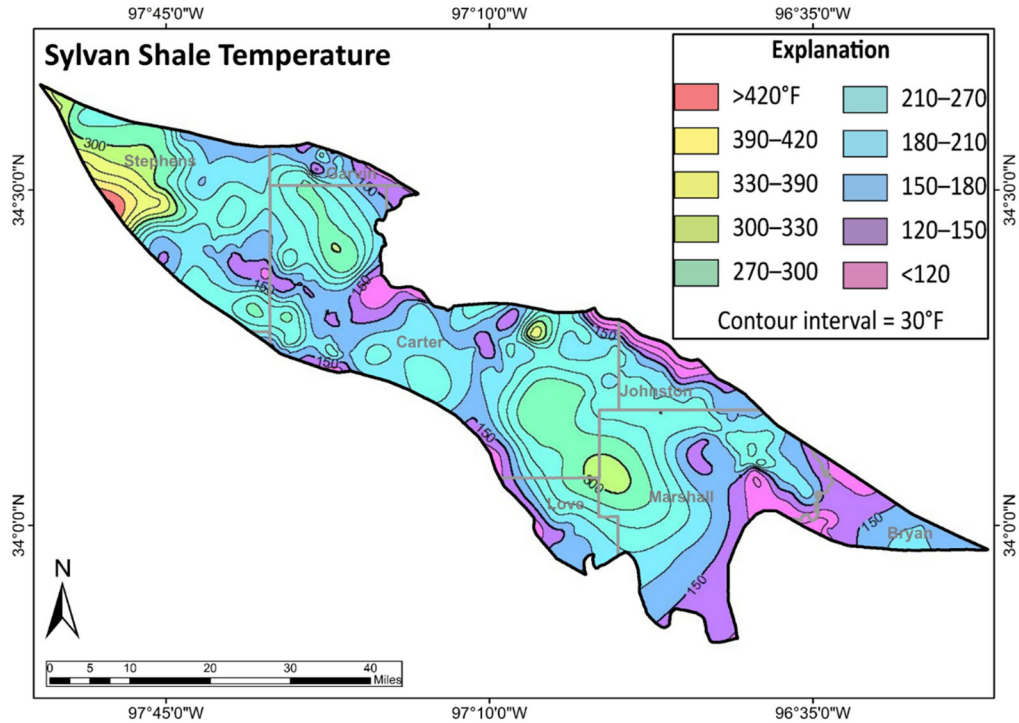


**Figure 39.** Contour map of *in situ* temperature at the top of the Woodford Shale in the Ardmore Basin.



**Figure 40.** Contour map *in situ* temperature at the top of the Hunton Group in the Ardmore Basin.





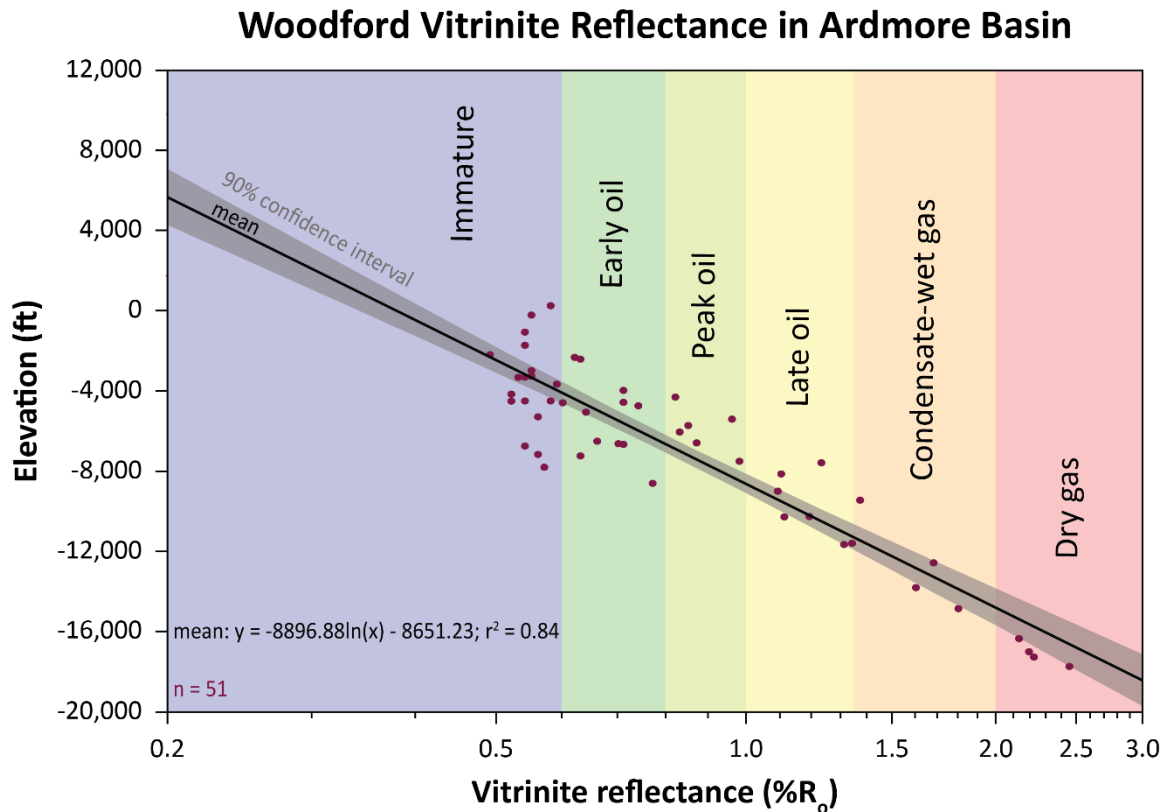
**Figure 41.** Contour map *in situ* temperature at the top of the Sylvan Shale in the Ardmore Basin.

### Vitrinite Reflectance Analysis

The Devonian–Mississippian shale section has a broad range of thermal maturity ranging from immature ( $\%R_o < 0.6$ ) to the dry gas window ( $\%R_o > 2.0$ ). Variations in heat flow related to thermal conductivity and structural history have resulted in a modest degree of scatter in the vitrinite reflectance–depth data.

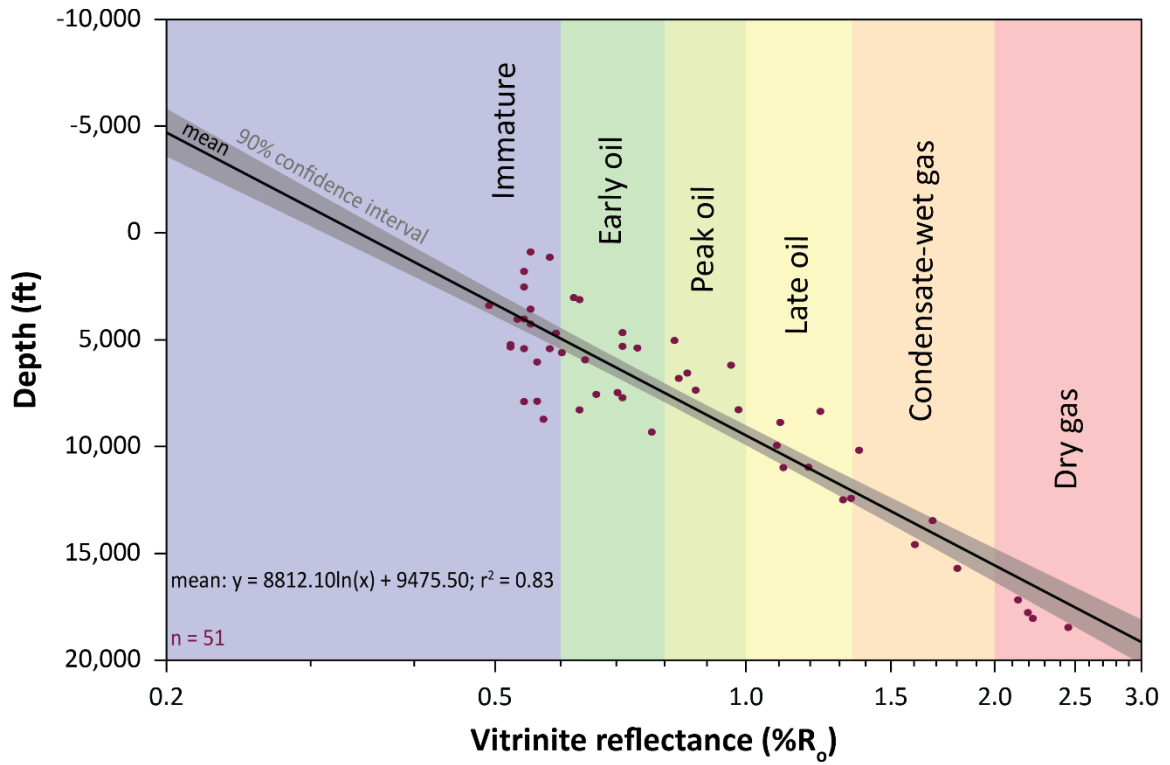
Vitrinite reflectance–elevation (Figure 42), vitrinite reflectance–depth (Figure 43), and vitrinite reflectance–temperature plots (Figure 44) generally display the same pattern with vitrinite reflectance data being dispersed at low levels of thermal maturity and converging at high levels of maturity. Some of this scatter is a result of general variability of organic composition, particularly at low maturity levels. A strong correlation exists for both vitrinite reflectance vs. elevation and

vitritinite reflectance vs. depth plots as least squares regression lines yield  $r^2$  values of 0.84 and 0.83, respectively (Figure 42–43). A y-intercept of approximately -5,000 ft for the logarithmic least squares regression line on the depth-vitritinite reflectance plot (Figure 43) indicates approximately 5,000 ft of Pennsylvanian and younger strata was eroded in the Ardmore Basin. A weaker correlation exists between vitritinite reflectance and *in situ* formation temperature (Figure 44) with an  $r^2$  value of 0.55, indicating that the current temperature field is quite different from that during maturation. This weaker correlation is likely due to variation in thermal conductivity throughout the basin, however, a trend exists in that vitritinite reflectance increases as temperature increases (Figure 43).



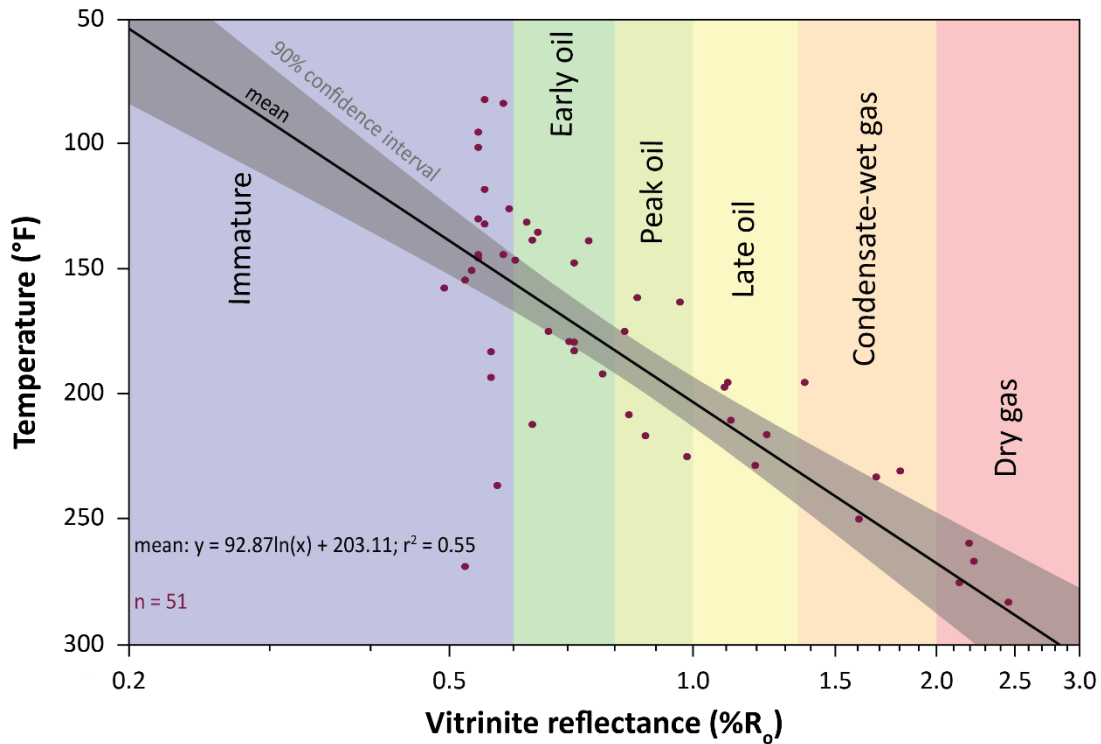
**Figure 42.** Vitritinite reflectance-elevation plot for the Woodford Shale showing thermal maturity trends in the Ardmore Basin. Regression analysis has determined a 90% confidence interval in the slope of the regression line.

### Woodford Vitrinite Reflectance in Ardmore Basin



**Figure 43.** Vitrinite reflectance-depth plot for the Woodford Shale showing thermal maturity trends in the Ardmore Basin. Regression analysis has determined a 90% confidence interval for the slope of the regression line.

## Woodford Temperature and Vitrinite Reflectance in Ardmore Basin

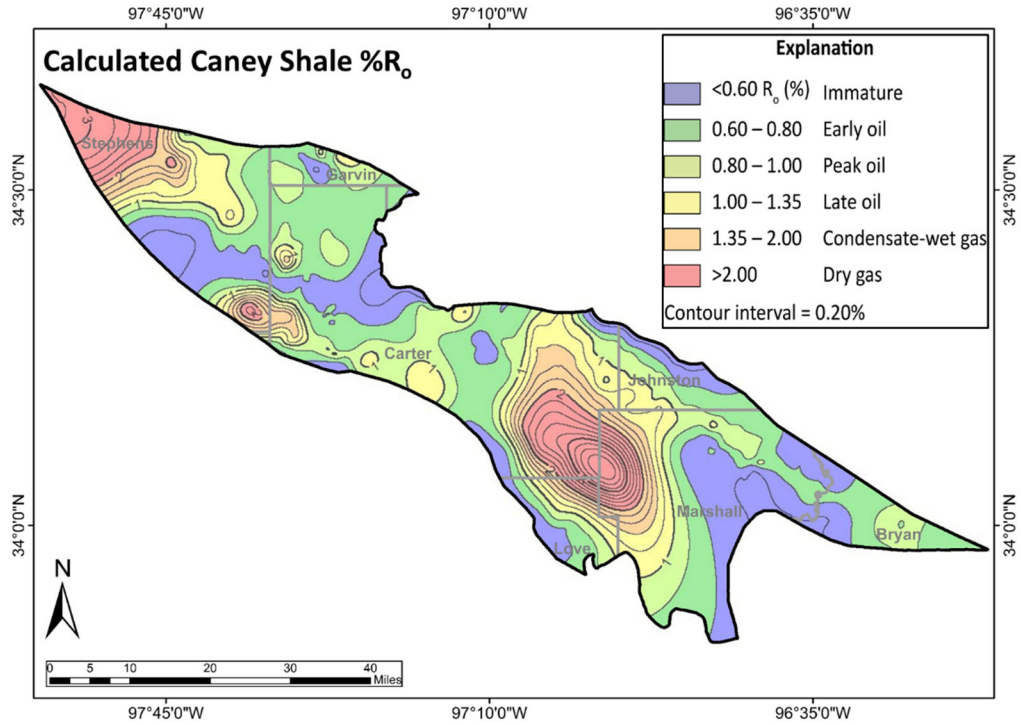


**Figure 44.** Vitrinite reflectance vs. *in situ* temperature of the Woodford Shale showing thermal maturity trends and temperature trends in the Ardmore Basin. Regression analysis has determined a 90% confidence interval for the slope of the regression line.

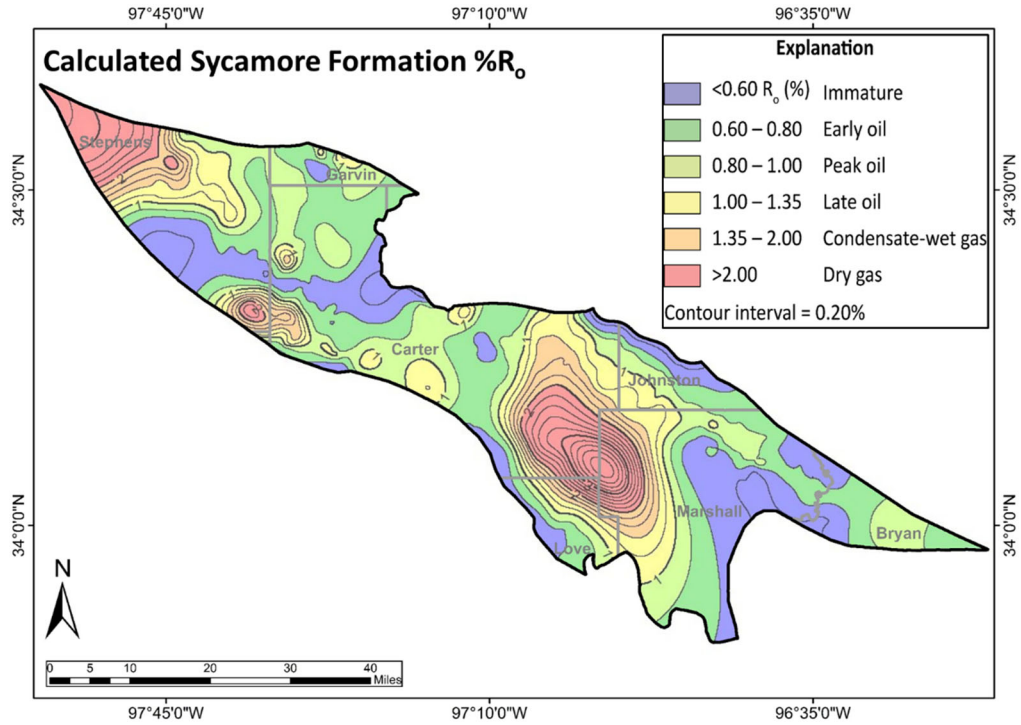
The logarithmic least squares regression equation of the vitrinite reflectance-elevation plot can be used to predict vitrinite reflectance for formations that underlie and overlie the Woodford Shale (Equation 2) (Figures 45–54). Calculated vitrinite reflectance of the top of the Caney Shale ranges from 0.3%–3.8% in the Ardmore Basin and is estimated to be 1.7% (condensate–wet gas window) in the Tomaney 1-35-34-27XHW well (Figure 45 and 50). Calculated vitrinite reflectance of the top of the Woodford Shale ranges from 0.3%–4.1% in the Ardmore Basin and is 1.8% in the Tomaney 1-35-34-27XHW well (condensate–wet gas window) (Figures 47 and 52).

$$\text{vitrinite reflectance } (\%R_o) = e^{\frac{y+8651.23}{8896.88}} \quad (2)$$

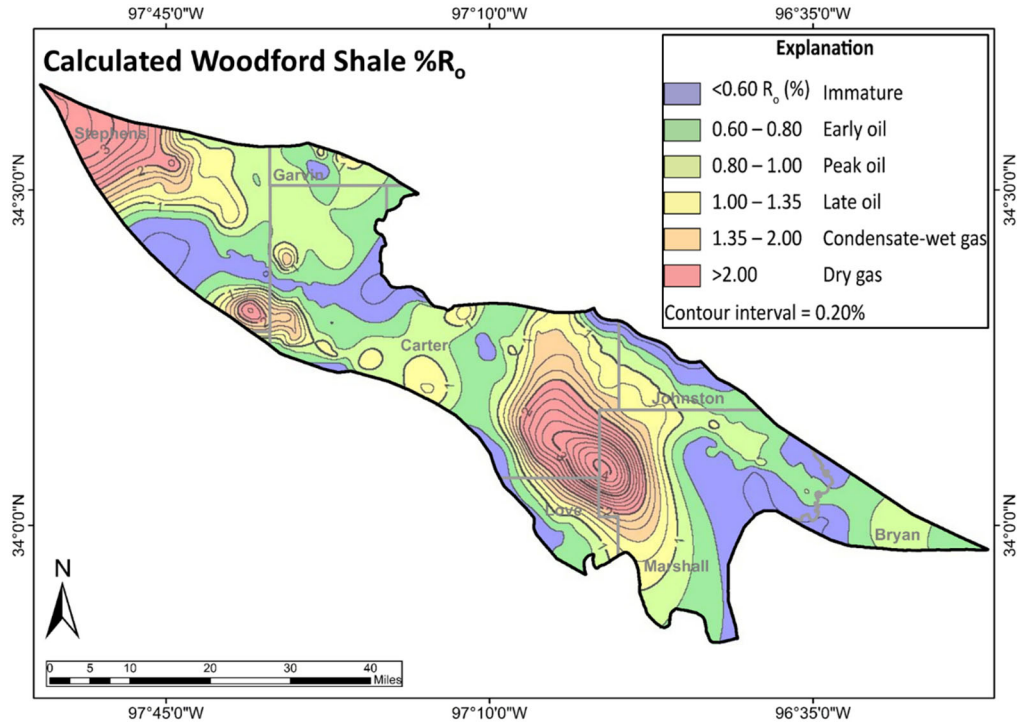
where y = elevation (ft)



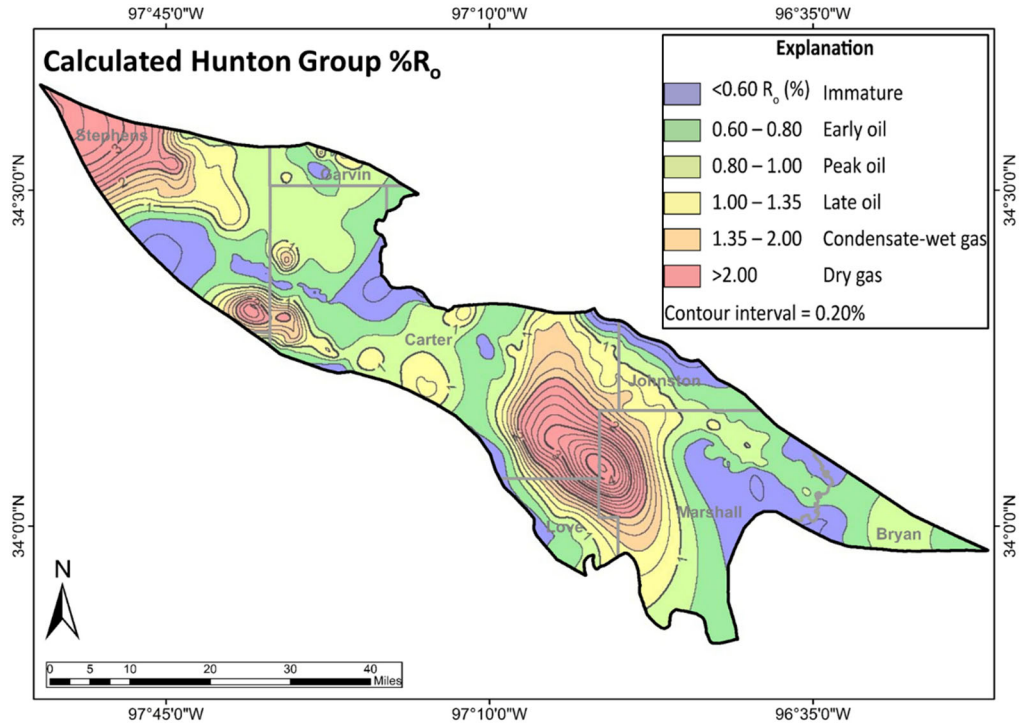
**Figure 45.** Calculated vitrinite reflectance contour map of the Caney Shale. Maximum reflectance is estimated to be about 3.4% in the Berwyn Syncline. Minimum reflectance is estimated to be about 0.3% near the surface.



**Figure 46.** Calculated vitrinite reflectance contour map of the Sycamore Formation. Maximum reflectance is estimated to be about 3.9% in the Berwyn Syncline. Minimum reflectance is estimated to be about 0.3% near the surface.

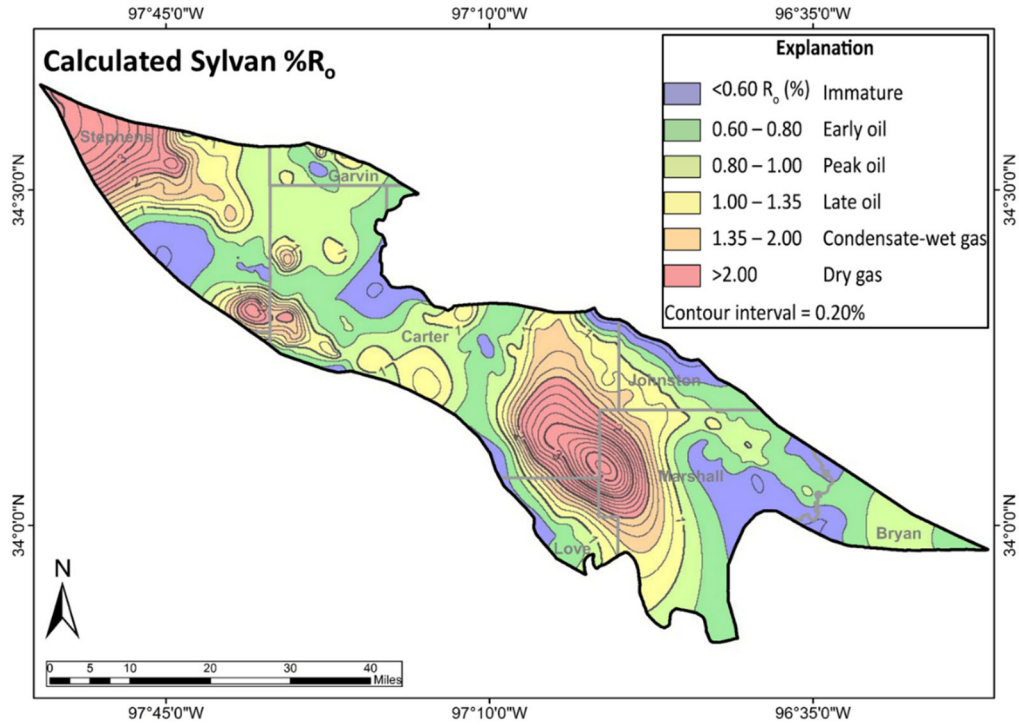


**Figure 47.** Calculated vitrinite reflectance contour map of the Woodford Shale. Maximum reflectance is estimated to be about 4.1% in the Berwyn Syncline. Minimum reflectance is estimated to be about 0.3% near the surface.

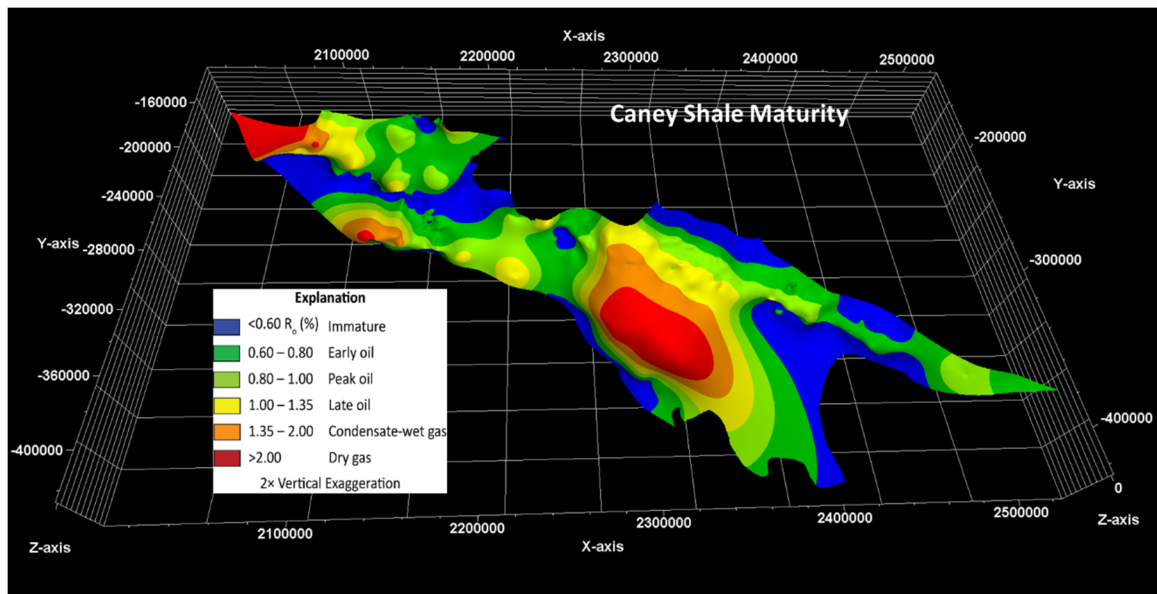


**Figure 48.** Calculated vitrinite reflectance contour map of the Hunton Group. Maximum reflectance is estimated to be about 4.2% in the Berwyn Syncline. Minimum reflectance is estimated to be about 0.3% near the surface.

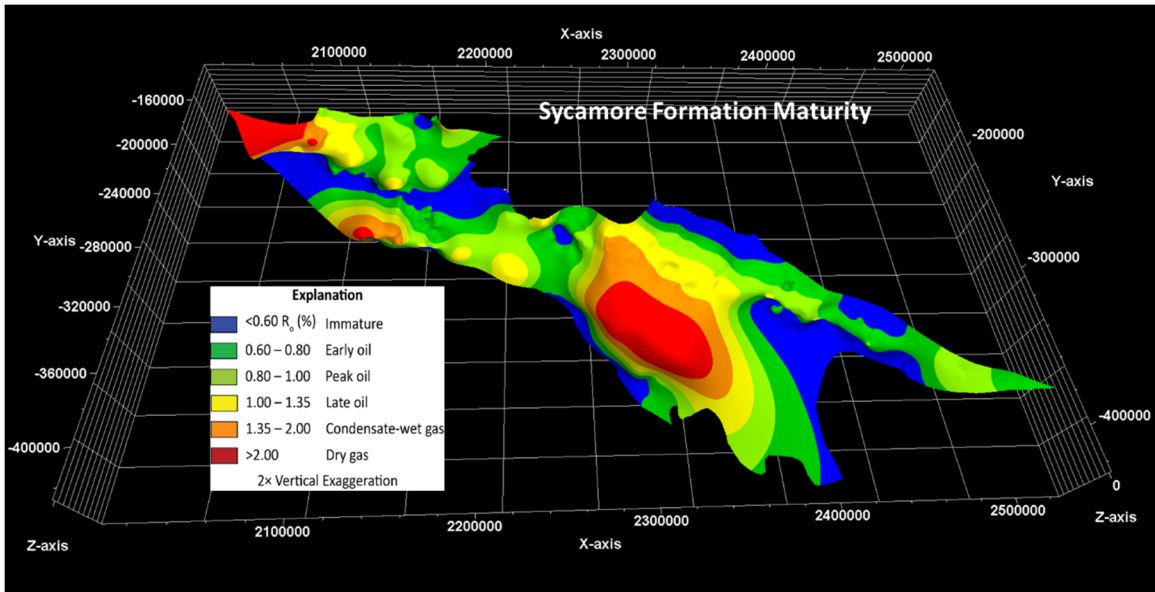




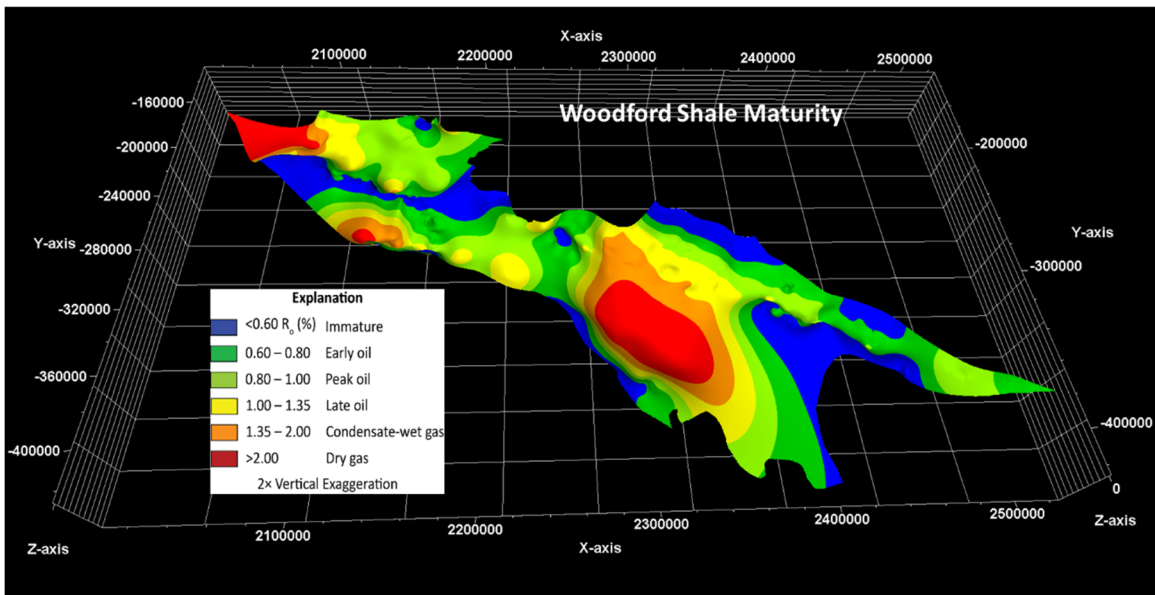
**Figure 49.** Calculated vitrinite reflectance contour map of the Sylvan Shale. Maximum thermal maturity is 4.3% in the Berwyn syncline. Minimum reflectance is estimated to be about 0.3% near the surface.



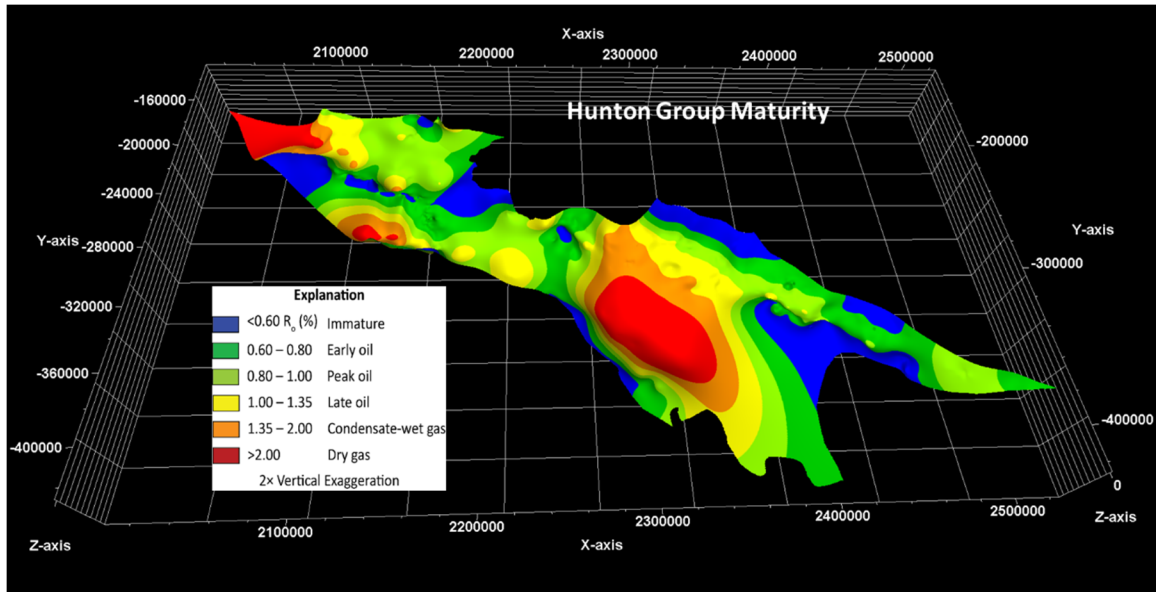
**Figure 50.** Calculated 3D vitrinite reflectance map of the Caney Shale draped over Caney Shale structure. Maximum reflectance is estimated to be about 3.4% in the Berwyn Syncline. Minimum reflectance is estimated to be about 0.3% near the surface. Units for axes are feet.



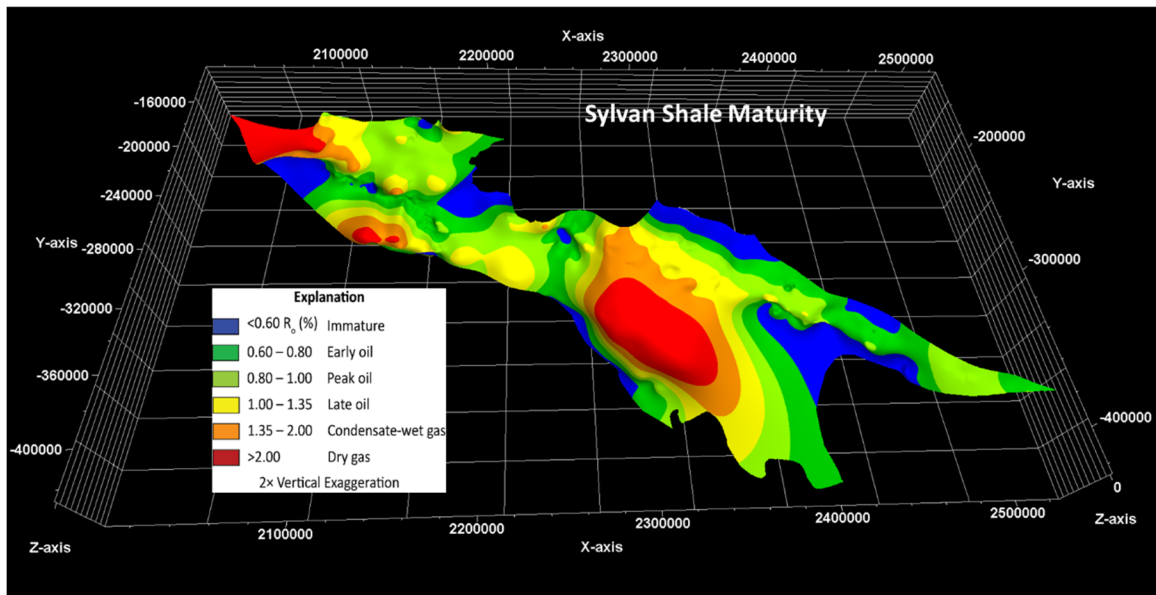
**Figure 51.** Calculated 3D vitrinite reflectance map of the Sycamore Formation draped over Sycamore Formation structure. Maximum reflectance is estimated to be about 3.9% in the Berwyn Syncline. Minimum reflectance is estimated to be about 0.3% near the surface. Units for axes are feet.



**Figure 52.** Calculated 3D vitrinite reflectance map of the Woodford Shale draped over Woodford Shale structure. Maximum reflectance is estimated to be about 4.1% in the Berwyn Syncline. Minimum reflectance is estimated to be about 0.3% near the surface. Units for axes are feet.



**Figure 53.** Calculated 3D vitrinite reflectance map of the Hunton Group draped over Hunton Group Structure. Maximum reflectance is estimated to be about 4.2% in the Berwyn Syncline. Minimum reflectance is estimated to be about 0.3% near the surface. Units for axes are feet.



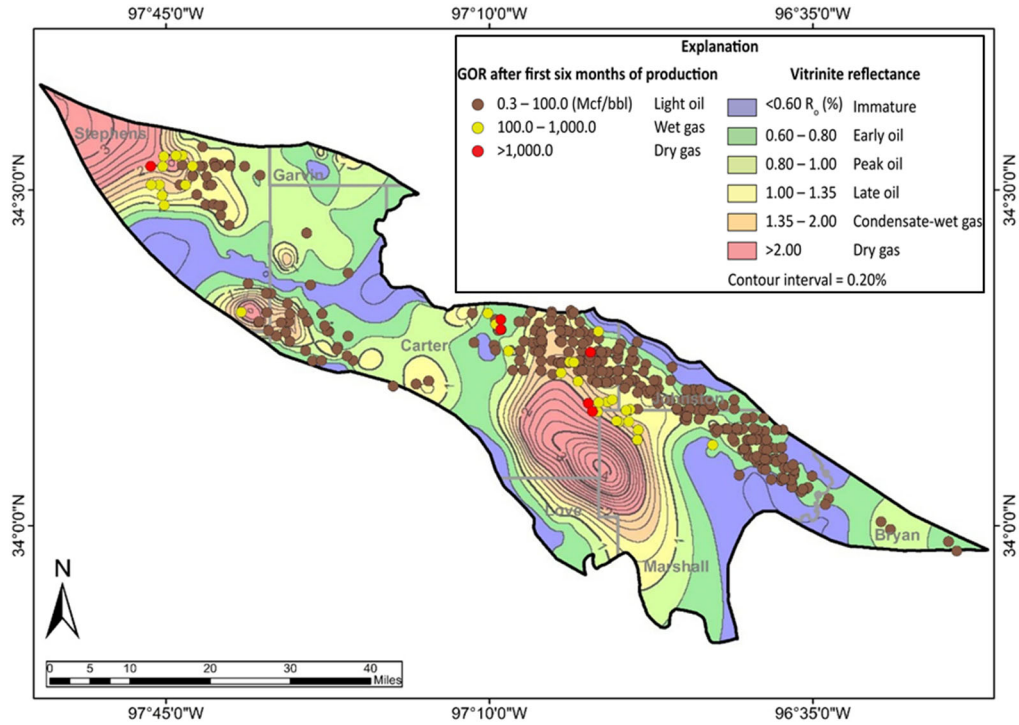
**Figure 54.** Calculated 3D vitrinite reflectance map of the Sylvan Shale draped over Sylvan Shale structure. Maximum thermal maturity is 4.3% in the Berwyn syncline. Minimum reflectance is estimated to be about 0.3% near the surface. Units for axes are feet.

Approximate present-day depths of maturity windows were calculated using Equation 2 and are tabulated in Table 3.

**Table 3.** Approximate present-day depth for thermal maturity windows in the Ardmore Basin.

<b>Maturity</b>	<b>Present-Day Depth (ft)</b>
Immature	<5,000
Early oil	5,000–7,500
Peak oil	7,500–9,500
Late oil	9,500–12,000
Condensate-wet gas	12,000–15,500
Dry Gas	>15,500

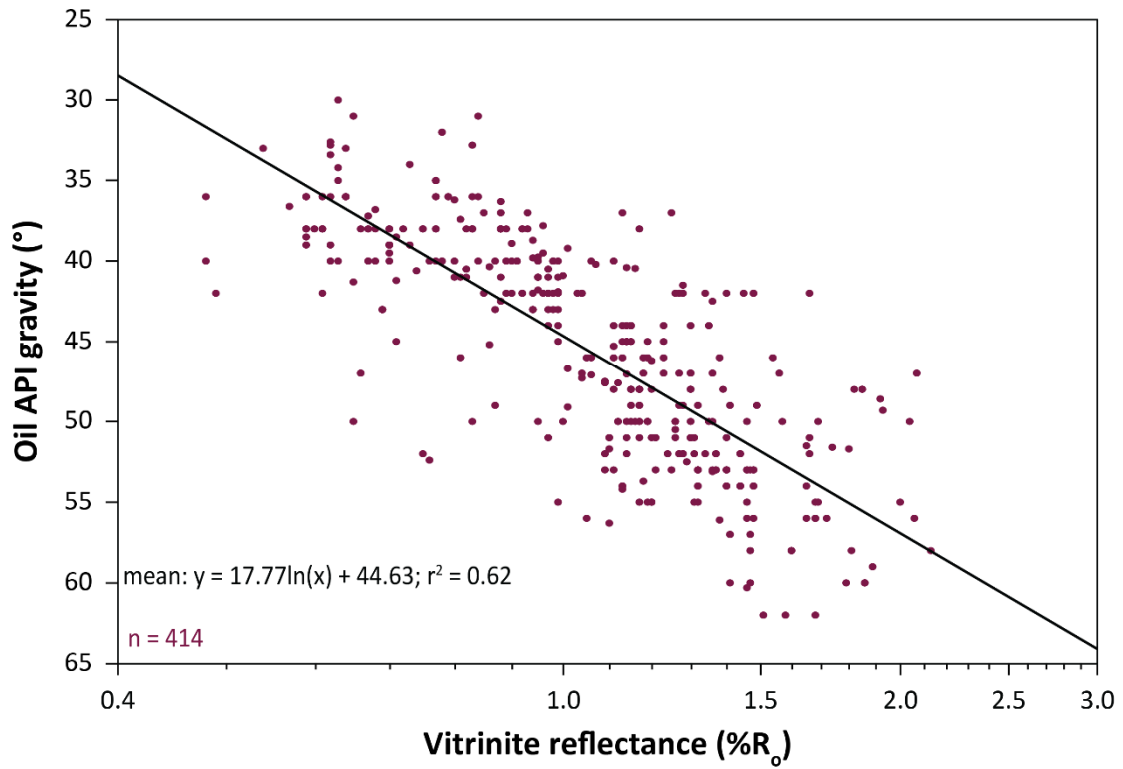
A general correlation exists between GOR and calculated thermal maturity of the Woodford Shale (Figure 55). Wells with low to moderate gas-oil ratios (0.3–100 Mcf/bbl) are at localities within the early oil–late oil windows. Wells with high gas-oil ratios (>1,000 Mcf/bbl) are mostly at localities within the condensate-wet gas–dry gas windows. GOR increases toward areas of higher thermal maturity. Outliers, where high gas-oil ratios are measured at areas of immature–early oil levels of maturity, for example, are possibly related to production methods such as choking. Additionally, it is assumed that petroleum migration has occurred within the Woodford Shale, and even more migration of the oil and gas that was expelled from the Woodford Shale has occurred. GOR ranges from 0.3–100 Mcf/bbl (light oil) near the Tomaney 1-35-34-27XHW well.



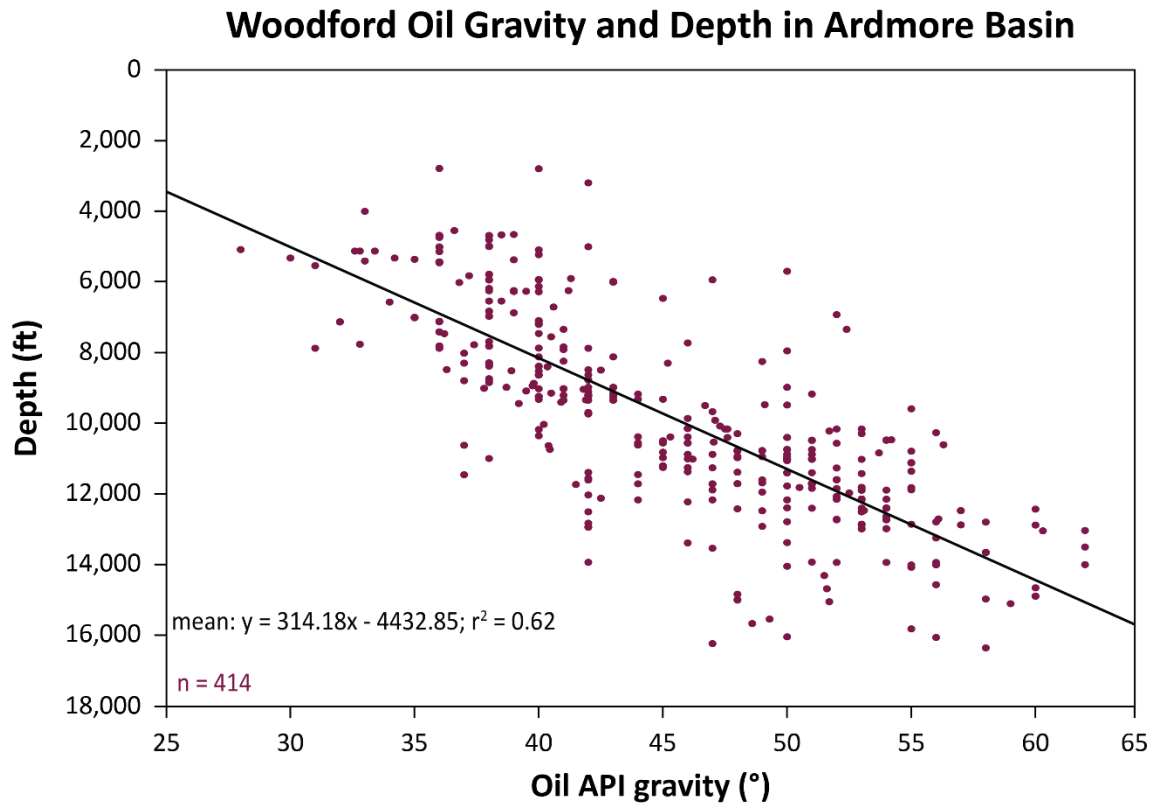
**Figure 55.** Calculated vitrinite reflectance contour map for the Woodford Shale superimposed by 499 GOR data points measured after six months of production from the Woodford Shale.

Woodford Shale oil API gravity data plotted against Woodford Shale vitrinite reflectance (Figure 56), depth (Figure 57), and temperature (Figure 58) can serve as metrics for validating accuracy of calculated maturity and for examining the extent and impact of lateral hydrocarbon migration within the Woodford Shale. An  $r^2$  value of 0.62 exists between API gravity and vitrinite reflectance (Figure 56). The graph displays API gravity increasing as vitrinite reflectance increases. An  $r^2$  value of 0.62 exists between Woodford oil API gravity data and Woodford Shale depth (Figure 57). As depth increases, oil API gravity increases. A weak correlation exists between API gravity and *in situ* formation temperature with an  $r^2$  value of 0.18; however, the general trend of the data is that formation temperature increases as oil API gravity increases (Figure 58).

## Woodford Oil Gravity and Vitrinite Reflectance in Ardmore Basin

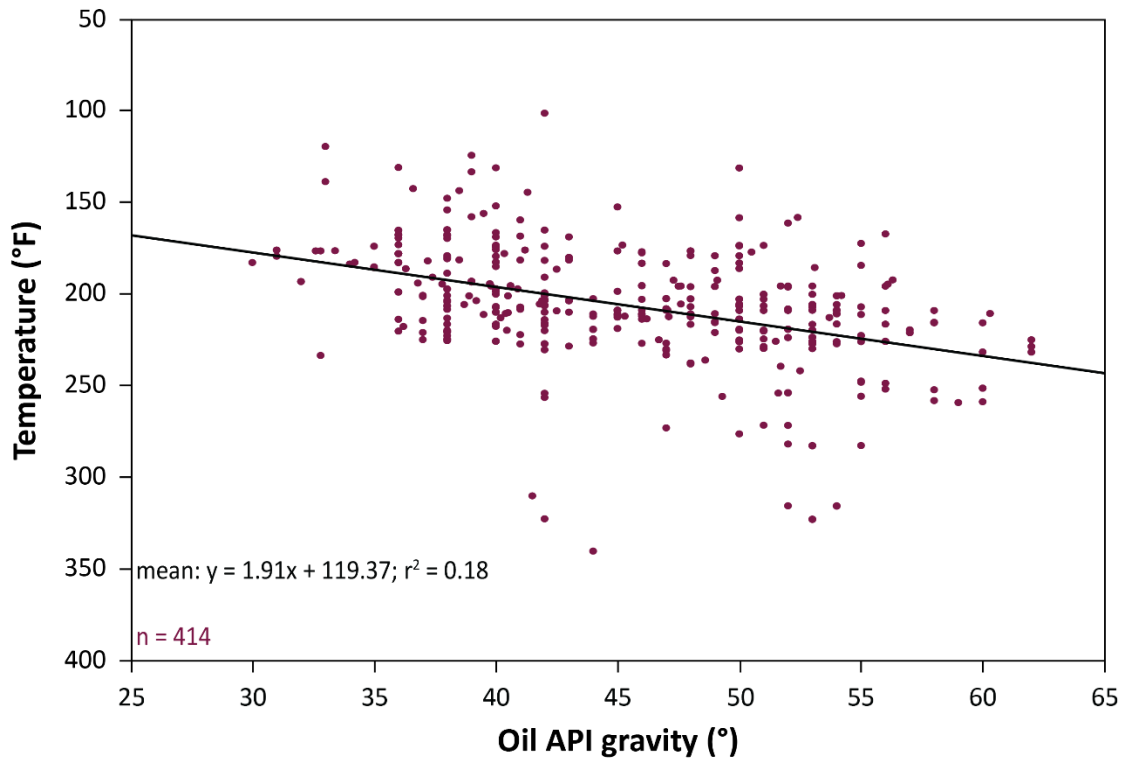


**Figure 56.** Vitrinite reflectance vs. oil API gravity plot for the Woodford Shale showing how maturity affects petroleum gravity in the Ardmore Basin.



**Figure 57.** API gravity vs. depth plot for the Woodford Shale showing how petroleum weight changes with depth in the Ardmore Basin.

## Woodford Oil Gravity and *in situ* Temperature in Ardmore Basin



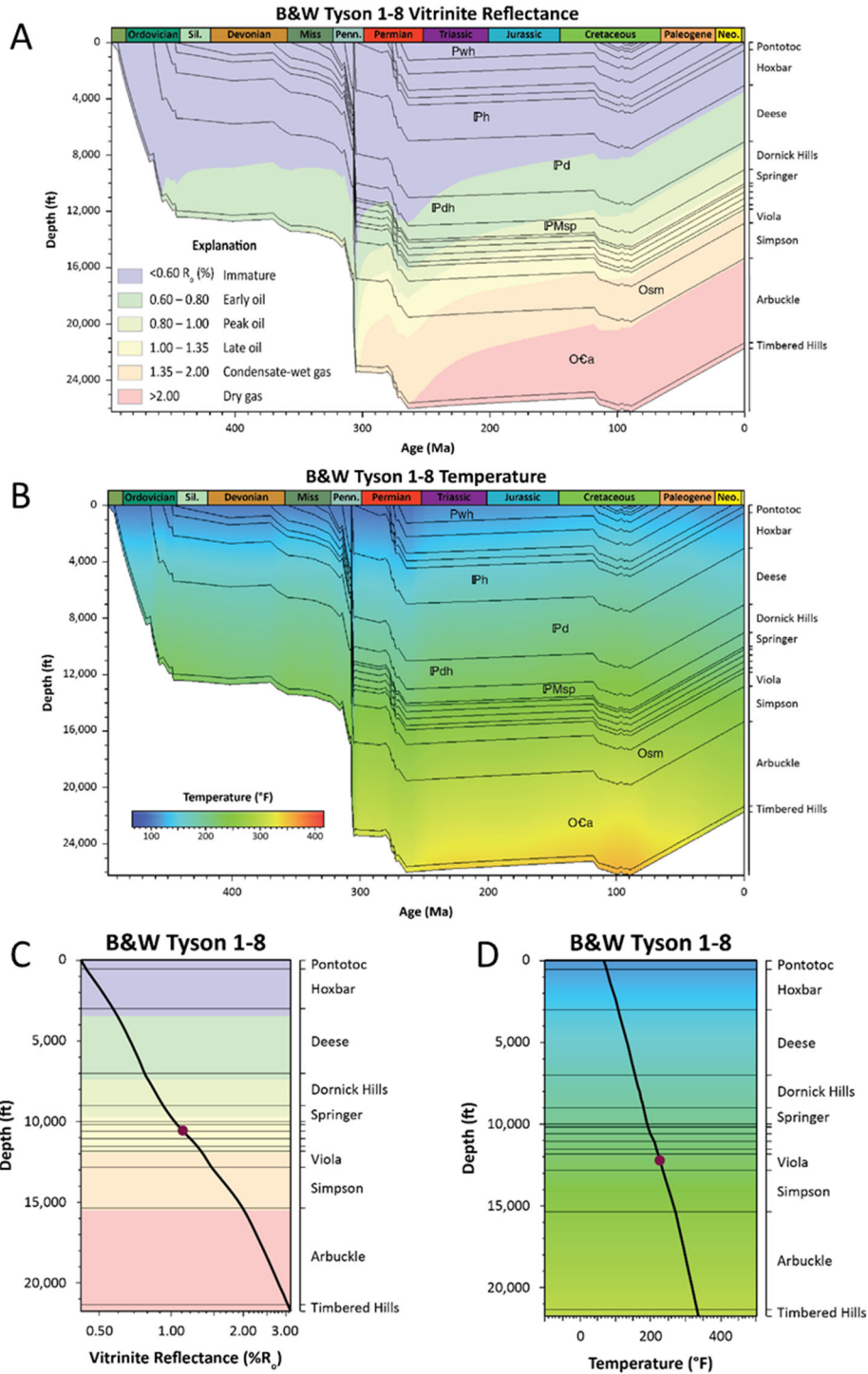
**Figure 58.** API gravity vs. *in situ* temperature plot for the Woodford Shale showing how petroleum weight changes with temperature in the Ardmore Basin.

### Basin Tectonism and Sediment Deposition

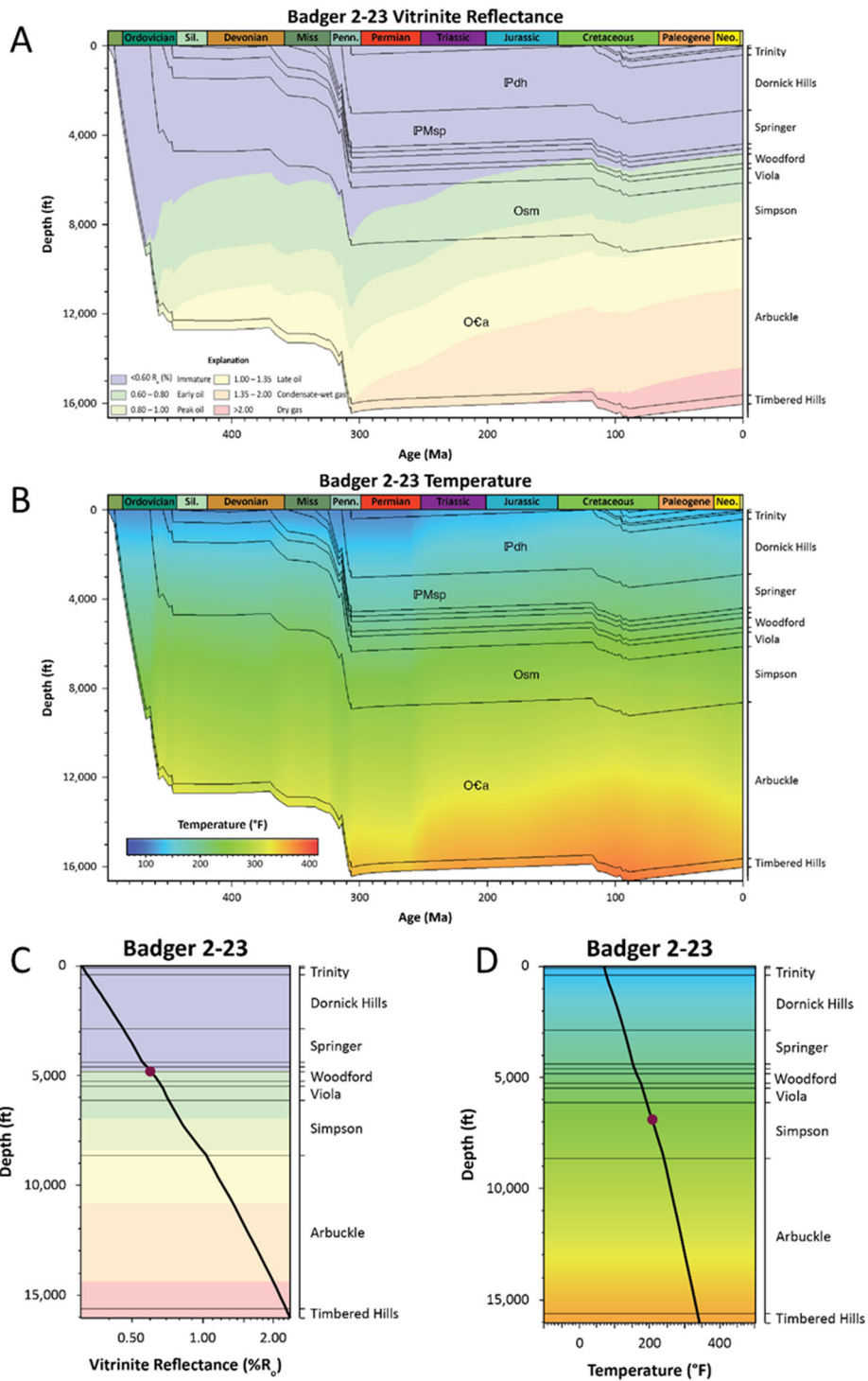
All burial history models display similar tectonic trends (Figures 59–70). Decelerating subsidence during the Cambrian–Devonian was followed by rapid pulses of subsidence that were initiated during the Late Mississippian. Subsidence rate peaked during the Pennsylvanian, and major subsidence continued through the Permian in the western Ardmore Basin. Collectively, these subsidence events deepened the basin by tens of thousands of feet. Four phases of Pennsylvanian subsidence are recognized in burial history models. The first pronounced pulse of subsidence occurs during Springer-Morrow deposition. Subsequent pulses of subsidence coincide



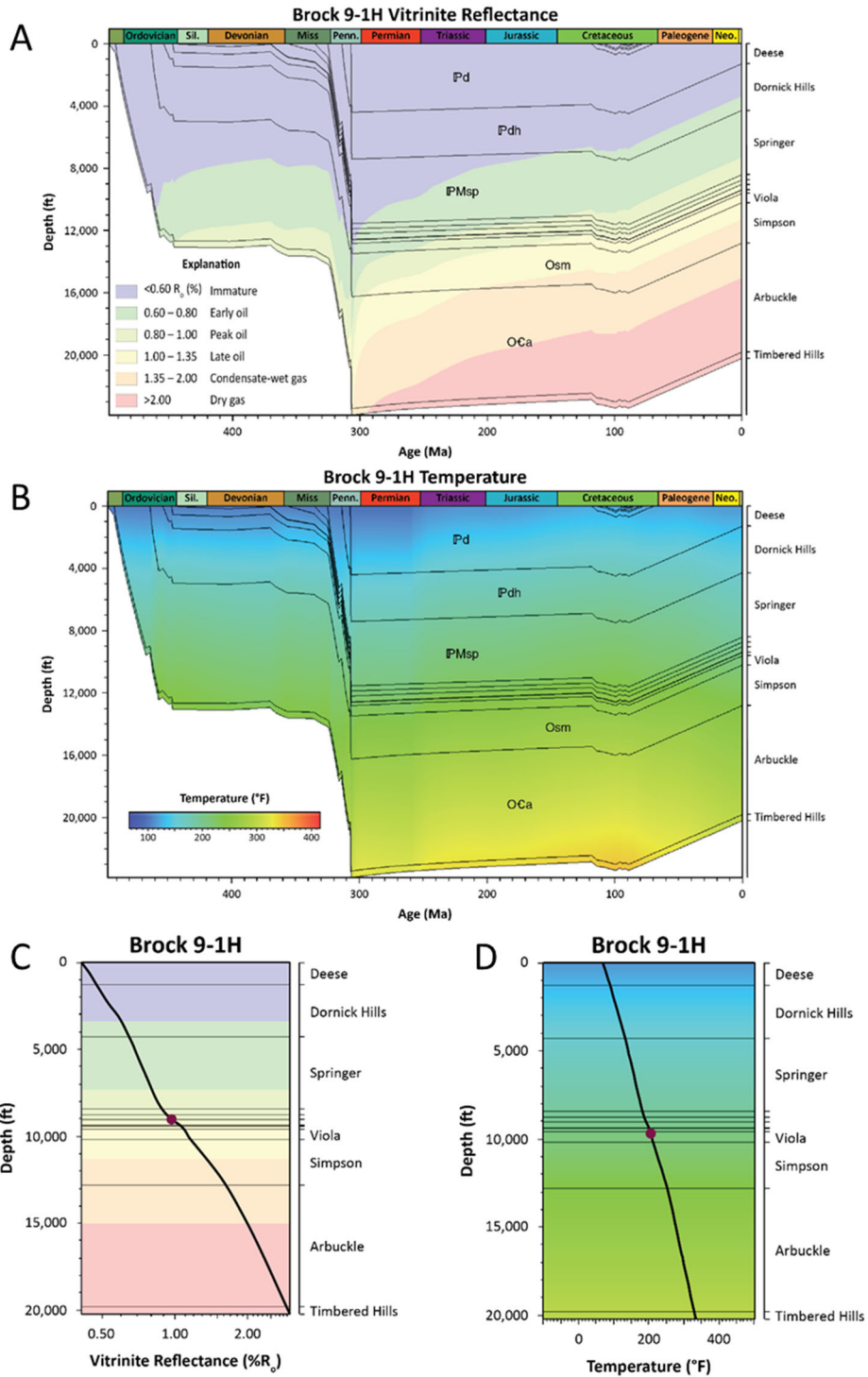
with deposition of the Dornick Hills (Atokan–Desmoinesian), Deese (Desmoinesian), and Hoxbar (Missourian) Groups. The Triassic and Jurassic periods were characterized by tectonic quiescence and minor erosion. Cretaceous deposition was modeled throughout the entire Ardmore Basin; however, paleothickness of this section never exceeded 4,500 ft. Modest uplift beginning perhaps as early as the Late Cretaceous coincides with minor erosion of the Paleozoic and Cretaceous sections. No post-Cretaceous deposition was required for calibration of the burial history models, and so if Tertiary sediment was deposited, it had insufficient thickness to have affected thermal maturation.



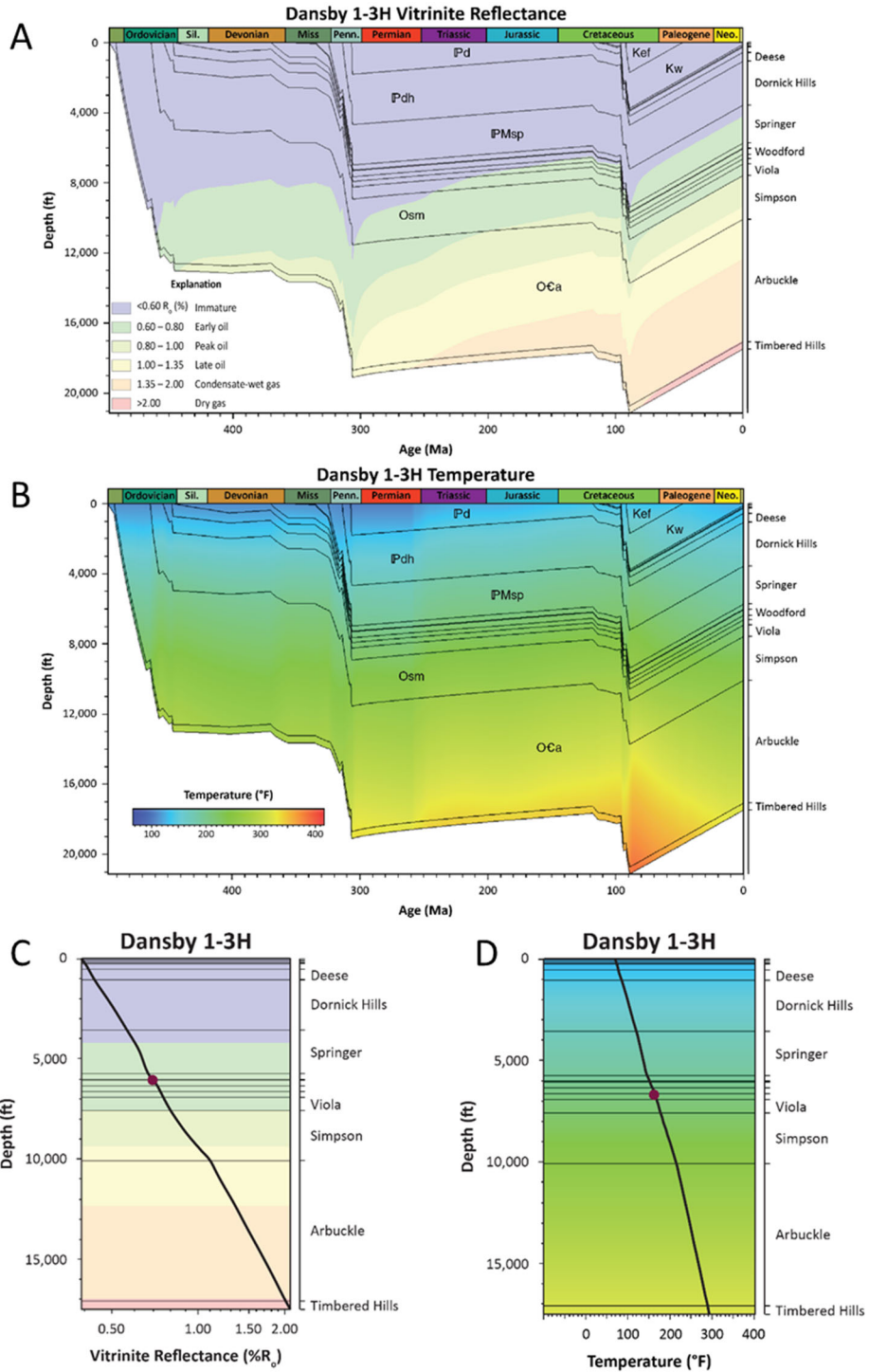
**Figure 59.** Burial and thermal history models of the B&W Tyson 1-8 well in the Ardmore Basin. A) Burial history model showing evolution of thermal maturity windows. B) Thermal history model showing relationship between formation temperature and burial history. C) Modeled vitrinite reflectance-depth plot showing calibration between simulated thermal maturity and control on vitrinite reflectance in the Woodford Shale. D) Modeled temperature-depth plot showing calibration between simulated temperature and corrected bottom-hole temperature.



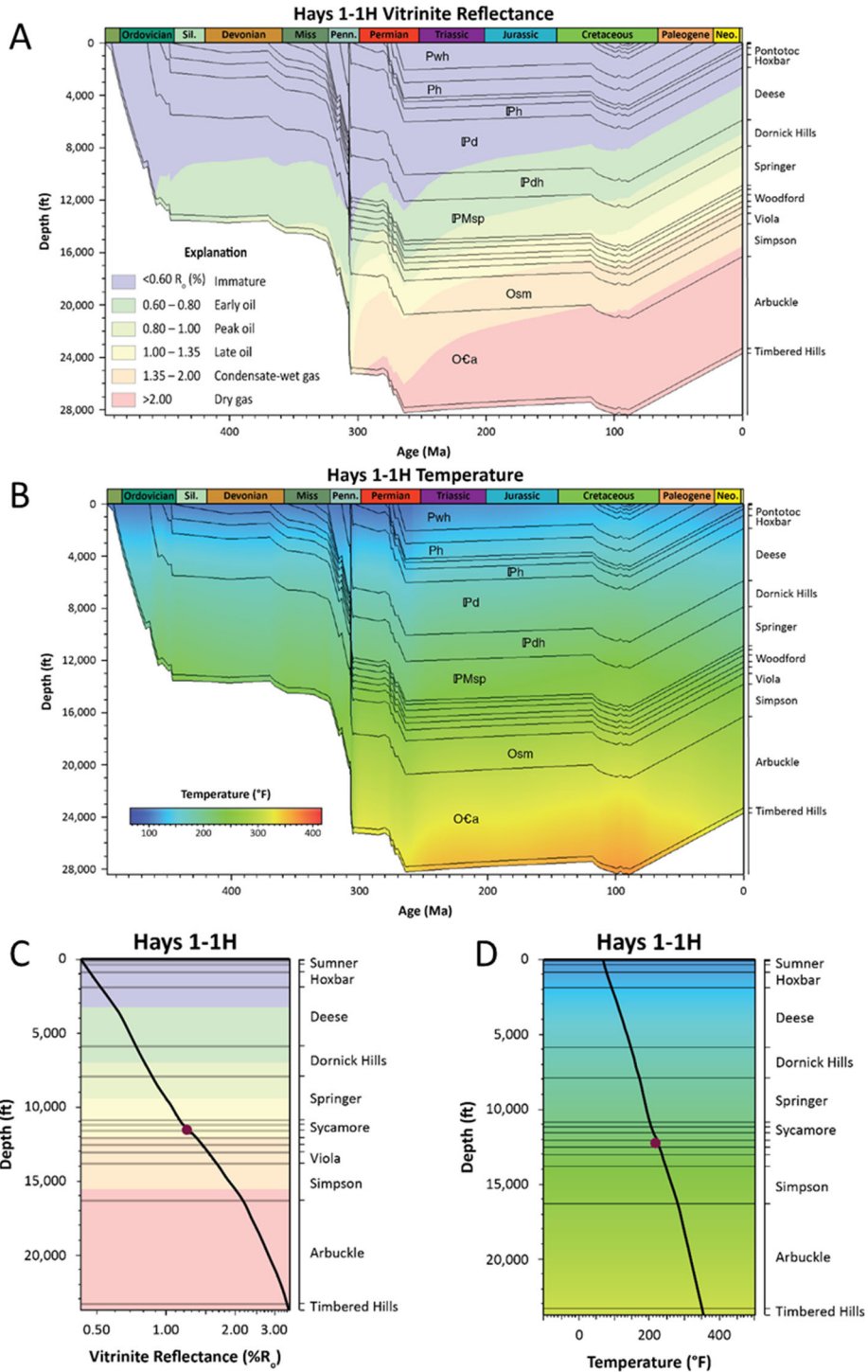
**Figure 60.** Burial and thermal history models of the Badger 2-23 well in the Ardmore Basin. A) Burial history model showing evolution of thermal maturity windows. B) Thermal history model showing relationship between formation temperature and burial history. C) Modeled vitrinite reflectance-depth plot showing calibration between simulated thermal maturity and control on vitrinite reflectance in the Woodford Shale. D) Modeled temperature-depth plot showing calibration between simulated temperature and corrected bottom-hole temperature.



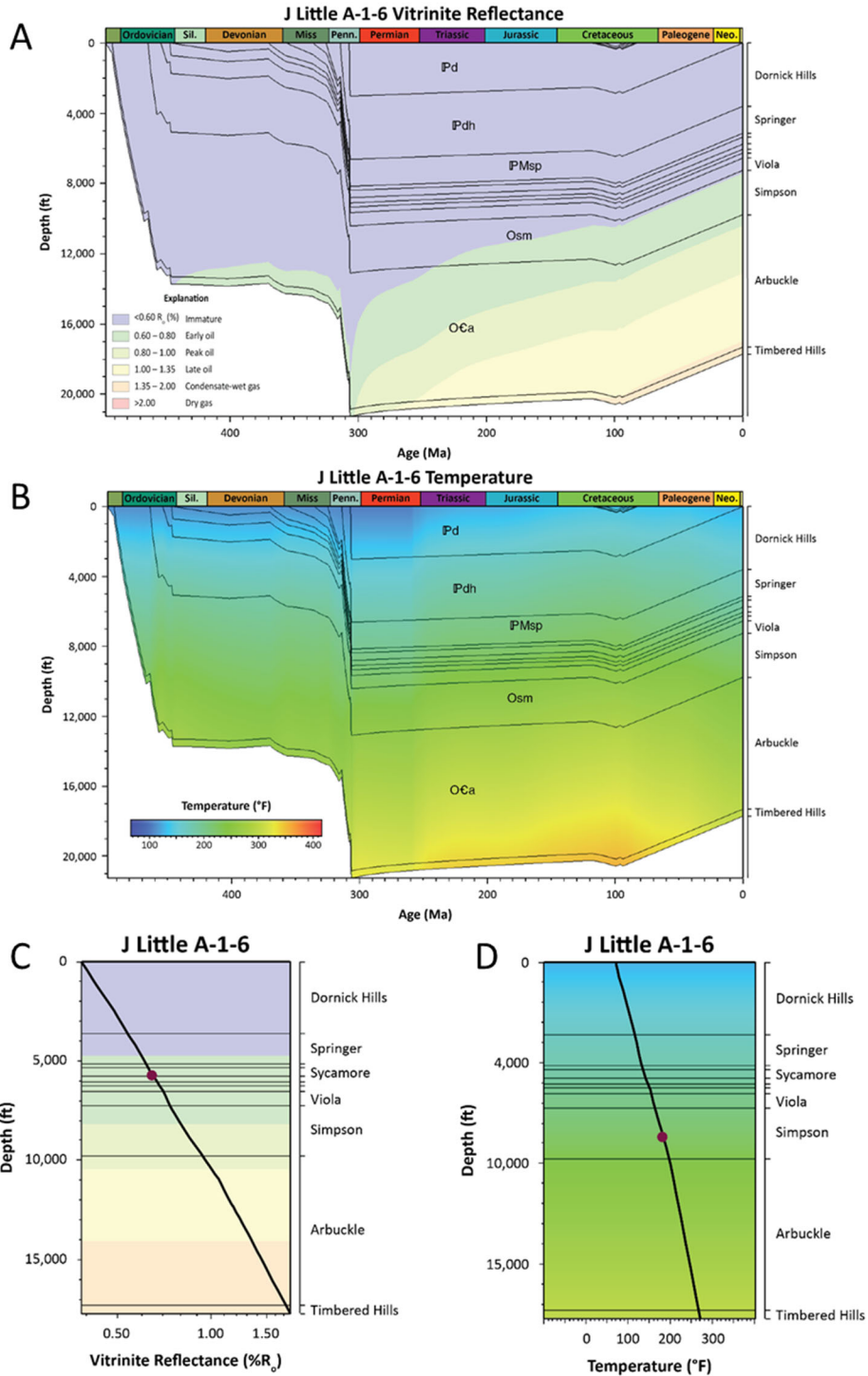
**Figure 61.** Burial and thermal history models of the Brock 9-1H well in the Ardmore Basin. A) Burial history model showing evolution of thermal maturity windows. B) Thermal history model showing relationship between formation temperature and burial history. C) Modeled vitrinite reflectance-depth plot showing calibration between simulated thermal maturity and control on vitrinite reflectance in the Woodford Shale. D) Modeled temperature-depth plot showing calibration between simulated temperature and corrected bottom-hole temperature.



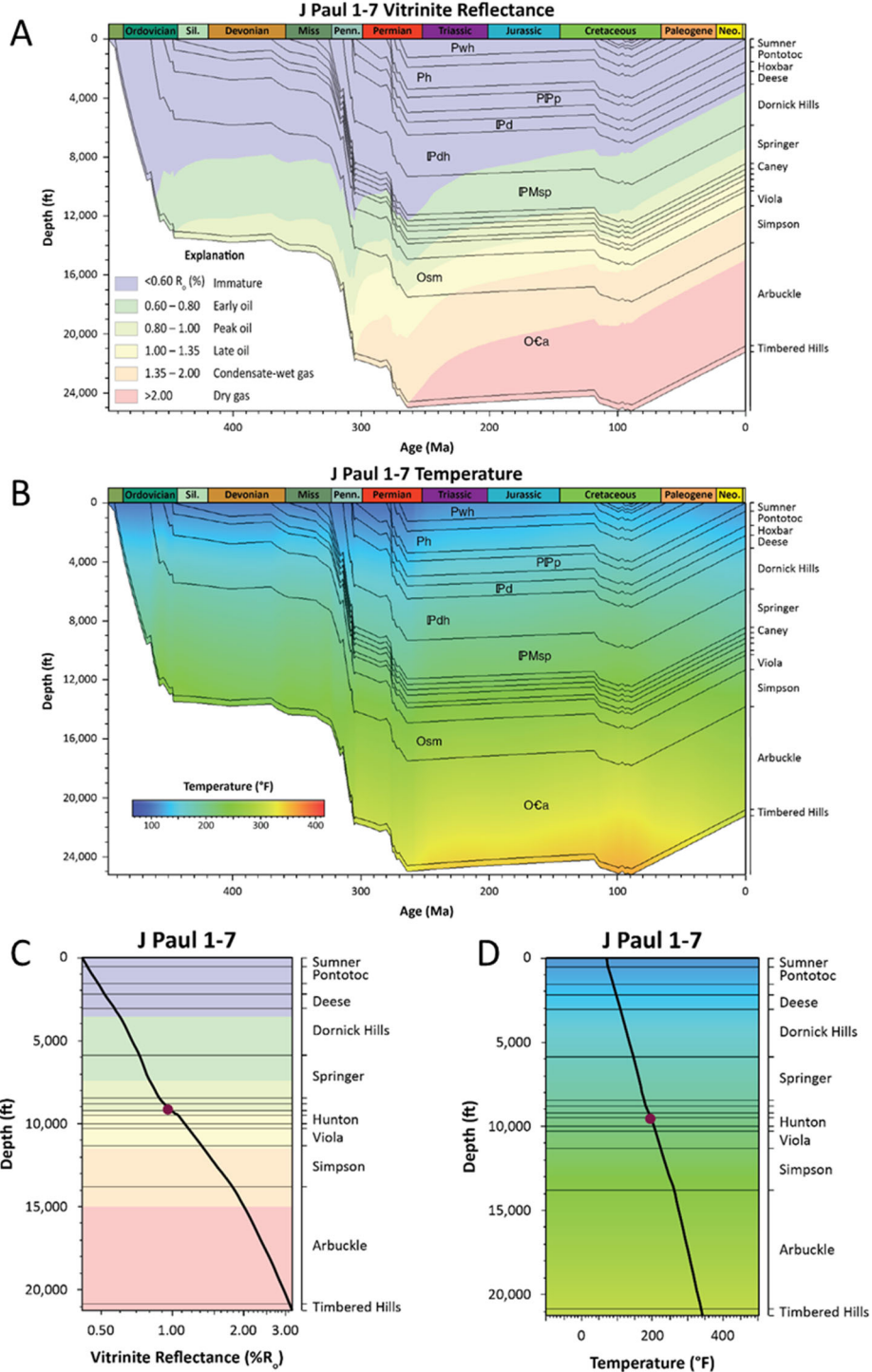
**Figure 62.** Burial and thermal history models of the Dansby 1-3H well in the Ardmore Basin. A) Burial history model showing evolution of thermal maturity windows. B) Thermal history model showing relationship between formation temperature and burial history. C) Modeled vitrinite reflectance-depth plot showing calibration between simulated thermal maturity and control on vitrinite reflectance in the Woodford Shale. D) Modeled temperature-depth plot showing calibration between simulated temperature and corrected bottom-hole temperature.



**Figure 63.** Burial and thermal history models of the Hays 1-1H well in the Ardmore Basin. A) Burial history model showing evolution of thermal maturity windows. B) Thermal history model showing relationship between formation temperature and burial history. C) Modeled vitrinite reflectance-depth plot showing calibration between simulated thermal maturity and control on vitrinite reflectance in the Woodford Shale. D) Modeled temperature-depth plot showing calibration between simulated temperature and corrected bottom-hole temperature.

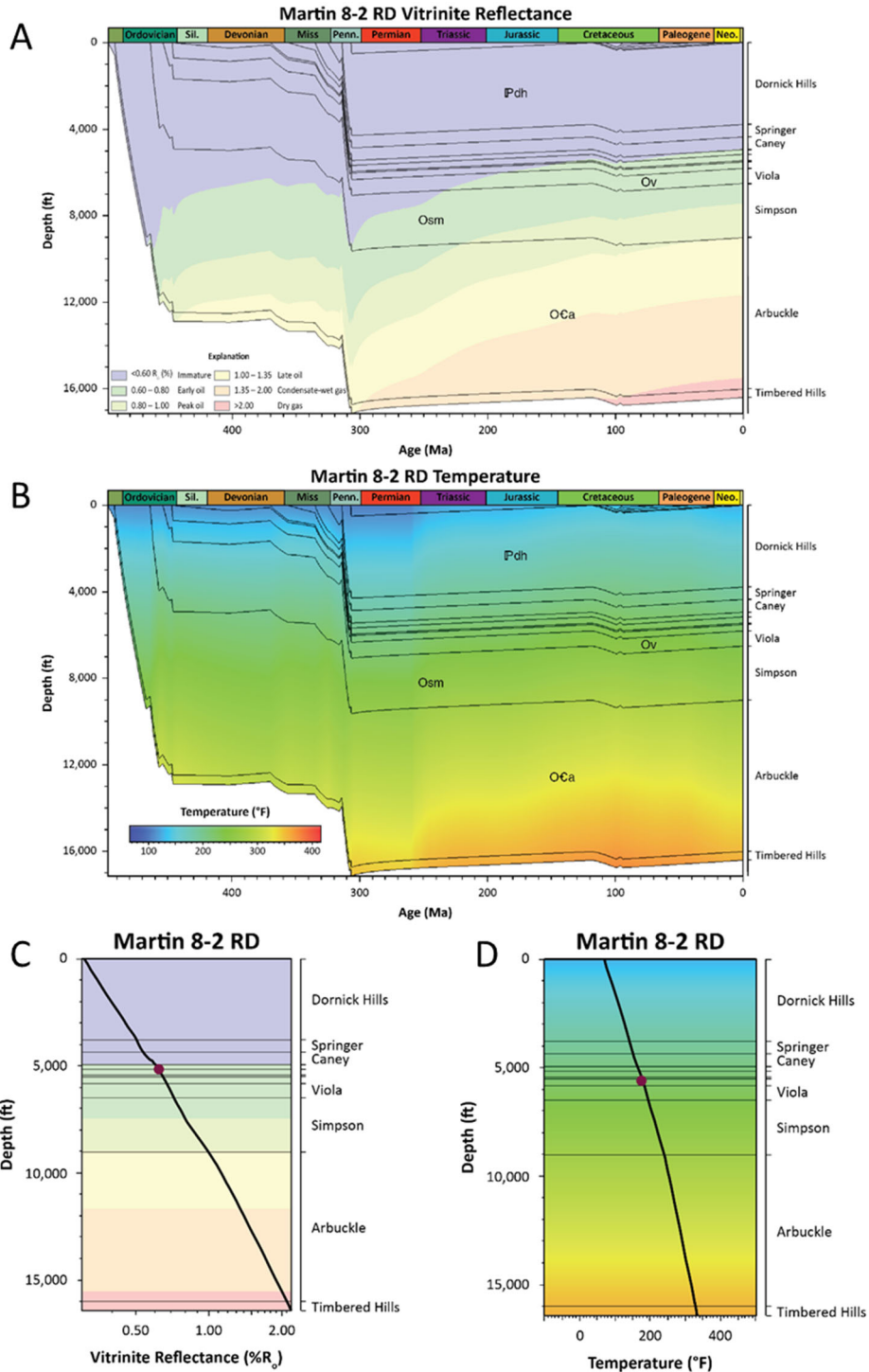


**Figure 64.** Burial and thermal history models of the J Little A-1-6 well in the Ardmore Basin. A) Burial history model showing evolution of thermal maturity windows. B) Thermal history model showing relationship between formation temperature and burial history. C) Modeled vitrinite reflectance-depth plot showing calibration between simulated thermal maturity and control on vitrinite reflectance in the Woodford Shale. D) Modeled-temperature depth plot showing calibration between simulated temperature and corrected bottom-hole temperature.

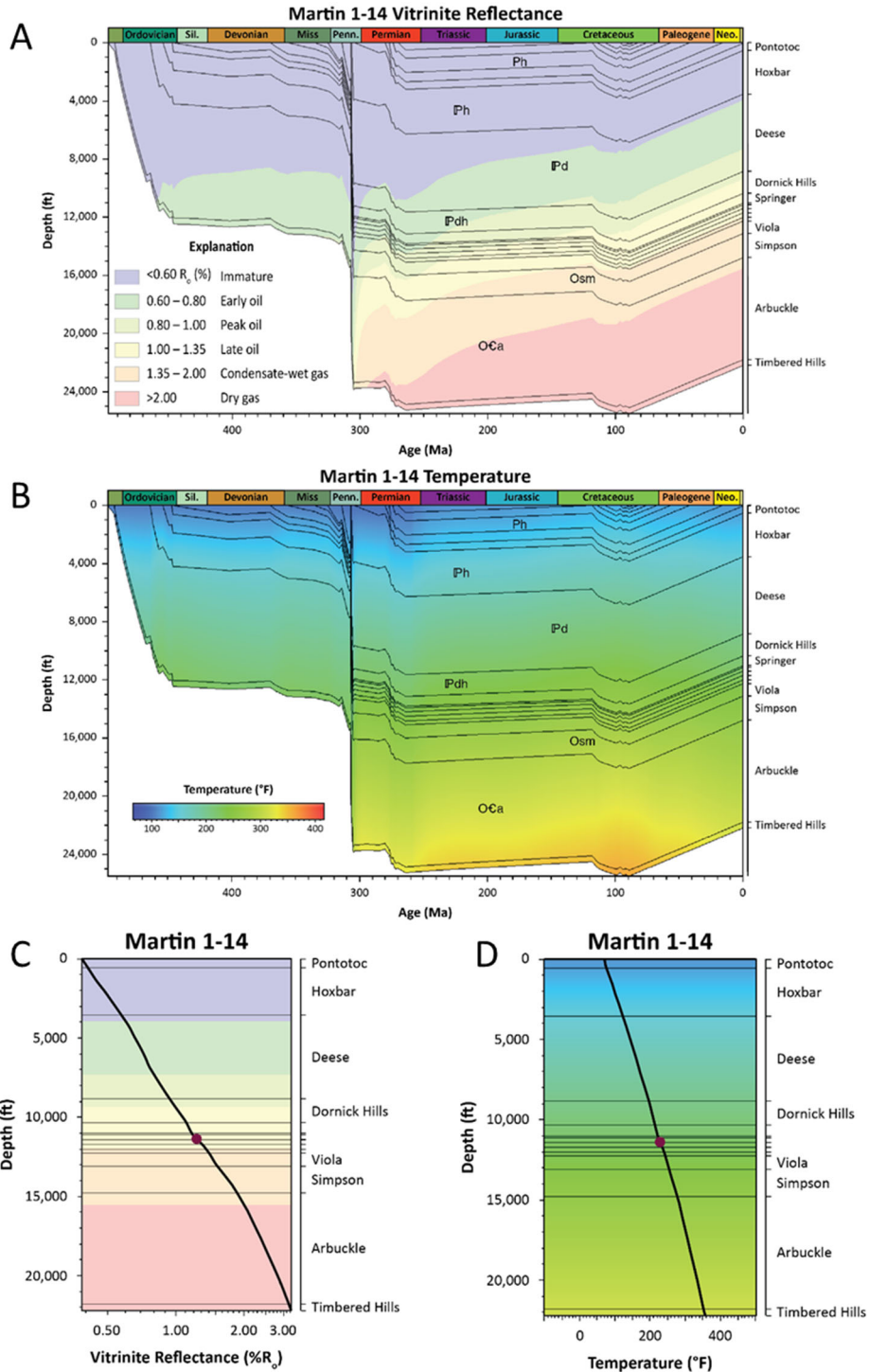


**Figure 65.** Burial and thermal history models of the J Paul 1-7 well in the Ardmore Basin. A) Burial history model showing evolution of thermal maturity windows. B) Thermal history model showing relationship between formation temperature and burial history. C) Modeled vitrinite reflectance-depth plot showing calibration between simulated thermal maturity and control on vitrinite reflectance in the Woodford Shale. D) Modeled temperature-depth plot showing calibration between simulated temperature and corrected bottom-hole temperature.

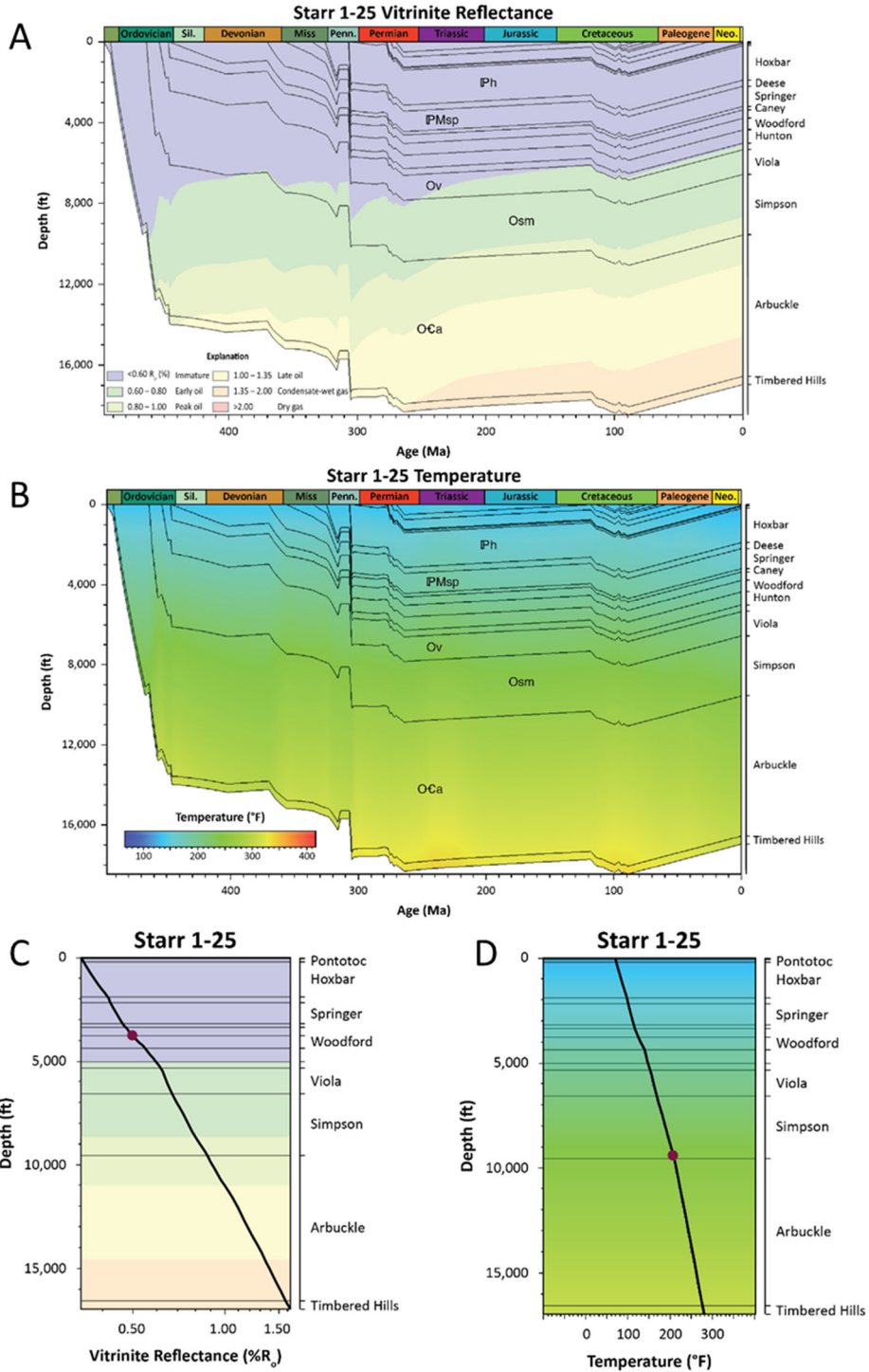




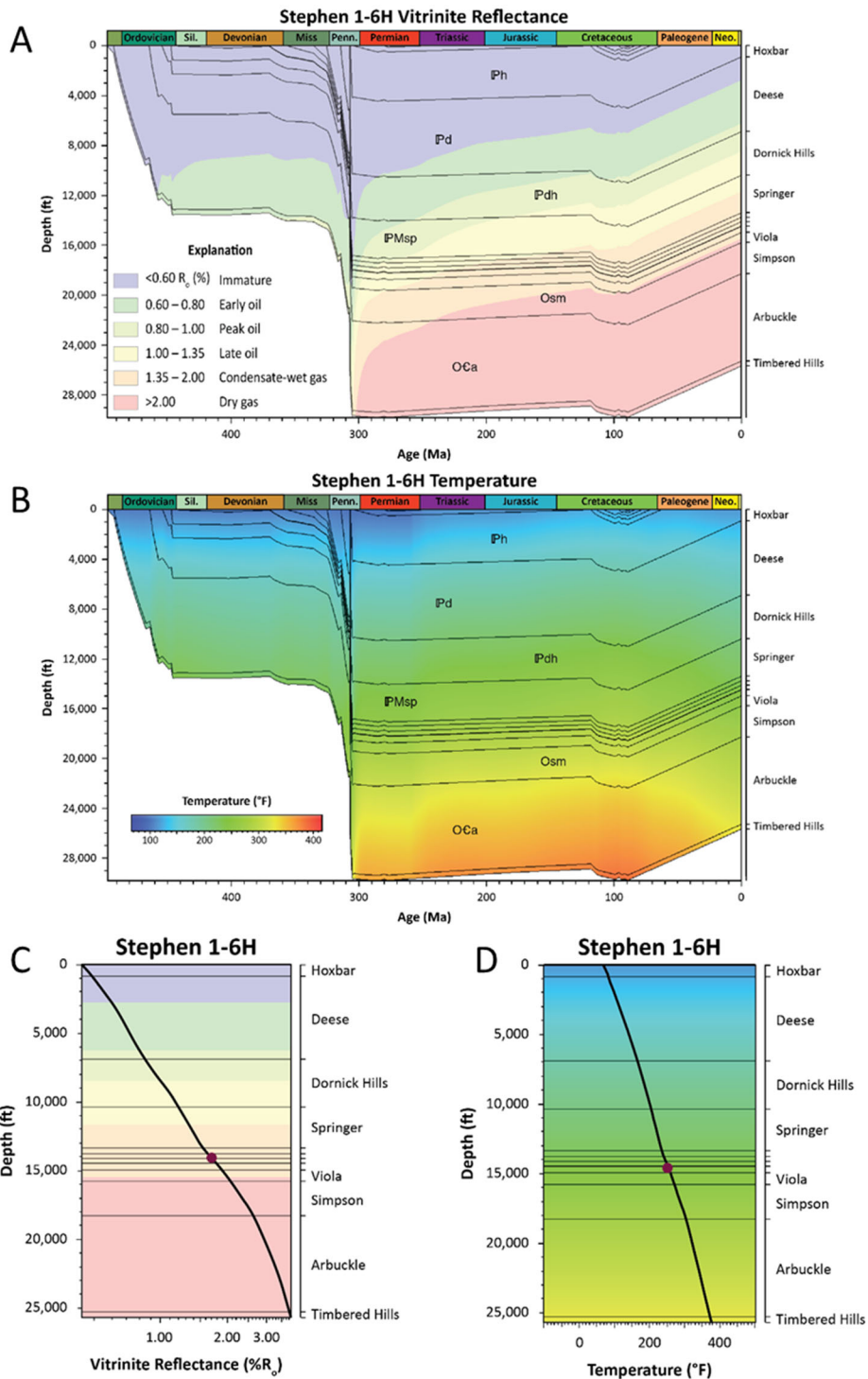
**Figure 66.** Burial and thermal history models of the Martin 8-2 RD well in the Ardmore Basin. A) Burial history model showing evolution of thermal maturity windows. B) Thermal history model showing relationship between formation temperature and burial history. C) Modeled vitrinite reflectance-depth plot showing calibration between simulated thermal maturity and control on vitrinite reflectance in the Woodford Shale. D) Modeled temperature-depth plot showing calibration between simulated temperature and corrected bottom-hole temperature.



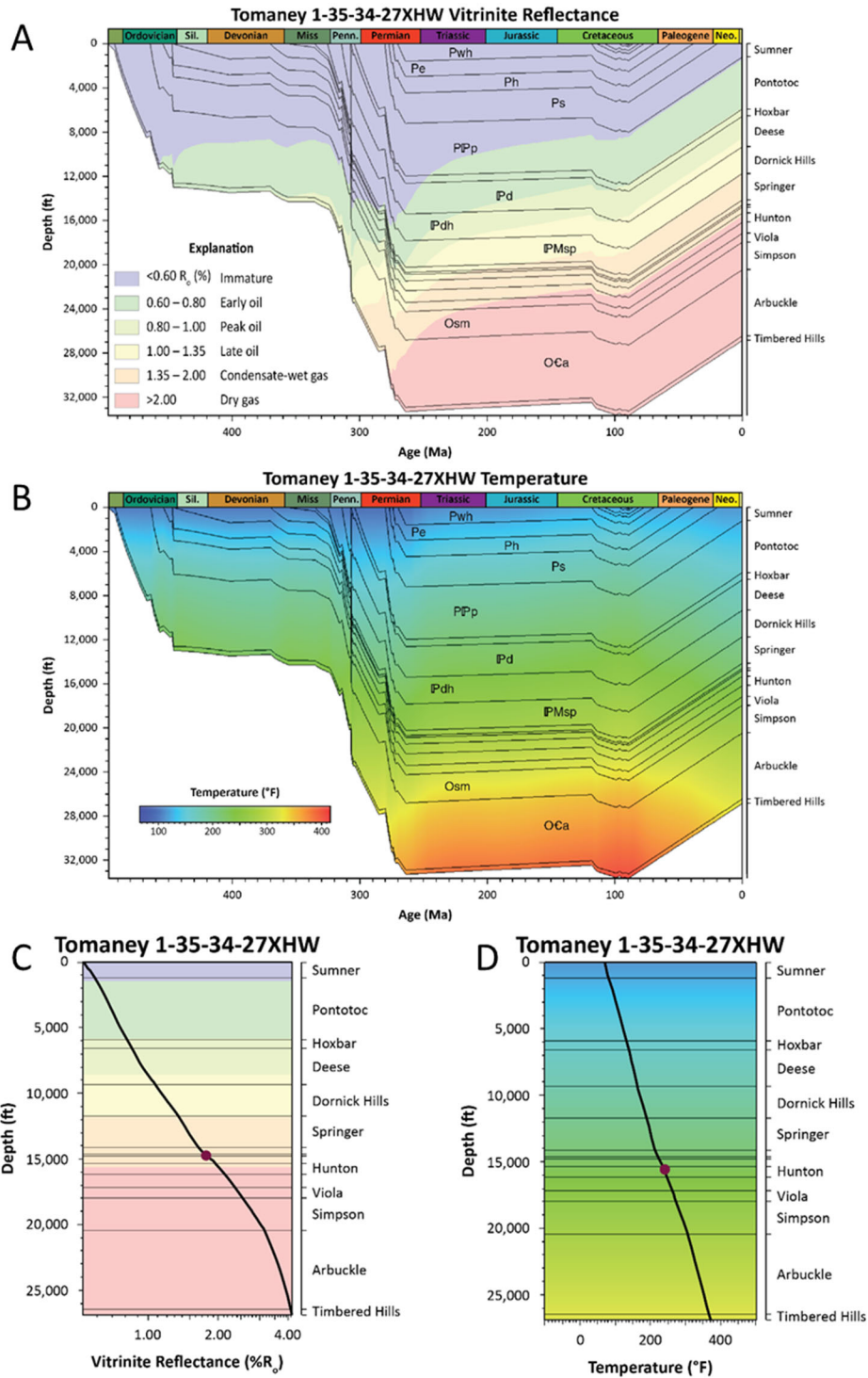
**Figure 67.** Burial and thermal history models of the Martin 1-14 well in the Ardmore Basin. A) Burial history model showing evolution of thermal maturity windows. B) Thermal history model showing relationship between formation temperature and burial history. C) Modeled vitrinite reflectance-depth plot showing calibration between simulated thermal maturity and control on vitrinite reflectance in the Woodford Shale. D) Modeled temperature-depth plot showing calibration between simulated temperature and corrected bottom-hole temperature.



**Figure 68.** Burial and thermal history models of the Starr 1-25 well in the Ardmore Basin. A) Burial history model showing evolution of thermal maturity windows. B) Thermal history model showing relationship between formation temperature and burial history. C) Modeled vitrinite reflectance-depth plot showing calibration between simulated thermal maturity and control on vitrinite reflectance in the Woodford Shale. D) Modeled temperature-depth plot showing calibration between simulated temperature and corrected bottom-hole temperature.



**Figure 69.** Burial and thermal history models of the Stephen 1-6H well in the Ardmore Basin. A) Burial history model showing evolution of thermal maturity windows. B) Thermal history model showing relationship between formation temperature and burial history. C) Modeled vitrinite reflectance-depth plot showing calibration between simulated thermal maturity and control on vitrinite reflectance in the Woodford Shale. D) Modeled temperature-depth plot showing calibration between simulated temperature and corrected bottom-hole temperature.



**Figure 70.** Burial and thermal history models of the Tomaney 1-35-34-27XHW well in the Ardmore Basin. A) Burial history model showing evolution of thermal maturity windows. B) Thermal history model showing relationship between formation temperature and burial history. C) Modeled vitrinite reflectance-depth plot showing calibration between simulated thermal maturity and control on vitrinite reflectance in the Woodford Shale. D) Modeled temperature-

depth plot showing calibration between simulated temperature and corrected bottom-hole temperature.

Early Paleozoic units are widespread throughout the Ardmore Basin, and unit thickness varies markedly. Generally, the Cambrian–Ordovician section is about 6,000 ft thicker than the Devonian–Mississippian section. A significant shift in rock composition is observed in which most early Paleozoic units are composed of carbonate while late Paleozoic units are largely siliciclastic.

Models in the far eastern part of the study area (Marshall and Bryan Counties) required significantly less Pennsylvanian deposition than those further west. For instance, paleo thickness of the Pennsylvanian section in the Dansby 1-3H is about 6,000 ft (Figure 62) while the Tomaney 1-35-34-27XHW model has a paleo thickness of about 8,600 ft (Figure 70). Additionally, sections in the east, such as the Dansby 1-3H (Figure 62) and Brock 9-1H (Figure 61) wells, as well as those in the west that are proximal to structural highs such as the Arbuckle Mountains and Criner Hills have been modeled as having incomplete Pennsylvanian sections. The Hoxbar Group is missing in these models.

Generally, significant Permian deposition (>11,000 ft in the Tomaney 1-35-34-27XHW model) was needed for calibration of models in the western Ardmore Basin, especially near the Anadarko Basin. No Permian deposition was added to the Martin 8-2 RD (Figure 66), Dansby 1-3H (Figure 62), Brock 9-1H (Figure 61), Badger 2-23 (Figure 60), and J Little A-1-6 (Figure 64) models in the eastern part of the basin. Conversely, Cretaceous strata was included in all models. However, calibration of models in the southeastern Ardmore Basin required significantly more Cretaceous deposition than models in the west. For example, 1,400 ft of Cretaceous sediment was added to the Hays 1-1H model (Figure 63) in the west, while 4,300 ft of Cretaceous sediment was added to the Dansby 1-3H model (Figure 62) in the east.

## Erosion

A source of uncertainty was modeling erosion of the post-Pennsylvanian section, which is only partially preserved. Modeling results for erosional thicknesses are tabulated in Table 4. Post-Pennsylvanian erosional thickness varies for each model but averages approximately 5,000 ft, corresponding with the y-intercept of the vitrinite reflectance-depth plot (Figure 42). Generally, erosion was greater for models in the west than in the east. Calibration of models requires less post-Pennsylvanian erosion on and proximal to major structural highs, such as the Arbuckle Mountains, than in the basin proper. For instance, 5,500 ft of post-Pennsylvanian erosion was needed to calibrate the B&W Tyson 1-8 model (Figure 59) in the center of the basin while 3,150 ft of post-Pennsylvanian erosion was needed to calibrate the J-Little A model (Figure 64) in the southeastern flank of the Arbuckle Mountains.

**Table 4.** Boundary conditions and modeled erosional thickness used to make burial history models of wells in the Ardmore Basin.

Well Name	Unit at Surface	Post-Hoxbar Eroded Thickness (ft)	Present-Day Basement Heat Flow (mW/m <sup>2</sup> )	Woodford Depth (MD)	Woodford Vitrinite Reflectance (%R <sub>o</sub> ) from Map	BHT Depth (ft)	Corrected BHT (°F)	Unit BHT Recorded
B&W TYSON 1-8	Permian Sumner Group	5,500	44	10,608	1.11	12,240	222.1	Viola Group
TOMANEY 1-35-34-27XHW	Permian Sumner Group	7,800	42	14,795	1.77	15,550	239.75	Hunton Group
J LITTLE A-1-6	Pennsylvanian Dornick Hills Group	3,450	42	5,762	0.65	8,700	179.24	Simpson Group
BADGER 2-23	Cretaceous Washita Group	1,080	58	4,846	0.6	6,900	208	Simpson Group
BROCK 9-1H	Pennsylvanian Deese Group	7,600	50	9,034	0.96	9,700	204.88	Viola Group
DANSBY 1-3H	Cretaceous Woodbine Formation	6,350	47	6,050	0.69	6,700	159.92	Sylvan
J PAUL 1-7	Permian Sumner Group	5,000	44	9,131	0.95	9,563	194.19	Hunton Group
MARTIN 8-2 RD	Pennsylvanian Dornick Hills Group	1,450	57	5,168	0.62	5,600	174.12	Sylvan
STARR 1-25	Permian Hennessey Group	2,050	42	3,784	0.5	9,400	202.54	Simpson Group
MARTIN 1-14	Permian Sumner Group	4,100	44	11,392	1.23	11,392	228	Woodford
STEPHEN 1-6H	Pennsylvanian Hoxbar Group	8,900	44	14,112	1.69	14,635	250.58	Sylvan
HAYS 1-1H	Permian Hennessey Group	5,200	42	11,588	1.24	12,275	217.37	Hunton Group
		4,873	46					
		Average	Average					



## Boundary Conditions

Using the approach formulated by McKenzie (1978), basement heat flow was estimated to be as high as  $\sim 90 \text{ mW/m}^2$  during Neoproterozoic–Cambrian Iapetan rifting, and included exponential thermal decay during the Cambrian and Ordovician to present-day values. Present-day heat flow is relatively uniform throughout the Ardmore Basin with values ranging from 42–60  $\text{mW/m}^2$  and averaging 46  $\text{mW/m}^2$  for the twelve models (Table 4). Heat flow gradually increases from west to east in the Ardmore Basin and generally is greater on structural highs with shallow basement and thin sediment cover. For example, calculated basement heat flow at the Martin 8-2 RD well, which is in a structural high near the Criner Hills, is estimated to be 57  $\text{mW/m}^2$ , while that at the Tomaney 1-35-34-27XHW well in the Harrisburg Trough is estimated to be 42  $\text{mW/m}^2$ .

## Thermal Maturation

Prior to the Pennsylvanian, only the Timbered Hills and Arbuckle Groups had entered petroleum generation windows (early–late oil) (Figures 59–70). These groups were subjected to higher temperatures during and after Mississippian–Permian burial. Throughout most of the Ardmore Basin, the Woodford and Caney Shales entered petroleum generation windows during accelerated Desmoinesian–Missourian subsidence and burial. For models located within synclines, such as the Stephen 1-6H (Figure 69) and Tomaney 1-35-34-27XHW (Figure 70), rapid subsidence and burial continued through the Guadalupian. Devonian–Mississippian source rocks continued to mature thermally during the Triassic–Jurassic, although, there was no additional burial or subsidence during that time.

Effects of Cretaceous deposition on maturity are negligible throughout much of the Ardmore Basin except for models in the far eastern part of the basin (Marshall and Bryan Counties) where a thicker Cretaceous section was added. For instance, in the Dansby 1-3H model (Figure 62), where the Cretaceous section has a paleo thickness of 4,300 ft, maturities of the Woodford and Caney Shales increase slightly, but remain in the same maturity window (early oil) as they were prior to Cretaceous deposition. Although the Ardmore Basin is no longer subsiding, Devonian–Mississippian source rocks are continuing to mature thermally at slow rates as isomaturity lines rise relative to stratigraphic position in thermal history models.

The highest modeled present-day vitrinite reflectance of the Woodford Shale is 1.9% (condensate-wet gas) in the Tomaney 1-35-34-27XHW well (Figure 70 and Table 5). The lowest present-day Woodford Shale vitrinite reflectance is 0.5% (immature) in the Starr 1-25 well (Figure 70 and Table 5). Modeled present-day vitrinite reflectance for the Caney Shale is highest in the Tomaney 1-35-34-27XHW well at 1.8% (condensate-wet gas) (Figure 72 and Table 5). The lowest modeled present-day Caney Shale vitrinite reflectance is 0.5% (immature) in the Starr 1-25 well, which is in a structural high near the Wichita Mountains (Figure 68 and Table 5).

The highest modeled present-day temperatures for the Woodford and Caney Shales were about 240°F and 252°F, respectively, in the Stephens 1-6H well (Figure 69 and Table 6), which is located near the Berwyn Syncline. Modeled present-day Woodford and Caney Shale temperatures were lowest at 121°F and 112°F, respectively, in the Martin 8-2 RD well (Figure 66 and Table 6), which is in a structural high near the Criner Hills. Simulated present-day temperatures of formations using the Sweeney and Burnham (1990) model (Figures 59–70) correspond within 5.6°C (10°F) of present-day temperature maps calculated from geothermal gradients (Figures 37–41).

**Table 5.** Modeled thermal maturities of the Woodford and Caney Shales in selected wells in the Ardmore Basin.

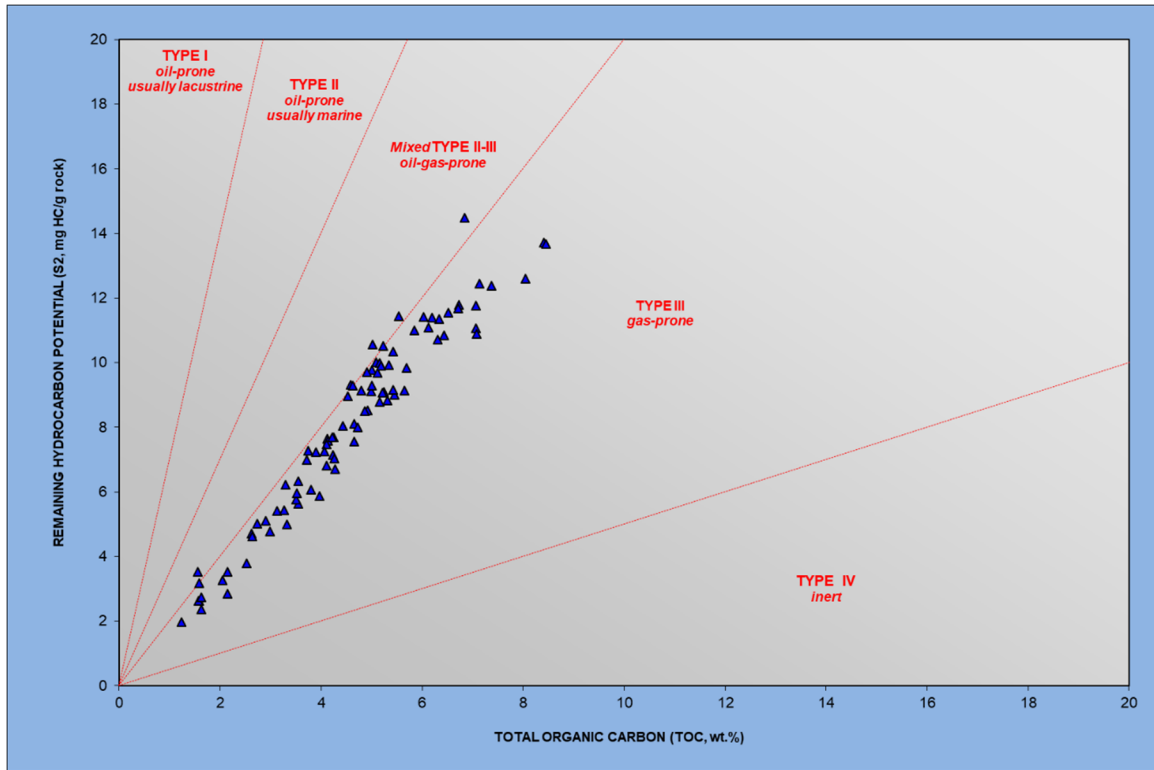
Well Name	Depth (TVD)				Sweeney & Burnham (1990) EASY %R <sub>o</sub> Present-Day Maturity (%R <sub>o</sub> )					
	Caney		Woodford		Caney			Woodford		
	Top	Base	Top	Base	Top	Base	Maturity Window	Top	Base	Maturity Window
B&W TYSON 1-8	10,026	10,212	10,608	11,066	1.03	1.07	Late oil	1.12	1.2	Late oil
TOMANEY 1-35-34-27XHW	14,151	14,606	14,795	15,335	1.64	1.75	Condensate-wet gas	1.78	1.94	Condensate-wet gas
J LITTLE A-1-6	5,137	5,359	5,761	6,051	0.62	0.63	Early oil	0.65	0.67	Early oil
BADGER 2-23	4,402	4,617	4,846	5,272	0.55	0.58	Immature	0.61	0.65	Early oil
BROCK 9-1H	8,412	8,745	9,033	9,381	0.88	0.93	Peak oil	0.96	1.05	Peak oil–Late oil
DANSBY 1-3H	5,730	6,017	6,047	6,372	0.67	0.69	Early oil	0.69	0.72	Early oil
J PAUL 1-7	8,456	8,827	9,177	9,520	0.87	0.93	Peak oil	0.97	1.06	Peak oil–Late oil
MARTIN 8-2 RD	4,360	4,943	5,168	5,452	0.53	0.60	Immature	0.62	0.64	Early oil
STARR 1-25	3,197	3,369	3,784	4,362	0.46	0.48	Immature	0.50	0.55	Immature
MARTIN 1-14	11,029	11,146	11,392	11,693	1.18	1.20	Late oil	1.23	1.31	Late oil
STEPHEN 1-6H	13,389	13,757	14,110	14,455	1.54	1.63	Condensate-wet gas	1.70	1.79	Condensate-wet gas
HAYS 1-1H	10,883	11,174	11,588	12,108	1.14	1.19	Late oil	1.25	1.37	Late oil–Condensate-wet gas

**Table 6.** Modeled formation temperatures of the Woodford and Caney Shales in selected wells in the Ardmore Basin.

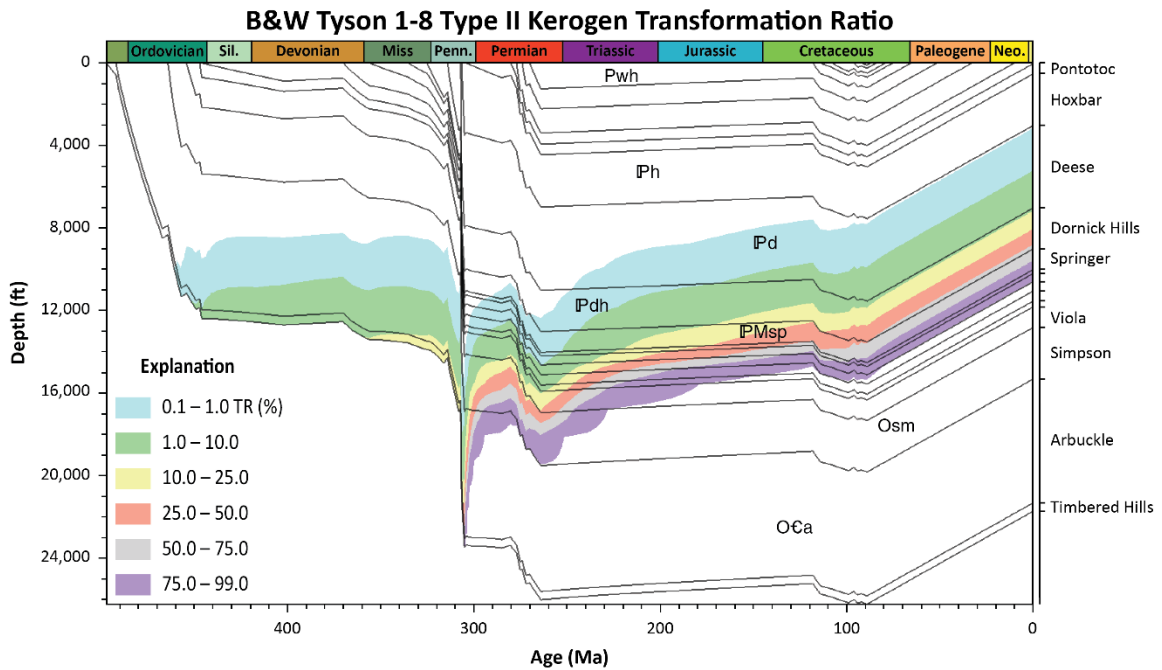
Well Name	Depth (TVD)				Sweeney & Burnham (1990) EASY %R <sub>o</sub> Present-Day Temperature (°F)					
	Caney		Woodford		Caney			Woodford		
	Top	Base	Top	Base	Top	Base	Maturity Window	Top	Base	Maturity Window
B&W TYSON 1-8	10,026	10,212	10,608	11,066	189.72	193.22	Late oil	198.67	209.62	Late oil
TOMANEY 1-35-34-27XHW	14,151	14,606	14,795	15,335	212.08	220.27	Condensate-wet gas	222.89	235.11	Condensate-wet gas
J LITTLE A-1-6	5,137	5,359	5,761	6,051	130.65	134.70	Early oil	139.95	146.98	Early oil
BADGER 2-23	4,402	4,617	4,846	5,272	151.86	157.30	Immature	161.66	175.21	Early oil
BROCK 9-1H	8,412	8,745	9,033	9,381	179.95	186.61	Peak oil	190.86	199.77	Peak oil–Late oil
DANSBY 1-3H	5,730	6,017	6,047	6,372	143.84	149.6	Early oil	150.04	158.64	Early oil
J PAUL 1-7	8,456	8,827	9,177	9,520	175.33	182.82	Peak oil	188.01	196.86	Peak oil–Late oil
MARTIN 8-2 RD	4,360	4,943	5,168	5,452	149.72	163.48	Immature	167.48	175.88	Early oil
STARR 1-25	3,197	3,369	3,784	4,362	112.11	115.44	Immature	121.32	135.82	Immature
MARTIN 1-14	11,029	11,146	11,392	11,693	221.05	223.22	Late oil	226.63	233.67	Late oil
STEPHEN 1-6H	13,389	13,757	14,110	14,455	233.75	240.06	Condensate-wet gas	244.69	252.02	Condensate-wet gas
HAYS 1-1H	10,883	11,174	11,588	12,108	200.52	205.76	Late oil	211.29	223.05	Late oil–Condensate-wet gas

## Hydrocarbon Generation

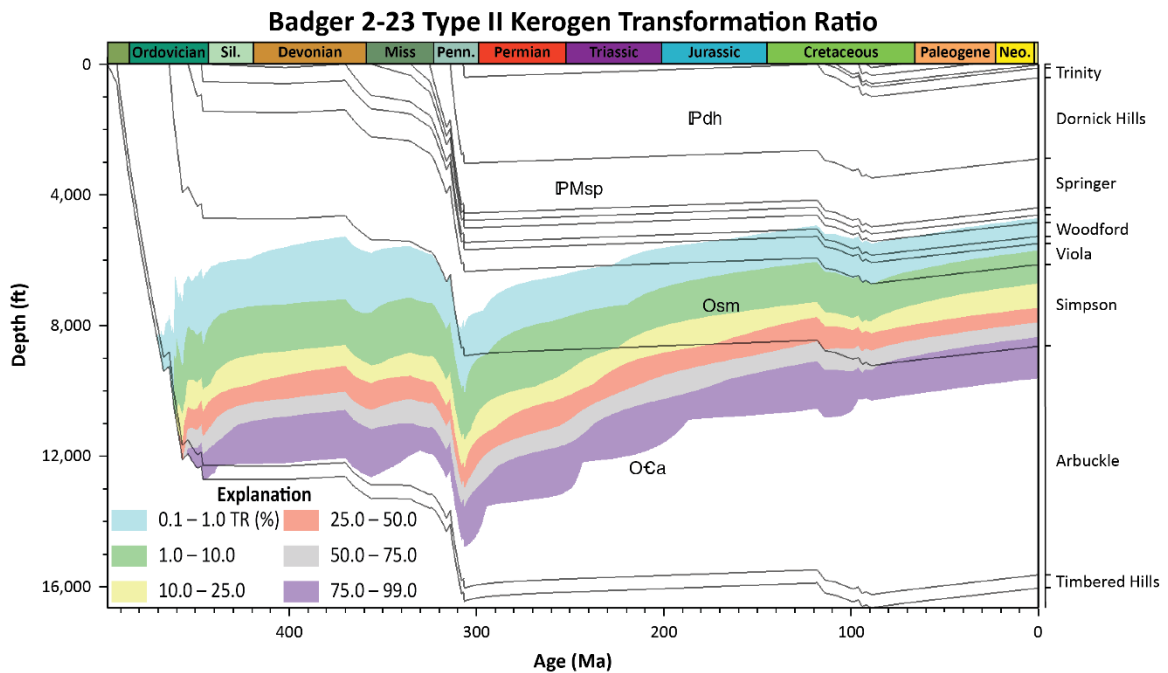
The types of kerogen present in the Caney Shale were approximated by plotting S<sub>2</sub> (remaining hydrocarbon potential) against TOC. Rock-Eval pyrolysis data were measured from the Caney Shale core recovered from the Tomaney 1-35-34-27XHW well. Organic matter in the Caney Shale in the Tomaney 1-35-34-27XHW well plots as sapropelic type II and humic type III kerogen (Figure 71), and the shale contains about 1-8% TOC. Accordingly, kinetic algorithms for type II kerogen in the Woodford Shale, developed and outlined by Lewan and Ruble (2002), were used to model transformation of type II kerogen in the Woodford and Caney source rocks for each model (Figures 72–85; Tables 7–9). No source rock kinetic algorithms have been developed specifically for the Caney Shale; however, the Caney and Woodford Shales possess similar lithological and geochemical properties.



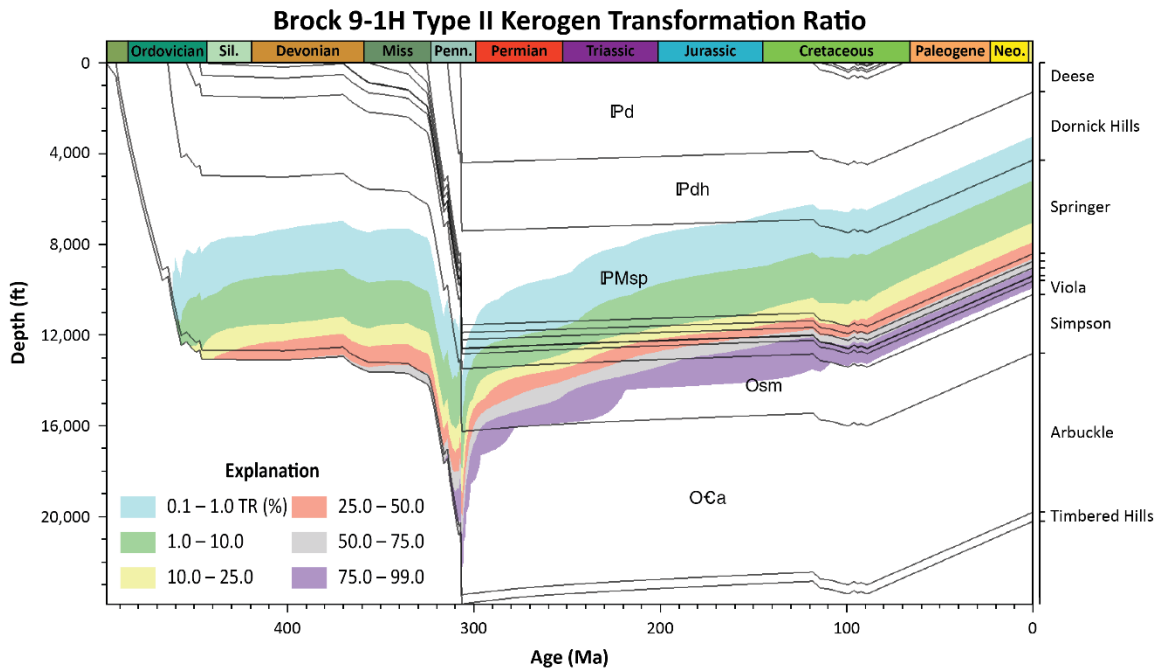
**Figure 71.** Kerogen quality diagram displaying the presence of various kerogen types within the Caney Shale in the core recovered from the Tomaney 1-35-34-27XHW well (Rock-Eval pyrolysis data measured at Chesapeake Energy’s Reservoir Technology Center).



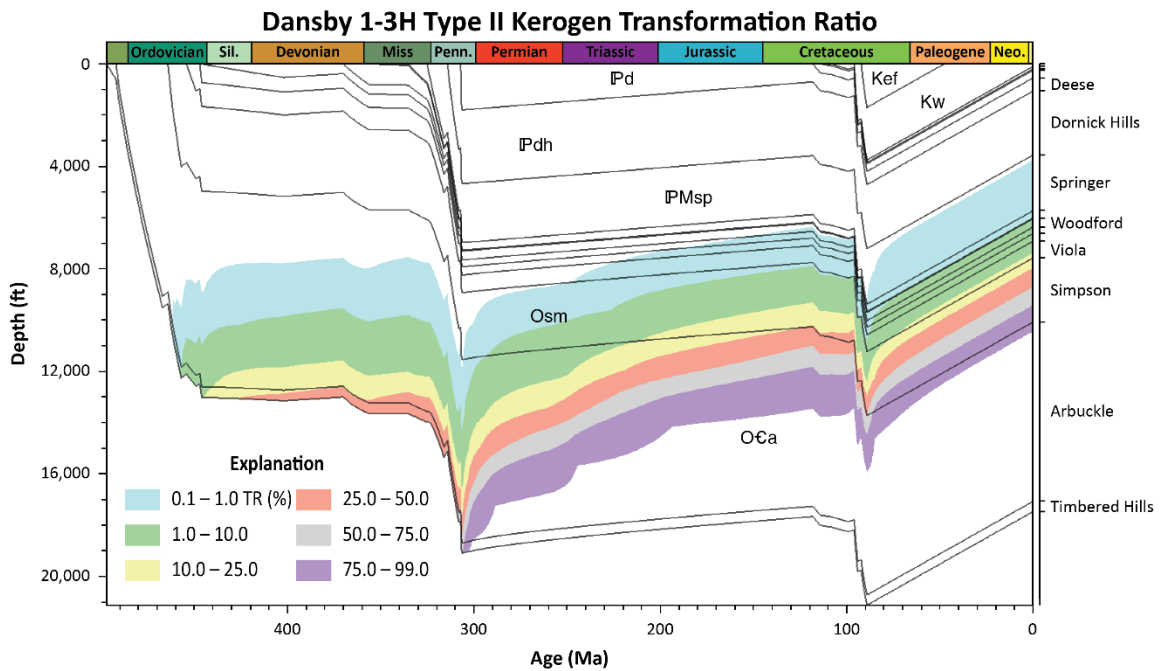
**Figure 72.** Burial history model of the B&W Tyson 1-8 well showing how transformation ratio (TR) for Type II kerogen evolved through geologic time and burial. Transformation ratio was calculated using hydrous pyrolysis kinetics for type II kerogen (Lewan and Ruble, 2002).



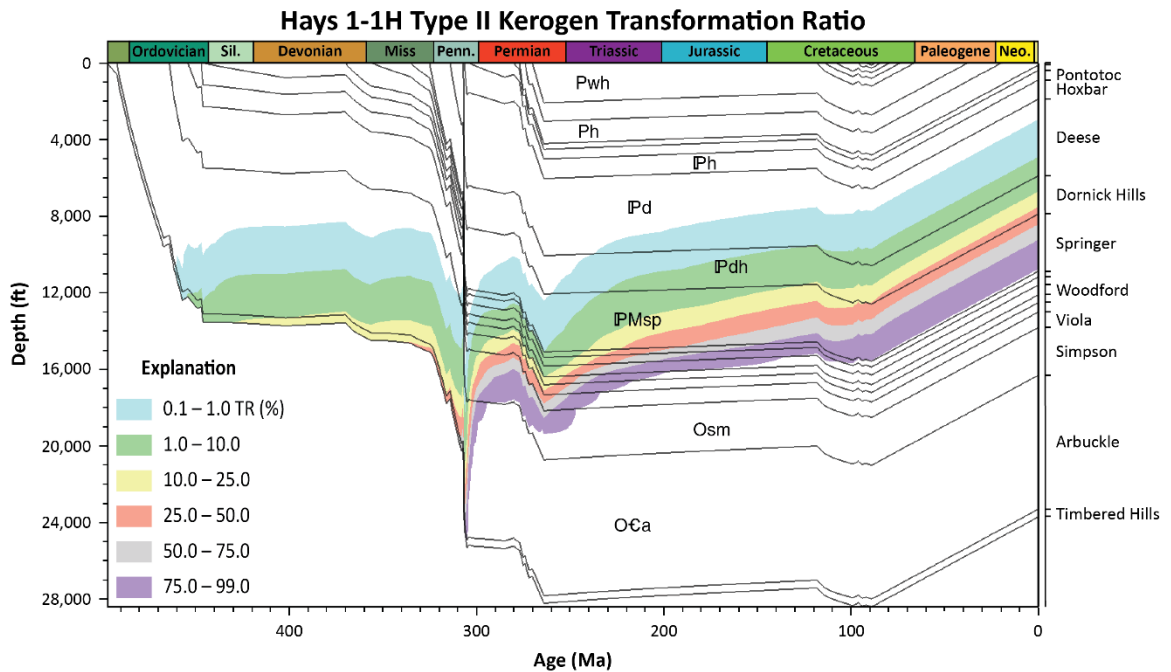
**Figure 73.** Burial history model of the Badger 2-23 well showing how transformation ratio (TR) for Type II kerogen evolved through geologic time and burial. Transformation ratio was calculated using hydrous pyrolysis kinetics for type II kerogen (Lewan and Ruble, 2002).



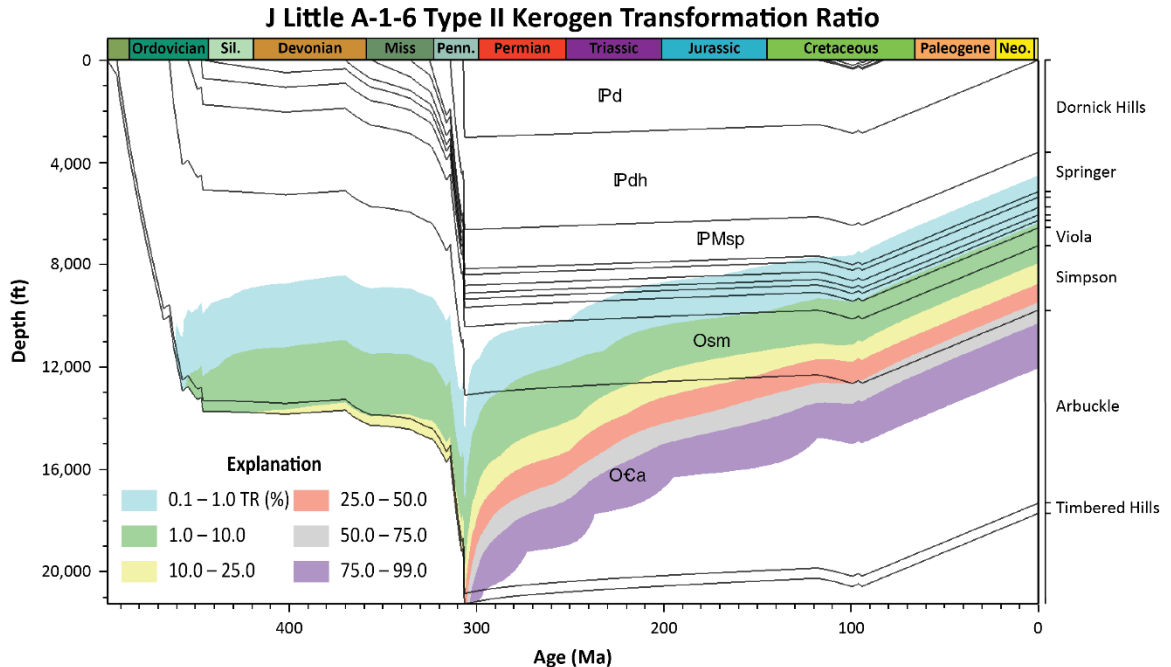
**Figure 74.** Burial history model of the Brock 9-1H well showing how transformation ratio (TR) for Type II kerogen evolved through geologic time and burial. Transformation ratio was calculated using hydrous pyrolysis kinetics for type II kerogen (Lewan and Ruble, 2002).



**Figure 75.** Burial history model of the Dansby 1-3H well showing how transformation ratio (TR) for Type II kerogen evolved through geologic time and burial. Transformation ratio was calculated using hydrous pyrolysis kinetics for type II kerogen (Lewan and Ruble, 2002).

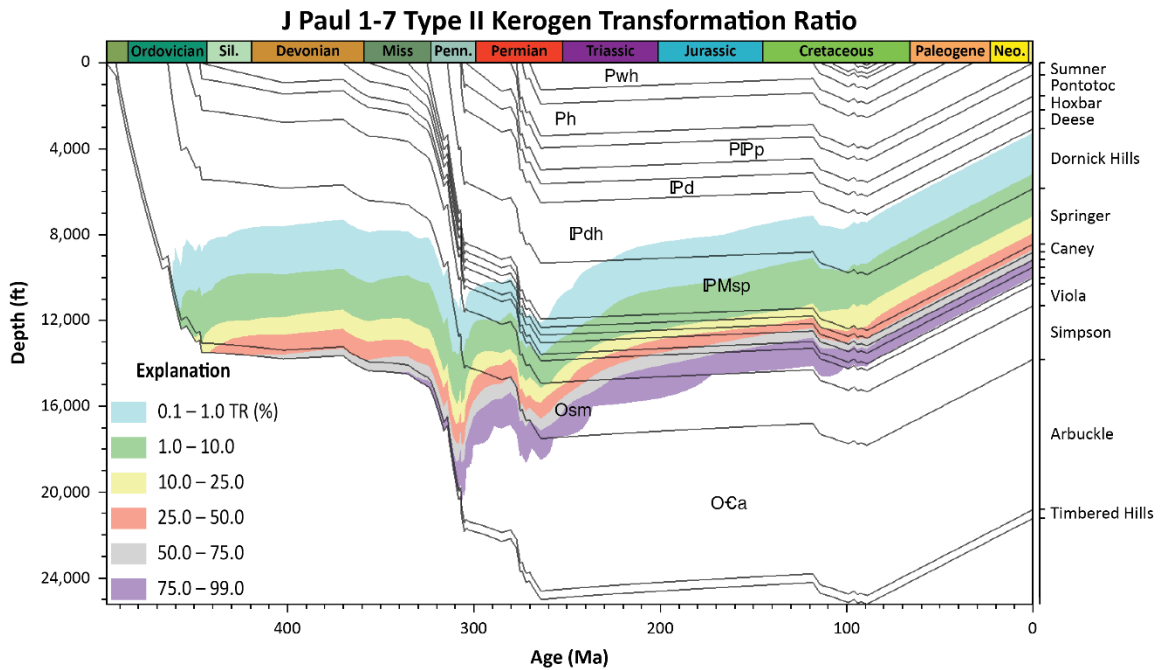


**Figure 76.** Burial history model of the Hays 1-1H well showing how transformation ratio (TR) for Type II kerogen evolved through geologic time and burial. Transformation ratio was calculated using hydrous pyrolysis kinetics for type II kerogen (Lewan and Ruble, 2002).

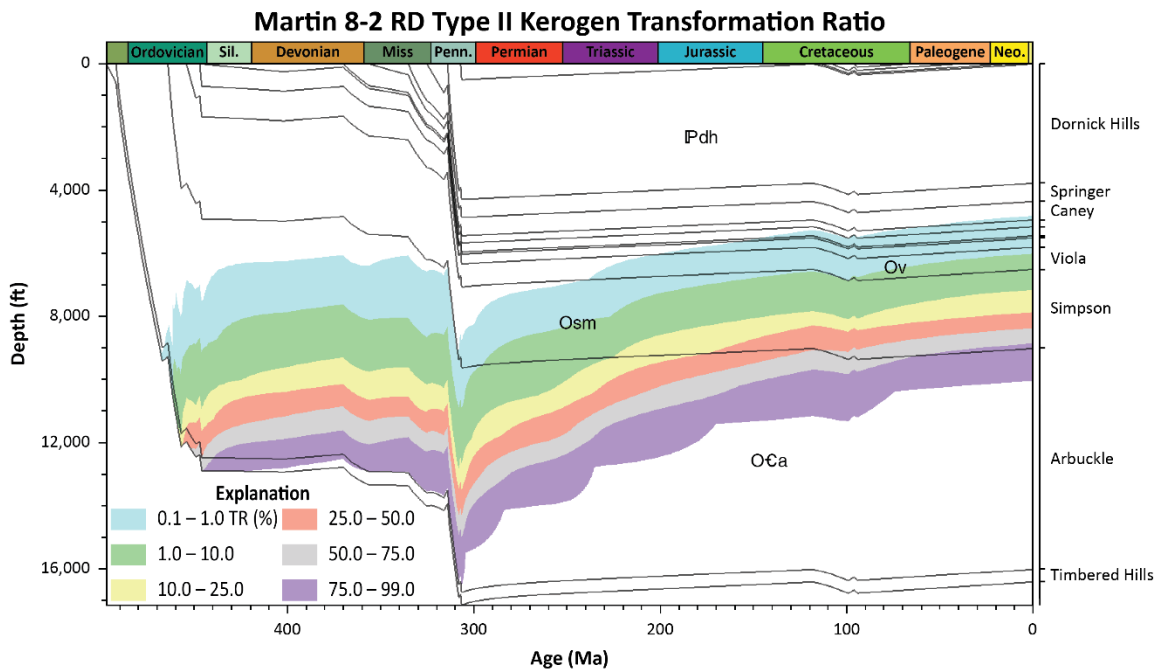


**Figure 77.** Burial history model of the J Little A-1-6 well showing how transformation ratio (TR) for Type II kerogen evolved through geologic time and burial. Transformation ratio was calculated using hydrous pyrolysis kinetics for type II kerogen (Lewan and Ruble, 2002).

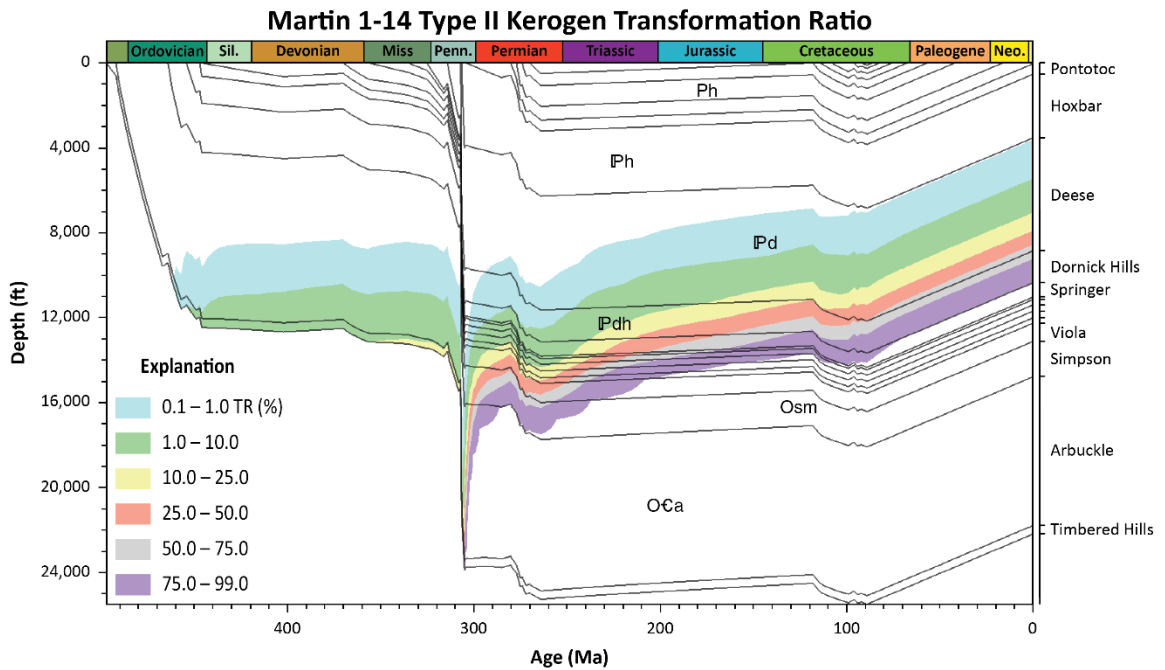




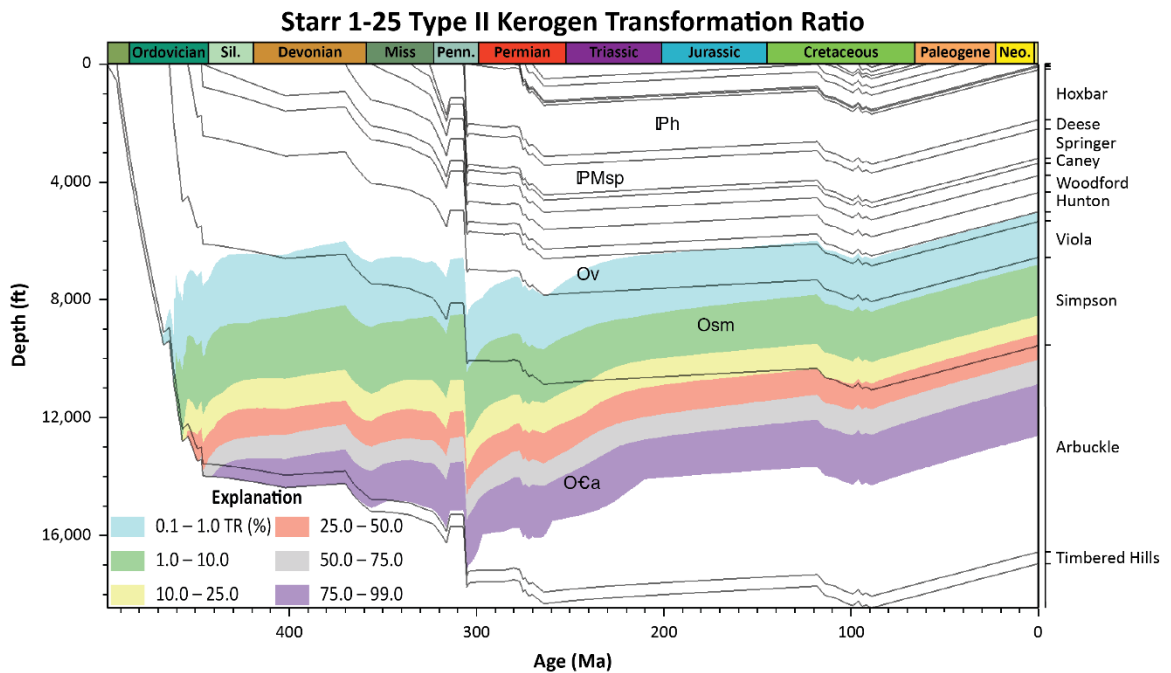
**Figure 78.** Burial history model of the J Paul 1-7 well showing how transformation ratio (TR) for Type II kerogen evolved through geologic time and burial. Transformation ratio was calculated using hydrous pyrolysis kinetics for type II kerogen (Lewan and Ruble, 2002).



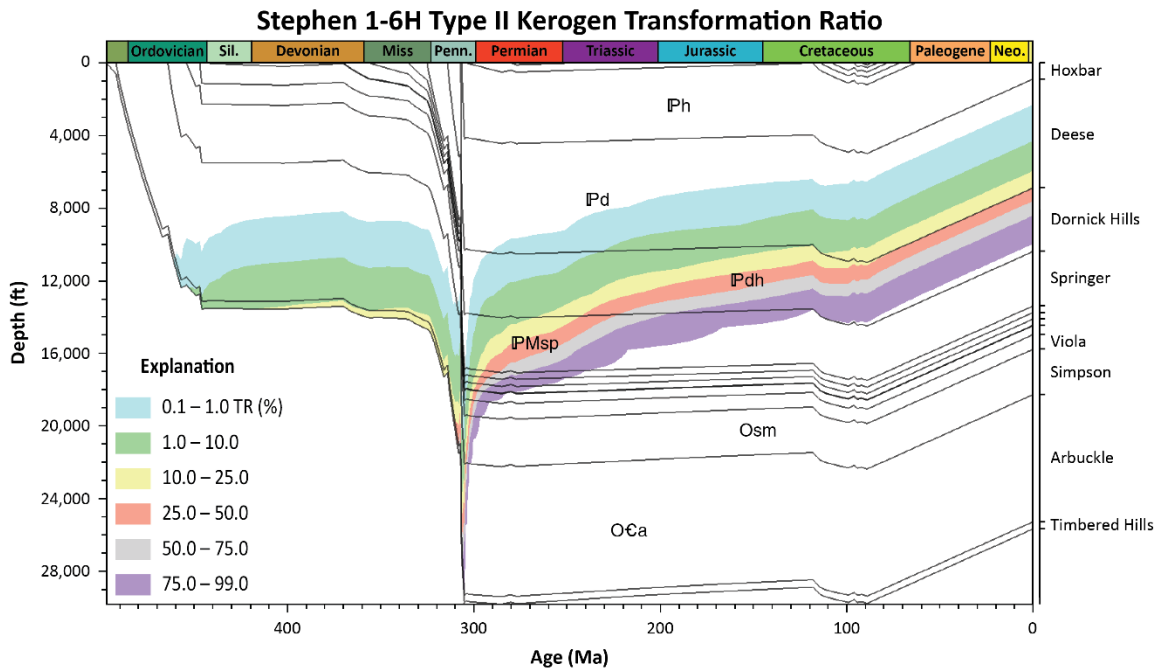
**Figure 79.** Burial history model of the Martin 8-2 RD well showing how transformation ratio (TR) for Type II kerogen evolved through geologic time and burial. Transformation ratio was calculated using hydrous pyrolysis kinetics for type II kerogen (Lewan and Ruble, 2002).



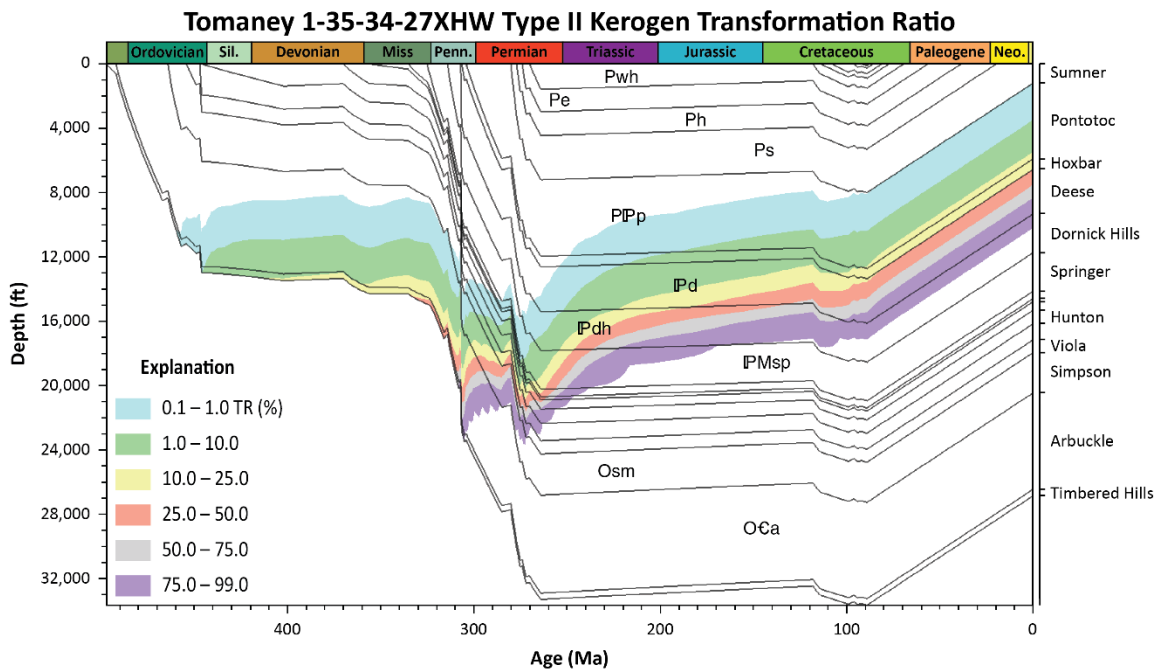
**Figure 80.** Burial history model of the Martin 1-14 well showing how transformation ratio (TR) for Type II kerogen evolved through geologic time and burial. Transformation ratio was calculated using hydrous pyrolysis kinetics for type II kerogen (Lewan and Ruble, 2002).



**Figure 81.** Burial history model of the Starr 1-25 well showing how transformation ratio (TR) for Type II kerogen evolved through geologic time and burial. Transformation ratio was calculated using hydrous pyrolysis kinetics for type II kerogen (Lewan and Ruble, 2002).

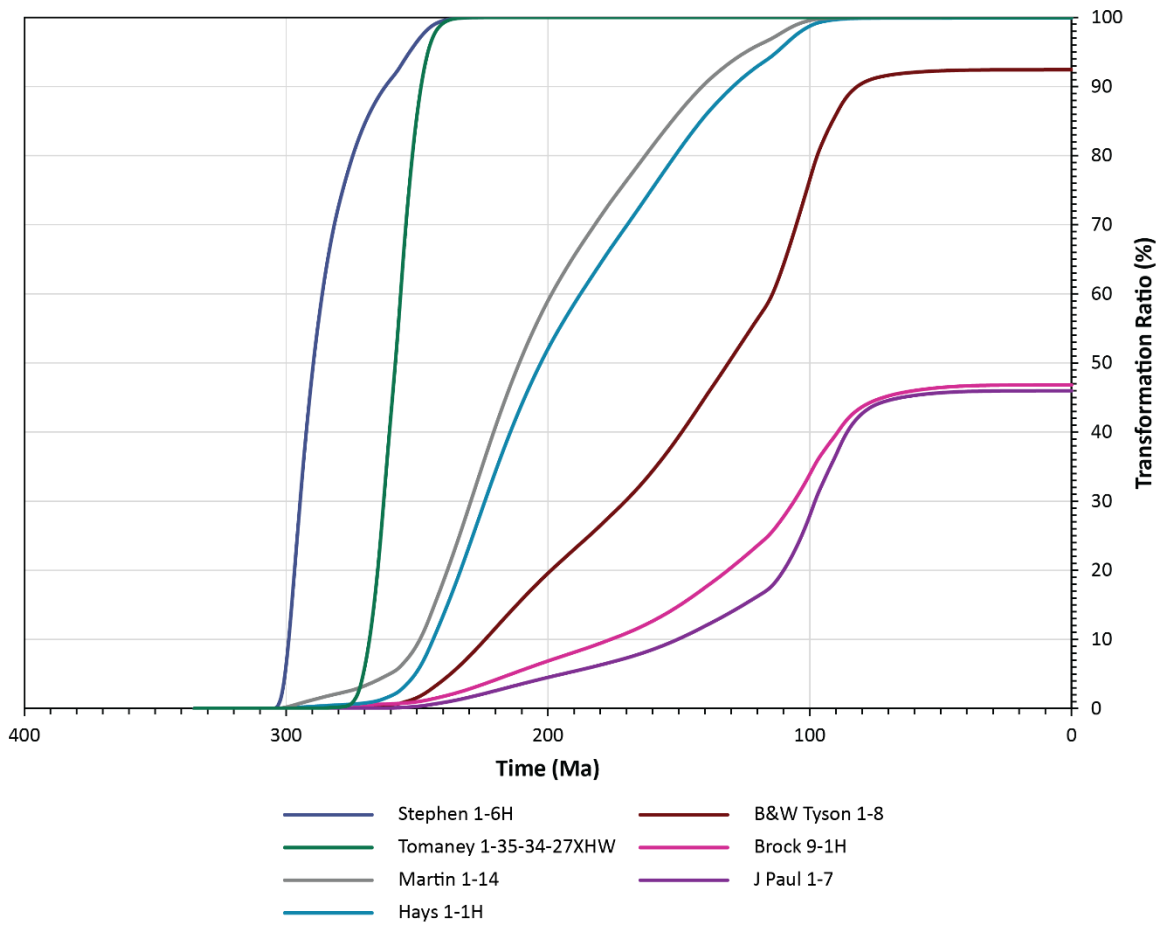


**Figure 82.** Burial history model of the Stephen 1-6H well showing how transformation ratio (TR) for Type II kerogen evolved through geologic time and burial. Transformation ratio was calculated using hydrous pyrolysis kinetics for type II kerogen (Lewan and Ruble, 2002).



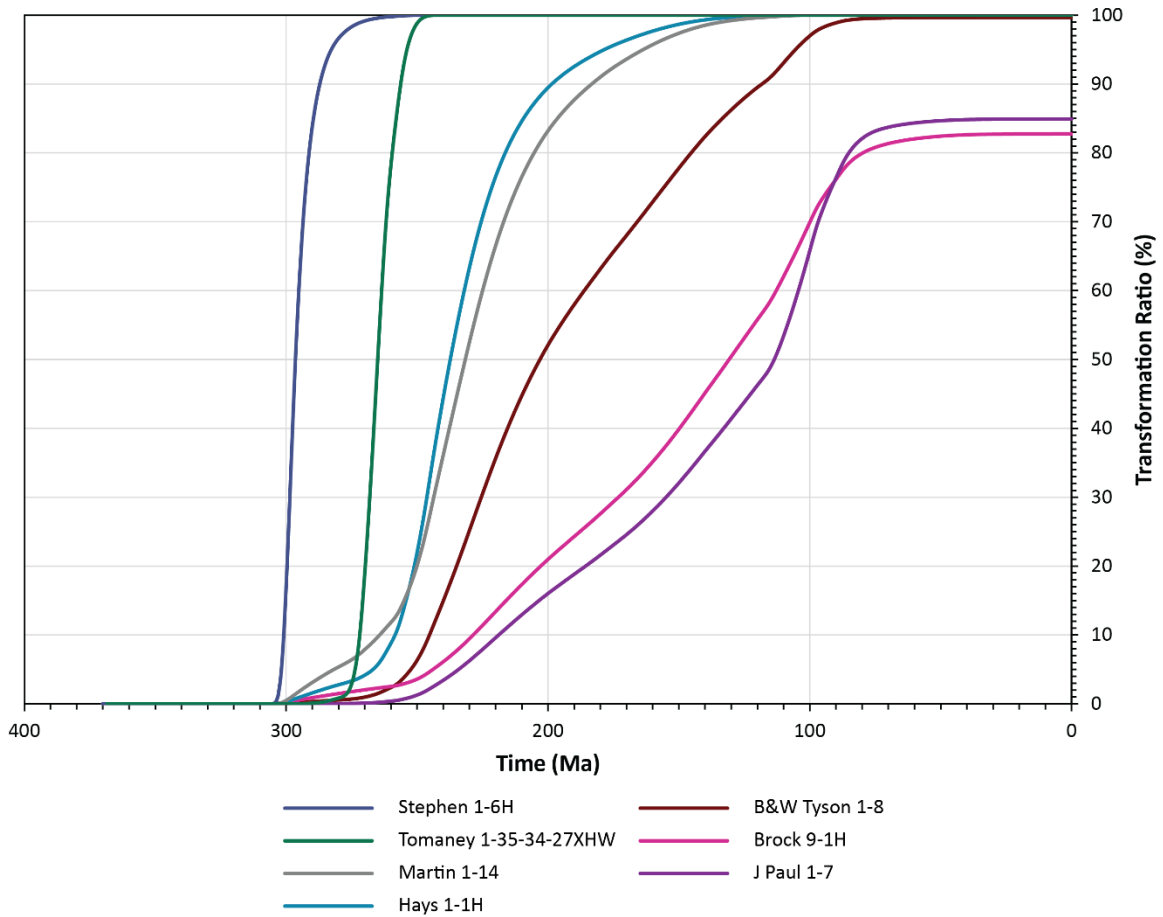
**Figure 83.** Burial history model of the Tomaney 1-35-34-27XHW well showing how transformation ratio (TR) for Type II kerogen evolved through geologic time and burial. Transformation ratio was calculated using hydrous pyrolysis kinetics for type II kerogen (Lewan and Ruble, 2002).

### Caney Shale Transformation Ratio (Type II Kerogen) vs. Time



**Figure 84.** Time vs. transformation ratio plot showing how oil was generated from the Caney Shale through geologic time in seven wells. Transformation ratio was calculated using Woodford Shale hydrous pyrolysis kinetics for type II kerogen (Lewan and Ruble, 2002).

### Woodford Shale Transformation Ratio (Type II Kerogen) vs. Time



**Figure 85.** Time vs. transformation ratio plot showing how oil was generated from the Woodford Shale through geologic time for seven wells. Transformation ratio was calculated using Woodford Shale hydrous pyrolysis kinetics for type II kerogen (Lewan and Ruble, 2002).

**Table 7.** Modeled time vs. transformation ratio (type II kerogen) results for the Woodford and Caney Shales in the Ardmore Basin.

Well Name	Present-Day Type II Kerogen Transformation Ratio (%)		Time of Onset of Oil Generation (Ma)		Time of Peak Oil Generation (Ma)		Time of 100% Oil Generation (Ma)	
	Caney	Woodford	Caney	Woodford	Caney	Woodford	Caney	Woodford
B&W TYSON 1-8	92	100	283 (Permian)	298 (Permian)	132 (Cretaceous)	203 (Triassic)	NA	79 (Cretaceous)
TOMANEY 1-35-34-27XHW	100	100	283 (Permian)	289 (Permian)	258 (Permian)	265 (Permian)	226 (Triassic)	241 (Triassic)
J LITTLE A-1-6	0	0	NA	NA	NA	NA	NA	NA
BADGER 2-23	0	0	NA	NA	NA	NA	NA	NA
BROCK 9-1H	47	83	298 (Permian)	302 (Pennsylvanian)	NA	131 (Cretaceous)	NA	NA
DANSBY 1-3H	1	2	88 (Cretaceous)	91 (Cretaceous)	NA	NA	NA	NA
J PAUL 1-7	46	85	259 (Permian)	271 (Permian)	NA	114 (Cretaceous)	NA	NA
MARTIN 8-2 RD	0	0	NA	NA	NA	NA	NA	NA
STARR 1-25	0	0	NA	NA	NA	NA	NA	NA
MARTIN 1-14	100	100	301 (Pennsylvanian)	302 (Pennsylvanian)	211 (Triassic)	231 (Triassic)	49 (Paleogene)	97 (Cretaceous)
STEPHEN 1-6H	100	100	304 (Pennsylvanian)	304 (Pennsylvanian)	290 (Permian)	297 (Permian)	224 (Triassic)	246 (Triassic)
HAYS 1-1H	100	100	298 (Permian)	302 (Pennsylvanian)	203 (Triassic)	237 (Triassic)	93 (Cretaceous)	102 (Cretaceous)

Onset of oil generation occurs at a transformation ratio of 0.10%

Peak oil generation occurs at a transformation ratio of 50%.

100% oil generation occurs at a transformation ratio of 100%.

NA = Not applicable

**Table 8.** Modeled depth vs. transformation ratio (type II kerogen) results for the Woodford and Caney Shales.

Well Name	Depth at Onset of Oil Generation (ft)		Depth at Peak Oil Generation (ft)		Depth at 100% Oil Generation (ft)	
	Caney	Woodford	Caney	Woodford	Caney	Woodford
B&W TYSON 1-8	11,480	12,082	13,639	14,627	NA	14,831
TOMANEY 1-35-34-27XHW	14,924	14,777	20,448	21,011	20,334	21,105
J LITTLE A-1-6	NA	NA	NA	NA	NA	NA
BADGER 2-23	NA	NA	NA	NA	NA	NA
BROCK 9-1H	11,693	12,375	NA	11,866	NA	NA
DANSBY 1-3H	9,480	9,084	NA	NA	NA	NA
J PAUL 1-7	12,107	12,010	NA	12,856	NA	NA
MARTIN 8-2 RD	NA	NA	NA	NA	NA	NA
STARR 1-25	NA	NA	NA	NA	NA	NA
MARTIN 1-14	12,053	12,534	13,689	14,225	12,904	14,664
STEPHEN 1-6H	16,980	17,745	17,181	17,875	17,072	17,904
HAYS 1-1H	12,061	12,877	15,010	15,997	15,654	16,401

**Table 9.** Modeled temperature vs. transformation ratio (type II kerogen) results for the Woodford and Caney Shales.

Well Name	Temperature at Onset of Oil Generation (°F)		Temperature at Peak Oil Generation (°F)		Temperature at 100% Oil Generation (°F)	
	Caney	Woodford	Caney	Woodford	Caney	Woodford
B&W TYSON 1-8	201	215	255	258	NA	205
TOMANEY 1-35-34-27XHW	214	214	279	284	299	310
J LITTLE A-1-6	NA	NA	NA	NA	NA	NA
BADGER 2-23	NA	NA	NA	NA	NA	NA
BROCK 9-1H	212	221	NA	255	NA	NA
DANSBY 1-3H	220	209	NA	NA	NA	NA
J PAUL 1-7	209	209	NA	259	NA	NA
MARTIN 8-2 RD	NA	NA	NA	NA	NA	NA
STARR 1-25	NA	NA	NA	NA	NA	NA
MARTIN 1-14	226	231	261	267	259	295
STEPHEN 1-6H	235	246	275	286	297	301
HAYS 1-1H	215	225	259	270	286	299

For all models that indicate any oil generation in the Woodford and/or Caney Shales, initiation of primary cracking typically occurred during the Late Pennsylvanian–Permian; however, cracking of kerogen was initiated as late as the Cretaceous in the Dansby 1-3H model (Table 7). Transformation percentages of 100% for both the Woodford and Caney Shales in the Tomaney 1-35-34-27XHW, Martin 1-14, Stephen 1-6H, and Hays 1-1H wells were attained during the Triassic–Paleogene (Figures 84 and 85; Table 7). In these models, Devonian–Mississippian source rocks underwent significant Pennsylvanian–Permian burial (averaging about 17,000 ft) and were subjected to temperatures greater than 250°F at completion of oil generation (Table 9).

Transformation ratios of 100% for the Woodford and Caney Shales were attained during the Middle and Late Triassic, respectively, in the Tomaney 1-35-34-27XHW and Stephen 1-6H models, which are the earliest of any models (Figures 84 and 85; Table 7). The Tomaney 1-35-34-27XHW and Stephen 1-6H models contain the thickest Pennsylvanian–Permian sections (averaging about 19,000 ft). In these models, the Woodford and Caney Shales were exposed to a temperature around 300°F at completion of oil generation (Table 9).

Complete transformation of Woodford Shale kerogen occurred during the Cretaceous in the B&W Tyson 1-8, Martin 1-14, and Hays 1-1H models, which is the latest time for completion of oil generation in the Woodford Shale (Figure 85; Table 7). These models have low present-day heat flow averaging about 44 mW/m<sup>2</sup> (Table 4), as well as thick modeled Pennsylvanian and Permian sections averaging about 15,000 ft. The latest time for Caney Shale kerogen to reach complete transformation was the Paleogene at a relatively shallow depth of 12,904 ft and a temperature of 259°F in the Martin 1-14 model (Figure 84; Tables 7–9).

Partial transformation of kerogen was modeled in Woodford and Caney source rocks in the Brock 9-1H, Dansby 1-3H, and J Paul 1-7 wells (Figures 85 and 86; Table 7). In the B&W Tyson 1-8 well, petroleum generation has concluded in the Woodford Shale but not in the Caney Shale, which has a transformation ratio of 92% (Figures 85 and 86; Table 7). The B&W Tyson 1-



8 model has a modest present-day heat flow of 44 mW/m<sup>2</sup> (Table 4) and thick Pennsylvanian and Permian sections with a collective paleothickness of about 15,500 ft. The temperature at completion of Woodford Shale oil generation in the B&W Tyson 1-8 model was 205°F (Table 9), which is the lowest of any model.

For the Brock 9-1H model, present-day transformation ratio is 83% for the Woodford Shale and 47% for the Caney Shale (Figures 84 and 85; Table 7). Unlike the B&W Tyson 1-8 model, the Brock 9-1H model has a relatively high present-day heat flow of 50 mW/m<sup>2</sup>, a partial modeled Pennsylvanian section (no Hoxbar Group), and no modeled Permian deposition (Table 4).

Essentially no petroleum has been generated in the Dansby 1-3H model with present-day transformation ratios less than 10% in the Woodford and Caney Shales (Table 7). The Dansby 1-3H model has a present-day heat flow of 47 mW/m<sup>2</sup> (Table 4), a partial Pennsylvanian depositional section (no Hoxbar Group), and no Permian deposition.

In the J Paul 1-7 model, present-day transformation ratios are 85% in the Woodford Shale and 46% in the Caney Shale (Figures 84 and 85; Table 7). Like the B&W Tyson 1-8 model, the J Paul 1-7 model has a modest present-day heat flow of 44 mW/m<sup>2</sup> (Table 4) but thick Pennsylvanian and Permian deposition with a collective paleothickness of about 12,300 ft.

## CHAPTER V

### DISCUSSION

#### **Basin Tectonism**

Observed burial history events correspond to major tectonic events. Subsidence during Cambrian–Ordovician time is indicative of decay of the Iapetan rift-related thermal regime. Subsidence was likely driven by thermal and isostatic subsidence of the Cambrian–Silurian carbonate bank. By Devonian–Late Mississippian time, the crust had cooled substantially, resulting in diminished rates of subsidence and associated sediment accumulation. Effective subsidence rates (without correction for compaction), on average, decreased from about 250 ft/m.y. during the Cambrian–Ordovician to about 20 ft/m.y. during the Silurian–Late Mississippian.

Rapid pulses of subsidence (~750 ft/my), initiated during the Late Mississippian and continuing at least through the Pennsylvanian, appear to be synorogenic, coinciding with sequential uplift of the Wichita Mountains (Morrowan–Atokan) and then the Arbuckle Mountains (Virgilian). In contrast to voluminous sediment deposition during the Pennsylvanian and Permian, the Triassic and Jurassic periods are characterized by a hiatus as the Ardmore Basin and surrounding region were subaerially exposed. Deposition of Late Cretaceous sediment and

associated subsidence during the Cretaceous–Paleogene reflects encroachment of the margin of the Gulf of Mexico Basin on the study area.

Iapetan rifting appears to have uniformly affected the region that was to become the Ardmore Basin. Early Paleozoic units are interregional, and all burial history models display comparable sediment thickness (~11,000 ft), and hence comparable rates and magnitudes of Cambrian–Ordovician subsidence.

All of the Ardmore Basin underwent major pulses of subsidence during Pennsylvanian deformation. Episodes of Pennsylvanian subsidence are related to orogenic events, unconformities, and periods of sediment deposition. The first Wichitan Orogeny (Morrowan), second Wichitan Orogeny (Late Atokan), and Arbuckle Orogeny (Virgilian) (Huffman et al., 1978) correspond to modeled Pennsylvanian unconformities and subsidence events at 314, 307, and 304 Ma, respectively. Springer (Chesterian–Morrowan) deposition occurred during the first Wichitan Orogeny. Dornick Hills (Atokan–Desmoinesian) and Deese (Desmoinesian) deposition occurred during the second Wichitan Orogeny. Deposition of the Hoxbar (Missourian) and Wolfcampian–Guadalupian units occurred during the Arbuckle Orogeny.

Rapid Pennsylvanian subsidence indicates the Ardmore Basin functioned as an elevator basin, which is typical of sedimentary basins in oblique-slip mobile zones. Although Pennsylvanian subsidence rates were comparable throughout the basin, magnitudes of subsidence were certainly greater behind major uplifts, such as the Arbuckle Mountains and Wichita Uplift. For instance, the Berwyn Syncline, adjacent to the Arbuckle Uplift and Arbuckle Mountains, is the deepest part of the basin and evidently underwent several thousand feet of subsidence during the Pennsylvanian. Subsidence was apparently load-induced, seemingly driven by thrust loading in the peripheral highlands and subsequent sediment loading.

Effects of the distal Late Cretaceous–Early Paleogene Sevier and Laramide Orogenies on the Ardmore Basin were minimal. Orogenic influences appear to have been more pronounced in the west and uplift was likely expressed as a regional south-southeastward tilt associated with

development of the Gulf of Mexico Basin. This regional incline is still exhibited today as surface elevation decreases from northwest to southeast across the Ardmore Basin.

### **Sedimentation**

Thermal subsidence during the Cambrian–Ordovician appears to have provided space to accommodate deposition of thick (~11,000 ft) early Paleozoic carbonate units. Decreasing subsidence rates during the Devonian–Mississippian resulted in deposition of thinner, mixed siliciclastic and units. The modeled Devonian–Mississippian section ranges in thickness from 870 ft in the Badger 2-23 well to 2,019 ft in the Tomaney 1-35-34-27XHW well. Appearance of siliciclastic sediment coincides with incipient uplift of peripheral highlands such as the Arbuckle Mountains; however, sediment was likely sourced from the Appalachian and Ancestral Rocky Mountains as well. Intervening periods of nondeposition and erosion during the Paleozoic can account for variations in stratigraphic thicknesses.

The Pennsylvanian section appears to have been unequally deposited throughout the Ardmore Basin as some models in the east (Marshall and Bryan Counties) and models proximal to paleo structural highs have partial Pennsylvanian stratigraphic sections. All these models lack the Hoxbar Group, which helps date the uplifts. It is proposed that uplift of structures within the Ardmore Basin and surrounding region began to outpace the rate of deposition during the Missourian and Virgilian. Uplift resulted in localized topographic highlands that were apparently deprived of Hoxbar and possibly some Deese sediment.

Like the Pennsylvanian section, Permian sediment appears to have been irregularly distributed in the Ardmore Basin. Structural highs appear to be devoid of Permian sediment. As

such, structures that protruded above sea level during the Pennsylvanian, likely remained topographically high during the Permian.

Permian strata appear to thin southeastward away from the Anadarko Basin by depositional thinning as well as erosional truncation. It is suggested that Permian sediment was never deposited in the eastern Ardmore Basin, and the present-day eastern extent of Permian strata was near the limit of original deposition. The Ouachita Mountains and adjacent foreland are thought to have achieved significant elevation during the Permian such that the eastern Ardmore Basin was elevated above the Permian sea in the west. Additional post-orogenic uplift may have been achieved via flexural rebound and uplift associated with Gulf of Mexico rifting. As previously stated, a Cretaceous sedimentary wedge disconformably overlies Mississippian units in the east (Huffman et al., 1978), suggesting Permian sediment may have never been deposited in the eastern Ardmore Basin. Permian depocenters were positioned along the flanks of structural highs and within synclines in the western Ardmore basin. By end of the Paleozoic, the region apparently was being eroded.

Stratigraphic evidence suggests no sediment deposition occurred during the Triassic–Jurassic. There is no evidence in the burial history models to suggest extensive erosion during the Triassic and Jurassic either, but it is suspected structures were exposed and weathering. Permian deposition coupled with Triassic–Jurassic erosion likely reduced topographic relief and produced a broad landscape that was in some measure comparable topographically to that seen today.

By the Early Cretaceous, the majority of the Ardmore Basin was at or close to sea level. Cretaceous strata of the Gulf of Mexico Coastal Plain are only present in the southeastern part of the basin, although they almost certainly blanketed southern Oklahoma in accordance with paleogeographic reconstructions of the Gulf of Mexico and the Cretaceous Western Interior Seaway (Scotese, 2002). Geologic mapping, well records, and burial history models indicate the Cretaceous sedimentary wedge thickened southeastward.

As stated above, post-Cretaceous deposition was not required for calibration of any burial history model. Sediment was shed from the Rocky Mountains to the west and deposited in western Oklahoma as part of an extensive alluvial plain during the Tertiary (e.g., the Ogallala Formation) (Johnson, 2008; Suneson, 2020), but there is no evidence to suggest these deposits made it as far east as the Ardmore Basin. Therefore, the Cenozoic is characterized principally as a time of hiatus and erosion.

### **Erosion**

Effects of the Laramide Orogeny on the Ardmore Basin were minimal and may have included minor uplift of the region and associated erosion.

As discussed, the eroded overburden section was not uniformly distributed, since Pennsylvanian-Permian uplifts, such as the Arbuckle Mountains, had significantly less sediment cover than the Ardmore Basin proper. Accordingly, post-Pennsylvanian erosional thickness on structural highs is less than that in the basin's synclinal structures due to greater exposure to weathering. However, an equivalent section of older Paleozoic strata was subjected to erosion on structural highs as evidenced by syntectonic conglomerate units containing abundant Cambrian-Devonian carbonate clasts (Huffman et al., 1978). On average, burial history model calibration required about 5,000 ft of post-orogenic erosion, which is consistent with the projection of the vitrinite reflectance-depth plot (Figure 43).

## **Heat Flow**

Present-day basement heat flow is relatively uniform throughout the Ardmore Basin and appears to be driven by conduction and convection rather than fluid movement (advection). Modeling of heat flow types can be completed via three-dimensional modeling and should be considered in future work. Steady, moderate heat flow is indicative of the stable thermal regime that prevails east of the Rocky Mountains which is consistent with cool, tectonically-inactive sedimentary basins. It is suggested heat flow is slightly greater on structural highs (up to 58 mW/m<sup>2</sup>) with shallow basement than within synclines because underlying basement igneous rocks typically have higher thermal conductivity than sedimentary rocks.

## **Thermal Maturation**

The Devonian–Mississippian Woodford Shale and Mississippian Caney Shale were quickly buried following deposition throughout most of the Ardmore Basin. Burial depth was dependent on structural position as structural highs received less sediment than synclinal structures. Accordingly, thermal maturity of these source rocks is strongly dependent on structural position, with immature strata preserved in uplifts and highly mature strata preserved in synclines. Because heat flow and geothermal gradient are relatively uniform throughout the Ardmore Basin, burial depth was evidently the dominant variable determining source rock maturity. Source rocks typically began to generate oil once buried to a depth greater than 9,000 ft (Table 8) and subjected to temperatures greater than 200°F (Table 9). After burial, source rocks only resurfaced in the flanks of regional uplifts such as the Arbuckle Mountains and Arbuckle

Uplift. Caney and Woodford Shale outcrops on these topographic highlands are immature due to rapid uplift, which resulted in insufficient burial depth.

Pennsylvanian–Permian deposition was very important for maturation of Paleozoic source rocks in the Ardmore Basin. Devonian–Mississippian source rocks are immature or marginally mature at localities where there apparently was little or no Permian deposition, such as the eastern Ardmore Basin. An exception is the Berwyn Syncline which received minor Permian deposition but was buried very deeply during the Pennsylvanian (>20,000 ft).

The wholesale shift to effective nondeposition during the Triassic and Jurassic had little effect on the thermal maturity of Caney and Woodford source rocks. Once buried, source rocks continued to steadily mature as evidenced by isomaturity lines that are oblique to bedding (Figures 59–70). Likewise, the deposited Cretaceous section was thin (never exceeding 4,500 ft) and had no more than a minor influence on source rock maturity in the Ardmore Basin. Burial during the Cretaceous only slightly increased the maturity of source rocks in the far eastern part of the basin where the Cretaceous section appears to have been thickest.

Thermal maturity is a function of time and temperature, the latter of which is highly dependent on burial depth in the Ardmore Basin. The same thermal maturity can be achieved by a source rock that was deeply buried and exposed to high temperature for a short time, as by a source rock that was not as deeply buried and exposed to a lower temperature for a longer period of time. An example of this is that while burial and thermal history models show no additional burial or subsidence during the Triassic and Jurassic, the Woodford and Caney Shales continued to mature as respective isomaturity lines rise relative to stratigraphic boundaries in all models.



## Hydrocarbon Generation

Oil generation in the Woodford and Caney source rocks from type II kerogen was initiated at different times and occurred at different rates. In most of the Ardmore Basin, oil generation began during the Late Pennsylvanian following substantial burial (Tables 7 and 8). Rapid burial correlates with high rates of petroleum generation. Devonian–Mississippian source rocks quickly attained 100% transformation in the Triassic where buried by thick (<19,000 ft) Pennsylvanian and Permian sections and subjected to temperatures greater than 300°F (Tables 7–9). Slower generation occurred where there was little or no Permian deposition, such as in the eastern Ardmore Basin. Accordingly, rates and magnitudes of Pennsylvanian and Permian deposition as well as sustained burial appear to have played an integral role in the timing of petroleum generation. Cretaceous deposition had only a minor effect on oil generation, considering that the Woodford and Caney Shales approached present-day transformation ratios before the Late Cretaceous (Figures 84 and 85; Table 7).

## CHAPTER VI

### CONCLUSION

All burial history models display a similar decelerating subsidence history during and following Cambrian Iapetan rifting, tectonic stability during a passive margin phase from the Silurian–Late Mississippian, synorogenic subsidence during the Pennsylvanian, inception of a mature basin following the Permian, and Gulf of Mexico Coastal Plain subsidence during the Cretaceous and perhaps into the Paleogene. Rapid Pennsylvanian subsidence appears to be synchronous with sequential uplift of the Wichita Mountains and then the Arbuckle Mountains in response to major left-lateral transpression. The rapidity of Pennsylvanian subsidence suggests that the Ardmore Basin functioned episodically as an elevator basin, which is typical of sedimentary basins in oblique-slip mobile zones (e.g., the Paradox Basin) (Baars and Stevenson, 1981).

A source of uncertainty is modeling erosion of the post-Pennsylvanian section, which is only partially preserved. Calibration of these models to honor measured thermal maturity data requires erosion of approximately 5,000 ft of Pennsylvanian and younger strata. The eroded overburden section was not uniformly distributed, as areas of high structural relief, such as the Arbuckle Uplift, appear to have had significantly less sediment cover than the basin proper. Regional variation of the thickness of eroded Permian sediment, which apparently formed a

wedge that thickened toward the Anadarko Basin, and the Cretaceous-Paleogene Gulf of Mexico sedimentary wedge, which apparently thickened southeastward, affected the burial and maturation history of the Ardmore Basin. There is no evidence to support significant deposition of Tertiary sediment in the Ardmore Basin.

Vitrinite reflectance and thermal gradients were calibrated to measured vitrinite reflectance and temperature data (corrected bottom-hole temperatures) respectively, to ensure model validity. The Devonian-Mississippian shale section has a broad range of thermal maturity ranging from immature ( $\%R_o < 0.6$ ) to the dry gas window ( $\%R_o > 2.0$ ). Thermal maturity is strongly dependent on structural position, with immature strata preserved in uplifts and highly mature strata preserved in synclines. Effects of Cretaceous deposition on maturity are negligible throughout much of the Ardmore Basin except for models in the far eastern part of the basin (Marshall and Bryan Counties) where a thicker Cretaceous section appears to have been deposited. Burial depth is evidently the dominant variable for determining source rock maturity as the Ardmore Basin has relatively uniform heat flow and geothermal gradient. Additionally, post-Permian tectonic dormancy allows for predictable Paleozoic source rock maturity.

Present-day basement heat flow in the Ardmore Basin averages  $46 \text{ mW/m}^2$ . Heat flow is slightly greater (up to  $58 \text{ mW/m}^2$ ) on structural highs with shallow basement and thin sediment cover than within synclines because underlying basement igneous rocks typically have higher thermal conductivity than sedimentary rocks. This thermal regime is consistent with a cool, tectonically-inactive basin.

In most of the Ardmore Basin, oil generation from the Woodford and Caney Shales was initiated during the Late Pennsylvanian and Permian following substantial burial. Rates and magnitudes of Pennsylvanian and Permian deposition as well as sustained burial appear to have played an integral role in the timing and duration of hydrocarbon generation. Cretaceous deposition had only a minor effect on petroleum generation as kerogen in the Woodford and Caney Shales approached present-day transformation ratios before the Late Cretaceous.

This study confirms that burial history modeling is an effective, economical approach for forecasting potential source rock maturity and minimizing exploration risk. Models indicate that Pennsylvanian deformation and late Paleozoic sediment deposition played an integral role in the thermal maturation of the Woodford and Caney Shales. The well-constrained maturity of the Woodford Shale can be used as a proxy for predicting maturity of the Caney Shale. The Caney Shale resides in appropriate maturity windows to produce economic quantities of oil and gas in the vast majority of the Ardmore Basin.

### **Future Work**

1D basin modeling is a quick and economically-advantageous method for constraining subsidence, source rock maturity, petroleum generation, and thermal history of a basin. A 1D model can be created with a well log which is typically available in a basin study. 1D basin modeling is limited in that a model only represents a single point in a basin and thus may not be (and likely is not) reflective of the entire basin. This project compensates for these limitations by using several 1D basin models, scattered throughout the Ardmore Basin, to capture regional variations in burial and thermal history.

Two and three-dimensional (2D and 3D) basin modeling should be considered for future work because they offer multi-dimensional control using the same parameters that are used for 1D models. This is especially useful for modeling fluid flow, such as petroleum migration, heat flow, and subsidence at a basin scale. Multi-dimensional models are still imperfect, however, in that they typically require proprietary material such as seismic data and are computationally intensive.

Although transformation ratios for type II kerogen were modeled in this study, modeling secondary cracking of oil to gas is advised. The Caney Shale is deep enough in the Ardmore Basin and achieves high enough thermal maturity to indicate that some kerogen directly generated gas and some oil has cracked to gas.

## REFERENCES

- Al-Hajeri, M.M., Al Saeed, M., Derks, J., Fuchs, T., Hantschel, T., Kauerauf, A., and Welte, D., 2009, Basin and petroleum system modeling: *Oilfield Review*, v. 21, no. 2, p. 14–29.
- Amati, L., and Westrop, S.R., 2006, Sedimentary facies and trilobite biofacies along an Ordovician shelf to basin gradient, Viola Group, South-Central Oklahoma: *PALAIOS*, v. 21, p. 516–529, doi: 10.2110/palo.2006.p06-069.
- Andrews, R.D., 2007, Stratigraphy, production, and reservoir characteristics of the Caney Shale in southern Oklahoma: *Shale Shaker*, v. 58, p. 9–25.
- Baars, D.L., and Stevenson, G.M., 1981, Tectonic evolution of the Paradox basin, Utah and Colorado, *in* Wiegand, D.L., ed., *Geology of the Paradox basin: Denver, Colorado, Rocky Mountain Association of Geologists, 1981 Field Conference Guidebook*, p. 23–31.
- Bickford, M.E., and Lewis, R.D., 1979, U-Pb geochronology of exposed basement rocks in Oklahoma: *Geological Society of America Bulletin*, v. 90, p. 540, doi: 10.1130/0016-7606(1979)90<540:ugoebr>2.0.co;2.
- Blackwell, D.D., Richards, M.C., Frone, Z.S., Batir, J.F., Williams, M.A., Ruzo, A.A., and Dingwall, R.K., 2011, SMU geothermal laboratory heat flow map of the conterminous United States, 2011, <http://www.smu.edu/geothermal> (accessed 20 October 2020).
- Bowring, S.A., Hoppe, W.J., 1982, U–Pb zircon ages from Mount Sheridan Gabbro, Wichita Mountains, *in* Gilbert, M.C., Donovan, R.N., eds., *Geology of the Eastern Wichita Mountains, Southwestern Oklahoma: Oklahoma Geological Survey Guide-book*, 21, p. 54–59.
- Brewer, J.A., Good, R., Oliver, J.E., Brown, L.D., and Kaufman, S., 1983, COCORP profiling across the southern Oklahoma aulacogen: Overthrusting of the Wichita Mountains and compression within the Anadarko basin: *Geology*, v. 11, p. 109–114, doi: 10.1130/0091-7613(1983)11<109:cpatso>2.0.co;2.
- Brown, A., 2002, Petroleum charge to the Mill Creek Syncline and adjacent areas, southern Oklahoma: *Oklahoma Geological Survey Circular* 107, p. 17–36.

- Brueseke, M.E., Hobbs, J.M., Bulen, C.L., Mertzman, S.A., Puckett, R.E., Walker, J.D., and Feldman, J., 2016, Cambrian intermediate-mafic magmatism along the Laurentian margin: Evidence for flood basalt volcanism from well cuttings in the Southern Oklahoma aulacogen (USA): *Lithos*, v. 260, p. 164–177, doi: 10.1016/j.lithos.2016.05.016.
- Burke, K., and Dewey, J.F., 1973, Plume-generated triple junctions: Key indicators in applying plate tectonics to old rocks: *Journal of Geology*, v. 81, p. 406–433, doi: 10.1086/627882.
- Cardott, B.J., 1989, Thermal maturation of the Woodford Shale in the Anadarko basin, *in* Johnson, K.S., ed., Anadarko basin symposium, 1988: Oklahoma Geological Survey Circular 90, p. 32–46.
- Cardott, B.J., 2007, Overview of Woodford gas-shale play in Oklahoma: Oklahoma Geological Survey, Woodford Gas Shale Conference, May 23, 2007, PowerPoint presentation.
- Cardott, B.J., 2009, Application of vitrinite reflectance to the Woodford gas-shale play in Oklahoma (abstract): AAPG Mid-Continent Meeting Official Program, p. 21.
- Cardott, B.J., 2012, Thermal maturity of Woodford Shale gas and oil plays, Oklahoma, USA: *International Journal of Coal Geology*, v. 103, p. 109–119.
- Cardott, B.J., 2013, Woodford Shale: From hydrocarbon source rock to reservoir: AAPG Search and Discovery Article #50817, 85 slides.
- Cardott, B.J., 2014, Bibliography of Woodford Shale: Oklahoma Geological Survey.
- Cardott, B.J., 2017a, Oklahoma Shale resource plays: *Oklahoma Geology Notes*, v. 76, no. 2, p. 21–30.
- Cardott, B.J., 2017b, Bibliography of Ardmore Basin: Oklahoma Geological Survey.
- Cardott, B.J., 2018, Bibliography of Caney Shale: Oklahoma Geological Survey.
- Cardott, B.J., and J.R. Chaplin, 1993, Guidebook for selected stops in the western Arbuckle Mountains, southern Oklahoma: Oklahoma Geological Survey, Special Publication 93-3, 55 p.
- Cardott, B.J., Metcalf, W.J., III, and Ahern, J.L., 1990, Thermal maturation by vitrinite reflectance of Woodford Shale near Washita Valley fault, Arbuckle Mountains, Oklahoma, *in* Nuccio, V.F., and Barker, C.E., eds., Applications of thermal maturity studies to energy exploration: SEPM, Rocky Mountain Section, p. 139–146.
- Carter, L.S., Kelly, S.A., Blackwell, D.D., and Naeser, N.D., 1998, Heat flow and thermal history of the Anadarko Basin, Oklahoma: *AAPG Bulletin*, v. 82, no. 2, p. 291–316, doi: 10.1306/1d9bc3f9-172d-11d7-8645000102c1865d.

- Climate of Oklahoma, n.d., [https://climate.ok.gov/index.php/site/page/climate\\_of\\_oklahoma](https://climate.ok.gov/index.php/site/page/climate_of_oklahoma) (accessed September 21, 2021).
- Dioniso, L., 1975, Structural Analysis and Mapping of the Eastern Caddo Anticline - Ardmore Basin Oklahoma, *Shale Shaker Digest*, no. 8, p. 95–115.
- Feinstein, S., 1981, Subsidence and thermal history of Southern Oklahoma Aulacogen- Implication for petroleum exploration: *AAPG Bulletin*, v. 65, p. 2521–2533, doi: 10.1306/03b599f9-16d1-11d7-8645000102c1865d.
- Fritz, R.D., Patrick M., Kuykendall, M.J., and Wilson, J.L., 2012, The geology of the Arbuckle Group in the midcontinent: Sequence stratigraphy, reservoir development, and the potential for hydrocarbon exploration, *in* Derby, J.R., Fritz, R.D., Longacre, S.A., Morgan, W.A., and Sternbach, C.A., eds., *The great American carbonate bank: The geology and economic resources of the Cambrian-Ordovician Sauk megasequence of Laurentia*: AAPG Memoir 98, p. 203–273.
- Gesch, D., Evans, G., Mauck, J., Hutchinson, J., Carswell, Jr., W.J., 2009, *The National Map: Elevation*, US Geological Survey Fact Sheet 2009-3053, 4 pp.
- Granath, J.W., 1989, Structural evolution of the Ardmore Basin, Oklahoma: Progressive deformation in the foreland of the Ouachita collision: *Tectonics*, v. 8, p. 1015–1036, doi: 10.1029/tc008i005p01015.
- Ham, W.E., 1969, Regional geology of the Arbuckle Mountains, Oklahoma: Oklahoma Geological Survey Guidebook 17, 52 p.
- Hanson, R.E., Puckett, R.E., Keller, G.R., Brueseke, M.E., Bulen, C.L., Mertzman, S.A., Finegan, S.A., and Mccleery, D.A., 2013, Intraplate magmatism related to opening of the southern Iapetus Ocean: Cambrian Wichita igneous province in the southern Oklahoma rift zone: *Lithos*, v. 174, p. 57–70, doi: 10.1016/j.lithos.2012.06.003.
- Harding, T.P., Gregory, R.F., and Stevens, L.H., 1983, Convergent wrench fault and positive flower structure, Ardmore Basin, Oklahoma *in* Balley, A.W., ed., *Seismic Expression of Structural Styles*: AAPG Studies in Geology, no. 15, v. 3, p 4.2–13–4.1-17.
- Harlton, B.H., 1956, The Harrisburg trough, Stephens and Carter Counties, Oklahoma, *in* Hicks, I.C., Westheimer, J., Thomlinson, C.W., Putman, D.M., and Elk, E.L., eds., *Petroleum geology of southern Oklahoma*: AAPG v. 1, p. 135–143.
- Heran, W.D., Green, G.N., Stoeser, D.B., 2003, A digital geologic map database for the state of Oklahoma. U.S. Geological Survey open-file report 97–23, U.S. Geological Survey, Oklahoma City, <http://pubs.usgs.gov/of/2003/ofr-03-247/> (accessed 20 October 2020).
- Higley, D. K., 2011, Undiscovered petroleum resources for the Woodford Shale and Thirteen Finger limestone: Atoka shale assessment units, Anadarko Basin: U.S. Geological Survey Open-File Report 2011–1242, 3 poster panels.

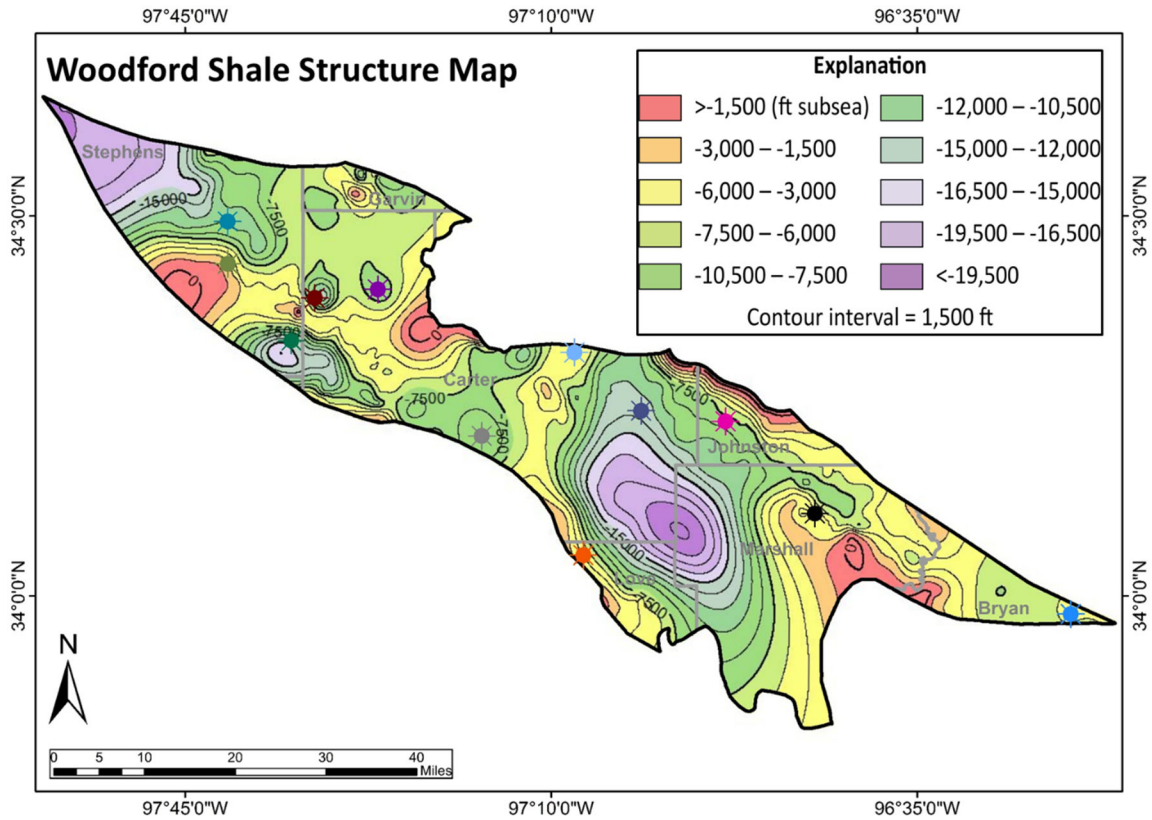


- Higley, D.K., 2013, 4D Petroleum System Model of the Mississippian System in the Anadarko Basin Province, Oklahoma, Kansas, Texas, and Colorado, USA: *The Mountain Geologist*, v. 50, p. 81–98.
- Higley, D.K., 2014, Thermal maturation of petroleum source rocks in the Anadarko basin province, Colorado, Kansas, Oklahoma, and Texas, *in* Higley, D.K., comp., *Petroleum systems and assessment of undiscovered oil and gas in the Anadarko Basin Province, Colorado, Kansas, Oklahoma, and Texas—USGS Province 58: U.S. Geological Survey Digital Data Series 69-EE*, chapter 3, 53 p., doi:10.3133 /ds69EE.
- Hoffman, P., Dewey, J.F., and Burke, K., 1974, Aulacogens and their genetic relation to geosynclines, with a Proterozoic example from Great Slave Lake, Canada: *SEPM Special Publication 19*, p. 38–55, doi: 10.2110/pec.74.19.0038.
- Huffman, G.G., Bridges, K.F., Ganser, R.W., Holtzman Jr., A.M., Merritt, M.L., 1987, *Geology and Mineral Resources of Marshall County, Oklahoma: Oklahoma Geological Survey Bulletin 142*, 126 p.
- Huffman, G.G., Hart, T.A., Olson, L.J., Currier, J.D., and Ganser, R.W., 1978, *Geology and mineral resources of Bryan County, Oklahoma: Oklahoma Geological Survey Bulletin 126*, 113 p.
- Johnson, K.S., 1989, Geologic evolution of the Anadarko Basin, *in* Johnson, K.S., ed., *Anadarko Basin symposium, 1988: Oklahoma Geological Survey Circular 90*, p. 3–12.
- Johnson, K.S., 2008, Geologic history of Oklahoma, *in* Johnson, K.S., and Luza, K.V., eds., *Earth sciences and mineral resources of Oklahoma: Oklahoma Geological Survey Educational Publication 9*, p. 3–5.
- Johnson, K.S., Amsden, T.W., Denison, R.E., Dutton, S.P., Goldstein, A.G., Rascoe, B., Jr., Sutherland, P.K., and Thompson, D.M., 1988, Southern Midcontinent region, *in* Sloss, L.L., ed., *Sedimentary cover-North American craton, U.S., The geology of North America: Boulder, Colorado., Geological Society of America*, v. D-2, p. 307–359.
- Johnson, K.S., and B.J., Cardott, 1992, Geologic framework and hydrocarbon source rocks of Oklahoma, *in* K.S. Johnson and B.J. Cardott, eds., *Source rocks in the southern Midcontinent, 1990 symposium: Oklahoma Geological Circular 93*, p. 21–37.
- Lewan, M.D., and Ruble, T.E., 2002, Comparison of petroleum generation kinetics by isothermal hydrous and nonisothermal open-system pyrolysis: *Organic Geochemistry*, v. 33, no. 12, p. 1457–1475, doi: 10.1016/s0146-6380(02)00182-1.
- McBee, Wilham, Jr., 1995, Tectonic and Stratigraphic Synthesis of Events in the Region of the Intersection of the Arbuckle and Ouachita Structural Systems, Oklahoma, *in* Johnson, K.S., ed, *Structural Styles in the Southern Midcontinent: 1992 Symposium, Oklahoma Geological Survey Circular 97*, p. 45–81.

- McGowen, J.H., Hentz, T.F., Owen, D.E., Pieper, M.K., Shelby, C.A., Barnes, V.E., 1967, Geologic atlas of Texas, Sherman sheet (revised 1991), University of Texas at Austin: Bureau of Economic Geology, Geologic Atlas of Texas 31, 1:250,000.
- McKenzie, D., 1978, Some remarks on the development of sedimentary basins: *Earth and Planetary Science Letters*, v. 40, no. 1, p. 25–32.
- Miser, H.D., 1954, Geologic map of Oklahoma: U. S. Geological Survey.
- Northcutt, R.A. and J.A. Campbell 1995, Geologic provinces of Oklahoma: AAPG Mid-Continent Section Meeting.
- Pepper, A.S., and Corvi, P.J., 1995a, Simple kinetic models of petroleum formation: Part I. Oil and gas generation from kerogen: *Marine and Petroleum Geology*, v. 12, p. 291–319.
- Pepper, A.S., and Corvi, P.J., 1995b, Simple kinetic models of petroleum formation: Part III. Modeling an open system: *Marine and Petroleum Geology*, v. 12, p. 417–452.
- Perry, W.J., 1989, Tectonic evolution of the Anadarko Basin region, Oklahoma: *US Geological Survey Bulletin* 1866-A, p. A1–A19, doi: 10.3133/b1866a.
- Prichett, B., 2015, Map of Oklahoma oil and gas fields distinguished by coalbed methane and field boundaries: Oklahoma Geological Survey, scale 1:500,000.
- Radonjic, M., Luo, G., Wang, Y., Achang, M., Cains, J., Katende, A., Puckette, J., Grammer, M., King, G.E., 2020, Integrated microstructural characterization of Caney Shale, OK: *SPE Reservoir Evaluation & Engineering*. Society of Petroleum Engineers, p. 1–11., doi: 10.15530/urtec-2020-2947.
- Scotese, C.R., 2002, <http://www.scotese.com>, (PALEOMAP website).
- Shatski, N.S., 1946, The great Donets Basin and the Wichita System; Comparative tectonics of ancient platforms: *Akademiya Nauk SSSR Izvestiya, Seriya Geologicheskaya* 6, p. 57–90.
- Stanley, T.M., and Chang, J.M., 2012, Preliminary geologic map of the Ardmore 30' × 60' quadrangle and the Oklahoma part of the Gainesville 30' × 60' quadrangle, Carter, Jefferson, Love, Murray, and Stephens Counties, Oklahoma: Oklahoma Geological Survey, scale 1:100,000.
- Suneson, N., 2020, *Roadside Geology of Oklahoma*: Missoula, MT, Mountain Press Publishing Company 385 p.
- Sweeney, J.J., and Burnham, A.K., 1990, Evaluation of a simple model of vitrinite reflectance based on chemical kinetics: *AAPG Bulletin*, v. 74, p. 1559–1570.
- Sweeney, R.E., and Hill, P.L., 2005, Nebraska, Kansas, and Oklahoma aeromagnetic and gravity maps and data: U.S. Geological Survey Data Series DS-138.

- Taff, J.A., 1901, Description of the Coalgate quadrangle [Indian Territory]: U.S. Geological Survey Geologic Atlas, Folio 74, p. 6.
- Thomas, W.A., 2011, The Iapetan rifted margin of southern Laurentia: *Geosphere*, v. 7, p. 97–120, doi: 10.1130/ges00574.1.
- Thomas, W.A., 2014, The southern Oklahoma transform-parallel intracratonic fault system in Suneson, N.H., ed., *Igneous and Tectonic History of the Southern Oklahoma Aulacogen*, Oklahoma Geological Survey Guidebook 38, p. 375–387.
- Tissot, B.P., and Welte, D.H., 1984, *Petroleum formation and occurrence*: Berlin, Germany, Springer Verlag, 699 p.
- Tomlinson, C.W., and W. McBee, Jr., 1959, Pennsylvanian sediments and orogenies of Ardmore district, Oklahoma, in *Petroleum geology of southern Oklahoma*: Ardmore Geological Society Publication, v. 2, p. 3–52.
- Turko, M., 2019, Structural analysis of the Wichita uplift and structures in the southeast Anadarko Basin, southern Oklahoma (Ph.D. Dissertation): Norman, University of Oklahoma, 188 p.
- Tweto, O., 1975, Laramide (Late Cretaceous-early Tertiary) orogeny in the southern Rocky Mountains, in Curtis, B., ed., *Cenozoic Geology of the Southern Rocky Mountains*: Geological Society of America Memoir 144, p. 1–44, doi: 10.1130/mem144-p1.
- Walker, W.M., 2006, Structural analysis of the Criner Hills, south-central Oklahoma (unpublished M.S. thesis): Waco, Baylor University, 64 p.
- Watts, A.B., and Ryan, W.B.F., 1976, Flexure of lithosphere and continental margin basins: *Tectonophysics*, v. 36, p. 35–44, doi: 10.1016/0040-1951(76)90004-4.
- Wavrek, D.A., 1992, Characterization of oil types in the Ardmore and Marietta basins, southern Oklahoma aulacogen, in Johnson, K.S., and Cardott, B.J., eds., *Source rocks in the southern Midcontinent*, 1990 Symposium: Oklahoma Geological Survey Circular 93, p. 185–195.
- Wygrala, B.P., 1989, Integrated study of an oil field in the southern Po Basin, north Italy: Jülich, Germany, *Berichte der Kernforschungsanlage Jülich* 2313, Zentralbibliothek der Kernforschungsanlage, 226 p.
- Ye, H., Royden, L., Burchfiel, C., and Schuepbach, M., 1996, Late Paleozoic deformation of interior North America: The greater Ancestral Rocky Mountains: *AAPG Bulletin*, v. 80, p. 1397–1432, doi: 10.1306/64ed9a4c-1724-11d7-8645000102c1865d.
- ZetaWare Utilities - BHT correction, 2003, <https://www.zetaware.com/utilities/bht/timesince.html> (accessed October 22, 2020).

APPENDICES



**Wells Used for Modeling**

- |              |               |                |                       |
|--------------|---------------|----------------|-----------------------|
| Starr 1-25   | Martin 1-14   | Dansby 1-3H    | B&W Tyson 1-8         |
| Hays 1-1H    | Martin 8-2 RD | Brock 9-1H     | Badger 2-23           |
| Stephen 1-6H | J. Paul 1-7   | J Little A 1-6 | Tomaney 1-35-34-27XHW |

**Figure 86.** Structural contour map of the top of the Woodford Shale and locations of wells used in burial and thermal history modeling.

**Table 10.** Locations and depths of corrected bottom-hole temperatures used in geothermal calculations.

UWI	Well Name	Surface Latitude	Surface Longitude	Depth (ft TVD)	Corrected Bottom-Hole Temp (°F)*
35019255380000	ALPINE MEADOWS	34.272162	-97.558471	10318	183
35019252420000	ARDMORE	34.291848	-97.030550	12925	216
35137251630000	BARNES WOOLF	34.540317	-97.899216	5876	151
35085212730000	BOSS HOGG	34.026714	-97.071204	12175	245
35137272940000	BULL DURHAM 10-3	34.403550	-97.607710	8050	184
35137273070000	BULL HEADED 4-2	34.407257	-97.616873	8550	187
35137273230000	BULL HEADED 4-3	34.411184	-97.620881	8070	186
35137273800000	BULL RIDER 9-5	34.399163	-97.626494	7835	170
35137237370000	COMMERCIAL-WHITE	34.394198	-97.718601	1671	144
35085212740000	DAISY DUKE	34.030429	-97.088699	12046	239
35137271730000	DYESS 1-1H	34.318153	-97.566000	14618	245
35019252880000	ELMORE	34.317167	-97.197556	11656	208
35095205660000	EXPLORER 8-6-7	34.050545	-96.604180	6679	176
35069000280000	F A CHAPMAN	34.238658	-96.820742	5026	132
35019248110000	FAMILY TRUST	34.327468	-97.145016	4300	163
35095205320000	FLENNIKEN	34.142945	-96.637199	5410	180
35137265780000	FLOYD SCOTT	34.611081	-97.936464	14800	237
35137266690000	FYNE	34.359485	-97.686411	2500	130
35069200820000	GODDARD	34.283388	-96.902822	10000	156
35095205200000	GODFREY	34.071231	-96.708868	2948	145
35095205180000	GODFREY	34.071295	-96.708697	5990	178
35137272080000	GOINS	34.565980	-97.730110	16267	244
35137274230000	GREEN RANCH 2-19	34.367977	-97.657816	3180	126
35137274770000	GREEN RANCH 5-19	34.371604	-97.661982	3200	130
35137274740000	GREEN RANCH 7-19	34.373386	-97.653185	2900	125
35049246760000	HICKS	34.534042	-97.481863	4000	150
35019260090000	HOMEWOOD RESORT	34.257583	-97.494283	8687	161
35013201530000	HONEA	33.962353	-96.323764	7800	182
35019248870000	JEAN	34.238899	-97.151362	6810	176
35013201350000	JOHNSON	33.995000	-96.550708	7400	186
35019250370000	KATHY	34.255433	-97.151378	6100	166
35049247100000	KILCREASE	34.544040	-97.414945	9974	144
35137274320000	NORTH ALMA PENN UNIT 112R	34.487693	-97.620790	5556	154
35137272090000	OCEANA	34.551183	-97.739020	17355	276
35049248360000	PARK A	34.556915	-97.478894	10899	193
35095204500000	PIERCE	34.068278	-96.948986	11250	194
35019258570000	POWERS	34.182773	-96.987794	15008	264
35137275040000	PRAIRIEDALE 1-35HW	34.520902	-97.701999	12720	186
35013201640000	RED RIVER SPUR 35-6-7	33.989097	-96.545149	11319	227
35137268710000	SCHOCK SIMS UNIT 10-4	34.429495	-97.585053	7300	162
35019254600000	SEOCU	34.259472	-97.382692	5680	150
35019259810000	SIERRA RANCH	34.256020	-97.524530	7672	182

35019254360000	STATE PARK	34.104531	-97.086067	11742	202
35137266630000	STEWIE GRIFFIN	34.616380	-97.924989	17946	269
35137260990000	SUTTLE	34.541321	-97.869102	5800	146
35019258650000	TATUMS DES MOINES	34.399193	-97.416920	2400	128
35019258460000	TATUMS DES MOINES	34.396824	-97.415607	2400	125
35019257060000	TATUMS DES MOINES	34.394649	-97.414280	2067	127
35013001140000	TURVILL TRUST	34.050714	-96.519614	8828	148
35095205170000	UNDERHILL	34.072806	-96.712639	3990	151
35095205100000	WHITSITT	34.068876	-96.583611	7000	182
35137261730000	WILDHORSE	34.612014	-97.919294	15939	226
35019259030000	WILLARD	34.170546	-96.980888	15477	242
35095205030000	WOODS	33.937097	-96.843695	10500	183
35019218140000	J LITTLE /A/	34.320861	-97.129717	11750	213
35019249850000	GORDAN	34.266409	-97.189504	9013	208
35019246020000	STRADER	34.312371	-97.109911	7182	170
35019262750000	CAROL	34.291008	-97.085138	3066	137
35019251630000	WALLS	34.265398	-97.087995	12021	236
35019251390000	STACY	34.265470	-97.104611	10095	204
35019252470000	RENO	34.260617	-97.132174	9016	207
35019252120000	CARTER	34.289300	-96.996835	10469	214
35019250100000	NICKEL HILL	34.267041	-96.959321	9979	199
35019252360000	KIRK	34.273752	-97.015699	17418	241
35019251780000	NICKEL HILL	34.259276	-96.934836	8804	204
35069200820000	GODDARD	34.283235	-96.902299	10000	173
35019248870000	JEAN	34.238766	-97.151097	6810	176
35069201000000	BARNES	34.230254	-96.932913	11370	219
35019257160000	ANDREW	34.302413	-97.423925	8366	163
35019255270000	LEDBETTER	34.291754	-97.423294	8875	180
35019258160000	WINKING OWL	34.301688	-97.441616	9980	184
35019262720000	SPRING CREEK	34.294400	-97.445999	9587	197
35019219730000	BOGGESS-BLANTON	34.290830	-97.445116	9701	206
35019253540000	ARBOR MIST	34.282826	-97.446005	8540	181
35019256870000	BLIND MOOSE	34.279826	-97.436866	7955	174
35019254670000	MAD DOG	34.276270	-97.428921	8200	184
35019253840000	LITTLE PENGUIN	34.260826	-97.420728	9717	192
35019255320000	SHARKS 29	34.272298	-97.437366	8442	188
35019253390000	CHARLES SHAW	34.268174	-97.429487	8800	172
35019254370000	BUFFALO SPRINGFIELD	34.257639	-97.441046	10931	217
35019253410000	PINK RIPPLE	34.284465	-97.459254	10504	188
35069201200000	WLC	34.231189	-96.850909	7814	175
35069200940000	BROCK	34.230071	-96.888920	9700	204
35069201010000	WASHITA RIVER	34.216773	-96.869998	9310	199
35069201060000	WLC	34.216636	-96.840052	8748	188
35069201150000	BICE	34.202331	-96.785278	4970	165
35069201520000	LOGAN BEARD	34.178192	-96.731764	7161	178
35069201570000	LOGAN BEARD	34.177156	-96.734612	7154	178
35069201530000	DOUGLAS HARRINGTON	34.184262	-96.744406	7924	182

35095206340000	LOGAN BEARD	34.170494	-96.725610	7488	186
35095206190000	LOGAN BEARD	34.163201	-96.730136	7640	183
35069200960000	BARKER	34.183528	-96.720936	6451	163
35095206350000	LOGAN BEARD	34.167060	-96.716599	7531	184
35095204650000	WATKINS TRUST	34.104042	-96.742248	7531	184
35095204680000	WATKINS TRUST	34.101540	-96.743049	5816	192
35095204760000	NEFF HEIRS 25	34.095166	-96.724892	6990	200
35095205200000	GODFREY	34.071288	-96.708873	2938	148
35085005930000	RHOADES-CAMERON UNIT	33.960339	-97.031338	7937	186

\*Bottom-hole temperatures corrected using ZetaWare's "Time Since Circulation Calculator".

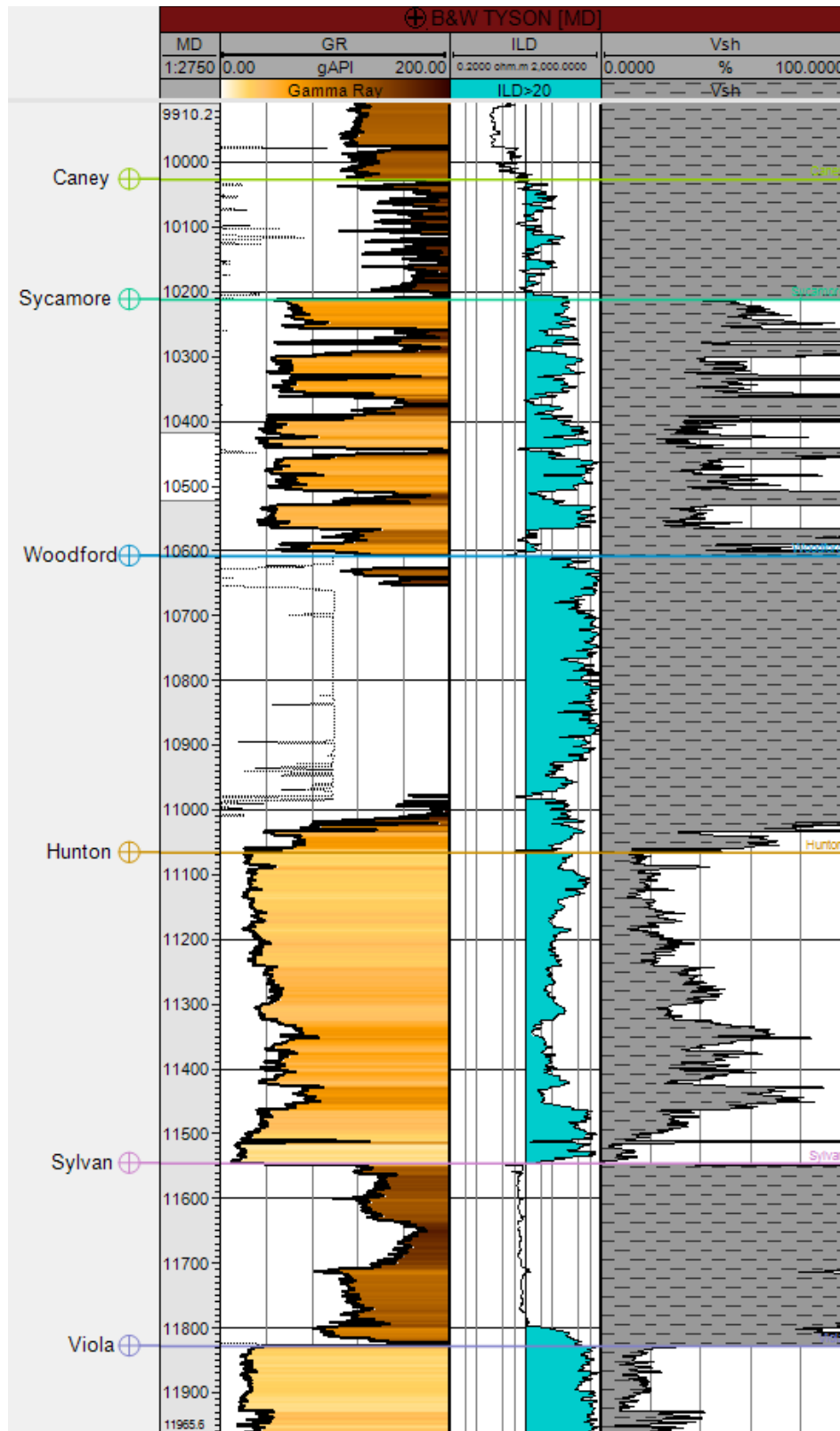
**Table 11.** Thermal maturity data from the Woodford Shale in the Ardmore Basin (from Cardott, personal communication, 2020).

<b>Latitude</b>	<b>Longitude</b>	<b>%R<sub>o</sub></b>	<b>Elevation*</b>	<b>Depth*</b>
34.133570	-96.768300	0.52	-4504.72	5332.3
34.124790	-96.612600	0.53	-3321.25	4013.07
34.335380	-97.287900	0.54	-5635.47	4662.06
33.998620	-97.085700	0.54	-1076.82	1792.14
33.971870	-97.062600	0.54	-3308.91	4023.87
34.078228	-97.151584	0.54	-1658.39	2549.06
34.359830	-97.506700	0.55	-3189.84	4274.52
34.076000	-96.559700	0.55	-2978.12	3591.21
34.008500	-96.564700	0.55	-386.03	873.29
34.089920	-96.712700	0.56	-5275.32	6025.96
34.009690	-97.043200	0.56	-7175.41	7871.54
34.335380	-97.287900	0.58	-5635.47	4662.06
34.343060	-97.284070	0.58	-558.49	286.73
34.371570	-97.557020	0.59	-3654.55	4704.69
34.327760	-97.478200	0.6	-4588.2	5613.23
34.050820	-96.641480	0.62	-2322.3	3013.3
34.414440	-97.503200	0.63	-7233.27	8276.23
34.075350	-96.716300	0.63	-2289.57	2940.97
34.309880	-97.137560	0.64	-5373.4	6058.09
34.288000	-97.124500	0.7	-7922.9	8588.21
34.086245	-96.635046	0.71	-4563.29	5315.6
34.073454	-96.584924	0.71	-3987.3	4665.9
34.040657	-96.555915	0.74	-4742.88	5396.07
34.261670	-96.961840	0.77	-8610.35	9326.35
34.069832	-96.635995	0.82	-4292.46	5017.63
34.113439	-96.672274	0.83	-6053.65	6807.71
34.298990	-97.172490	0.85	-5724.49	6553.99
34.127908	-96.665648	0.87	-6601.26	7363.02
34.164020	-96.730083	0.96	-5411.71	6200.54
34.173551	-96.792293	0.98	-7503.29	8259.96
34.269030	-97.507719	1.09	-9095.74	10033.54
34.244260	-96.912410	1.1	-8135.21	8872.92
34.244800	-96.974320	1.11	-10277.12	10975.79
34.182531	-96.862247	1.19	-10264.72	10955.89
34.159060	-96.787916	1.23	-7574	8357.76
34.287887	-97.072195	1.31	-11647.01	12477.02
34.289783	-97.072131	1.34	-11580.71	12411.5

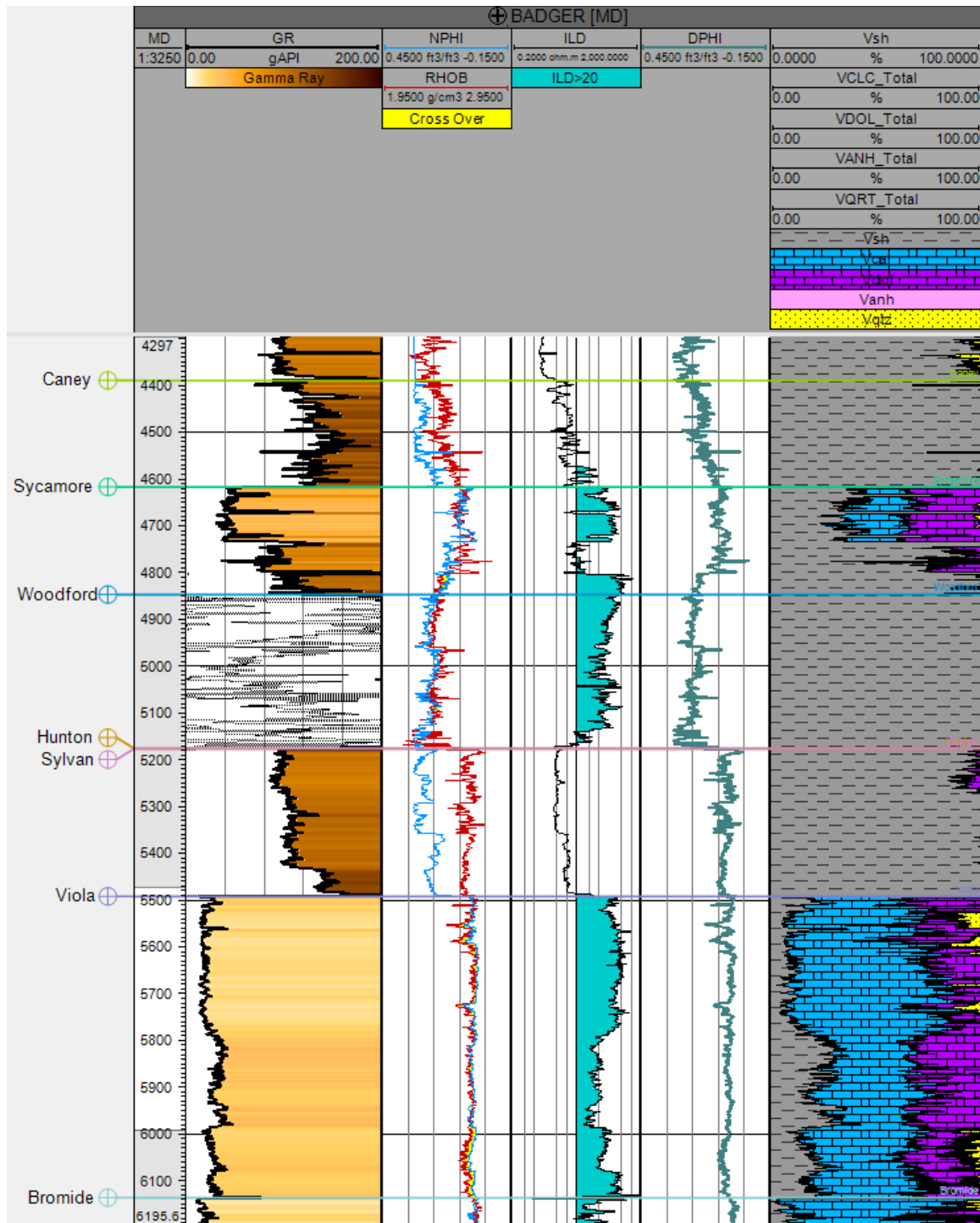


34.215359	-96.949727	1.37	-9440.8	10173.53
34.231707	-97.059026	1.6	-13826.32	14584.77
34.155397	-96.914614	1.68	-12491.59	13479.69
34.169898	-96.971634	1.8	-14854.03	15686.68
34.153270	-97.093400	2.13	-16374.51	17196.9
34.111260	-97.068100	2.19	-17036.62	17819.19
34.090780	-97.033300	2.22	-17304.99	18098.31
34.043870	-96.954300	2.45	-17778.9	18497
34.446367	-97.559333	0.71	-6955.85	7982.12
34.550075	-97.535236	0.66	-7366.47	8418.11
34.498237	-97.541930	0.57	-8857	9798.04
34.586453	-97.714621	0.54	-8066.23	9218.56
34.458510	-97.781556	0.52	-2105.11	2982.49
34.423181	-97.679815	0.49	-2233.97	3419.61

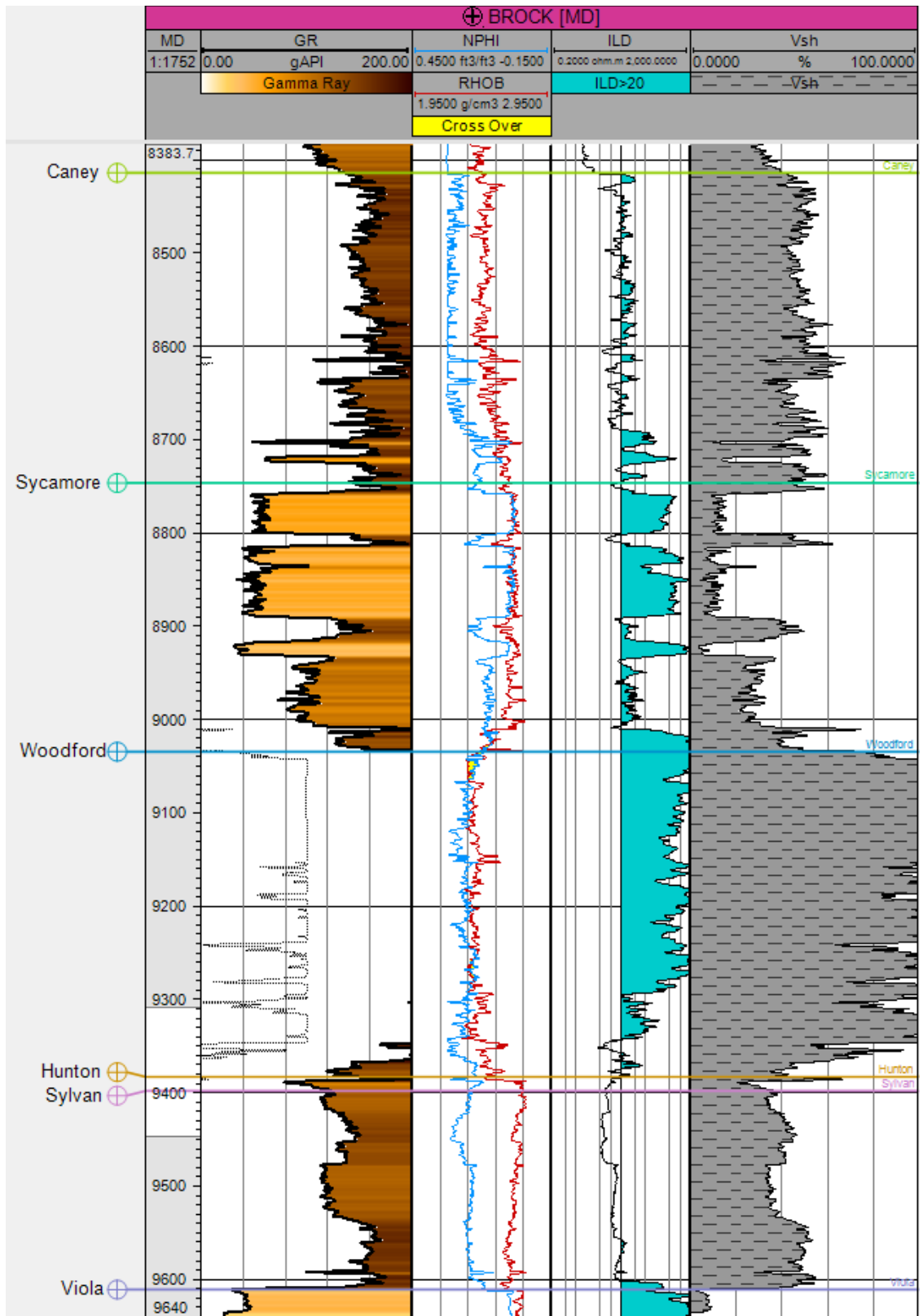
\*Elevations and depths derived from project mapping efforts.



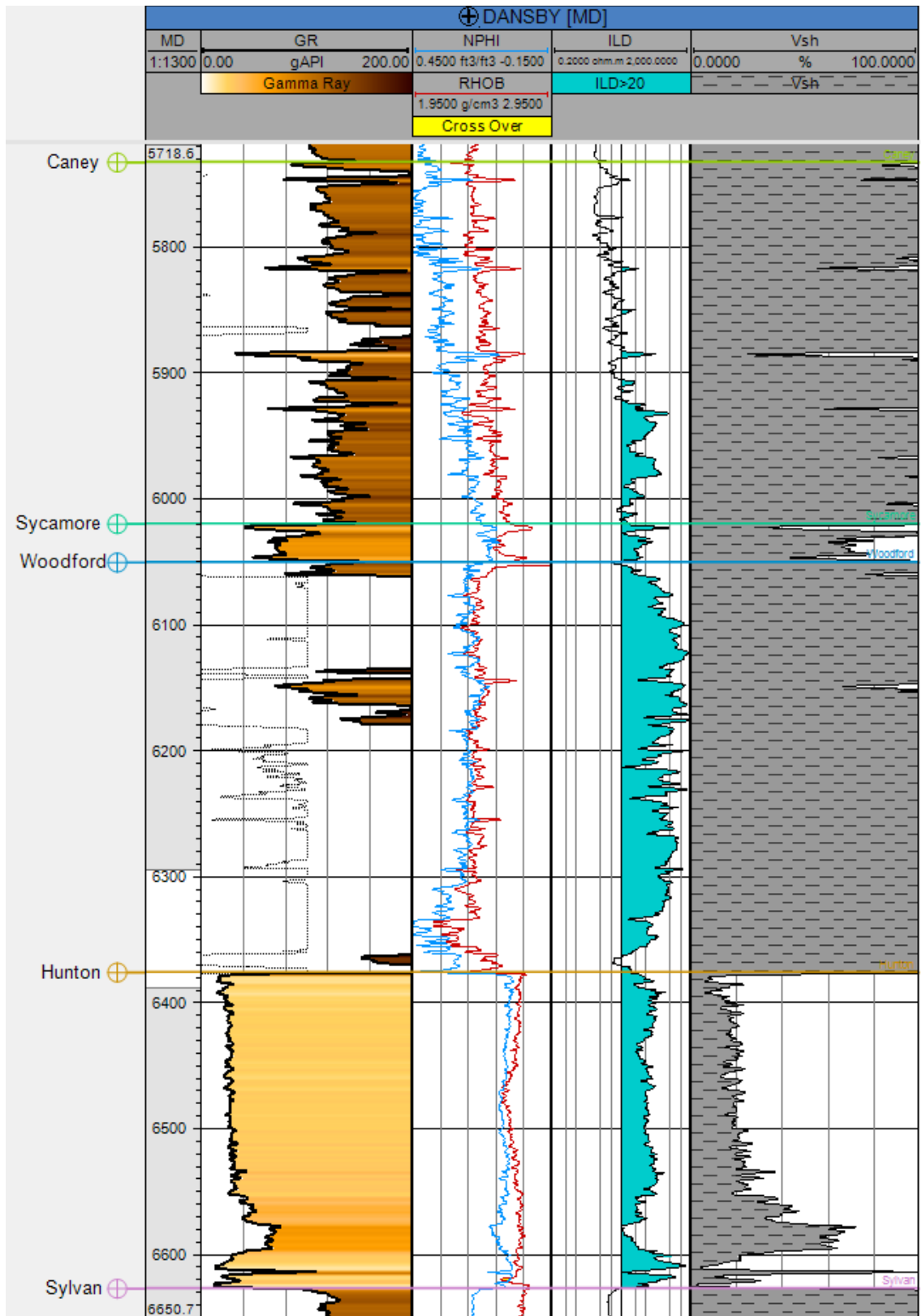
**Figure 87.** Geophysical well log of the B&W Tyson 1-8 well. GR = gamma ray, ILD = deep resistivity, Vsh = shale volume.



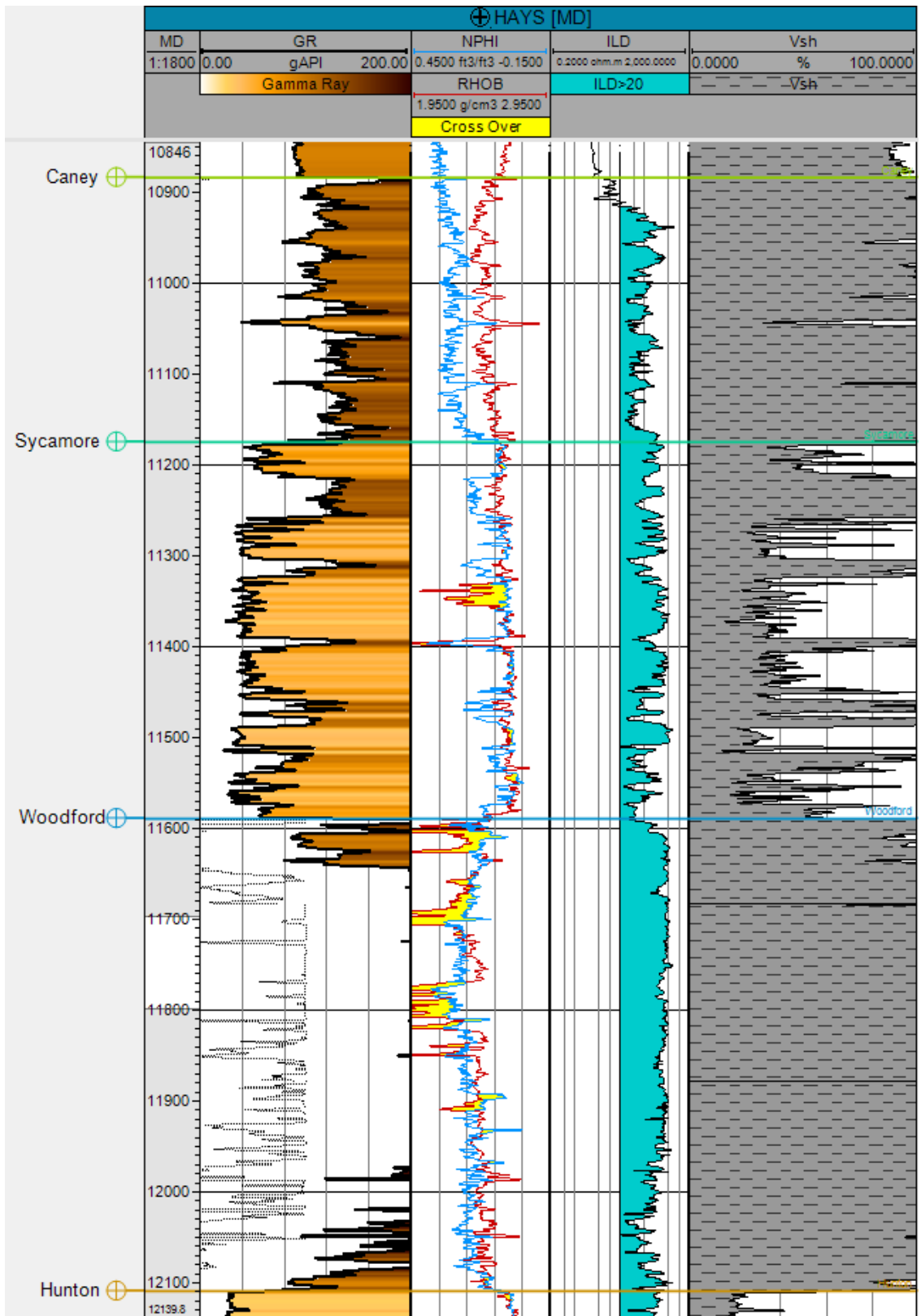
**Figure 88.** Geophysical well log of the Badger 2-23 well. GR = gamma ray, NPHI = neutron porosity, RHOB = bulk density, ILD = deep resistivity, DPHI = density porosity, Vsh = shale volume, VCLC\_Total = calcite volume, VDOL\_Total = dolomite total, VANH\_Total = anhydrite volume, VQRT\_Total = quartz volume.



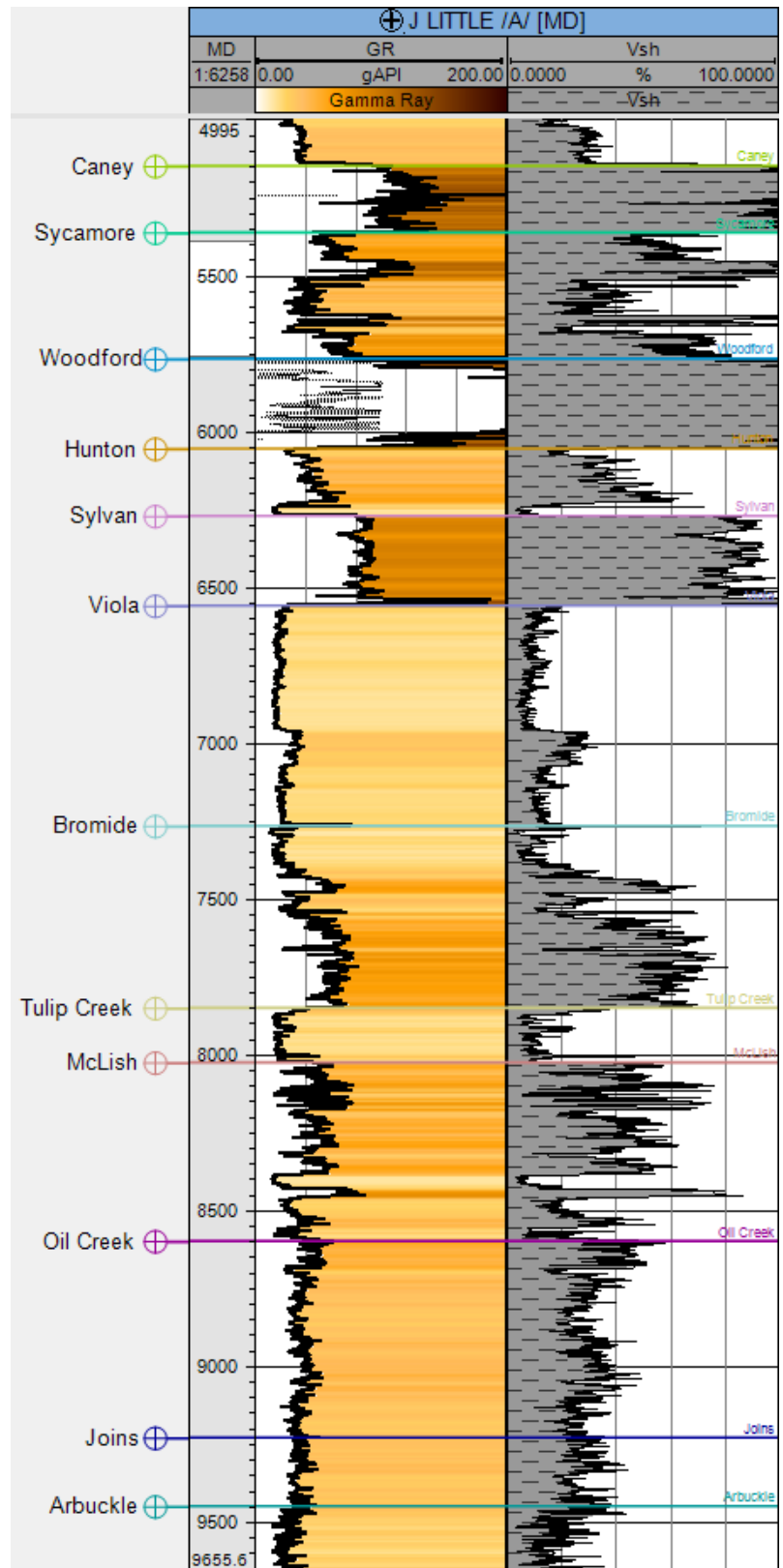
**Figure 89.** Geophysical well log of the Brock 9-1H well. GR = gamma ray, NPHI = neutron porosity, RHOB = bulk density, ILD = deep resistivity, Vsh = shale volume.



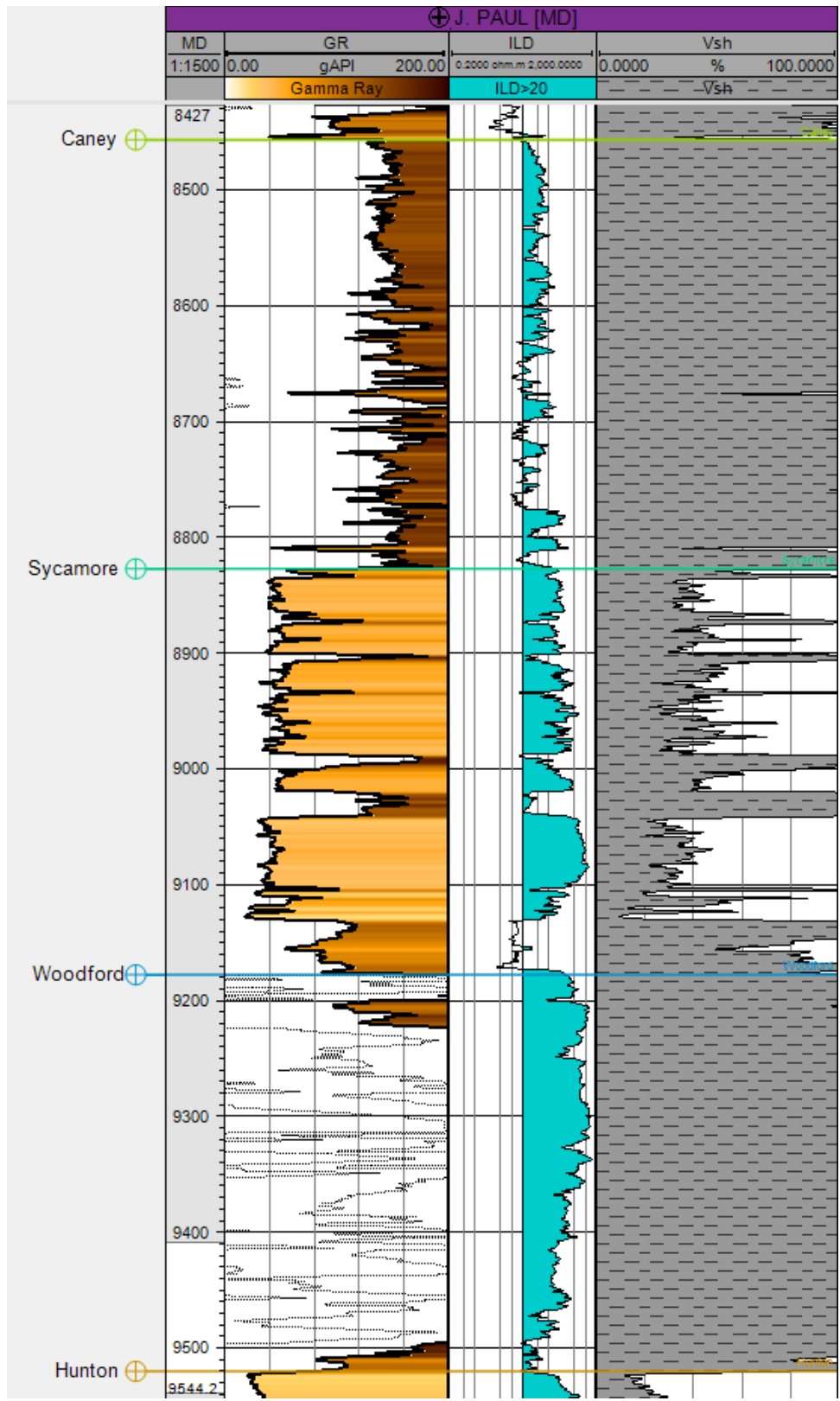
**Figure 90.** Geophysical well log of the Dansby 1-3H well. GR = gamma ray, NPHI = neutron porosity, RHOB = bulk density, ILD = deep resistivity, Vsh = shale volume.



**Figure 91.** Geophysical well log of the Hays 1-1H well. GR = gamma ray, NPHI = neutron porosity, RHOB = bulk density, ILD = deep resistivity, Vsh = shale volume.

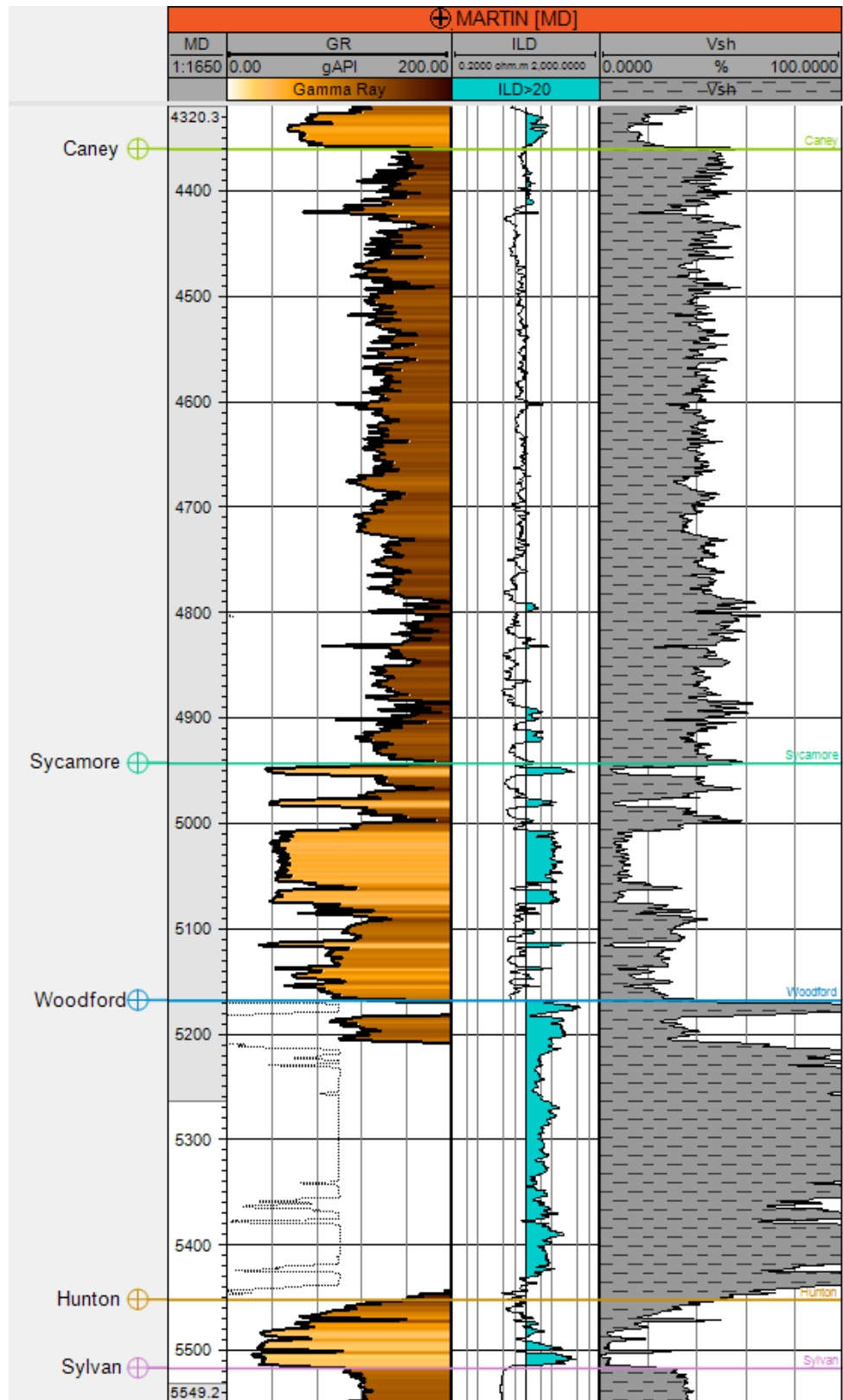


**Figure 92.** Geophysical well log of the J Little A-1-6 well. GR = gamma ray, Vsh = shale volume.

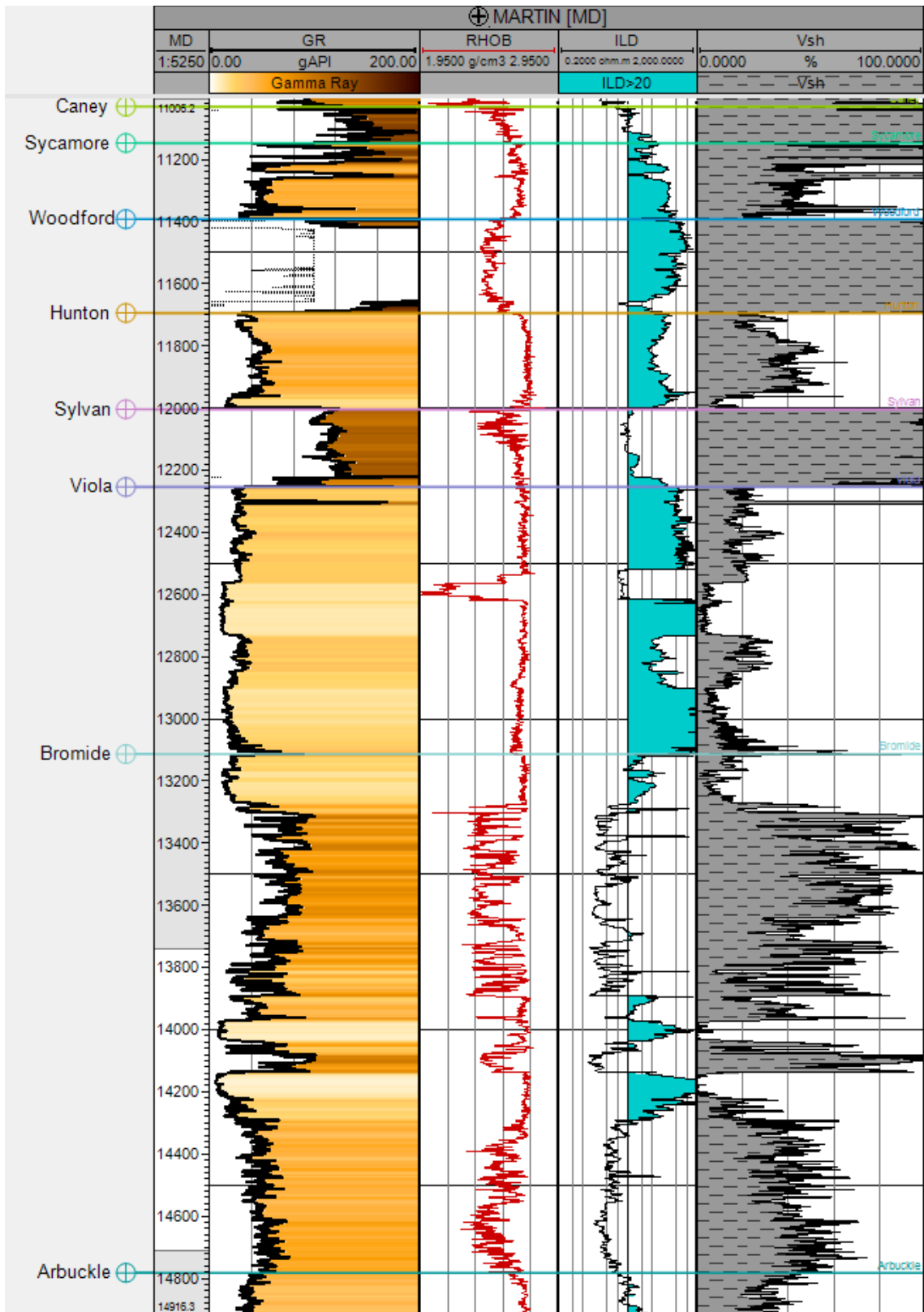


**Figure 93.** Geophysical well log of the J Paul 1-7 well. GR = gamma ray, ILD = deep resistivity, Vsh = shale volume.

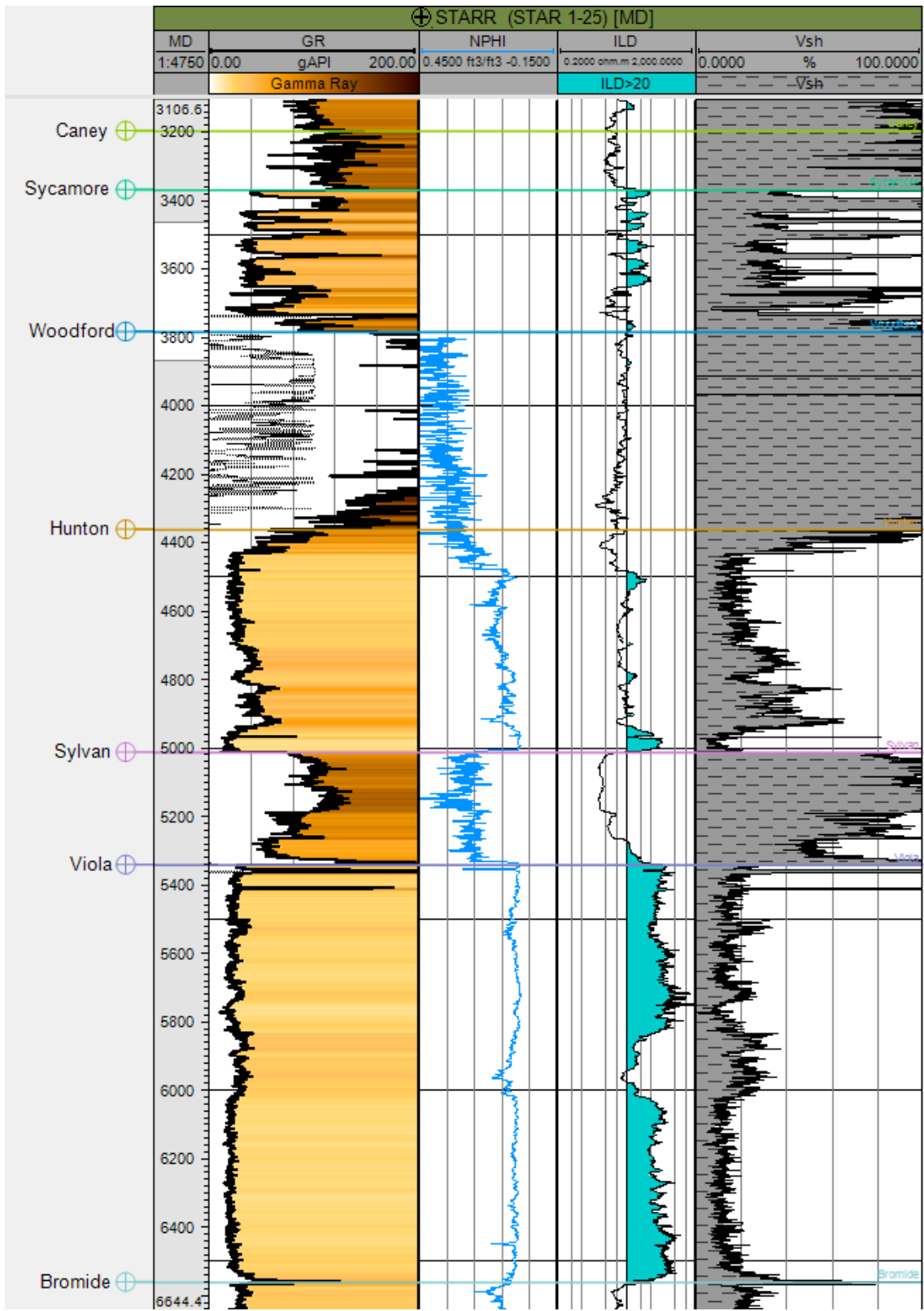




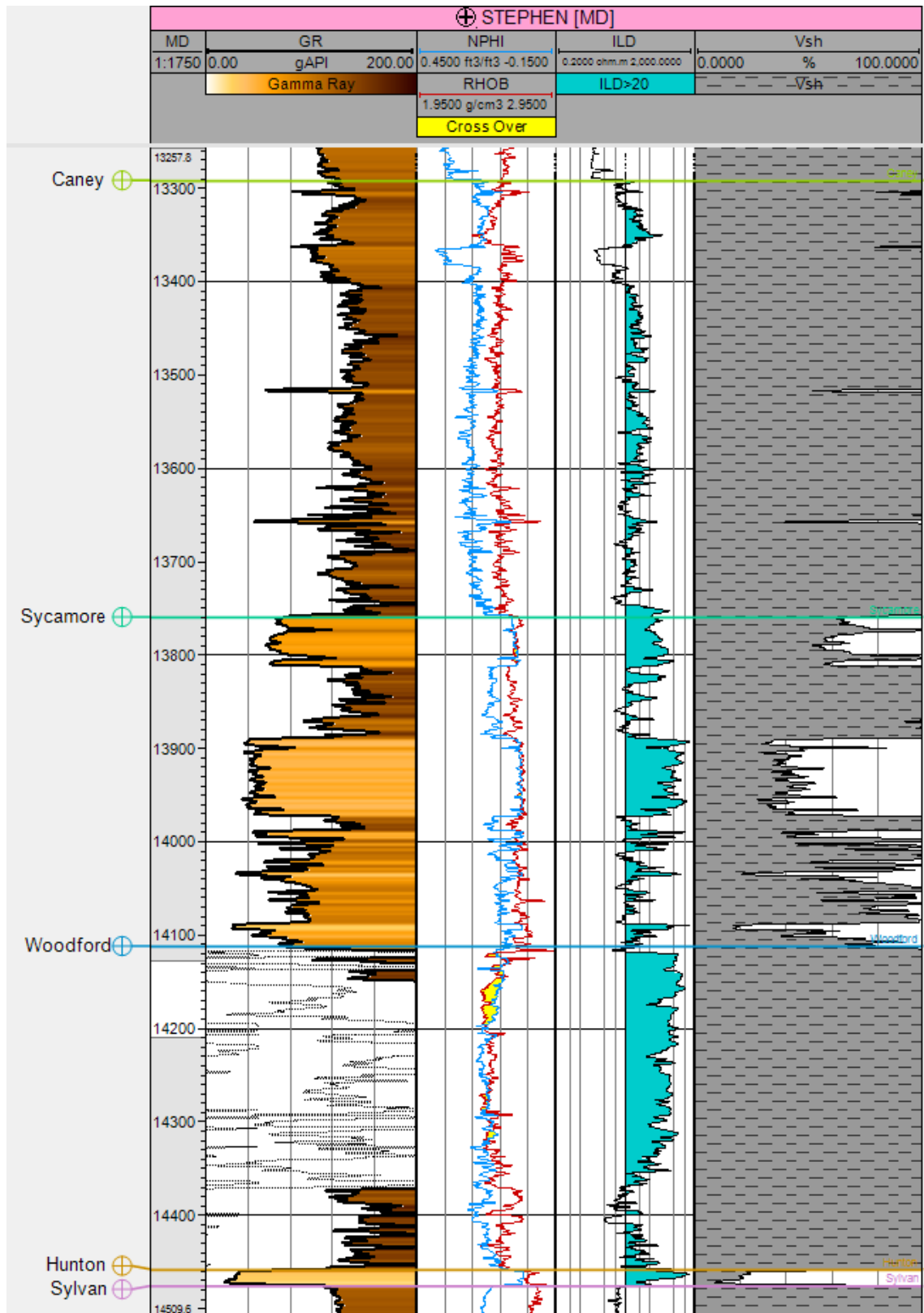
**Figure 94.** Geophysical well log of the Martin 8-2 RD. GR = gamma ray, ILD = deep resistivity, Vsh = shale volume.



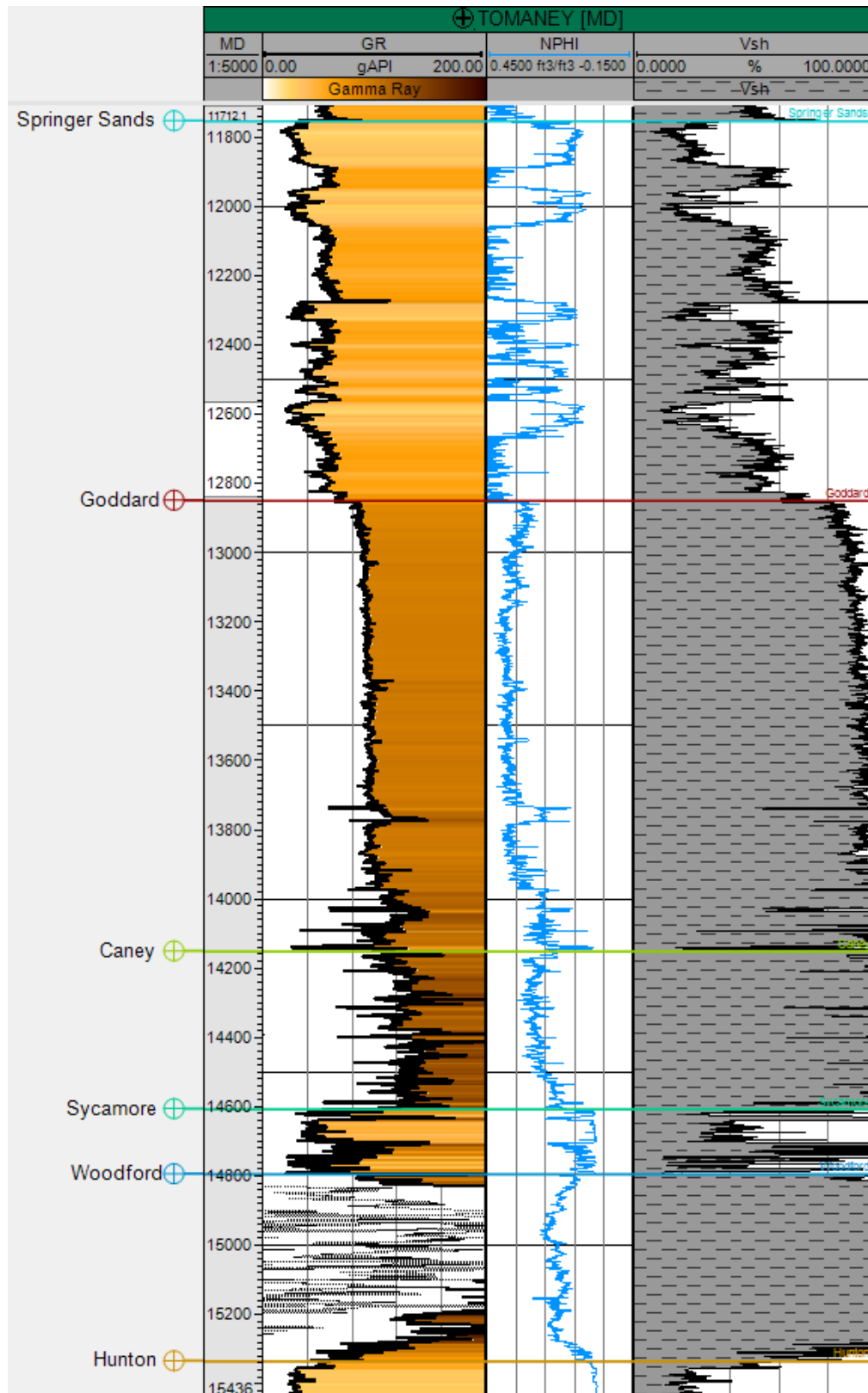
**Figure 95.** Geophysical well log of the Martin 1-14 well. GR = gamma ray, RHOB = bulk density, ILD = deep resistivity, Vsh = shale volume.



**Figure 96.** Geophysical well log of the Starr 1-25 well. GR = gamma ray, NPHI = neutron porosity, ILD = deep resistivity, Vsh = shale volume.



**Figure 97.** Geophysical well log of the Stephen 1-6H well. GR = gamma ray, NPHI = neutron porosity, RHOB = bulk density, ILD = deep resistivity, Vsh = shale volume.



**Figure 98.** Geophysical well log of the Tomaney 1-35-34-27XHW well. GR = gamma ray, NPHI = neutron porosity, Vsh = shale volume.

## VITA

Ian Anthony Allan Cox

Candidate for the Degree of

Master of Science

Thesis: INTEGRATED STRATIGRAPHIC, STRUCTURAL, TECTONIC, AND  
PETROLEUM SYSTEMS ANALYSIS OF THE MISSISSIPPIAN CANEY  
SHALE, ARDMORE BASIN, SOUTHERN OKLAHOMA

Major Field: Geology

Biographical:

Education:

Completed the requirements for the Master of Science in Geology at Oklahoma State University, Stillwater, Oklahoma in December, 2021.

Completed the requirements for the Bachelor of Science in Geology at Western Colorado University, Gunnison, Colorado in 2019.

Experience:

Intern Exploration Geologist, Lehigh Hanson Inc., May 2021–August 2021

Intern Petroleum Geologist, Concho Resources Inc., June 2020–August 2020

Intern Exploration Geologist, Newmont Mining Corp., May 2017–August 2017

Well Site Geologist / Mud Logger / Geosteerer, Décollement Consulting Inc.,  
May 2016–August 2016

Intern Exploration Geologist, Antero Resources Corp., May 2015–August 2015

Professional Memberships:

Registered Geologist-In-Training in Kansas, American Association of  
Petroleum Geologists, Geological Society of America, Oklahoma City  
Geological Society, Rocky Mountain Association of Geologists, Society for  
Mining, Metallurgy & Exploration, Tulsa Geological Society